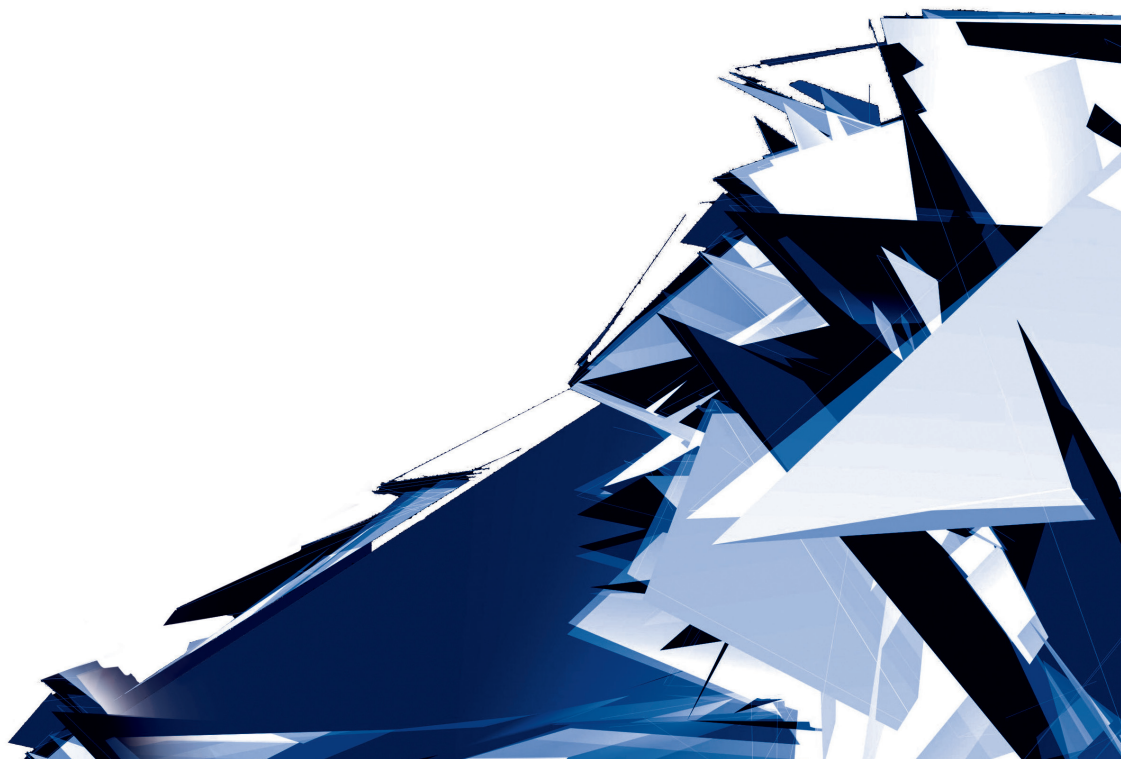


# Technical Transactions

Czasopismo Techniczne

Issue 12

Volume 2018 (115)



**Chairman of the Cracow University of Technology Press Editorial Board**  
**Przewodniczący Kolegium Redakcyjnego Wydawnictwa Politechniki Krakowskiej**

Tadeusz Tatara

**Editor-in-chief**  
**Redaktor naczelny**

Józef Gawlik  
jgawlik@mech.pk.edu.pl

**Scientific Council**  
**Rada Naukowa**

Jan Błachut – University of Liverpool (UK)  
Wojciech Bonenberg – Poznan University of Technology (Poland)  
Tadeusz Burczyński – Silesian University of Technology (Poland)  
Massimo Corcione – Sapienza University of Rome (Italy)  
Leszek Demkowicz – The University of Texas at Austin (USA)  
Joseph El Hayek – University of Applied Sciences (Switzerland)  
Ameen Farooq – Technical University of Atlanta (USA)  
Zbigniew Florjańczyk – Warsaw University of Technology (Poland)  
Marian Giżewski – Warsaw University of Technology (Poland)  
Sławomir Gzell – Warsaw University of Technology (Poland)  
Allan N. Hayhurst – University of Cambridge (UK)  
Maria Kušnierova – Slovak Academy of Sciences (Slovakia)  
Krzysztof Magnucki – Poznan University of Technology (Poland)  
Herbert Mang – Vienna University of Technology (Austria)  
Arthur E. McGarity – Swarthmore College (USA)  
Antonio Monestiroli – Polytechnic of Milan (Italy)  
Ivor Samuels – University of Birmingham (UK)  
Miroslaw J. Skibniewski – University of Maryland (USA)  
Günter Wozny – Technical University in Berlin (Germany)  
Roman Zarzycki – Lodz University of Technology (Poland)

**Native Speakers**

**Weryfikacja językowa**

Tim Churcher  
Robin Gill  
Mike Timberlake

**Section Editor**  
**Sekretarz Sekcji**

Dorota Sapek  
dsapek@wydawnictwo.pk.edu.pl

**Editorial Compilation**  
**Opracowanie redakcyjne**

Aleksandra Urzędowska  
aurzedowska@pk.edu.pl

**Typesetting**  
**Skład i łamanie**

Anna Basista

**Design**  
**Projekt graficzny**

Michał Graffstein

**Series Editors**  
**Redaktorzy Serii**

**ARCHITECTURE AND URBAN PLANNING**

Mateusz Gyurkovich  
mgyurkovich@pk.edu.pl

**CHEMISTRY**

Radomir Jasiński  
radomir@chemia.pk.edu.pl

**CIVIL ENGINEERING**

Marek Piekarczyk  
mpiekar@pk.edu.pl

**ELECTRICAL ENGINEERING**

Piotr Drozdowski  
pdrozdow@usk.pk.edu.pl

**ENVIRONMENTAL ENGINEERING**

Michał Zielina  
mziel@vistula.wis.pk.edu.pl

**PHYSICS, MATHEMATICS  
AND COMPUTER SCIENCES**

Włodzimierz Wójcik  
puwojczik@cyf-kr.edu.pl

**MECHANICS**

Andrzej Sobczyk  
andrzej.sobczyk@mech.pk.edu.pl

[www.ejournals.eu/Czasopismo-Techniczne](http://www.ejournals.eu/Czasopismo-Techniczne)  
[www.technicaltransactions.com](http://www.technicaltransactions.com)  
[www.czasopismotechniczne.pl](http://www.czasopismotechniczne.pl)

© 2018 Cracow University of Technology  
ISSN 0011-4561

Creative Commons (CC BY-NC-SA 4.0)  
<https://creativecommons.org/licenses/by-nc-sa/4.0/legalcode.pl>

Basic version of each Technical Transactions magazine is its online version  
Pierwotną wersją każdego zeszytu Czasopisma Technicznego jest jego wersja online

## Contents

### ARCHITECTURE AND URBAN PLANNING

Małgorzata Lisińska-Kuśnierz, Michał Krupa <i>Eye tracking in research on perception of objects and spaces</i> .....	5
Łukasz Kamil Mazur <i>Living in the future – analysis of selected housing environments</i> .....	23
Filip Suchoń <i>The hidden treasure</i> .....	33
Ewelina Woźniak-Szpakiewicz, Shouliang Zhao <i>Modular construction industry growth and its impact on the built environment</i> .....	43

### CIVIL ENGINEERING

Michał Grodecki, Aleksander Urbański <i>Landsliding slope supported by gabions – a case study and the methodology of numerical modelling</i> .....	53
Mariusz Maślak, Piotr Woźniczka, Michał Pazdanowski <i>Forecast of a fire spreading in a large-area shopping hall</i> .....	61
Edyta Pięciorak, Marek Piekarczyk, Henryk Ciurej, Michał Betlej <i>The determination of moment resistance for a liner tray restrained by sheeting according to european standard PN-EN 1993-1-3</i> .....	77
Aleksander Urbański, Krzysztof Podleś <i>A 2D/3D method of the groundwater flow and stability analysis of a slope with dewatering wells</i> .....	95
Andrzej Więckowski, Karol Ryż, Wojciech Sikora <i>Failures of suspended ceilings and execution errors</i> .....	107

### COMPUTER SCIENCES

Marcin Jaraczewski <i>Reactive T-topology four-terminal-network compensator for multiharmonic current</i> .....	117
--	-----

### ELECTRICAL ENGINEERING

Włodzimierz Jefimowski, Adam Szelaż <i>Assessment of AC traction substation influence on energy quality in a supplying grid</i> .....	127
--	-----


### ENVIRONMENTAL ENGINEERING

Tomasz Baczyński, Piotr Beńko <i>A commentary on the respirometric evaluation of biodegradable COD fractions in industrial wastewater</i> .....	139
--	-----

## MECHANICS

Andrzej Bąkowski, Leszek Radziszewski, Paweł Świetlik, Milan Žmindak <i>Analysis of information content of in-cylinder pressure signal deviations from the mean values</i> .....	151
Łukasz Dragun, Jerzy Jaroszewicz, Leszek Radziszewski, Vladimir Antoniuk <i>Selected operating problems of central pumps</i> .....	159
Monika Krzywicka, Szymon Tofil, Krzysztof Pałka <i>Selection of parameters for laser surface texturing of titanium alloys</i> .....	167
Dariusz Kurczyński, Piotr Łagowski, Vasyl Tomyuk <i>Selected aspects of dual-fuelling of the perkins 1104D-E44TA engine with natural gas and diesel fuel</i> .....	173
Medard Makrenek, Wojciech Żórawski, Anna Góral <i>Using the taguchi method to optimize controlled variables in the experiment to produce a Ti coating by cold spraying</i> .....	179
Tomasz Milek <i>The effect of degree of deformation on forward slip in experimental research on cold longitudinal rolling of flat bars made from EN AW-6063 aluminium alloy</i> .....	185
Łukasz J. Orman, Norbert Radek, Andrej Kapjor, Dariusz Karpisz <i>Passive methods of boiling heat transfer enhancement</i> .....	193

Małgorzata Lisińska-Kuśnierz  [orcid.org/0000-0003-0087-6427](https://orcid.org/0000-0003-0087-6427)  
Faculty of Commodity Science and Product Management, Cracow University of Economics

Michał Krupa  [orcid.org/0000-0003-0093-2249](https://orcid.org/0000-0003-0093-2249)  
[michal.krupa@pk.edu.pl](mailto:michal.krupa@pk.edu.pl)  
Faculty of Architecture, Cracow University of Technology

## EYE TRACKING IN RESEARCH ON PERCEPTION OF OBJECTS AND SPACES

## OKULOGRAFIA W BADANIACH POSTRZEGANIA OBIEKTÓW I PRZESTRZENI

### Abstract

The article is devoted to the visual perception of selected architectonic objects and urban space in the health resort in Rabka-Zdrój. Eye-tracking research was presented in its theoretical aspect, and then results of research carried out using a stationary eye-tracker were also presented. An analysis of experiment results allowed for determining the usefulness of eye-tracking research in learning the range and manner of perceiving architectonic objects and urban spaces by people looking at them. The usefulness of the discussed research in working out assumptions and activities related to protecting historic objects and spaces as well as educational activities was indicated.

**Keywords:** eye-tracking method, visual perception, architectonic objects and urban space

### Streszczenie

Artykuł poświęcony jest percepcji wzrokowej wybranych obiektów architektonicznych i przestrzeni urbanistycznych w uzdrowisku Rabka-Zdrój. Zaprezentowano w ujęciu teoretycznym badania okulograficzne, a następnie przedstawiono wyniki badań przeprowadzonych z wykorzystaniem eye-trackera stacjonarnego. Analiza wyników eksperymentu pozwoliła na stwierdzenie przydatności badań okulograficznych do poznania zakresu i sposobu postrzegania obiektów architektonicznych i przestrzeni urbanistycznych przez osoby na nie patrzące. Wskazano na przydatność przedmiotowych badań przy opracowywaniu założeń i działań związanych z ochroną obiektów i przestrzeni zabytkowych oraz działań edukacyjnych.

**Słowa kluczowe:** metoda eye tracking, percepcja wzrokowa, obiekty architektoniczne i przestrzeń urbanistyczna

## 1. Introduction

The issue of learning the reasons why the very poor condition of historic objects is accepted in many, particularly small, historic Polish towns in which local communities do nothing or do too little to prevent degradation of those objects is important with regard to the effectiveness of revalorization and protection activity [1].

The aim of this work is presenting the usefulness of eye-tracking research in assessing what conditions social attitudes towards architectonic objects and urban spaces, especially indifference towards degradation of objects in the closest vicinity.

So far, eye-tracking research has been found useful in such disciplines as psychology, medicine, ergonomics, interaction man-computer or marketing [2–4]. Nowadays research has also commenced concerning man's perception of works of art, industrial forms and products and their packaging [5–7].

Applying the eye-tracking method in this new suggested area should allow for evaluating the range and manner of perceiving architectonic objects and urban spaces by people looking at them. Hence, it will allow for relatively objectively assessing the manner of perceiving diverse information reaching a man and affecting the way of building and the structure of his own knowledge and awareness.

An example of a town that struggles with a serious threat to its cultural landscape is Rabka-Zdrój, which is the subject of studies concerning urban-architectonic aspects of cultural heritage conducted by the authors of this work for many years. The undertaken research regarding assessing the visual perception of visualisations of selected objects and spaces in Rabka-Zdrój constitute the next stage of research aimed at finding the answer to the question whether one of the reasons behind the poor state of the cultural landscape of that health resort could be ignoring its cultural heritage and, consequently, lack of awareness of its value [8, 1].

## 2. Nature of eye-tracking research

The issue concerning the eye-tracking method has been addressed in work presenting scientific assumptions referring to conducting an experiment and indicating possibilities of its application. Among the most important volumes in the literature on the subjects are publications by D. Richardson [9], A. Duchowski [10] and K. Hoolmovist, M. Nystrom, R. Andersson and others [11], which constitute a compendium of knowledge about that research method. Other studies worth mentioning are: a publication by A. Bojko [12] and the work edited by M. Horsley, M. Eliot, B. Knight and R. Reilly [13]. Among Polish publications indirectly concerning the application of the eye-tracking method also in the research on the perception of space one should point out the publication by R. Wawer [14], as well as by R. Wawer and M. Pakuła [15]. So far, the issue of usefulness of the method in the research on historical architectonic space has only been addressed in the work by M. Krupa [8] and in the work by B. Kabaj and M. Krupa [16]. In the world the issues connected to eye tracking in the research on architecture and space have been discussed by the team: Ch. Lebrun, A. Sussman, W. Crolius, and G. van der Linde

from the Institute for Human Centered Design in Boston [17], and D. Junker and Ch. Nollen from the University of Applied Science in Osnabruck [18].

It is worth mentioning that although the application of the method in the architecture-related research is innovative, the method itself was invented in the 19<sup>th</sup> century, or more precisely in 1878, by Louis E. Jave, who had a fluorescent gauge fixed to the eye cornea, which allowed him to record and analyse eye movements. Another step in the development of the method was made by R. Dodge and T.S. Cline who created the first eye-tracker, which took place in the United States in the year 1901 [9]. In the following years, both the method and the device were improved. Around the mid-20<sup>th</sup> century, H. Hertridge and L.C. Thomson devised an eye tracker in the form of a helmet, thanks to which the research yielded even better effects. In the year 1958, A. Mackworth improved the method by combining the recorded information with the changing image [14]. In time computer work was added to the eye tracking method, thanks to which its results are even more precise and, first of all, can be analysed and examined from multiple angles [14, 15].

Nowadays, in the literature of the subject eye tracking is presented as a method for measuring, recording and analysing data about the position and movements of eye balls within a given time bracket. The functioning of eye trackers is based on the method called the corneal reflection. A high-resolution camera tracks the position of pupils which are illuminated by infrared light invisible to man. The infrared light is mirrored in the eyes creating reflections (known in physics as Purkinje reflection) clearly visible in the pupils, which serve to identify the place which the viewer is looking at in a given moment [12, 2, 3].

Thus it is possible to precisely present the eye movements of the research participant.

A typical measurement involves the analysis of:

- ▶ fixation – eye movements that stabilise the retina above an immobile object (they are very short; last between 100 and 600 milliseconds),
- ▶ saccade – a rapid shift from observing one focal point to another (they take between 20 and 40 milliseconds),
- ▶ total or average time devoted to observing given elements,
- ▶ number of revisits – repeated viewing of given elements [10].

It is assumed that the cognitive process occurs during the fixation, i.e. information reaches the brain and is consciously processed. On the other hand, during the saccade stimuli reaching the brain are not analysed and the cognitive process does not take place [14].

Eye movements are recorded in the form of quantitative data. Additionally, measurements are created that allow for interpreting the way of perceiving elements presented on the screen. Eye tracker software makes it possible to generate data visualisations. Input data include identification of places at which the research participant looked, the time spent viewing the material and marking the path that his eyes followed. The most frequently used forms of graphic presentation of the data obtained during the research are: heat maps, a scan path and an analysis of areas of interest [13, 10, 4].

A heat map allows for determining which of the presented elements attracted the research participant's attention. In the case of each material presented on the screen, it is possible to use different colours to show places where the research participants fixed their eyes while

presenting concise results for attention focus in each group of research participants. Focusing attention in one point for a longer time is marked by an intensive warm colour, while cool colours indicate a shorter focusing time. Places devoid of colouring indicate fragments that were completely ignored by the viewer. A specific example of a heat map is the reversed version showing exclusively the spots on which research participants focused their attention. Other areas remain darkened [12, 2].

The second form of graphic presentation is a scan path that indicates the order in which particular areas were noticed while observing a given image. Circles indicate subsequent spots on which the viewer focused his attention (fixations). The bigger the diameter of the circle, the longer the viewer kept his eyes on a given object. Numbering within the circle shows the order of viewing, and lines symbolise saccade movements indicating the scan path the eye followed to the next focal point [10, 11, 9].

The third form of graphic presentation is the AOI – Area of Interest. An analysis allows here for selecting those looks, from among a large number of them, which refer to specific places presented on the screen. AOI can be designed independently by the leader of the research (in the shape of a rectangle, an ellipsis or a polygon) or generated automatically with a percent recording of the distribution of focus. The advantage of areas of interest over heat maps lies in the possibility of obtaining concrete Figures that allow for carrying out a thorough quantitative analysis of focus and using parametric measurements. The applied so called statistics vary depending on the aim of the research.

While analysing the areas of interest it is standard to determine the following measurements:

- ▶ the time that passes until the first fixation in the given AOI (ITFF – Time to First Fixation); allows for determining how much time the viewer needs to find a given area significant from the viewpoint of realisation of the research goal,
- ▶ the number of fixations within a given AOI during observation for one of all research participants; it is assumed that a larger number of fixations confirms a more intensive interest in a given area,
- ▶ the time all the fixations within a given area last,
- ▶ the number of visits within a given area during observation for one or all research participants; it is assumed that the larger number of visits within an area, the more interesting it is from the perspective of the viewer (can present interest in a novelty or difficult content, hence the return to them in order to understand information) [12, 13, 10, 2].

In each area or photograph considered in the research, after determining AOI there is usually an area that remains unclassified (Not on AOI). That latter area, though uninteresting from the viewpoint of measuring the degree of perception of objects constituting an AOI, can also be included in an analysis taking into account the possible occurrence of other attractors (elements attracting attention) and distractors (elements distracting the viewer) [14, 15].

Summing up, the main advantage of the eye-tracking research is the fact that it allows for objectively assessing the perceptive activity of the research participants. Tracking eye movement allows for reflecting those elements in the analysed image of the object to which a viewer really pays attention. Therefore results are based on facts, and not declarations or assumptions [11, 16, 8].



### 3. Research on perception of selected objects and spaces in Rabka-Zdrój

The research using the above described method (ET) for perceiving architectonic objects and urban spaces in Rabka-Zdrój was carried out in a group of 100 people. Research participants were selected at random. The number of research participants was sufficient from the perspective of methodological assumptions; moreover, it considerably outnumbered the populations taking part in the research concerning other disciplines [5, 3, 6, 14, 15]. The group of participants differed in respect of age, education and sex. The structure of population regarding the sex of the examined inhabitants of Lesser Poland included: 60% females, and 40% males.

Every research participant was informed about the research procedure, though it was not stated what the aim of the research was or how the scan paths would be analysed. This information was deliberately concealed, so as not to suggest the participants which areas to focus on or pay attention to. Research participants declared that their eyesight was not impaired, which is imperative for this method [3]. 4 photographs of urban spaces in the health resort of Rabka-Zdrój were selected. Such shots were selected which showed both historical and modern objects, in good and poor technical condition, as well as additional objects not related to architecture but occurring in that space. The photos considered in the research and analysed presented the buildings along Poniatowskiego Street on the south-east side (2 shots) and Orkana St. on the south-west side (2 shots). Each photograph was shown to the viewer on the screen for 15 seconds. The research was carried out using a stationary device Eye tracker Tobii X2-30 Compact with special software [19].

An analysis of the results obtained from the conducted research began by generating heat maps as visual data indicating places on which the participants' attention was focused, as well as places ignored i.e. unobserved. The distribution of heat maps constituted a basis for determining Areas of Interest with regard to research goals. The determined areas of interest concerned objects and architectonic space, as well as other elements e.g. commercial banners, information boards, objects in the public space which were attractive to viewers.

The analysis determined areas of interest for each photographic material was carried out using the so called statistics, i.e. such parameters as: the average time till the first fixation, the number of fixations during observation, an average number of fixation per research participant, the total time of all fixations, the number of visits during observation and an average number of visits per participant. The generated numerical data for each area of interest took into account the sex difference between participants.

The first photo (Fig. 1) shown to research participants presents the initial fragment of Poniatowskiego St. viewed from the south-east (Fig. 1). The buildings along that street developed at the beginning of the 20<sup>th</sup> century. From that period several wooden villas representing the health-resort style have survived until the present. The most historical objects have been preserved at the beginning of the street. Dilapidated or ruined buildings are adjacent to well-maintained modern architecture which, however, does not allude to traditional models of spa architecture [8]. On the left side of the picture in the background there is an area of non-historical buildings, while on the right side in the street frontage one can see a modern house

and, slightly further, historical buildings. The foreground of the photo shows the street with parked cars further back. A visualisation of research results in the form of heat maps (Fig. 2) indicated that the cognitive process among participants did not concern the whole view of objects on the left side of the image, or the whole view of the contemporary object, or the farther historic buildings. In the case of buildings the cognitive elements were mainly porches, not whole elevations. The focus of participants' attention and warm colours (red), confirming a longer observation time, referred mainly to the street with the cars parked along it. The above analysis allowed for determining three areas of interest: area 1\_AOI1 comprises the non-historical buildings on the left side of the photo; area 1\_AOI2 includes the contemporary house and farther historic buildings; and area 1\_AOI3 is not related to architectonic objects i.e. the road surface. The indicated areas (Fig. 3) did not include the part of building development screened by greenery. Numerical data, so called statistics (tab. 1), were generated for the indicated areas of interest. The analysis of obtained results indicates that the road with cars parked on it seemed to have the greatest ability of focusing viewer's attention, and making the first impression, then the contemporary house and further historic buildings, while the anonymous non-historic buildings on the other side of the street were the least attractive. It is confirmed by mainly such parameters as the average time until the first fixation, the number of fixations during observation or the total time of all fixations. The number of visits during observation for all research participants and for each participant, with an analogical distinction regarding sex and other parameters, could be evidence of both interest and difficulty in understanding the information contained in the objects and space.

The next photo (Fig. 4–6) shown to research participants also depicts the buildings along Poniatowskiego St. photographed from the south-east (Fig. 4). In the frame selected for research there are both historic buildings in the shape of historical villas, as well as contemporary buildings, namely an apartment block. The heat map distribution (Fig. 5) indicated the occurrence of a cognitive process in relation to architectonic details in both kinds of buildings. In the apartment block those were windows and balconies, and porches with columns in the area of historic villas. Those objects without the greenery screening them were attributed areas of interest: the apartment block was 2AOI1, and historic villas were 2\_AOI2 (Fig. 6).

So called statistics were generated for selected areas (tab. 2). An analysis of obtained results allows for stating that the area with historic buildings was perceived as more attractive than the one with contemporary buildings (an apartment block). It concerns mostly the first impression where attention drawn most quickly, which is confirmed by lower value of time until the first fixation for 2\_AOI2 in comparison with 2\_AOI1. It is also related to the fact that architectonic details in historical objects aroused more interest than those in the apartment block, the evidence of which is the larger number of fixations by over 50%, as well as a greater number of visits during observation by over 20%. And in this case, the cognitive process did not refer to the entire historical area, but only its fragments.

Next shots presented to research participants display views of two fragments of Orkana Street. It is the main street in Rabka-Zdrój along which were built health-resort villas and public utility objects, constituting significant elements of the cultural landscape of the town [8].

Photo no. 3 (Fig. 7–9) shows a built-up fragment of Orkana Street in the vicinity of the church dedicated to St. Mary Magdalene on the south-west side (Fig. 7). The church was erected at the beginning of the 20<sup>th</sup> century in the neo-Gothic style. Its fence, built from brick at the same time as the church, is divided into spans with posts. The brick fence with the main entrance gate to the church yard is visible on the left side of the photo. On the other side of the street one can see non-historic buildings with a large number of advertising boards of varying size. In the foreground of the photo there is a road with pavements. An analysis of the distribution of generated heat maps (Fig. 8) indicated that research participants showed little interest in either the historic wall surrounding the church or the buildings on the other side of the street. Warm colours implying the longer period of observation concerned mainly the street and advertisement and information boards put up along the street. Areas of interest were established in order to analyse the cognitive process among participants. The area including the historic object (the wall surrounding the church) was marked as 3\_AOI1, while the areas of interest linked to architectonic objects comprising attractors drawing viewers' attention were marked as 3\_AOI2 (larger board) and 3\_AOI3 (smaller advertising board). The largest area of interest included in the analysis was the area outlined by the street and marked as 3\_AOI4 (Fig. 9). Then, data was generated concerning parameters for the established areas of interest (tab. 3). Values of all parameters showed that the process of learning concerning the first impression and arousing interest during observation referred mainly to the message conveyed by elements of road infrastructure and parked cars, as well as by the large advertising board located by the side of the building.

The next shot (no 4) is a view of another fragment of Orkana Street from the south-west (Fig. 10). The central place in the presented shot is taken by objects situated on the right side of the street, including a historic villa of high cultural value [8] and a contemporary market pavilion. Further back, behind the historic object there is anonymous non-historical architecture with advertising boards (see Fig. 3). A considerable section of the elevation of the historic villa is hidden behind a hanging advertising banner. The ground floor and the first floor of the market pavilion have many advertising signboards. Generated distributions of heat maps (Fig. 11) allowed for establishing areas of interest. It was assumed that 4\_AOI1 will denote the elevation of the historic villa not screened by the advertising banner, 4\_AOI2 – the area of the advertising banner on the villa elevation, 4\_AOI3 – the ground floor of the market pavilion with shop-signs, 4\_AOI4 – the first floor of the pavilion with advertising boards, and 4\_AOI5 – the advertising board visible behind the historic villa (Fig. 12).

Generated numerical data for the parameters describing the cognitive process (tab. 4) allow for stating that a large advertising banner could be an attractor determining the first impression on the part of a viewer observing various objects and spaces, and the cognitive process with memorised information content. The banner located on the elevation of a historic object strongly affects the process of visual perception of the value of historic objects, which is confirmed by numerical data.

For the 4\_AOI1, namely the historic villa, the time to the first fixation was 5 times longer, the number of fixations during observation was lower by 60%, the length of time of all fixations was 3 times shorter, and the number of visits lower by 40% than in the case of the

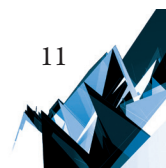




Fig. 1. View of the built-up fragment of the early section of Poniatowskiego St. from the south-east (photo no. 1)

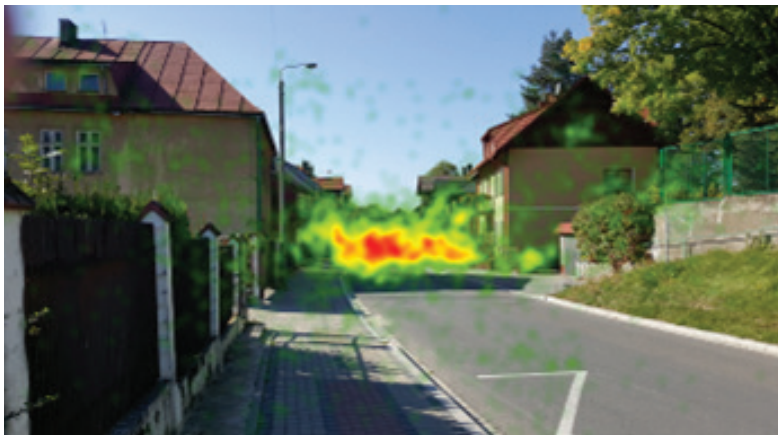


Fig. 2. Visualisation of results in the form of heat map for all participants (photo no. 1)



Fig. 3. Established areas of interest (photo no. 1)

Table 1. Research results for photo no. 1 (Fig. 1-3)

Statistic (parametr)	Research participants	1_Aoi1	1_Aoi2	1_Aoi3
Average time to first fixation [s]	Women	1.89	2.02	0.94
	Men	1.43	1.69	1.2
	Total	1.69	1.87	1.05
Number of fixations during observation	Women	387	487	652
	Men	351	357	507
	Total	738	844	1159
Average number of fixations per person	Women	6.24	7.85	10.52
	Men	7.63	7.76	11.02
	Total	6.83	7.81	10.73
Length of time of all fixations [s]	Women	156.46	187.24	265
	Men	137.64	133.17	215.33
	Total	294.1	320.42	480.93
Number of visits during observation	Women	243	285	309
	Men	185	201	232
	Total	428	486	541
Average number of visits (in proportion to number of research participants)	Women	3.92	4.6	4.98
	Men	4.02	4.37	5.04
	Total	3.96	4.5	5.01

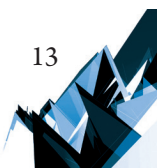




Fig. 4. View of the built-up fragment of Poniańskiego St. from the south-east (photo no. 2)

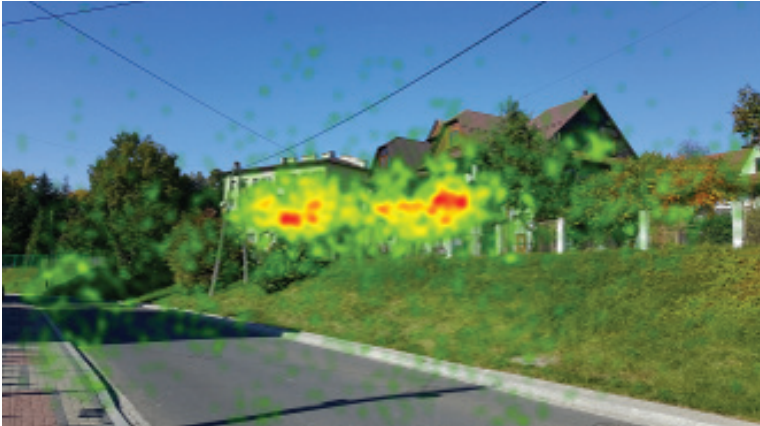


Fig. 5. Visualisation of results in the form of heat map for all participants (photo no. 2)



Fig. 6. Established areas of interest (photo no. 2)

Table 2. Research results for photo no. 2 (Fig. 4–6)

Statistic (parametr)	Research participants	2_Aoi1	2_Aoi2
Average time to first fixation [s]	Women	1.16	0.61
	Men	1.04	1.33
	Total	1.11	0.93
Number of fixations during observation	Women	368	584
	Men	287	414
	Total	655	998
Average number of fixations per person	Women	5.94	9.42
	Men	6.24	9
	Total	6.06	9.24
Length of time of all fixations [s]	Women	150,28	248.46
	Men	131.22	182.56
	Total	281.51	431.02
Number of visits during observation	Women	241	298
	Men	184	226
	Total	425	524
Average number of visits (in proportion to number of research participants)	Women	3.89	4.81
	men	4	4.91
	Total	3.94	4.85

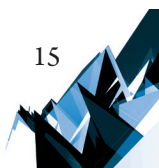




Fig. 7. View of the built-up fragment of Orkana St. in the vicinity of the new church from the south-west (photo no. 3)

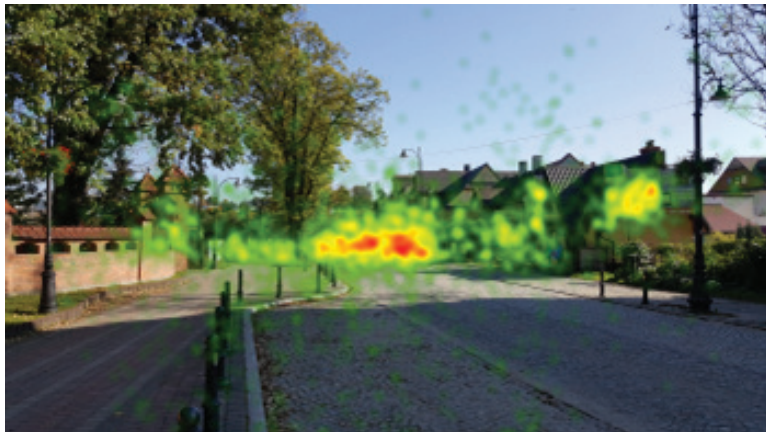


Fig. 8. Visualisation of results in the form of heat map for all participants (photo no. 3)



Fig. 9. Established areas of interest (photo no. 3)



Table 3. Research results for photo no. 3 (Fig. 7–9)

Statistic (parametr)	Research participants	3_Aoi1	3_Aoi2	3_Aoi3	3_Aoi4
Average time to first fixation [s]	Women	2,95	3,13	4,48	0,93
	Men	3,06	2,15	6,51	0,89
	Total	2,99	2,67	5,33	0,92
Number of fixations during observation	Women	161	148	30	879
	Men	105	153	18	654
	Total	266	301	48	1533
Average number of fixations per person	Women	2,6	2,39	0,48	14,18
	Men	2,28	3,33	0,39	14,22
	Total	2,46	2,79	0,44	14,19
Length of time of all fixations [s]	Women	57,42	66,5	13,21	347,2
	Men	38,74	73,73	9,9	267,55
	Total	97,16	140,23	23,12	614,75
Number of visits during observation	Women	100	99	29	325
	Men	68	84	17	233
	Total	168	183	46	558
Average number of visits (in proportion to number of research participants)	Women	1,61	1,6	0,47	5,24
	Men	1,48	1,83	0,37	5,07
	Total	1,56	1,69	0,43	5,17

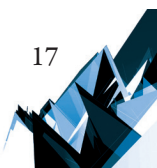




Fig. 10. View of the built-up fragment of Orkana St. from the south-west (photo no. 4)



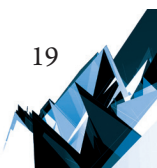
Fig. 11. Visualisation of results in the form of heat map for all participants (photo no. 4)



Fig. 12. Established areas of interest (photo no. 4)

Table 4. Research results for photo no. 4 (Fig. 10–12)

Statistic (parametr)	Research participants	4_Aoi1	4_Aoi2	4_Aoi3	4_Aoi4	4_Aoi5
Average time to first fixation [s]	Women	4.94	0,86	3,99	4,51	7,97
	Men	3.12	0,58	4,95	4,96	6,62
	Total	4,15	0,74	4,34	4,73	7,35
Number of fixations during observation	Women	139	380	218	80	56
	Men	145	311	140	86	40
	Total	284	691	358	166	96
Average number of fixations per person	Women	2,24	6,13	3,52	1,29	0,9
	Men	3,15	6,76	3,04	1,87	0,87
	Total	2,63	6,4	3,31	1,54	0,89
Length of time of all fixations [s]	Women	47,07	158,79	76,01	26,21	22,66
	Men	48,73	120,43	52,04	29,64	17,38
	Total	95,81	279,21	128,05	55,84	40,04
Number of visits during observation	Women	100	173	91	61	47
	Men	100	171	67	63	37
	Total	200	344	158	124	84
Average number of visits (in proportion to number of research participants)	Women	1,61	2,79	1,47	0,98	0,76
	Men	2,17	3,72	1,46	1,37	0,8
	Total	1,85	3,19	1,46	1,15	0,78



4\_AOI2, i.e. the advertising banner located on the object. The other attractors of advertising character were of varying cognitive attractiveness to viewers, with the area of interest including the farthest advertising board being the least effective in conveying the message, which is confirmed by the values of parameters related to the occurring fixations.

To sum up, the carried out experiment allowed for stating that the historic or contemporary character of an object or a space had no bearing on drawing attention or perception by individuals participating in the research. Architectonic objects were not seen as a whole by participants. Fragments of buildings, mostly windows and balconies, were the architectonic elements attracting attention and consciously noticed and remembered. Therefore, the character and style of an object were not identified by research participants. Hoardings, signboards and information boards were the elements associated with objects, because of being mounted on their elevations, which focused viewers' attention. The attention-drawing elements occurring in the space around the analysed architectonic objects were primarily parked cars and road infrastructure. Like advertising elements on elevations of buildings, elements in the public space also interfere with the perception of objects valuable for our cultural heritage.

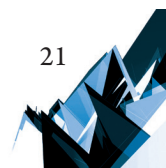
#### **4. Conclusion**

Both studies of literature and the empirical research confirmed the effectiveness of the eye-tracking method in the research on visual perception of architectonic objects and urban spaces. Applying the eye-tracking method allows for learning the range and manner of perceiving objects and spaces by people looking at them. It also allows for obtaining objective information concerning external stimuli such as details of architectonic objects and spaces with their information content, which are merely noticed in the process of perception, as well as those which are additionally learned, understood and memorised. It is essential in determining the causes of the low level of social awareness concerning the value of cultural heritage and people's indifference to the degradation of historic objects in their vicinity. Obtained results allowed for confirming the rule of perceptive competition among details of both historic and contemporary objects and spaces. Focusing one's attention and perceiving those details instead of whole objects or areas of interest, regardless of the length of observation time, is the main reason for the lack of evaluation of the viewed surroundings. Simultaneous occurrence of attractors, i.e. elements attracting attention and demanding to be noticed, disturbs the content conveyed by objects with historic and contemporary learning value. It has also been shown that various forms of external advertising and information boards have a strong impact here.

To conclude the findings established while carrying out the research using the eye-tracking method, it should be admitted that the method is useful in preparing guidelines and concrete activities connected to protecting historic objects and spaces, as well as educational activities addressed to local communities and people sightseeing places representing historic and architectonic values. The above findings refer to Rabka-Zdrój, but can also be more generally applied.


## References

- [1] Kuśnierz-Krupa D., *Problematyka rewaloryzacji willi w miejscowościach uzdrowiskowych na przykładzie willi Primavera, Jaworzyna oraz Wawel w Rabce Zdrój*, "Czasopismo Inżynierii Lądowej, Środowiska i Architektury – Journal of Civil Engineering, Environment and Architecture", Vol. 62 (2)/2015, 223-231.
- [2] *Eye Tracking in User Experience Design*, edit. J. Bergstrom, A. Schall, Elsevier Inc, Waltham 2014.
- [3] Garczarek-Bąk U., *Użyteczność badań eye trackingowych w pomiarze utajonych determinant zachowań zakupowych nabywców*, "Ekonometria – Econometrics", Vol. 3 (53)/2016, 54–71.
- [4] Szymusiak H., *Neurobiologiczne techniki stosowane w biznesie*, EUP, Poznań 2012.
- [5] Cholewa-Wójcik A., Świda J., *A Study and Assessment of Selected Elements of the Visual Aspects of Collectible Chocolate Packaging with the Use of the Eye-tracking Method*, "Indian Journal of Marketing", Vol. 45 (7)/2015, 7–18.
- [6] Kabaja B., Lisińska-Kuśnierz M., *The Assessment of the Food Packaging Labelling Systems with the Use of Eyetracking Method*, [in:] *Towaroznawstwo w badaniach i praktyce. Kierunki badań i rozwoju produktów nieżywnościowych*, edit. R. Salerno-Kochan, A. Wolak, PTT, Kraków 2017, 33–46.
- [7] Lisińska-Kuśnierz M., Jaracz E., *The Effect of the Visual Aspect of Packaging on Consumer Perception of Energy Drinks*, [in:] *Food Products Marketing. Concepts and Research*, edit. M. Gębarowski, T. Hermaniuk, University of Maribor, Celje 2015, 115–124.
- [8] Krupa M., *Rabka-Zdrój. Aspekty urbanistyczno-architektoniczne dziedzictwa kulturowego*, DWE, Wrocław-Kraków 2018.
- [9] Richardson D., *Eye-Tracking: Characteristics and Methods*, Stanford University, 2004.
- [10] Duchowski A., *Eye Tracking Methodology. Theory and Practice*, Springer, London 2007.
- [11] Holmqvist K., Nystrom M., Andersson R., Dewhurst R., Jarodzka H., Weijer J., *Eye Tracking: A Comprehensive Guide to Methods and Measures*, Oxford University Press, New York 2011.
- [12] Bojko A., *Eye tracking the user experience. A practical guide for research*, Rosenfeld, New York 2013.
- [13] *Current Trends in Eye Tracking Research*, edit. M. Horsley, M. Eliot, B. Knight, R. Reilly, Springer International Publishing, Switzerland 2013.
- [14] Wawer R., *Eyetracking w przestrzeniach edukacji medialnej*, Lubelskie Towarzystwo Naukowe, Lublin 2014.
- [15] Wawer R., Pakuła M., *Zastosowanie techniki eyetrackingowej do analizy postrzegania historycznej przestrzeni wystawienniczej przez osoby starsze i młodzież – teoretyczne i metodologiczne podstawy badań*, "Zeszyty Naukowe Uniwersytetu Szczecińskiego. Ekonomiczne Problemy Usług", Vol. 88/2012, *Gospodarka elektroniczna: wyzwania rozwojowe*, Vol. 2, 698–707.
- [16] Kabaja B., Krupa M., *Możliwości wykorzystania metody eye tracking do badań nad historyczną przestrzenią architektoniczną w kontekście jej postrzegania przez użytkowników*



(na przykładzie Rabki-Zdrój) – Część I – Uwagi wstępne, ”Wiadomości konserwatorskie – Journal of Heritage Conservation”, Vol. 52/2017, 74–85.

- [17] Lebrun Ch., Sussman A., Crolins W., Van der Linde G., *Eye Tracking Architecture: A Pilot Study of Building in Boston*, Institute for Human Centered Design&Ecole de Design Nantes Atlantique, Boston 2016.
- [18] Junker D., Nollen Ch., *Mobile eye tracking in landscape architecture. Analysing behaviours an interactions in natural environments by use of innovative visualisations*, [in:] Proceedings of the International Conference “Between Data and Senses. Architecture, Neuroscience and the Digital Worlds”, edit. A.Korandinon, UEL, London 2017, 16–18.
- [19] *User Manual – Tobii Studio, Version 3.2. Rev A*, Tobii Technology AB, Stockholm 2012.

Łukasz Kamil Mazur  [orcid.org/0000-0002-3799-4446](https://orcid.org/0000-0002-3799-4446)  
lukasz.mazur@pwr.edu.pl  
Faculty of Architecture, Wrocław University of Science and Technology

## LIVING IN THE FUTURE – ANALYSIS OF SELECTED HOUSING ENVIRONMENTS

---

### FORMY ZAMIESZKANIA LUDZI W PRZYSZŁOŚCI – ANALIZA WYBRANYCH KONCEPCJI ŚRODOWISK MIESZKANIOWYCH

#### Abstract

Futuristic concepts of housing environments show people, how it will be possible to live in the near future. These projects inspire engineers, scientists and researchers who bring modern technologies to life. It seems that technology is the key to solving the problems that humanity faces today. Housing environments need a new interpretation adapted to contemporary people who are looking for a new quality of living. In the article, the author will characterize futuristic visions of housing in the future, based on their location: on land, underground, in the air, under or on water.

**Keywords:** housing environment, residential complexes, futuristic architecture, the quality of housing in the future, city of the future

#### Streszczenie

Futurystyczne koncepcje środowisk mieszkaniowych przybliżają odbiorcom, w jaki sposób będzie możliwe zamieszkiwanie Ziemi w przyszłości. Projekty inspirują inżynierów, naukowców i badaczy, którzy wprowadzają do życia nowoczesne technologie. Wydaje się, że technologia jest kluczem do rozwiązania współczesnych problemów ludzkości. Środowiska mieszkaniowe potrzebują nowej interpretacji dostosowanej do współczesnych ludzi, którzy poszukują nowej jakości zamieszkania. W przedstawionym artykule autor scharakteryzuje współczesne wizje sposobu zamieszkiwania w przyszłości, ze względu na ich lokalizację: na lądzie, pod ziemią, w powietrzu, pod lub na wodzie.

**Słowa kluczowe:** środowiska mieszkaniowe, architektura futurystyczna, jakość mieszkaniowa w przyszłości, miasto przyszłości

„My interest is in the future because I am going to spend the rest of my life there.”  
Charles Kettering [10, p. 429]

## 1. Introduction

The twenty-first century began with a series of groundbreaking and innovative scientific achievements, motivated by faith in human possibilities. On the list of accomplishments that will surely revolutionize human civilization, there is, for instance, the construction of a space station, the discovery of a particle accelerator or the teleportation of proton particles. However, the heyday of humanity’s possibilities is not devoid of threats – worsened by social, economic and cultural difficulties. Wars, forced migrations, poverty, degradation of the natural environment and overcrowded cities are just examples of problems that modern civilization is struggling with. In the article, the author will focus on the situation of overcrowding and will present the characteristics of a vision of future housing environments.

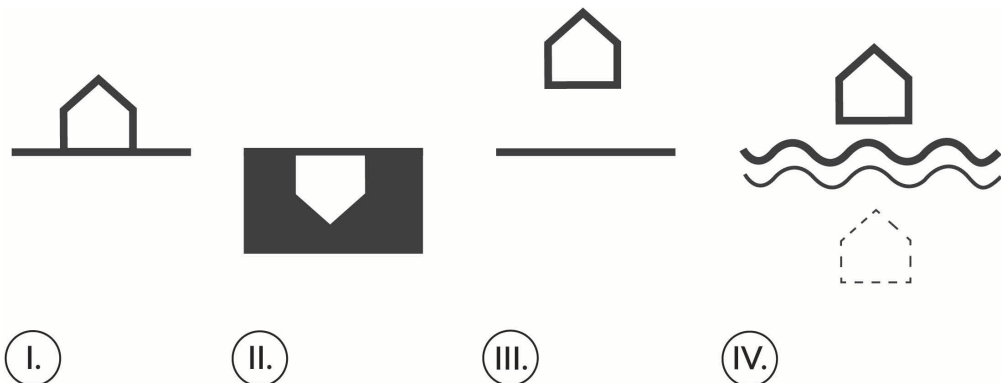


Fig 1. Graphics depicting futuristic concepts of housing environments depending on location: I – habitat on land, II – underground habitat, III – airborne habitat, IV – habitat under or on water (graphics by the author)

At present, the issue of population density in cities is becoming more and more important. Cities attract new residents with the promise of a good job or a vision of a better quality of life. According to United Nations data, in 2016 more than 54.5% of the world’s population inhabited an urban environment [22, p. 1–13]. Urban areas will be relatively concentrated in terms of population density. It is forecast that by 2050, they will be inhabited by over 66% of the Earth’s population – this means that one in three citizens will live in a city [22, p. 1–13]. The urban community already experiences negative factors such as poor air quality, noise, stress, traffic jams, inefficient urban infrastructure, overpopulation, anonymity or social pathologies [14, p. 99–105]. This situation makes today’s urban environment an increasingly difficult place to live. Housing spaces need a new interpretation adapted to today’s residents and to neutralize negative factors. How will humanity adapt to living conditions in the future and how will places of residence look like?



In the article, the object of research are selected examples of the concept futuristic housing environments and ideas of how people will live in the future. The thematic scope refers only to conceptual designs, because only such bold visions will allow us to approximate possible scenarios of people's lives in the future. However, the author wishes to emphasize that the presented architectural projects are but a few from among an uncountable number of possibilities. After all, today's decisions determine the appearance of the world in 2050, and that will be the foundation of the life of residents in 2100 [4, p. 9].

The main source of examples of the housing environment in the future are works of architects and designers. The most interesting of these are the futuristic visions of designers like – Zaha Hadid or Vincent Callebaut. In addition, visions of future architecture are also provided by academic centers<sup>1</sup> for example as a part of didactic courses for young students. The theme is also promoted by foundations which organize architectural competitions<sup>2</sup>, they present visions of the future formulated by architectural adepts. Another important source focusing on the visual transmission of living in the future is popular-science cinematography<sup>3</sup>. Two issues of the „Housing Environment” scientific journal constitute interesting bibliographic sources regarding the housing situation in the future. The author used non-reactive research, a method of content analysis including the analysis of books, articles and graphics.

## 2. Futuristic concepts of residential environments

Man inhabits the Earth creating its environment for living on continents and islands (land occupies about 29% of the Earth's surface) [7, p. 11]. This area is currently occupied by about 7.2 billion people and the United Nations organization estimates that by 2100 this number will increase to 11.0 billion [22, p. 1–13]. Today's concepts of futuristic housing environments are looking for answers to the problem of increasing population in urban areas. One of the solutions is to indicate alternative places in which human life will be possible. According to the analysis, concepts of futuristic housing environments can be divided on the basis of their location and natural environment. Housing environments can be designed: on land, underground, in the air on or underwater, as well as beyond planet Earth, i.e. in a spaceship or on another planet<sup>4</sup>. The author will characterize futuristic residential environments depending on their location further in the article.

---

<sup>1</sup> E.g. Wrocław University of Science and Technology Faculty of Architecture, course “Futurological Architecture”.

<sup>2</sup> E.g. eVolo Magazine, the organizer of the future skyscraper competition.

<sup>3</sup> E.g. *Metropolis* (1927) directed by Fritz Lang. The city of Metropolis is presented as a futuristic urban dystopia.

<sup>4</sup> In this article, the author focuses solely on futuristic ways of living on planet Earth. Visions of inhabiting spacecraft or other planets will not be discussed.

## 2.1. Habitat on land

Modern cities strive to counteract the negative effects of overpopulation by trying to transform into more sustainable and healthy places to live [18, p. 166]. Examples of such actions could be, i.a. the Paris Smart City 2050 project or Sustainable Singapore 2050. According to them, futuristic housing environments will be designed in accordance with the principles of sustainable development, focused on renewable energy sources and a better quality of life for their residents.

The idea of **sustainable settlements** (Fig. 2 – I) is based on the creation of self-sufficient ecological colonies, in which, through the work of residents and harmony with nature, positive social changes can take place. These changes concern positive relationships with other people, self-fulfillment and abandonment of excessive consumption. Sustainable settlements<sup>5</sup> are already being created, inhabited by a community of people who want to change their lives. The community designs buildings made of natural materials available in the immediate area – such as wood, clay, straw, as well as hemp. The idea of sustainable settlements on a larger scale can be seen in the Venus Project by Jacques Fresco and Roxanne Meadows. The organization founded by the authors of the project assumes the improvement of the living conditions of society by adopting sustainable development, effective energy management, natural materials and modern technologies. Housing environments in the Venus Project are focused mainly on multi-family housing, in which intelligent technologies are applied to ensure the greatest possible comfort for residents. There is also occasional single-family housing, designed from repetitive prefabricated modules, ensuring a high level of performance with the possibility to adapt the project to the preferences of future families [9, p. 34–36].

**Sustainable urban housing** (Fig. 2 – II) is characterized by the search for ecological solutions and attractive new forms of living in cities. Designers are looking for an experimental architectural form in conjunction with the landscape, nature and the relationship with the environment. Buildings feature low-energy solutions and the use of various types of renewable energy to reduce the negative impact of the building on the natural environment [19, p. 305–306]. A conceptual proposal prepared for the authorities of Paris, in which the architect presented an interesting way of transforming the urban fabric while respecting historic buildings can be an example of this. The capital of France features dense development, causing various types of social and housing problems. In addition, life becomes more and more difficult, i.a. due to high pollutant concentrations, smog and climate change. The city authorities decided to take corrective action and transform Paris into an ecological future city by 2050. In 2014, the City Council commissioned the preparation of a project of the redevelopment of Paris according to the requirements of the Paris climate agreement i.a. to reduce greenhouse gas emissions [16, p. 14]. The Belgian architect Vincent Callebaut started researching – he created a vision of a green, sustainable and hyper-ecological city of the future,

---

<sup>5</sup> The Eko-osada Brzozówka foundation was established in 2015, where in the Cielądz village in the province of Łódź (Poland) is implementing the project of sustainable settlements. More information on the website <http://eko-brzozowka.pl>.

which includes renewable energy, tall green buildings, hanging gardens, smog-absorbing towers and flat buildings with a characteristic honeycomb structure [23].

**Residential towers** (Fig. 2 – III) are buildings characterized by considerable height and development density. The popularity of such development projects results from the possibility of constructing a very large number of apartments on a limited plot, comparable in scale to a typical housing estate [25, p. 61].

The concept of residential towers is promoted by the works of the eVolo architectural competition, organized by the magazine under the same name. The competition has been organized since 2006 – its addressees are architects, students, engineers and artists from around the world. One of the examples is the “Adaptive Capacity: A socio-ecological Vertical Community in Tanzania” residential tower, designed by Adrienne Jeevananthan. The conceptual proposal presents an alternative solution for slum dwellers in Tanzania. The author intends to solve the problems of the local population by designing a “vertical village”, to provide residents with a higher quality of life. The building will fulfill all the functions necessary for residents, such as places for living, working, recreation and childcare, as well as a healthcare and educational facilities[8].



Fig 2. Graphics showing the Future of housing environments designed on the ground: I – sustainable settlements, II – Sustainable urban housing, III – Residential towers (graphics by the author)

## 2.2. Underground habitat

Designers of a futuristic residence concepts are wondering how to use the areas below the surface of the earth. Cities are growing mainly towards to the sky, constructors are outdoing themselves in designing buildings meant to be the tallest in the world. What will happen when we start to develop the free area under the surface of cities? It is known that no land can be wasted in the urban structure. It is possible that with this assumption, the authorities of

the cities of the future will want to transfer at least some of the city's functions to the surface of the earth.

One example of a design featuring the idea of transferring housing environments below ground level is the conceptual proposal of developing the main square in Mexico by architects from BNKR arquitecturan. This project goes 300 meters below the central Plaza de la Constitución in Mexico, forming an **inverted pyramid**, which refers to the most characteristic Aztec buildings (Fig. 3 – IA). The “roof” (240 × 240 m) of this underground habitat is completely glazed, developed as a public square serving the residents as a public space. The proposal was created as an alternative to the growing need to increase the city's housing stock. The innovative design additionally fits perfectly into the urban tissue, by following the urban restrictions of the historic part of the main square in Mexico. The city's urban planners introduced a ban on erecting buildings on eight floors. The inverted pyramid „Earthscraeper” essentially creates an underground mini-city, in which there will be a centre of culture or commerce outside the residential area [1, p. 527–529].

Another example of a historical vision of life underground is the „depthscraeper” project (Fig. 3 – IB), which was designed by Japanese engineers as a possible solution to the problems of earthquakes. The project was inspired by the 1923 Tokyo disaster – an earthquake that ruined the entire city in 10 minutes and caused 142 000 deaths. Japanese scientists, in order to counteract such cataclysms in the future, began research on a structure which can resist the negative effects of earthquakes. The researchers noticed a very interesting phenomenon – underground tunnels and structures suffer a little damage during seismic shocks compared to those on the earth's surface. The designers proposed a **cylindrical structure** of the building with massive concrete walls that will vibrate together as one element during an earthquake. Residents will have access to fresh air and daylight through an opening in the structure. Additionally, to increase the amount of incoming light, a large mirror will be installed on the surface of the earth and illuminate the lowest parts of the structure [15].

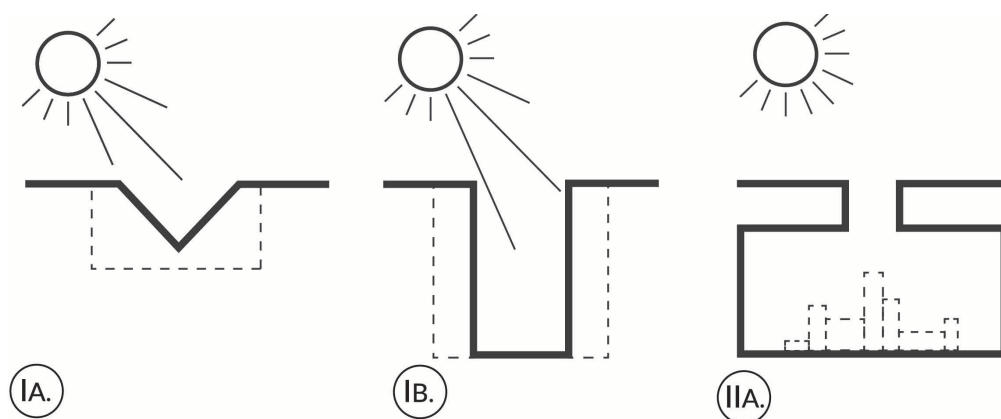


Fig 3. The graphic presents possible ways of designing housing environments below ground level: IA inverted pyramid, IB – Cylindrical structure, IIA – Transferring certain urban functions underground (graphics by the author)

The international organization Associated Research Centers for the Urban Underground Space [12] supports activities aimed at using land under the surface. This organization promotes, i.a. the concepts of **transferring certain urban functions underground** (Fig. 3 – IIA) [3] – an example of such a solution is the project of an underground scientific city in Singapore. Singapore is a city-state with an area of 719.1 square kilometres [20, p. 1], therefore, it is important to use every piece of land rationally on such a limited area. 4,200 people will work in the underground scientific city, and the construction will reach up to 80 m deep into the earth. The project will only use spot lighting in the main atrium of the building, while the remaining part will be artificially illuminated [21].

### 2.3. Airborne habitat

At present, thanks to the perseverance and strength of the human mind, the eternal dream of flying has become a reality. Airplanes allow free movement of people and goods around the world. Futuristic designers inspired by the human desire to fly, but also the possibilities of modern technology, proposed the idea of flying cities.

One of the first conceptual **flying cities** (Fig.1 – III) was a project of sky-high tensegrity spheres (Cloud Nine) by American architects Buckminster Fuller and Shoji Sadao from 1960. The project presents a gigantic lightweight tensegrity sphere being the main structure that can levitate by heating the internal air above ambient temperature. The proposed structure becomes more stable when it grows, due to the way in which it distributes stresses on the surface of the sphere. Fuller suggested that the mass of the tensegrity sphere, a mile wide, would be negligible compared to the mass of air trapped in it. Then the air inside this sphere would be heated up to one degree higher than the ambient temperature, and could freely float above cities. He calculated that such a flying structure could lift a heavy weight, allowing “small cities” to be built. The construction of such city can be moored to a chosen place on earth or be freely levitated around the globe [5, p. 190].

### 2.4. Habitat under or on water

The seas and oceans are still among the least researched areas of the earth’s surface. Scientists are constantly discovering new species of animals or unexplored mountain ranges in the deep sea. Water spaces are used to a small extent as a place for human life e.g. on oil platforms or ships. The potential is huge as, in the end, life began in the sea and there are thousands of animals that live in it. This fact is used by designers presenting self-contained housing units, designed underwater and drifting freely above sea waves.

An example of a futuristic concept of living **under the waves** is the Sub-biosphere 2 (Fig. 4 – I) project by Phil Pauley, who specializes in the design of underwater cities. The project consists of a central geometric sphere – a biome, which is designed to control the living conditions in the entire complex, including air and water quality, food and electricity. The biome is surrounded by eight spheres, in which up to 100 inhabitants can live [17, p. 173].

An example of the concept of life **on the water** is a project by architect Vincent Callebaut, which proposed a futuristic concept of a self-sufficient floating city – Lilypad (Fig. 4 – II).

Designed to provide shelter for future refugees due to global warming. According to scientists, the level of the ocean is gradually increasing, absorbing large areas of land. The Maldives, where by 2070 seventy percent of the country's area will be under water, can serve as an example [13, p. 239]. The project operates as an amphibious half-aquatic and half terrestrial city, and is anticipated to being able to accommodate 50 000 inhabitants. The floating Ecopolis will also be in a positive energy balance with zero carbon emission through the integration of all renewable energies (solar, thermal and photovoltaic energies, wind energy, hydraulic, tidal power station, osmotic energies, phyto-purification, biomass) allowing the production of more energy than it consumes [6, p. 304–305].

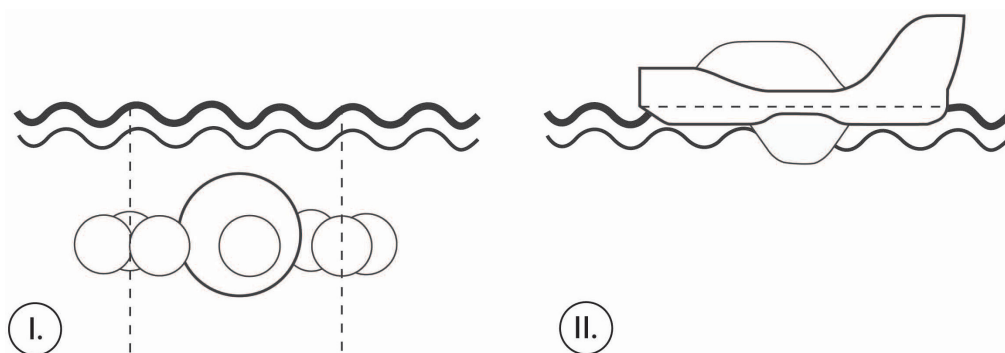


Fig. 4. The graphic presents possible ways of designing housing environments under and on water: I – habitat under water with the ability to float to the surface on sunny days, II – habitat floating on the water surface (graphics by the author)

### 3. Summary and conclusion

Conceptual proposals of housing environments of the future are, in many cases ahead of the available technical capabilities, representing their authors' far-reaching creativity. The presented examples are a joint attempt to deal with the current housing problems of humanity and life in the city. Most of the examples and analyses mentioned above present solutions for housing problems and overpopulated cities. In addition, most of the discussed projects are looking for human contact with the natural environment. Projects supporting the development of construction taking into account sustainable development and aimed at dealing with the problem of overcrowding in cities and hunger in the world. The characteristics of futuristic housing environments presented by the author and divided on the basis of project location make it possible to systematize the research topic. Each of the presented locations – i.e. on the ground, underground, in the air, on or underwater - brings together projects in which the promoted idea of the designer is the common denominator.

Projects on land have a balanced approach to the way of life of people in the future, regardless of where they live. The growing number of people and society's efforts to improve living conditions lead to the development of an economy that affects the degradation of the

natural environment. Conceptual designs have an educational value and communicate to the public how important it is to respect the natural environment.

Conceptual proposals of projects implemented below ground level combine the idea of using undeveloped land under the city. At present, urban residents feel the high costs of living in the city. Because of this situation, people are choosing smaller and smaller apartments that they can afford. The Japanese “geki-sema”, translated as “human locker room”, are an example of this. These are rooms for rent in Tokyo, often with dimensions of 2–3 m<sup>2</sup>. In this space, young Japanese sleep and hold all their belongings – often, such rooms are grouped and have a shared kitchen and toilet [11, p. 87].

The vision of flying housing environments combines the idea of freedom and the free movement of people on earth. Flying cities will be able to move away from places threatened by a cataclysm, they will eliminate, i.a. problems of earthquakes, whirlwinds or tsunamis. It will also allow access to unlimited solar power, and arable farms could operate all year round. Certainly, the future development of this idea is related to the invention of fast flying cars, flying backpacks and teleportation [2, p. 159]. The very conceptual idea brought with it new opportunities for people as well as potential threats, e.g. during technology failures.

In turn, projects of centers of life above or under the water promote the idea of greater use of the oceans in the fight against overpopulation on earth. This idea is gaining popularity because of climate change. According to the Polish Humanitarian Action, by 2050, due to the heating of the planet, 150 million people may be forced to migrate [24, p. 123]. In light of this situation, the idea of adapting the oceans to serve as an alternative living environment seems rightly justified.

All the futuristic concepts share a common vision of human adaptation to living conditions in the future. According to the presented conceptual proposals, the city of the future is waiting for overpopulation, but it is not always shown in a negative way. Certainly, futuristic concepts today show a small fraction of how a person can live in the future.

## References

- [1] Aiello C., *Evolvo Skyscrapers 1*, Evolo, Los Angeles 2013.
- [2] Anderson D., *Imaginary Cities: A Tour of Dream Cities, Nightmare Cities, and Everywhere in Between*, The University of Chicago Press, Chicago 2015.
- [3] Associated Research Centers for the Urban Underground Space, <https://www.acuus.org/index.php/what-is-acuus/the-urban-underground-space> (access: 11.02.2017).
- [4] Attali J., *Krótką historia przyszłości*, Prószyński i S-ka, Warszawa 2008.
- [5] Baldwin J., *Bucky Works: Buckminster Fuller’s Ideas for Today*, Wiley, New York 1996.
- [6] Callebaut V., *Lilypad: Floating Ecopolis for Climatical Refugees*, [In:] *Large Floating Structures: Technological Advances*, eds. C. M. Wang, B. T. Wang, Springer, Singapore 2015, 303–327.
- [7] DK Publishing, *DK complete atlas of the world*, Dorling Kindersley Publishing, New York 2012.

- [8] Evolo, <http://www.evolo.us/featured/adaptive-capacity-a-socio-ecological-vertical-community-in-tanzania/> (access: 10.02.2017).
- [9] Fresco J., Meadows R., *Designing the Future*, The Venus Project, Venus 2007.
- [10] Herreid C. F., *Start with a story: the case study method of teaching college science*, National Science Teachers Association, Arlington 2007.
- [11] Huang S., *Urbanizing Carescapes of Hong Kong, two systems, one city*, Lexington Books, Lanham 2015.
- [12] Mavrikos A. A., Kaliampakos D. C., *Underground development in urban areas: the birth, the evolution and the perspectives of the trend*, [In:] *Sustainable Development and Planning III*, eds. A. Kungolas, C. A. Brebbia, E. Beritos, WIT Press, Ashurst 2007, 219–226.
- [13] Mazur Ł., *Burza piaskowa*, [In:] *Architektura niezrównoważona*, eds. K. Pobłocki, B. Świątkowska, Fundacja Bęc Zmiana, Warszawa 2016, 230–240.
- [14] Mazur Ł., *Mental health condition of residents in the urban environment. Conceptualisation of research problems and search for architectural solutions*, “Architectus”, No. 2(50)/ 2017, 99–105.
- [15] Modern Mechanix, <http://blog.modernmechanix.com/depthscrapers-defy-earthquakes/> (access: 11.02.2017).
- [16] *Paris Agreement*, eds. M. de Serpa Soares, United Nations, New York 2015.
- [17] Quirk J., *Seasteading: How Floating Nations Will Restore the Environment, Enrich the Poor, Cure the Sick, and Liberate Humanity from Politicians*, Free press, New York 2017.
- [18] Schneider-Skalska G., *The quality of an urban housing environment – threats and chances*, “Technical Transactions”, Vol. 1-A/2/2012, 165–173.
- [19] Seruga W., *Tomorrow’s Sustainable Residential Complexes*, “Housing Environment”, No. 11/2013, 303–308.
- [20] *Singapore in Figures 2017*, Singapore Department of Statistics, Singapore 2017.
- [21] The New York Times, <http://www.nytimes.com/2013/09/26/business/international/crowded-singapore-looks-below-for-room-to-grow.html> (access: 11.02.2017).
- [22] United Nations, Department of Economic and Social Affairs, Population Division, *World urbanization prospects: the 2014 revision: highlights*, United Nations 2014.
- [23] Vincent Callebaut Architectures, [http://vincent.callebaut.org/object/150105\\_parissmartcity2050/parissmartcity2050/projects/user/](http://vincent.callebaut.org/object/150105_parissmartcity2050/parissmartcity2050/projects/user/) (access: 05.02.2017).
- [24] Ypersele J., Born R., Lebre La Rovere E., Santos Pereira A., Jiahua P., Bidwai P., Green A., Polycarp C., Lutes M., Murray A. L., Mozaharul A., Nyoung A., Yamin F., Rahman A., Huq S., Sharma A., Shukla R. P., Reid H., Bachram H., Leff E., *Zmiany klimatyczne - impas i perspektywy. Punkt widzenia krajów globalnego Południa*, Polska Akcja Humanitarna, Warszawa 2010.
- [25] Zychowicz E., *Wieże mieszkalne*, „Materiały Budowlane”, No. 12(424)/2007, 61.



Filip Suchoń  [orcid.org/0000-0002-3098-0025](https://orcid.org/0000-0002-3098-0025)  
filip\_suchon@yahoo.com

Institute of Urban Design, Faculty of Architecture, Cracow University of Technology

## THE HIDDEN TREASURE

---

## UKRYTY SKARB

### Abstract

The paper describes the forgotten realization of the forgotten creator – Edgar Kováts, a Polish architect of Hungarian origin, operating at the turn of the 19th and 20th centuries in Vienna, Zakopane and Lviv, the rector of the Lviv Polytechnic. The neo-baroque church in Mystków was the subject of research and inventory using a laser scanning as well as design work carried out by the author of this paper.

**Keywords:** sacred architecture, neo-baroque architecture, laser scanning

### Streszczenie

Artykuł opisuje zapomnianą realizację zapomnianego twórcy – Edgara Kovátsa, polskiego architekta węgierskiego pochodzenia, działającego na przełomie XIX i XX wieku w Wiedniu, Zakopanem i we Lwowie, rektora Politechniki Lwowskiej. Neobarokowy Kościół w Mystkowie był przedmiotem badań i prac inwentaryzacyjnych przy pomocy skanowania laserowego, a także prac projektowych prowadzonych przez autora artykułu.

**Słowa kluczowe:** architektura sakralna, architektura neobarokowa, skanowanie laserowe

## 1. Introduction

Mystków is located 10 km to the south east of Nowy Sącz. A structure erected in accordance with a design by the architect Edgar KOVÁTS has survived in this small locality. The subject of this paper is a building survey of the facades of the historical parish church of the Apostles Phillip and Jacob the Younger in Mystków, documenting the extant state of the structure, with particular emphasis on elements of historical value.

## 2. The Main Theoretical Part

### 2.1. Historical outline

The history of the parish in Mystków dates as far back as the fourteenth century – it was established between 1320 and 1326, founded by king Wladyslaw the Elbow-high and his wife, queen Jadwiga [5]. The current parish church of the Apostles Saint Phillip and Jacob the Younger was built in the years 1905–1910, in accordance with a design by the architect and painter Edgar KOVÁTS [3, 6, 7], as a result of the efforts of its then-parish priest, father



Fig. 1. Parish church in Mystków – aerial view, photo by Kamil Ogórek



Fig. 2. Parish church in Mystków – façade details

Jan JARZEBIŃSKI. The design of the church was developed probably in 1902, which is supported by documents that have been preserved at the Diocese Archives in Tarnów (*Akta lokalne parafii Mystków 1881–1946*) [7].

In 1924 the church was consecrated by the Tarnów diocese bishop, Leon WAŁĘGA.

The building became a site listed in the voivodship historical sites registry under the number A-81, by decision of the 15<sup>th</sup> of November 1988 (NSz) [8].

## 2.2. Description of the building

The parish church in Mystków is a freestanding building, situated atop a hill in the centre of the locality, near powiat road no. 1573 K, which runs between Nowy Sącz and Cieniawa.

The church property is surrounded by a low, openwork fence. A procession path with a stony surface has been delineated around the temple. A line of around a dozen grand, long-lived deciduous trees has been planted along the fence – consisting of sycamore maples (*Acer pseudoplatanus*) and largeleaf lindens (*Tilia platyphyllos*).

The single-nave temple has been built on a Latin cross-shaped plan, with a semicircularly enclosed presbytery. The lower parts of the building, housing a sacristy and a chapel, have been built adjacent to the sides of the presbytery. A square tower, which dominates the facade, has been placed at the front of the nave. The brick walls of the nave and the transept have a thickness of around 89 cm (3½ bricks), while the walls of the sacristy and the chapel – of around 51 cm (2 bricks).

The body of the church is covered by a steep, gabled roof, its roof surfaces having an incline of around 45 degrees. The roof truss is made out of timber and is open, with collar beams and struts in the shape of St. Andrew's cross. The tower is covered by an onion dome



Fig. 3. Parish church in Mystkow – façade details

topped with a spire. Above the intersection of the nave and the transept there is a ridge turret with a lantern. The roof and dome surfaces are covered with copper sheets placed on timber boards. The parapets around the outline of the facade, as well as the volutes of the gables and the transept, are also covered by copper sheets.

### 2.2.1. Facades

Locally available materials were used. Magura sandstone, grey and yellow in colour after weathering, was obtained from the currently inactive quarry on the slopes of Mount Rosochatka. The brick used in the construction – rough, formed by hand – was manufactured at the construction site, with the use of seasoned clay obtained from the parish's field.

Father Jarzębiński – the coordinator of the work – laid out the segregation of duties. Residents of the village of Cieniawa were assigned the task of performing excavations (removing the surfaces of the stone deposit) at a private stone quarry at Mount Rosochatka, cutting the stone into large, almost 70 cm thick blocks and delivering them to the pickup site. Afterwards, the residents of the village of Mszalnica, as the owners of sturdy carts and strong workhorses, were to transport them to a square in front of the church. The stone was delivered from Ptaszkowa, which was located at a distance of almost 9 km away. Due to the considerable distance and the small number of means of transport, only two courses per day could be made, and thus only two stone blocks could have been transported daily. Their sorting took place in front of the temple, as did the selection of their front face according to scale, hardness and colour, as well as their processing, all the way to giving the cut precisely set dimensions, concordant with its place of setting within the wall of the church. The residents of the village of Królowa Polska had the duty of transporting sand, which had been gathered at the edges of Królowka Creek, to the construction site. The residents of Mystków were assigned to produce bricks [1].

The facades of the church are decorated with belts of alternately laid coarse-textured stone elements and bricks, starting at the stone plinth. They have been crowned with a decorative stone and brick parapet along the perimeter. The corners were accentuated with smooth stone lesenes. Large arched windows were placed within the walls of the naves, in addition to semicircularly enclosed, horizontal window openings. Large semicircular openings filled with blinds were placed in the upper storey of the tower.

A somewhat similar colour diversification of the facade of a religious building was used by Jan Zawiejski in the parish church in Krynica, in this case making a reference to early Italian Renaissance. This distinct form of the shape of the surface appeared, however, much earlier in Berlin circles, including in designs by August Stüler. The temples that constitute comparative material for the church in Mystków – e.g. the design by Carl Haybäck for Brno of 1887, or the Viennese Kaasgrabenkirche of 1909 – appear as referring to more visually expressive Baroque forms.

The main entrance in the frontal facade (the eastern one) features a stone portal flanked with smooth pilasters, with a broken jerkinhead and a round window placed above. Windows in the facades of the transept (the north and south) also possess such decoration, in addition to the filled-in niche in the western facade.

The top of the facade and the arms of the transept are framed with volutes and crowned by segmental arches. The surfaces of the gables are filled in with axial compositions: three semicircularly crowned, blind openings – a window with a blind and shallow niches with statues symmetrically placed at either side, while above there is a stone and brick decoration in the shape of a Greek cross.

We can observe the qualities of E. KOVÁTS' individual style here, which he himself considered to be the "principles of modern architecture" [4] – a flat wall design, with the simultaneous accentuation of the decorative value of the line and contour, a "horizontality of classicism in lines", an expressive highlighting of the structure and material. The church building can be described as neo-baroque – the historical revival decoration of the facade constitutes a formal reference to Roman Baroque, including the use of semicircular windows, whilst in the design of the gables and the transept there are clear references to the eighteenth-century Baroque church of St. Anthony in Lviv [7]. KOVÁTS' many years of work on Baroque building restoration projects (including in Vienna) and a particular fondness for the art of the Baroque surely had an influence on the selection of forms from the repertoire of this historical style [6, 7].

The window openings located in the lower parts of the facade are protected by steel trellises composed of horizontal flats and vertical bars, which have ends decorated in the shape of lilies.

The door openings are filled in with massive timber doors with decorative panels, elaborate fittings and handles – double doors in the main entrance have additionally been decorated with a blind, semicircular fanlight.

Considering the over one-hundred-years-long period without considerable renovation work, the facades have been preserved in relatively good technical condition. There are a few spots in which mortar and stone elements are slightly damaged due to atmospheric factors (in accordance with annotations contained in the graphical part of the survey documentation and in the photographic documentation). Considerable areas of surface delamination have been observed on a portion of

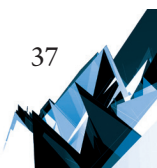




Fig. 4. Parish church in Mystkow – main entrance façade, photo by Kamil Ogórek

the plinth. In the brick parts of the walls there are also traces of punctures and hammering which occurred during the many years of occupancy – and which were later infilled with mortar. There are elements of contemporary illumination and sound installations on the facades (above the entrance to the sacristy and to the technical space underneath the chapel).

A gravel bed, enclosed with a concrete border, has been built along the facade in contemporary times.

Shaft stairs that run along the northern facade of the chapel have recently been covered with a styleless covering from polycarbonate, supported by a steel substructure. A gas connection box has been installed – in the colour yellow – in the outer wall which fulfilled the role of a protective barrier, in addition to that of the covering's foundation.

### 2.2.2. Interiors

The walls inside are divided by pilasters. Vault ceilings with lunettes span the presbytery, nave and transept. The architectural decoration was focused on the external facades, while the interior of the temple was treated relatively modestly by the author of the design. The interior furnishings and the polychromes that decorate the interior, both figurative and ornamental, are outside of the scope of this paper.

The windows of the temple are filled with stained glass, assembled according to a design by the painter and stained glass window artist Stefan W. MATEJKO, at the S.G. Żeleński Krakow Stained Glass Production Plant in 1907 [2].

The largest, figurative stained glass windows, are located in the presbytery – *St. John of Nepomuk*, *St. Kinga* and in the transept – *St. Stanisław Szczepanowski* (bishop) and *St. Kazimierz the prince from Poland*. In the lower part of the figurative stained glass windows, we can also read, apart from their title, the name of the artist, the name of the production plant and the date of assembly.

In the semicircular windows of the nave there are also stained glass works with hieroglyphs, placed in golden cartouches – *IHS*, *MARIA*, *IOZIF* (JOSEPH), *A and Ω*.

In the side windows of the arms of the transept, in the sacristy and in the chapel near the presbytery there are simple, geometric and floral stained glass works.

The remaining stained glass windows placed in round openings, also designed by S. MATEJKO, were probably assembled around the year 1927 [2]. Above the altar is *The Lord's Ascension*, in the facade - *St. Cecilia playing a portative organ*, in the upper window of the transept to the left – *the Heart of Mary*, and in the upper window of the transept to the right – *the Heart of Jesus* [2].

The stained glass windows are preserved in good condition, although in the lower parts of the figurative stained glass windows there is some damage to the stained glass. The stained glass windows in circular openings have recently been secured from the outside through sheets of acrylic glass mechanically fastened to the frames of the openings.

### 2.3. Surveying measurements

The author of this paper, at the request of the parish, carried out a number of design and survey works related to the planned restoration. The measurements of the building's facade were performed using the FARO Focus 3D Sensor laser scanner. Thanks to modern 3D laser scanning



**W1** — Prezbiterium - witraż "św. Jan Nepomucen"  
skala 1:20

Hp = 129 cm



**W3** — Prezbiterium - witraż "św. Kinga"  
skala 1:20

Hp = 130 cm

**Kościół Parafialny**

Ekumeniczny

Parafia Rzymskokatolicka  
w parafii w Mystkowie  
Filipa i Jakuba Wł.

Mystków 9, 33-334 kamionka Wielka

Opisano

arch. Filip Suchon Lipa, MFCMA, 0062/2007/  
arch. Józyna Orłowski (MPCOM/11/2017)

**A3**

Oryginały format A3





**fs** filip suchon  
architekt

30-693 Kraków, ul. Bolesława 15/17, tel. 555 035 550  
Niniejsze opracowanie jest częścią w kosztowności usług  
INWENTARYZACJA ARCHITEKTONICZNA  
I PROJEKTOWANIE PRACOWNIA ARCHITEKTURA

Projekt

**IN-04.2**

Kraków, maj 2018

Fig. 5. Parish church in Mystków – stained glass – survey drawings, by Filip Suchon





technology it was possible to precisely project the tectonics of the facade in detail, in addition to the building's complex architecture details – which are typically not accessible from ground level. A camera placed on a drone was used in order to collect photographic documentation in hard-to-reach places and from perspectives that were difficult to obtain under normal conditions. All this allowed to obtain not only very precise measurements and data, but also significantly accelerated the performance of these activities in the field. Most of the work on site was done in one day.

### 3. Conclusions

A significant part of the original construction was supervised on site by the parish priest, and the original design documentation has not been preserved [1, 7]. The more interesting and valuable it is, that with the help of modern technical means it was possible to make complete drawings documenting the said church building. This testimony efforts not only of eminent creators, who have gone into oblivion, but also of many anonymous residents involved in construction over a century ago.

Quickly and accurately performed inventory, measurements, and research becomes necessary in the process of designing and proceeding permits of heritage offices. Laser scanning is a documentation method that is more and more a standard in the conservation of monuments. Combined with photogrammetry it allows for not only accurate, but also impressive documentation.

### References

- [1] Borowik A., *Dzieje, architektura oraz twórcy Zakładu OO. Jezuitów w Chyrowie. Twórczość Antoniego Łuszczkiewicza oraz Edgara Kovátsa na tle epoki*, Katowice 2012, 197–200.
- [2] Fijałkowska G., *Projektował Stefan Witold Matejko*, Kraków 2015.
- [3] Kornecki M., *Kościół diecezji tarnowskiej*, [In:] *Rocznik diecezji tarnowskiej na rok 1972*, Tarnów 1972.
- [4] Kováts E., *O zasadach architektury nowoczesnej*, *Architekt*, 1902, iss. 4, 41–46.
- [5] Kumor B., *Archidiakoniat sądecki. Opracowanie materiałów źródłowych do Atlasu historycznego Kościoła w Polsce*, Archiwa, Biblioteki i Muzea Kościelne, Lublin 1964.
- [6] Łoza S., *Słownik architektów i budowniczych Polaków oraz cudzoziemców w Polsce pracujących*, Warszawa 1931.
- [7] Szybisty T., *Wokół baroku. Kilka uwag o działalności Edgara Kovátsa (1849–1912) na polu architektury*, In: *Barok i barokizacja. Materiały sesji oddziału Krakowskiego Stowarzyszenia Historyków Sztuki*, Kraków 3–4 XII 2004, Brzezina K., Wolańska J. (ed.), Kraków 2007, 311–324.
- [8] *Wykaz obiektów wpisanych do rejestru zabytków nieruchomości województwa małopolskiego z uwzględnieniem podziału na powiaty i gminy. Stan październik 2017*, [www.wuoz.malopolska.pl](http://www.wuoz.malopolska.pl) (access: 1.10.2017).

**Ewelina Wozniak-Szpakiewicz**

ewozniak-szpakiewicz@pk.edu.pl

Chair of Urban Composition, Institute of Urban Design, Faculty of Architecture,  
Cracow University of Technology, Cracow, Poland

**Shouliang Zhao**

School of Architecture and Urban Planning, Huazhong University of Science  
and Technology, Wuhan, China

## MODULAR CONSTRUCTION INDUSTRY GROWTH AND ITS IMPACT ON THE BUILT ENVIRONMENT

---

### DYNAMICZNY ROZWÓJ BUDOWNICTWA MODUŁOWEGO I JEGO WPLYW NA PRZESTRZEŃ ARCHITEKTONICZNO-URBANISTYCZNĄ

#### **Abstract**

The article deals with the problem of increasing demand for modular buildings as an answer to the construction industry's current situation. The author addresses the following question regarding the near future of the modular construction industry: How would it reflect on urban space, living space and the whole attitude toward modular construction issues? What is the role of the architect during the design-build process? Is it possible to make references to "beauty" in a modular construction context?

**Keywords:** volumetric modular construction, modular construction, off-site, assembled architecture, permanent modular architecture

#### **Streszczenie**

Artykuł podejmuje problematykę rosnącego popytu i zapotrzebowania na realizację obiektów na podstawie wolumetrycznej technologii modułowej. Autor stawia pytanie o przyszłość budownictwa modułowego. Jaki wpływ będzie ono miało na kształtowanie przestrzeni miejskiej i na przestrzeń życiową? Jaka jest rola architekta podczas procesu zaprojektuj-wybuduj? Czy możliwe jest odniesienie wartości „piękna” do rozwiązań w systemie modułowym?

**Słowa kluczowe:** wolumetryczne budownictwo modułowe, prefabrykacja, budownictwo modułowe, architektura

## 1. Introduction

Investment in the construction sector has been dynamically growing for several years. According to the European Construction Market Forecast [1] the growth is expected to continue into 2019 and 2020. European construction growth is broad-based and occurs in all major sectors: residential, non-residential and civil engineering [14]. The construction market is at a significant moment. However, this idea relates not only to the dynamic and constant growth of the industry's input but also to many issues which construction is currently facing.

There are several factors shaping the current situation. Mark Farmer, in his report on the UK's market "Modernise or Die" [2] suggests that the UK's construction industry faces "inexorable decline" unless longstanding problems are addressed. He identified several critical symptoms of failure, particularly the labor shortage (which relates to demographic issues as well as the poor image of the construction industry), low predictability in the sector, its lack of innovation and collaboration, and its non-existent research and development (R&D) culture. These symptoms are common to many countries in the European Union and North America. High levels of cost inflation, driven by labour shortages, have caused numerous delays as costs have risen prohibitively.

This current situation pushes the construction industry into a modern method of building and has a direct impact on the increased demand for modular construction. There are many advantages of the modular construction method. However, in the majority of cases, one of the main reasons for using modular technology is to speed up the delivery time which, compared to traditional on-site construction, can create buildings in a much shorter time frame. The schedule reduction is the biggest incentive that this method of construction ensures. It is also one of the largest claims that the industry has and the major motivation behind why permanent modular construction is used in the projects [4, p.10]. As evidence of the changing approach, it is worth mentioning that many of the public tenders in Germany require the modular construction method instead of the traditional. This is an absolutely great opportunity for the modular industry market to grow. At the same time, this challenge carries a major threat, when time is the main goal. The design and build process characteristic of the modular construction industry often limits the role of the architect and architectural design. The most promoted features are related to schedule-reduction, cost-reduction, number of units, and multiplication. The values such as relation to the urban context, aesthetic and architectural form seem to be overlooked. How would they reflect on the urban space, living space and whole attitude to modular construction issues? What is the role of the architect in the modular construction industry? Is it possible to make references to "beauty" in the context of modular construction?

## 2. Background – The Advantages of Modular Construction

Modular construction is a process in which a building is constructed off-site, under controlled plant conditions, using the same materials and designing that meet the same codes and standards as conventionally built facilities – but in half the time (Fig. 1). Buildings are

produced in “modules” that when put together on site, reflect the identical design intent and specifications of the most sophisticated site-built facility – without compromise (Modular Building Institute). There are two types of modular construction: Permanent Modular Construction (PMC) and Relocatable Buildings. Permanent Modular Construction is a method of construction that greatly differs from temporary buildings, such as construction trailers or mobile homes. According to the Modular Building Institute’s definition, PMC is an innovative, sustainable construction delivery method utilizing offsite, lean manufacturing techniques to prefabricate single or multi-story whole building solutions in deliverable module sections. PMC buildings are manufactured in a safe and controlled setting, and can be constructed of wood, steel, or concrete. The structures are 60% to 90% completed in a factory-controlled environment and transported and assembled at the final building site [11]. PMC, as an off-site solution, is deemed a higher quality, faster to market, and a greener solution than traditional stick-built, site-built construction. They are custom-designed commercial buildings much the same as their traditional site-built counterparts (MBI Website). In many cases, using PMC does not change the design, structural system, or options for finish materials. The main difference is the method of construction [3, p. 17].

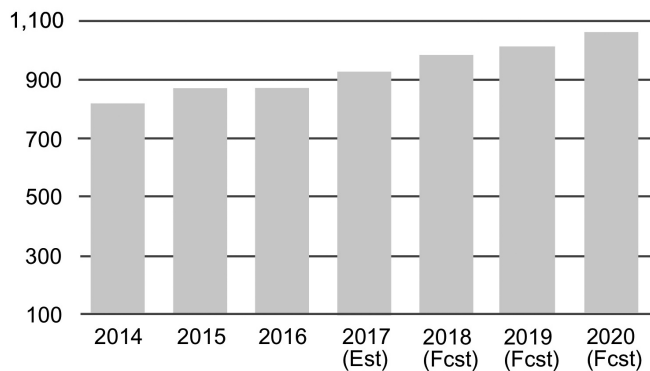


Fig. 1. Diagram of Modular Construction Schedule vs. Site Built Construction Schedule (Source: [11])

Many studies and reports indicate the undeniable superiority of modular construction over traditional buildings<sup>1</sup>. According to a recent report entitled, “Permanent Modular Construction: Process, Practice, Performance”<sup>2</sup> – published in 2015 by the University of Utah – the following are the key findings which prove that there are several advantages of permanent modular construction, when compared with traditional construction. Regarding the Quantitative Analysis, the resources saved are:

- ▶ Schedule: 39%
- ▶ Cost: 16%

<sup>1</sup> One of the most recent reports is: [4].

<sup>2</sup> The research focuses on commercial construction and does not include single family residential. The research uses a case study method to compare PMC projects to traditional site-built projects globally for construction performance parameters such as cost, schedule, quality, and safety.

- ▶ Quality: 5.4 Average Change Orders
- ▶ Safety: 0.25 Average Safety Incidents

Regarding the key benefits (there are more, ones related to ecological issues, etc.) of using permanent modular construction, they are the following: schedule reduction during the construction phase, product quality (the monitoring system ensures stable, constant quality) and site operations [4. p. 3–15]. However, when analyzing numerous documents and articles, including the abovementioned, it is noted that one important element is frequently omitted – aesthetically pleasing architectural design. Nevertheless, architecture based on modular construction should still represent a work of art. According Vitruvian theory, a good building should satisfy the three principles of durability, utility, and beauty (Latin: *firmitas, utilitas, venustas*) [19]. Unfortunately, the majority of modular buildings reduce the architecture to numerical parameters and engineering. The assessment criteria usually concerns execution time, manufacturing time, assembly time, and the number of units [15]. This problem increases with the dynamics of the development of this construction sector, which in recent years has gained a very high rate of growth.

### 3. The Boom of Modular Construction

Last years present extremely dynamic growth of the modular construction industry market. One of the fastest growing markets are the United Kingdom, the United States and China. For example, in China, in March 2017, the Ministry of Housing and Construction promulgated the “Thirteenth Five-Year Plan” of Action for Assembled Buildings, which calls for the comprehensive promotion of the development of assembled buildings. By 2020, the proportion of assembled buildings in new buildings in China will reach more than 15%. In some promoted key areas – like the urban agglomeration in the Pearl River Delta – by the end of 2025, the proportion of assembled buildings to new buildings will be more than 35%, and the proportion of government-invested projects to assembled buildings will be more than 70%. The fact that China is the country with the world’s largest population (1 390 080 000 inhabitants) and the third largest in terms of size, enables one to conclude that assembled buildings in China will have a significant impact on the global construction industry.

Regarding the U.S. market, which is the fourth largest country in the world in terms of size, modular broadly is estimated to make up 3–5 % of the total construction industry (MBI, 2018) and is still growing. Since 2014, the value has increased from 2,38% to 3,27% for year 2017<sup>3</sup>.

While focusing on European examples, the UK market for modular buildings is estimated to have increased by 6% in 2017. What is very important to indicate that the UK government is to priorities use of offsite manufacturing to improve the cost effectiveness, productivity and speed of construction delivery<sup>4</sup>. The market value includes factory-made, fully assembled

<sup>3</sup> Based on the presentation on Dave Sikora, the MBI’s Board Member, at the MBI Meeting in Munich, on 26<sup>th</sup> Sept. 2018.

<sup>4</sup> There are several publications ordered by UK government, i.e.: Farmer Review 2016: Modernise of Die; The Farmer Review of the UK Construction Labour Model’ was commissioned in February 2016 by the Construction Leadership Council at the request of the government.



Fig. 2. UK Market for Volumetric Modular Building and Temporary Accommodation – 2014–2020  
(Source: [8])

3-dimensional modules. The biggest market for modular construction products includes housing (including majority part of temporary accommodation), education, healthcare and hospitality industry (hotels). Over the next few years, to 2020, steady growth is forecasted in the sector. Importantly, there is now a strong likelihood of an increase in the use of volumetric to help meet the chronic housing shortage and cope with the lack of traditional construction skills within the construction industry [8].

#### 4. Modular Buildings: From Container-Based Temporary Accommodation to Modular Turn-Key Luxury Hotels

It is difficult to overlook the EU migrant crisis<sup>5</sup> which has seriously increased the demand for modular construction in the European Union as well as the image of modular construction, including a negative impact on the urban space [10]. There are many modular housing estates or complexes (permanent as well as temporary accommodation) built “in a rush” for refugees in Germany, including in such cities as Hamburg, Munich and Dresden. However, there is still a huge lack of housing, as well as schools and kindergartens for new inhabitants-migrants. There are more than 400,000 apartments needed in Germany to meet increasing demand [9]. Conventional construction methods (based on long-term processes and on-site construction) have not been able to carry this challenge in such a time frame. Modular construction methods of building are the most promoted by both public sectors (tenders) and private ones.

What does this demand actually mean – aside from the economic benefits – for the modular construction industry and built environment? Facing such a big challenge in a very short time frame means that the risk of failure is much higher. From the architectural and urban perspective, the failure mostly refers to the architectural design and the quality, resulting in an impact on the urban landscape and the society. Providing fast solutions often means creating temporary

<sup>5</sup> The European refugee crisis in the 21<sup>st</sup> century is described as the most serious since the Second World War. According to Eurostat, in 2015, EU member states received over 1.2 million first time asylum applications, a number more than double that of the previous year [1]. The highest number of first time applicants was registered in Germany, with 35% of all first time applicants in the EU member states [1].

shelters, low quality grey boxes or containers. Indeed, many projects are planned as temporary accommodations that will be relocatable or will just collapse in three to five years. [15]. However, many of them will remain permanently in the built environment, shaping the housing environment and human life.

Time and money are indeed the key benefits of factory-built construction versus traditional construction, and the main reasons for increasing demand for permanent modular construction. It is good to see that, next to those key advantages that define important boundaries for the whole design and build process, there are examples, in which values such as architectural form and its impact on the urban space constitute an important element of the project based on modular construction technology.

Parallel to this situation in Europe, there is a quality modern hospitality industry growth driven by modular construction. Some experts even note the revolution in the hospitality industry, the modular construction method a major contributor to this process. The world hotel chains, including some of the largest, started to use modular construction method to provide their hotels in a much shorter time frame (thus ensuring a quick return on investment). For example, a Netherlands-based hotel chain – CitizenM – build several hotels based on turn-key modular guestrooms in Europe and US. One of the most interesting project is the Hotel CitizenM Tower of London which is located in London, within the World Heritage Site. The scheme was developed with consideration of the historical part and was designed to integrate within Trinity Square’s townscape, as well as to work harmoniously with the numerous historical assets within the site’s surroundings. The site design phase has involved the creation of a complex basement, connecting two lifts to the Tower of London tube station [16]. The project was designed by AnyoStudio



Fig. 3. Modular Hotel: CitizenM Tower of London, London, UK  
(Source: Image via official citizenM website [20])



and presents a breakthrough in which the modular building – designed with particular care - is located in the historical and central part of the City, creating sensitive and contextual contribution to the World Heritage Site. The architectural focus on details, proportions, materials, as well as relation to the urban landscape presents very good example of cutting-edge modular architecture.

Another example presents the biggest hotel chain and well recognized world luxury hotel brand –the International Marriott, is strategically expanding in North America based on modular construction. In the next few years, the company plans to build around 50 modular hotels in North America. If such a powerful brand can choose this method, it represents a big step in moving modular construction to a higher level, one in which high quality luxury products and modular construction can be identified as integral elements. At the turn of 2019 and 2020 AC Marriott plans to open the world's tallest modular hotel. A new 25-story AC Hotel by Marriott is planned at 842 Sixth Avenue, very prestige location in Manhattan, New York City. The hotel will include 168 turn-key modular guestrooms, which will create 21 modular stories (the base, which includes the first four stories, will be built with conventional technology). The hotel is designed by New York-based architect Danny Forster, who makes a significant statement on his website “high-quality consistency marries inventive architectural expression, with a sophisticated balcony strategy that puts to rest the

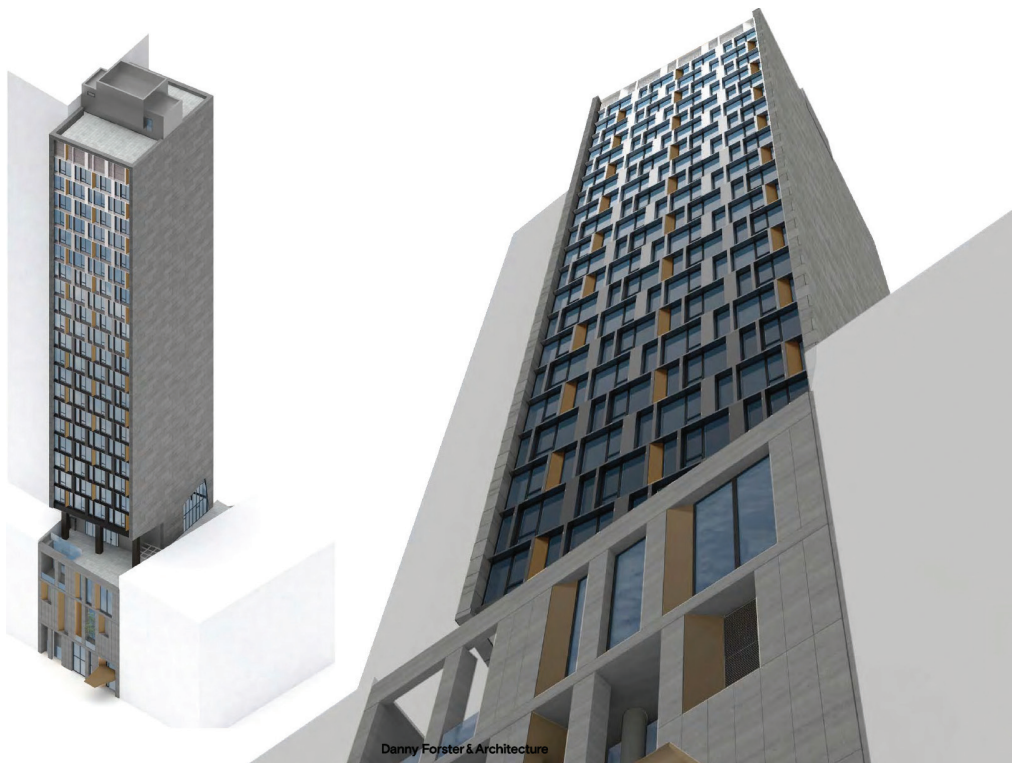


Fig. 4. Modular Hotel: AC hotel by Marriott, project destination: Manhattan, New York, UK (Source: [17])

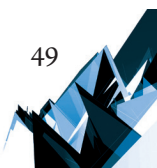




Fig. 5. Modular Hotel Extension: Bonifacio Spa and Sport Resort, Sochocin, n/Warsaw, Poland (Source: [18])

stigma of the cheap pre-fab double-wide” [17]. This idea is a proper expression of the current trend in the modular construction industry, where, more and more, architects are emerging as creators and image-transformers.

Another interesting modular example is extension of the four-star Hotel Bonifacio Spa and Sport Resort in Poland. The hotel is located in the center of a wonderful landscape, on a forest clearing in the picturesque scenery of the Wkra valley, about 70 km from Warsaw. The sophisticated location is an intriguing challenge that only this technology could meet. The development of the hotel in such a lush place, while ensuring the silence and comfort of guests staying in the existing part of the hotel, was only possible by limiting the heavy work to a minimum, and thus the noise, pollution and discomfort characteristic of traditional construction methods. The new section, which consists of 34 modules, was assembled in less than 10 days, while in traditional construction, it would take around eight months. The add-on consists of a two-story building. The first floor includes the spa rooms and the fitness facility, while the second one includes eight guestrooms. Due to the extension, the new modular segment had to follow the props and composition of the existing part, since it would consist of a new and better quality in relation to the existing building. The project was designed and built by DMDmodular[18], the Polish-based manufacturing company lead by architects that aims to integrate three crucial features: beauty, design, and modular technology.

## 5. Conclusions

Despite the overwhelming presence of the modular construction developments lacking high aesthetic values which are a carrier of negative connotations, there is more and more projects that present the changing approach to the modular construction market. Modular Construction technology gives some huge possibilities for architectural creations. The key benefits – competing for traditional technology – are also a base of a much wider range of aesthetic options that allow designers to achieve architectural variety. The last years demonstrated the growing role of the architect during the design-build process based on modules. Architects emerged as stigma-breakers and image-transformers of the dominant negative associations with off-site construction.

Although the process of using modular technics by hospitality sector is very fresh, because it started significantly only three years ago, it is suspected that hospitality sector based on modular construction might play a crucial role in redefining image, the position on modular architecture in wider design & visual context by providing cutting-edge architecture.

## References

- [1] European Construction Market Forecast from 2015–2020, <https://buildingradar.com/construction-blog/european-construction-market-forecast> (access: 15.09.2018).
- [2] Farmer M., *Farmer Review 2016: Modernise or Die*, Construction Leadership Council, 2016.
- [3] Piper Ch. (Ed.), *Introduction to Commercial Modular Construction*. USA: Modular Building Institute, 2015.
- [4] Smith R., *Permanent Modular Construction: Process, Practice, Performance*, University of Utah, Integrated Technology in Architecture Center, College of Architecture and Planning, Report, April 2015.
- [5] Smith R., *Pre-Fab Architecture: A guide to Modular Design and Construction*, Hoboken, New Jersey: John Wiley & Sons, 2010.
- [6] Schoenborn J., *A Case Study Approach to Identifying the Constraints and Barriers to Design Innovation for Modular Construction*, Blacksburg: VA, 2012.
- [7] *Permanent Modular Construction 2013 Annual Report*. USA: Modular Building Institute, 2013.
- [8] Prefabricated Volumetric Building Systems Market Report – UK 2018-2022, AMA Research, 29/03/2018.
- [9] Tomkiw, Lydia. Europe Refugee Crisis: Germany Debates Housing In Airports And Cemeteries As Possible Solutions, *International Business Time*, 01/22/16 AT.
- [10] UNHCR Global Appeal 2015 Update – Europe summary. The UN Refugees Agency, 2015, (online): <http://www.unhcr.org/5461e5f80.html> (access: 15.02.2018).
- [11] *Why Build Modular*, *Modular Building Institute*, (online): [http://www.modular.org/htmlPage.aspx?name=why\\_modular](http://www.modular.org/htmlPage.aspx?name=why_modular) (access: 15.04.2016).

- [12] Website of DMDmodular Sp.zo.o.: [www.dmdmodular](http://www.dmdmodular.com), (access: 1.10.2018).
- [13] WorldofModular2016,(online):[http://www.modular.org/HtmlPage.aspx?name=2016\\_world\\_of\\_modular\\_welcome](http://www.modular.org/HtmlPage.aspx?name=2016_world_of_modular_welcome) (access: 10.06.2016).
- [14] 85th EUROCONSTRUCT Conference Helsinki, 8 June 2018, [https://euroconstruct.org/jart/prj3/wifo/data/uploads/euroconstruct/press/2018\\_85%20-%20Press-Release%20Helsinki.pdf](https://euroconstruct.org/jart/prj3/wifo/data/uploads/euroconstruct/press/2018_85%20-%20Press-Release%20Helsinki.pdf) (access: 1.10.2018).
- [15] Woźniak-Szpakiewicz, E., *EU migrant crisis and increasing demand for modular construction: modular social housing complex for refugees in Munich*, [in:] *Back to the Sense of the City: 11th VCT International monograph book*, Year 2016, Krakow, Eds. Barcelona A., Rolando B., Gyurkovich M., Barcelona 2016.
- [16] [www.anyostudio.com](http://www.anyostudio.com); <https://studioanyo.com/work/citizenm-london-hotels/> (access: 1.09.2018).
- [17] [www.dannyforster.com](http://www.dannyforster.com); [http://www.dannyforster.com/project/ac-nomad/%22?\\_ct=5dxq7lf6cgn4](http://www.dannyforster.com/project/ac-nomad/%22?_ct=5dxq7lf6cgn4) (access: 1.09.2018).
- [18] [www.dmdmodular.com](http://www.dmdmodular.com) (access: 1.09.2018).
- [19] Vitruvius, *The Ten Books on Architecture*, Harvard University Press, 1914.
- [20] <https://www.citizenm.com> (access: 1.09.2018).

Michał Grodecki

Aleksander Urbański  [orcid.org/0000-0002-5544-9134](https://orcid.org/0000-0002-5544-9134)

[aurbansk@pk.edu.pl](mailto:aurbansk@pk.edu.pl)

Department of Geotechnics, Faculty of Environmental Engineering, Cracow University of Technology

LANDSLIDING SLOPE SUPPORTED BY GABIONS –  
A CASE STUDY AND THE METHODOLOGY OF NUMERICAL MODELLING

---

ZABEZPIECZENIE OSUWISKA MUREM OPOROWYM Z GABIONÓW –  
PRZYKŁAD ZASTOSOWANIA I METODYKA ANALIZY KOMPUTEROWEJ

**Abstract**

The paper presents results of numerical analysis of the gabion retaining wall stability. A few of the possible design variants were analyzed and the optimal one was chosen.

**Keywords:** gabion, retaining wall, FEM, stability

**Streszczenie**

Praca przedstawia rezultaty analiz numerycznych stateczności muru oporowego z gabionów. Przeanalizowano możliwe warianty projektowe i wybrano optymalne.

**Słowa kluczowe:** gabion, mur oporowy, MES, stateczność

## Symbols

- $\phi$  – internal friction angle [deg]
- $\gamma$  – soil bulk density [kN/m<sup>3</sup>]
- $c$  – cohesion [kPa]
- SF – stability factor [–]

## 1. Introduction

The landslide which is analysed in this work is localised in a sub-mountain area of southern Poland, near the city of Nowy Sącz. It is located at lower parts of slopes of a V-shaped valley. At the valley floor a stream runs, which normally carries minimal flow (less than 0.5 cubic metre/sec), but it temporarily grows up to several cubic metres per second. Exact hydrological data were not available; however, evidence of such events in the past was visible, along the banks of the stream. Erosion related to this was the most probable cause of landslide activation, endangering the municipal road crossing it. Signs of massive movements were observed, both as the deterioration of the road surface and terrain deformation. In order to protect the road, and to fix the problem of stream bank strengthening, a gabion retaining wall is proposed. Also ecological and landscape preservation issues were taken into account

The whole landslide has a length of about 300 m, but the length of its lowest part, protection of which is considered here, is of 60 m. Remaining parts of the road crossing the landslide was protected by other structural means (Tessina-wall).

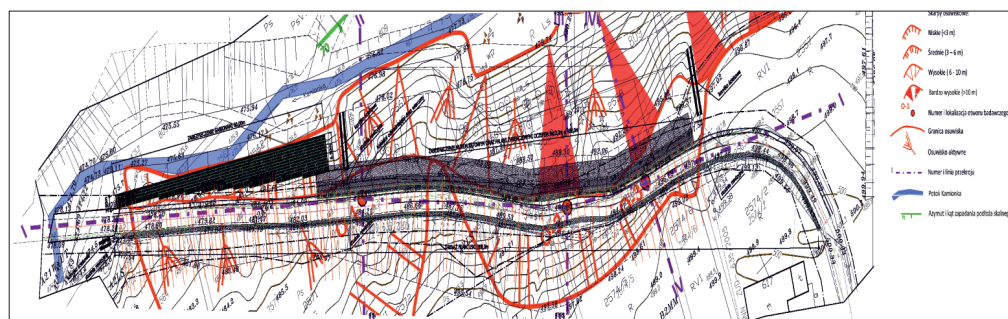


Fig. 1. Situation of the landslide area (gabion wall at the left, marked dark)

The design history and the possible construction variants (especially the final one) analysed are described. Special attention is paid to numerical analysis, which was used to perform static calculations (in order to check stability conditions of the landslide and estimate internal forces in structural elements).

The height of the slope beneath the road reaches 7.5 m, so it looks quite possible to construct a gabion retaining wall as a protective structure.

According to existing geotechnical evidence, the existing slope is built mostly from weak clays (cohesion  $c$  about 11 kPa, internal friction angle  $\phi$  about 11°). Rocks with compressive

strength  $f_c$  about 0.36 MPa are found at about 4 m below the terrain level, stronger rock (with  $f_c$  about 0.78 MPa) – 6 m below the terrain level. A load of 25 kPa due to road traffic was introduced at the municipal road according to Polish legal regulations [8].

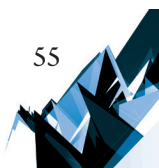
## 2. Numerical simulations

Numerical simulations were performed using ZSoil v16 code. The  $c-\phi$  reduction method (described in [5–7]) was used to estimate Stability Factor SF. All simulations were performed in the plane strain conditions. The Coulomb – Mohr elastic-plastic model was used for the soil. The soil-water composite was treated as a single-phase media, mainly because the geotechnical documentation, which was prepared prior to the author’s involvement in the case, only contains data allowing for this kind of approach. For gabions (made of 60 x 80 x 3.3 mm wire mesh and filled with crushed aggregate), the Coulomb-Mohr model with additional cohesion (described in [2], parameters estimated with use of mesh strength parameters according to [1]) was used. Interface elements between gabions and soil and between gabions were used. Interface parameters were estimated according to [3] (friction angle between gabions and between gabions and subsoil equal to 90% of the internal friction angle) and [4] (cohesion in the interface elements responsible for the limited tensile strength of the joints between gabions estimated as 20 kPa). The truss elements responsible for modelling of the joints between gabions resistance to gap opening were used, with tensile strength of the joints of 20 kN/m (see [4] for details).

Table 1. Parameters of the gabion and soil used in the stability analysis

Material	E [MPa]	$\gamma$ [kN/m <sup>3</sup> ]	$\phi$ [°]	c [kPa]
I (uncontrolled embankment)	100	21.0	20	5
II (silty clay + rubble)	13	22.5	11	11
IVa (clay rubble)	15	21.5	12	12
Va (rubble)	400	24.0	55	57
VI (soft rock)	500	24.0	55	123
Gabions $h = 1$ m	200	22.0	40	30.75
Gabions $h = 0.5$ m	200	22.0	40	61.5
Concrete	24000	24.0	-	-

First of all, a stability analysis of the existing “in situ” state of the slope was performed (numerical model – see Fig. 2). The value of the stability factor SF = 1.028 obtained (without road load) shows that slope is practically in the limit state of the stability (Fig. 4). So design of the protecting structure was really necessary.



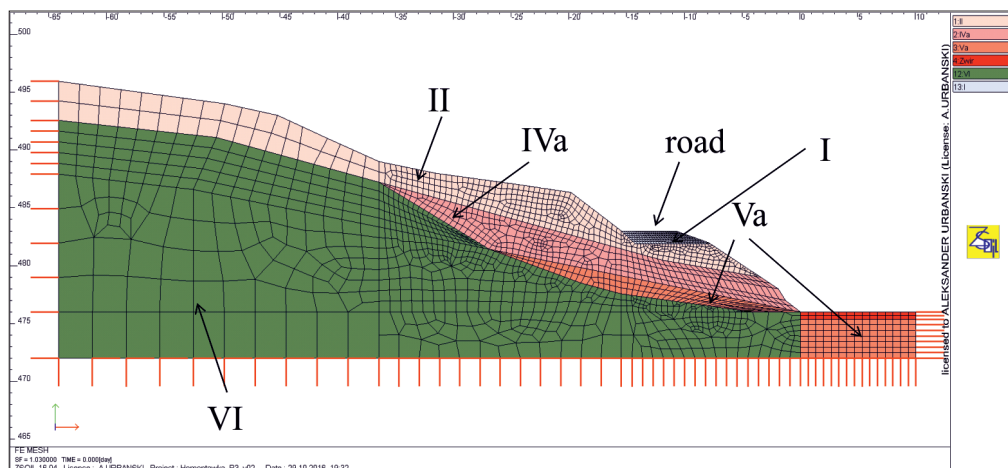


Fig. 2. Numerical model of the existing landslide

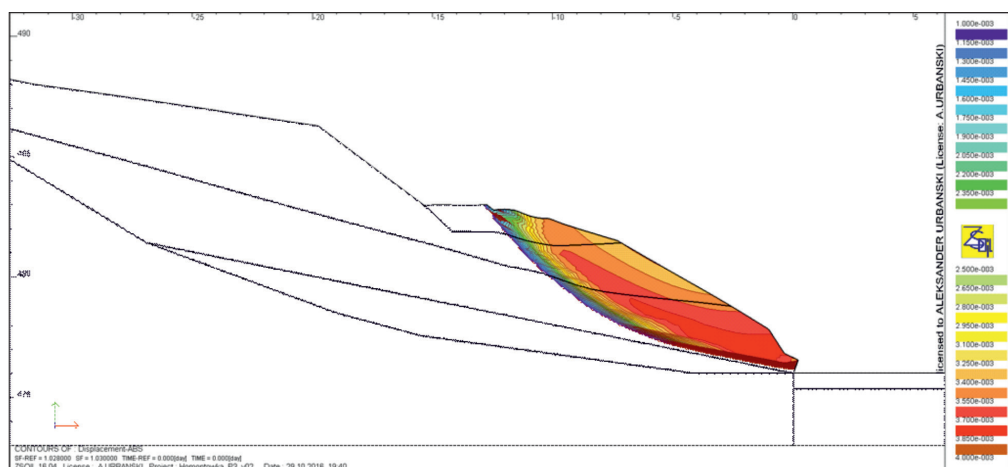


Fig. 3. Failure mode (sliding surface) of the existing landslide, SF = 1.028

The first variant of the gabion wall consists of one 1 m high and eleven 0.5 m high gabions. Numerical simulation shows that such a construction does not improve the stability of the landslide (SF = 1.01 without road load). It's worth noticing that the destruction mode of this variant includes lowest gabion failure due to shearing. So taking into account the limited shear strength of the gabions is essential for safe design.

In order to obtain a satisfactory value of SF, about 1.50, anchoring of the wall was analysed. Titan 40/20 type anchors with 90 mm drilling tool diameter were used. An anchoring length of 12 m (including 5 m active zone), distance between anchors of 5 m and prestress  $\sigma_0 = 20$  MPa was applied.

Firstly, one anchor level was proposed (Fig. 5) and an SF = 1.20 (Fig. 6) with road load was achieved. So anchoring of the gabions wall leads to some increase of the SF, but the result obtained is still not satisfactory.



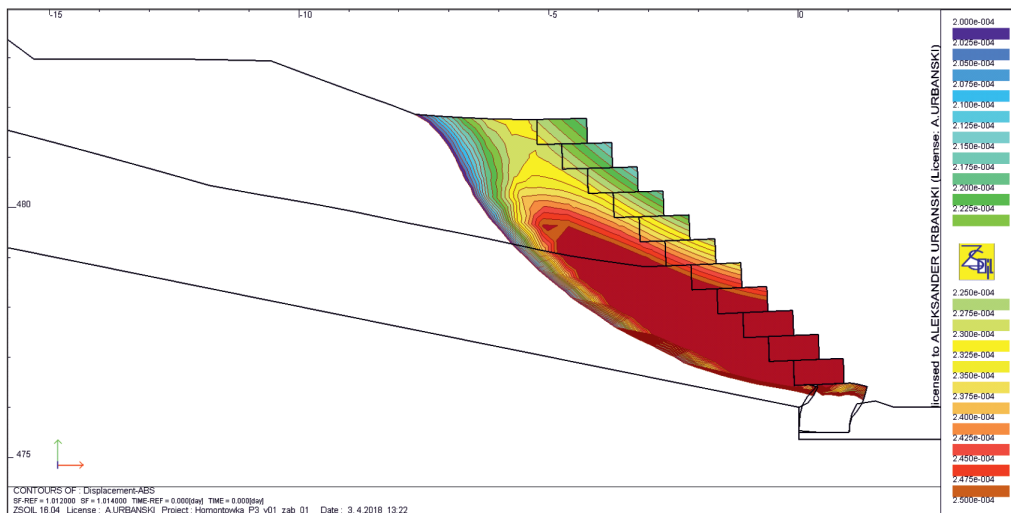


Fig. 4. Failure mode (sliding surface) of the landslide supported by gabions without anchors, SF = 1.01

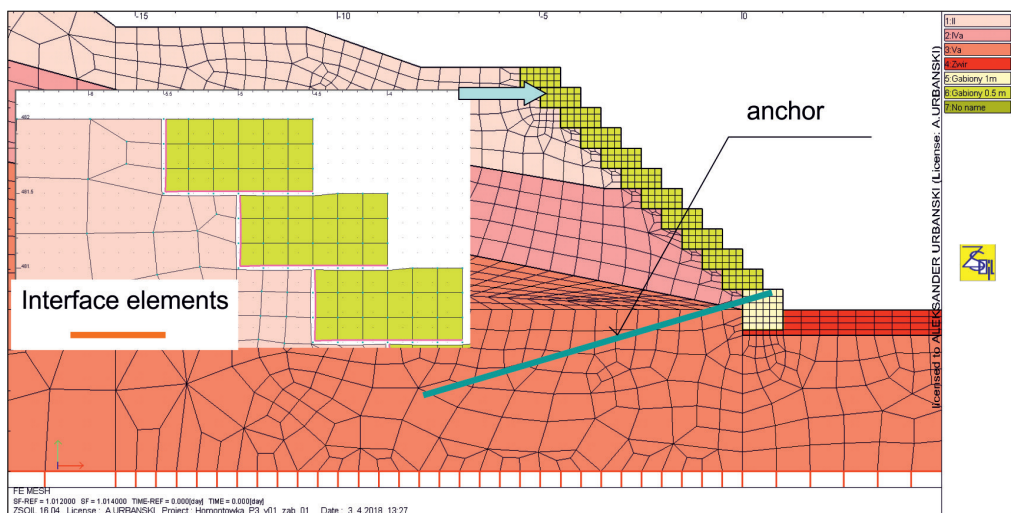


Fig. 5. Numerical model of the gabions wall with 1 level of anchoring. Detail of gabions modelling

Two levels of anchors results in an SF = 1.26 (with road load), which is still not satisfactory. Finally, a variant with 4 levels of anchors was proposed and a satisfactory SF = 1.63 (with road load) was achieved.

This variant was chosen as the optimal one and selected for realisation. One important detail is the way of strengthening the gabion surface in a situation where large forces from the anchors are introduced, by means of a continuous reinforced concrete beam (section 0.3 x 0.5 m), placed on the anchor levels. This is shown in drawings (Fig. 8).

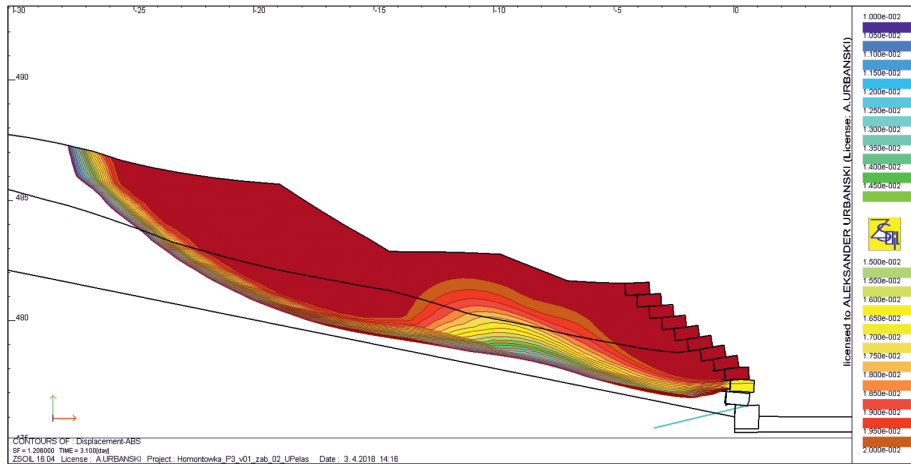


Fig. 6. Failure mode (sliding surface) of the landslide supported by gabions with 1 anchor level, SF = 1.20

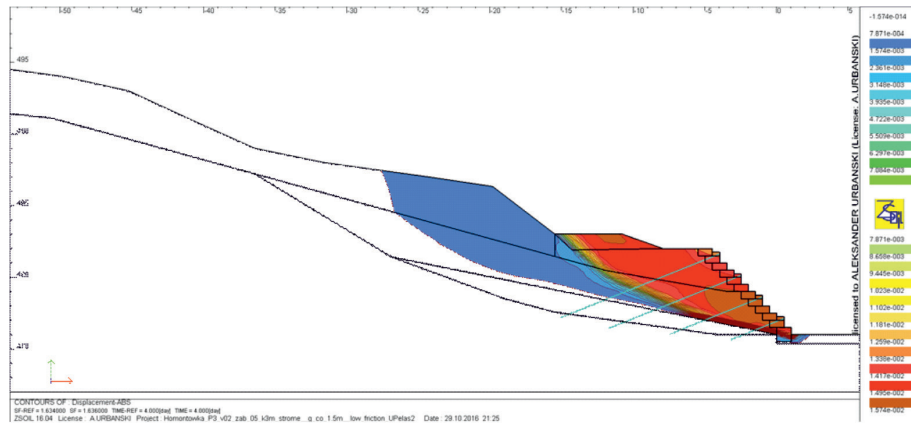


Fig. 7. Failure mode (sliding surface) of the landslide supported by gabions with 4 anchor level, SF = 1.63

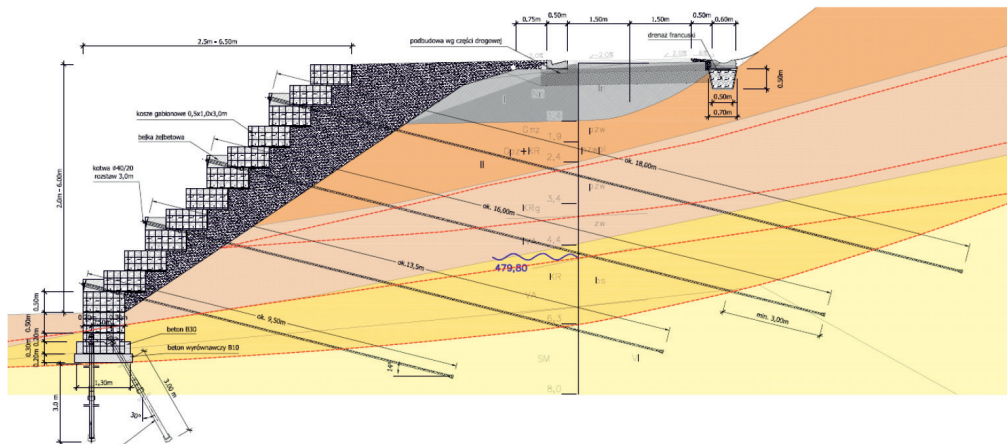


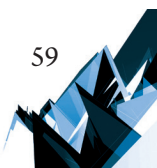
Fig. 8. Final structural solution of anchored gabions securing the roads.

### 3. Final remarks

The numerical simulations of the landslide protected with gabions presented show that such simulations could be a useful tool in the design process. It was possible to analyse several variants of the structure and to choose the optimal one. It's worth noticing that in some cases stability loss occurs with shearing of the gabions or failure of the connection between gabions. Therefore, the limited shear strength of the gabions and limited joints strength should be taken into account.

### References


- [1] A 975 – 97 *Standard Specification for Double-Twisted Hexagonal Mesh Gabions and Revet Mattresses (Metallic-Coated Steel Wire or Metallic-Coated Steel Wire With Poly(Vinyl Chloride) (PVC) Coating)*, American Society for testing and materials, 2011.
- [2] Bathurst R.J., Rajagopal K., *Large-scale triaxial compression testing of geocell reinforced granular soils*, "Geotechnical Testing Journal" Vol. 16, No. 3/1993, 296–303.
- [3] Bergado D.T., Youwai S., Teerawattanasuk C., Visudmedanukul P., *The interaction mechanism and behavior of hexagonal wire mesh reinforced embankment with silty sand backfill on soft clay*, "Computers and Geotechnics" 30/2003, 517–534.
- [4] Grodecki M., *Numerical modelling of gabion joints*, "Technical Transactions" 2/2017, 83–89.
- [5] Griffiths D.V., Lane P.A., *Slope stability analysis by finite elements*. "Geotechnique" 49/1999, 387–403.
- [6] Matsui T., San K-C., *Finite element slope stability analysis by shear strength reduction technique*. "Soils and Foundations" 32/1992, 59–70.
- [7] Zimmemann Th., Truty A., Urbański A., Podlęs K., *Z\_Soil.PC 2003 manual. Theory*, Elmeppress international & Zace Services ltd., Lauzanne, Switzerland 2005.
- [8] Rozporządzenie Ministra Transportu i Gospodarki Morskiej z dnia 2 marca 1999 r. w sprawie warunków technicznych, jakim powinny odpowiadać drogi publiczne i ich usytuowanie. Dz.U. 1999 nr 43 poz. 430.





Mariusz Maślak  [orcid.org/0000-0003-3592-429X](https://orcid.org/0000-0003-3592-429X)  
mmaslak@pk.edu.pl

Piotr Woźniczka  [orcid.org/0000-0002-5471-9526](https://orcid.org/0000-0002-5471-9526)  
Institute of Building Materials and Structures, Faculty of Civil Engineering, Cracow  
University of Technology

Michał Pazdanowski  [orcid.org/0000-0003-1344-1342](https://orcid.org/0000-0003-1344-1342)  
Institute for Computational Civil Engineering, Faculty of Civil Engineering, Cracow  
University of Technology

## FORECAST OF A FIRE SPREADING IN A LARGE-AREA SHOPPING HALL

### PROGNOZA ROZPRZESTRZENIANIA SIĘ POŻARU W WIELKOPOWIERZCHNIOWEJ HALI HANDLOWEJ

#### Abstract

The specifics of a forecast fire development in a single fire compartment consisting of a shopping hall characterised by a large area and a relatively low height are analysed in this paper. The fire initiated locally, and after initiation, depending on the ventilation conditions in the zone, more or less intensively spread to the neighbouring areas with or without full development. The propagation of hot exhaust plume was simulated within the environment of the FDS computer code. Three formal models differing in zone size and stacking height have been subjected to analysis. The influence of automatically activated smoke vents has been accounted for.

**Keywords:** shopping hall, spread of a fire, numerical simulation, fire compartment, ventilation conditions, stacking height

#### Spis treści

Przeanalizowano specyfikę rozwoju pożaru w pojedynczej strefie pożarowej, którą stanowi hala handlowa charakteryzująca się dużą powierzchnią przy stosunkowo małej wysokości. Modelowany pożar został zainicjowany lokalnie, a następnie, w zależności od warunków wentylacji strefy pożarowej, rozwijał się z mniejszą lub większą intensywnością w strefach sąsiadujących z pierwotnym źródłem ognia, aby w końcu ulec lub też ewentualnie nie ulec pełnemu rozgorzeniu. Przebieg propagacji gorących gazów spalinowych symulowano z użyciem programu FDS. Rozważono trzy scenariusze rozwoju pożaru, różniące się wzajemnie rozmiarem strefy pożarowej i wysokością składowania towarów stanowiących obciążenie ogniowe. Uwzględniono również wpływ, jaki na ten rozwój ma zastosowanie w rozpatrywanej hali automatycznie otwieranych klap dymowych.

**Słowa kluczowe:** hala handlowa, rozprzestrzenianie się pożaru, symulacja numeryczna, strefa pożarowa, warunki wentylacji, wysokość składowania

## 1. Introduction

Large-area shopping halls, usually constituting separate fire zones, belong to the peculiar group of enclosed compartments having a relatively low height and a limited number of access openings. Geometries of this type, even when the smoke vents required by law are present and sufficiently numerous, are characterised by difficulties in the efficient ventilation of the considered zone, and this results in a high uncertainty level in forecasting the fire development scenario. Determination, whether in such a case during a fire exposure the developing conditions would allow for the creation of a fully developed fire, or for the whole duration the fire would remain localised with limited intensity and affected area, seems to be the key. A credible reply to the question stated above may be different, depending on the size and geometry of the fire compartment, the fire load accumulated in the compartment, availability of oxygen in exchange with immediate surroundings and the stacking height of the merchandise present [2]. Three mutually corresponding numerical models are analysed in detail here. For each of these models, the fire development is simulated. Each of these models results in a different scenario, i.e. in a different estimate of the warranted safety level.

## 2. Description of the considered numerical models

A numerical simulation of fire development in a large area shopping hall is performed in each case within the environment of the FDS (*Fire Dynamic Simulator*) computer program, developed by Mc Grattan et al. [7]. It is assumed that the fire load is created by the merchandise stacked on racks. It is also assumed that the merchandise has the parameters of cellulose. For comparative purposes, two alternative scenarios are considered in each case, i.e. when there are automatically activated smoke vents installed, and when there are no such vents. In the first example, a small hall is considered (Fig. 1a), while in the second and third example a substantially larger hall is considered (Fig. 1b) [3]. The difference between the second and third example is in the merchandise stacking height. The simulation performed yields the temperature of gases in the fire plume specified in the selected cross-sections of the hall after various fire exposure periods. The spatial area affected by fire as well as the temporal fire development are compared. The obtained results allow for observation how, at the given height above the floor and at the selected cross-section, the temperature of exhaust gases evolves. Knowledge of this type allows for drawing more rational conclusions pertaining to fire scenario, and thus allows for better selection of necessary active and/or passive fire protection measures.

In all the considered cases convection, radiation and heat transfer through the partitions have been accounted for. The initial heat source was modelled as a localised fire with heat generation intensity of  $500 \text{ kW/m}^2$  and total heat output of 25 MW (this value is recommended in [1] as the maximum for the steel structure used to store flammable materials). The duration of this initial fire was assumed as 120 seconds, and its location

is indicated on the pictures enclosed below. The fire initiated in this manner developed further progressing or not to adjacent shelf racks located in the hall, but the intensity of this development was conditioned by the geometry of the fire compartment, the fire load gathered in this compartment and available ventilation. The materials stockpiled on the shelf racks has been modelled with the following parameters: the specific heat  $1.36 \text{ J}/(\text{kg}\times\text{K})$ , heat conductivity  $0.25 \text{ W}/(\text{m}\times\text{K})$ , volumetric weight  $1100 \text{ kg}/\text{m}^2$ . The flash point has been set at  $250^\circ\text{C}$  while the chemical composition has been modelled in a simplified manner, as for cellulose.

### 3. Scenario A – fire development simulated in a shopping hall of a limited area

It has been assumed that the dimensions of the smaller of two modelled halls are equal to  $52.00 \text{ m}$  by  $36.00 \text{ m}$  in plan with a constant height of  $4.50 \text{ m}$ . The existing and permanently open access gates have been assumed in the numerical model of the hall. These are in particular: one large gate having the dimensions of  $3.50 \text{ m}$  by  $3.00 \text{ m}$ , located in the front, shorter wall of the hall and two smaller gates, having the dimensions of  $1.00 \text{ m}$  by  $2.50 \text{ m}$  each, located in the side wall (Fig. 1). The sheathing of the hall has been modelled as made of the typical sandwich panels with  $15.00 \text{ cm}$  thick mineral wool core. The properties of the insulating material, depending on the value of the temperature affecting it have been assumed according to paper [8]. It has been also assumed that before the initiation of the fire the temperature within the hall has been equal to  $20^\circ\text{C}$  and was evenly distributed. Moreover, the considered hall was equipped mostly with storage racks of equal stacking height of  $3.50 \text{ m}$ . On these storage racks are stored materials for sale made of cellulose derivatives (mostly paper materials). These materials yielded the main fire load in the considered fire compartment. In addition  $3\times 5 = 15$  smoke vents having the dimensions of  $2.00 \text{ m}$  by  $2.50 \text{ m}$  each have been evenly distributed in the roof of the hall (Fig. 1). These vents have been activated individually by sensors set to the activation temperature of  $74^\circ\text{C}$ . For comparison, the fire development scenario in the same hall, but without smoke vents in the roof has been analysed as well.

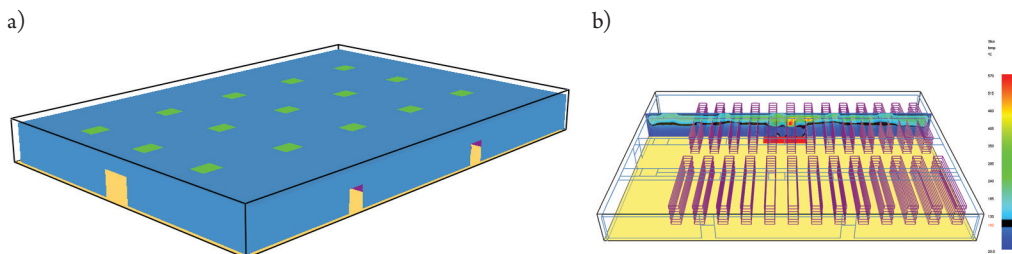


Fig. 1. The scheme of a small area shopping hall considered in scenario A: a) distribution of vertical access gates and horizontal smoke vents affecting the ventilation of the fire zone, b) distribution of the storage racks with combustible materials stacked and location of the vertical cross-section selected by the Authors to analyse the progress of fire [3]

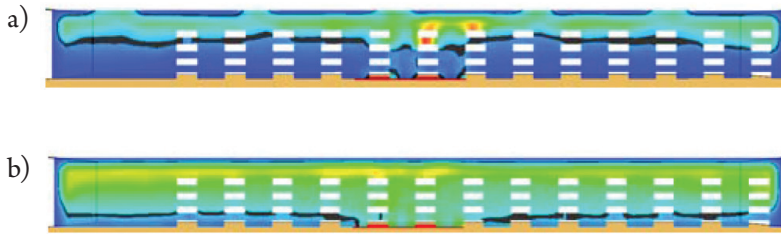


Fig. 2. Exhaust plume gas temperature maps obtained after 10 minutes of a fire exposure in the case of a smaller hall considered in scenario A, including: a) results for the hall equipped with smoke vents, b) results for the hall not equipped with smoke vents [4]

The detailed results obtained for the fire forecast in the smaller of analysed halls are depicted in Fig. 2 and in Fig. 3. Furthermore, in Fig. 1b the location of fire source initiating the development of fire is precisely indicated. This location determines the location of a cross-section in which the temperature of fire plume is mapped in subsequent moments of fire exposure. Let us consider the fire plume temperature distribution obtained after 10 minutes of a fire, under the assumption that the smoke vents operate as indicated above, as the reference one. This reference distribution is depicted in Fig. 2a. The  $100^{\circ}\text{C}$  isotherm is depicted in black in this picture. Thus the temperature of a fire plume contained within this isotherm is higher. Let us note that in this case this isotherm is located relatively high with respect to the floor level, and thus the thickness of the cool air layer above floor should allow for safe evacuation of all occupants. The limited thickness of the hot fire plume near the ceiling is a direct result of operating smoke vents evacuating the hot gases outside the building. This result may be referred to in Fig. 2b, where the analogous distribution of temperature, obtained in the same cross-section of the hall and after the same time of fire exposure, is depicted for the case of a hall not equipped with smoke vents. In this figure it is shown, how much faster would the fire develop in the same geometry of the fire compartment, with the same floor area as well as with the same location of the vertical openings (i.e. permanently open gates described at the beginning of this paper) ventilating the fire zone, in the case of a hall lacking the obligatory additional safety devices. As may be observed in Fig. 2b, the occupant of the fire compartment after 10 minutes of a fire stands no chance for safe evacuation since the temperature of a fire plume along almost the whole height of the considered cross-section, even at the layer just above the floor, reaches or exceeds the level of  $100^{\circ}\text{C}$ .

A comparison of a fire plume temperature distribution in the horizontal cross-section of the hall at the height of 4.00 m above floor level, obtained after 10, 15 and 20 minutes of a fire exposure (Fig. 3) may be interesting for an observer analysing the development of a fire in the smaller of considered halls. One may easily find out that in the 20<sup>th</sup> minute of the fire forecast for this hall the fire reaches the stage of a fully developed fire in a large area of the considered fire compartment, as most of the combustible materials gathered in the affected zone are on fire and the temperature within the fire plume tends to equilibrate. But this progress to the stage of a fully developed fire is of rather localised character, as it does not affect the whole area of the considered hall.



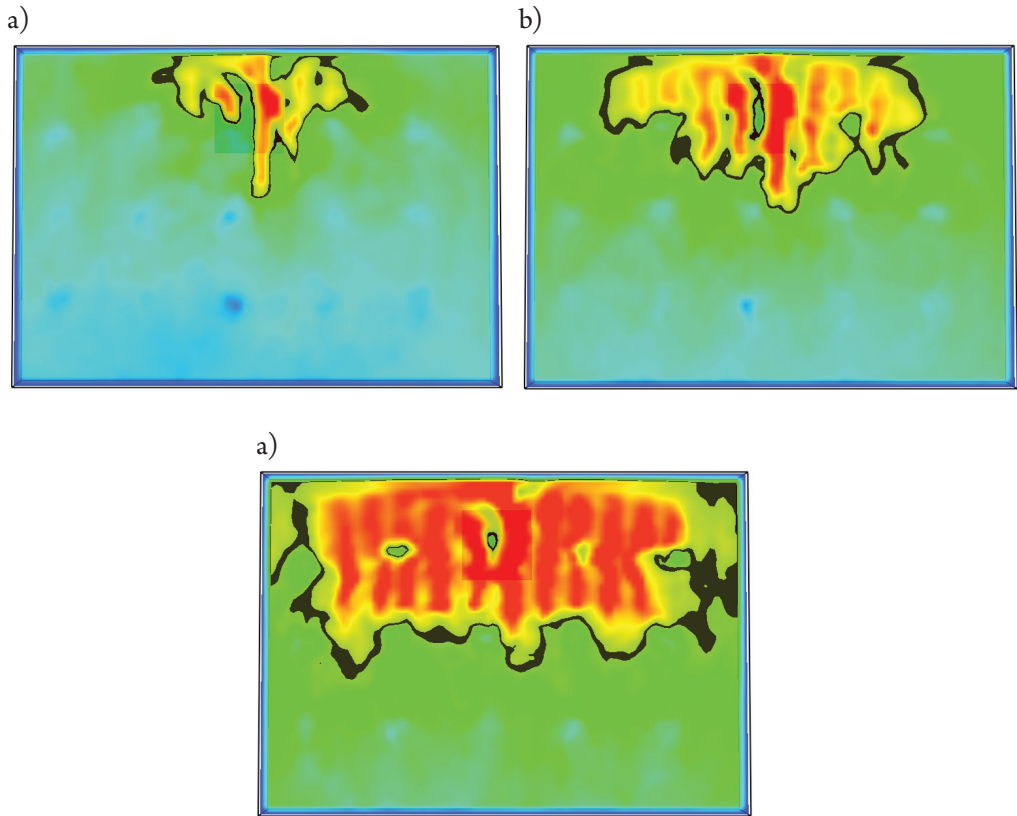


Fig. 3. Fire plume temperature maps obtained for the horizontal cross-section of the smaller hall at the height of 4.00 m above the floor level with smoke vents operating, after: a) 10 minutes, b) 15 minutes, c) 20 minutes of a fire exposure, respectively. The isotherm depicted in black on these figures corresponds to the temperature of 350°C. The location of a fire source initiating the fire is indicated by the darkened square [4]

The constataion of fire flaring up in this zone seems to be corroborated by the graph of a fire plume temperature reached in the cross-section depicted in Fig. 1b, 4.00 m above the floor level, somewhat later, i.e. after one hour of a fire exposure. It is depicted in Fig. 4, where the results of simulation for a hall equipped with smoke vents are plotted accompanied by the results obtained for the same hall devoid of these vents.

Undoubtedly, the fire plume temperature obtained in the whole considered cross-section after so long time period is almost evened out. As may be interesting, in the case of the hall equipped with operating smoke vents the temperature at the considered height is much higher than the analogous temperature forecast for the identical structure devoid of smoke vents. In the case of hall lacking the smoke vents the temperature of the fire plume reached level allowing for flare up and continued combustion of the combustible materials gathered in the fire compartment, but the intensity of a fire was strongly affected by the lack of oxygen supporting combustion [6], as this oxygen could reach the fire only through the permanently open access gates relatively distant to the considered cross-section. Thus, in this case, the fire

development scenario became typical for the ventilation driven fires and not, as will be in the case of the larger hall, fire driven by the availability of the combustible material.

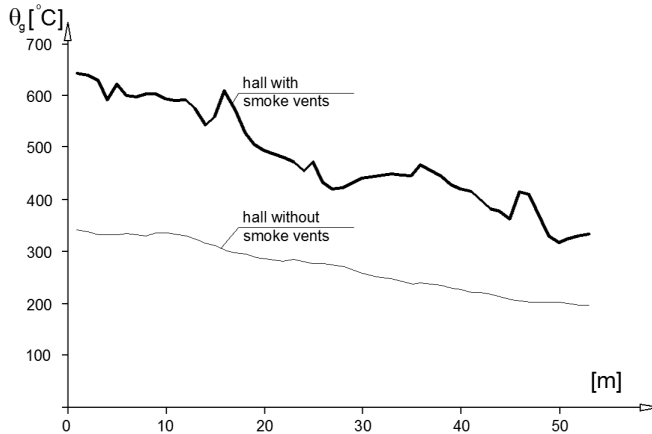


Fig. 4. Graphs of a fire plume temperature obtained after one hour of a fire exposure in the authoritative cross-section of the smaller of analysed halls (depicted in Fig. 1b), at the height of 4.00 m above the floor level [3]

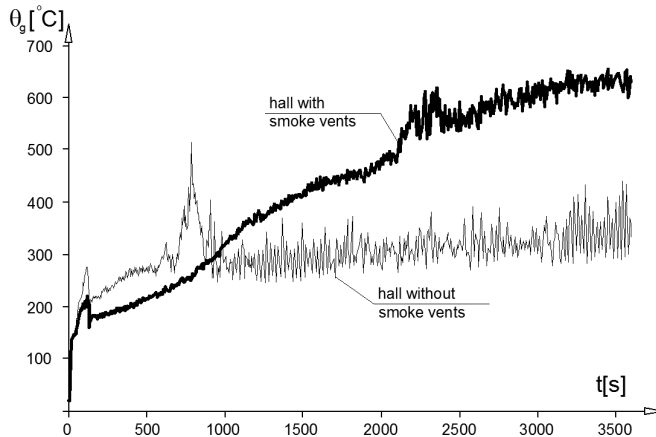


Fig. 5. Evolution of a fire plume temperature during the fire, obtained for the smaller hall at the distance of 3.00 m from the initial fire axis and at the height of 4.00 m above floor level. In the case of the hall with operating smoke vents, a monotonous increase of the averaged measured temperature is observed during the whole analysed fire exposure. For the hall devoid of smoke vents the fire intensity limitation by the lack of available oxygen is visible, and results in the fire development scenario typical for fires driven by ventilating conditions [5]

This conclusion is corroborated by the analysis of Fig. 5, where the temporal changes of a fire plume temperature are depicted as measured at the distance of 3.00 m from the initial axis of a fire representing the fire source, at the height of 4.00 m above floor level. As one may easily observe, in the case of a hall equipped with smoke vents the temperature averaged in the random combustion process increased monotonously during the whole hour of analysed fire

exposure. The results obtained for the same hall, but devoid of smoke vents, seem to indicate a completely different fire development scenario. This time the fire plume temperature measured could not reach the sufficiently high level and subsequently increase, similarly to the scenario considered before, because of limited oxygen availability. Due to the temporary damping of a fire this temperature initially rapidly decreased, and subsequently stabilised at the level resulting from a state of equilibrium conditioned by the effective ventilation of a fire zone.

#### 4. Scenario B – fire development simulated in a higher large-area shopping hall with the same stacking height

With respect to the larger of the analysed halls, it was assumed that its plan dimensions are 135.00 m by 60.00 m. The height of the hall is at the same time increased and reaches 7.00 m (Fig. 6). The location and size of access gates are analogous to those assumed for the smaller hall. The only difference lies in the fact that there are three instead of two smaller gates in the longer wall (Fig. 6). The sheathing of walls and roof, the stacking height on the racks and the initial conditions of the simulated fire are identical to those described for scenario A.

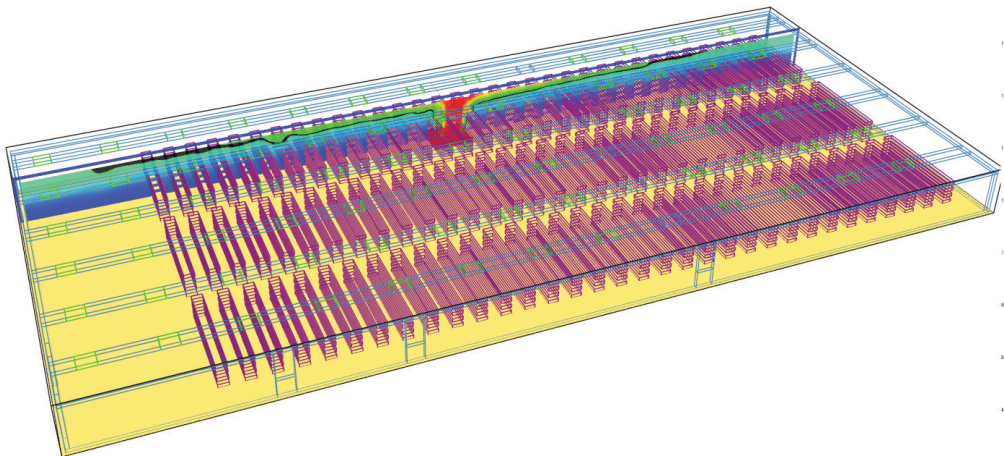


Fig. 6. Scheme of the larger of the analysed shopping halls. The location of storage racks used to hold paper materials constituting the fire load is indicated. The locations of smoke vents are indicated as well. The cross-section oriented parallel the longer wall is also shown here, for which the map of a fire plume temperature has been determined in selected time intervals [3]

The fire development scenario simulated by us earlier for the smaller of the considered halls is not typical for the halls of the same type, but having a larger area. Should the fire zone size be sufficiently large (this is understood as not only the surface area, but also the volume of the hall) the probability of a fire reaching the fully developed stage becomes negligibly small, as for such an event to occur a gathering of combustible materials exhibiting sufficiently high combustion efficiency, and distributed evenly over the whole fire compartment would have to

be accompanied by sufficiently favourable ventilating conditions, determined by the existence of numerous and big enough permanently open gate openings in the near vicinity of the fire. Thus the analysis performed in this paper seems to indicate that for large-area shopping halls the properly numerically modelled localised fire would be more appropriate. This statement is in full agreement with observations presented by the authors in [2].

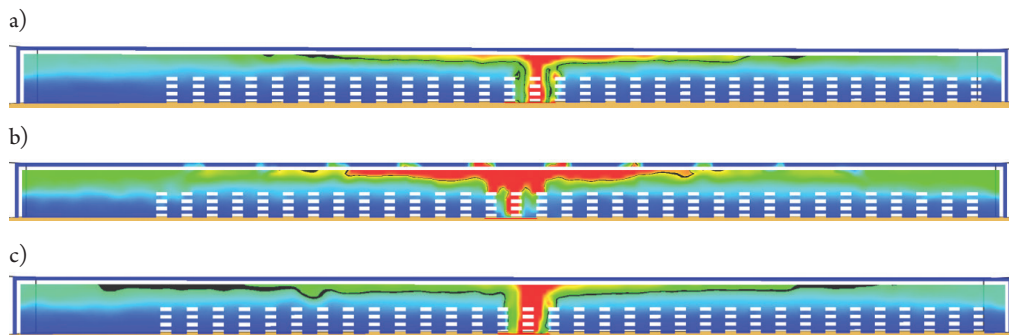


Fig. 7. Exhaust plume gas temperature maps obtained after 60 minutes of a fire exposure in the case of a larger hall considered in fire scenario B, including: a) results for the hall with operating smoke vents, obtained for the cross-section located between vent axes, b) results for the hall with operating smoke vents, obtained for the cross-section located along vent axes, c) results for the hall devoid of any smoke vents [4]

Detailed analysis of a fire plume temperature, similar to those depicted above in Fig. 2, but this time obtained after 60 minutes of a fire exposure and related to the authoritative cross-section specified for the larger of the considered halls, of the scheme depicted in Fig. 6, completely corroborates this opinion. The appropriate maps are depicted in Fig. 7, at the top for the hall with operating smoke vents, i.e. in Fig. 7a for the cross-section localised between the vent axes (the location exactly as depicted in Fig. 6), and in Fig. 7b for the cross-section localised along the vent axes, and at the bottom, in Fig. 7c, for the identical object but devoid of any vents. This time the 100°C fire plume temperature isotherm is depicted in black.

The comparison of maps depicted in Fig. 7 with corresponding maps depicted above in Fig. 2 should be begun with the reminder that the second hall is substantially higher (7.00 m) than the first one (4.50 m). The assumption that the stacking height of combustible materials is kept the same in both halls and equal to 3.50 m, results in a substantial difference in the volume of the open space between the top of storage racks and the ceiling of the hall. Those 3.50 m of empty space below the ceiling kept the fire modelled for the whole 60 minute fire exposure time from developing into the stage of a fully developed fire. The thickness of the fire plume below the ceiling, even after one hour of intensive fire action, proved to be too small to ignite the combustible materials stored on the racks below in the nearest vicinity of the source of a fire. With such a fire development scenario the activation of smoke vents did not substantially affect the temperature of air just above the floor, and thus did not affect the evacuation time available for the occupants. The conclusion of the localised character of the fire attributed to its development after 60 minutes of fire exposure seems to be corroborated by the fire plume temperature values obtained after several periods of duration in the cross-

section of the considered hall, but this time 6.00 m above the floor level. These maps are analogous to the maps depicted in Fig. 3 for the smaller of considered halls. The first group of maps depicted below pertains to the hall with operating smoke vents. These maps are presented in Fig. 8. The second group refers to the analogous hall but devoid of any flaps. The maps of this type are depicted in Fig. 9. The comparison of maps depicted in Fig.8d and 9d indicates a slightly larger area affected by the fire in the hall devoid of vents when compared to the hall equipped with vents, which did activate during fire, but this difference seems to become marked only after one hour of fire duration, and in addition seems to be qualitatively and quantitatively inconsequential with respect to the safety warranted to the users of the considered structure.

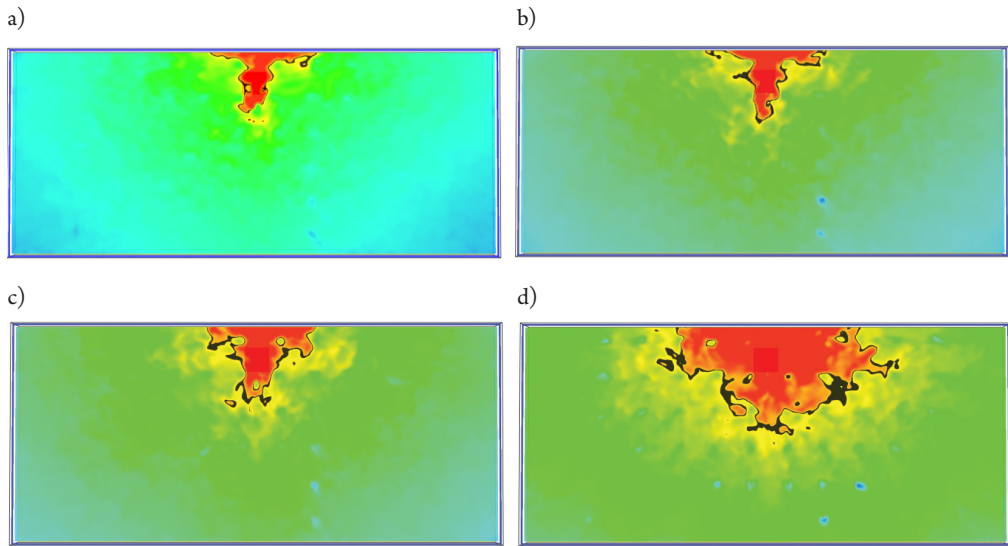


Fig. 8. Fire plume temperature maps obtained in the cross-section of the considered hall (fire scenar-io B), at the height of 6.00 m above the floor level, under the assumption of smoke vents operating correctly, after: a) 10 minutes, b) 20 minutes, c) 30 minutes, d) 60 minutes of fire exposure, respectively. The isotherm depicted in black corresponds to the fire plume temperature of 100°C [4]

An additional confirmation of the localised fire action observed in scenario B after 60 minutes of fire exposure is visible after the analysis of a fire plume temperature distribution obtained in the cross-section of the larger hall indicated in Fig. 6, at the height of 6.00 m above floor level. This distribution is depicted in Fig. 10. The graph of temperature forecast for the case of a hall with operating smoke vents is accompanied there with the graph of temperature forecast for the hall devoid of vents. Undoubtedly, in both cases, the maximum of temperature is reached in the direct vicinity of a fire source and diminishes rapidly with increasing distance from that source. The shapes of both graphs are thus substantially different than the shapes of the graphs depicted in Fig. 4, obtained for the smaller of the considered halls. Let us note, however, that that the difference between the results obtained for the larger hall equipped with operating smoke vents, and the same hall devoid of any vents, is mostly negligible.

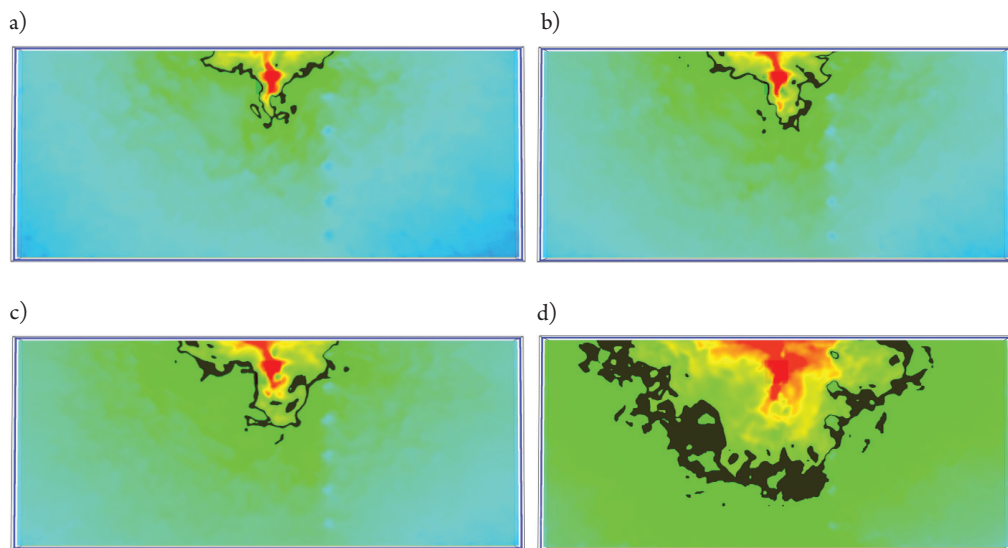


Fig. 9. Fire plume temperature maps obtained in the cross-section of the larger of considered halls at the height of 6.00 m above the floor level, under the assumption that there are no smoke vents, after: a) 10 minutes, b) 20 minutes, c) 30 minutes, d) 60 minutes of fire exposure, respectively. The isotherm depicted in black corresponds to the fire plume temperature of 100°C [4]

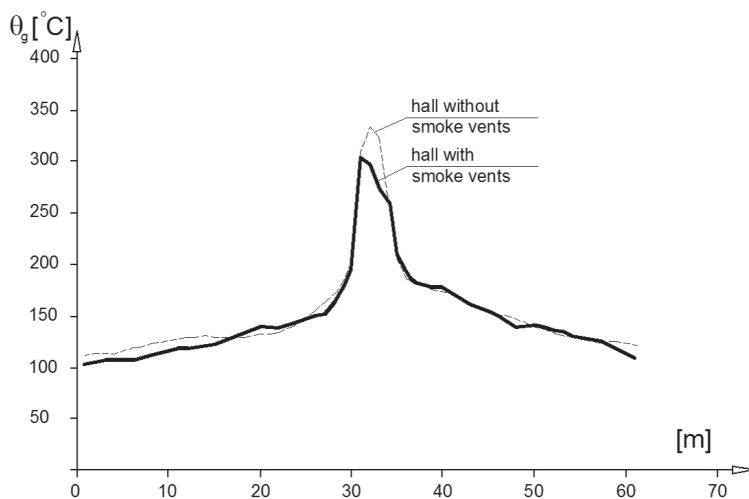


Fig. 10. Distribution of a fire plume temperature in the cross-section of the larger of considered halls at the height of 6.00 m above floor level, obtained for the hall equipped with operating smoke vents and for the other hall devoid of smoke vents, respectively [3]

The next graph depicted in this paper (Fig. 11) allows for a direct comparison of the fire plume temperature evolution at a point located 3.00 m off the initial axis of a fire, at a height of 6.00 m above the floor level. This comparison corresponds to the juxtaposition depicted in Fig. 5, where the analogous results obtained for the smaller hall are depicted. This time,

the forecast fire plume temperature increased monotonously regardless of the smoke vents. Thus, there was no question of the possible fire suppression. Such suppression is in any way difficult in such a large volume of the fire zone. The temperature of the fire plume increased in the current case relatively slowly. A quicker increase in the fire plume temperature would have to be a result of a cascading ignition of combustible materials stockpiled on the racks more and more distant from the fire source. Therefore, if in the presented simulation the conditions were lacking for this type of increasing fire development intensity, it must mean that only the energy released in the localised fire, affecting the limited volume of the fire zone, contributed to the increase in the exhaust gas temperature.

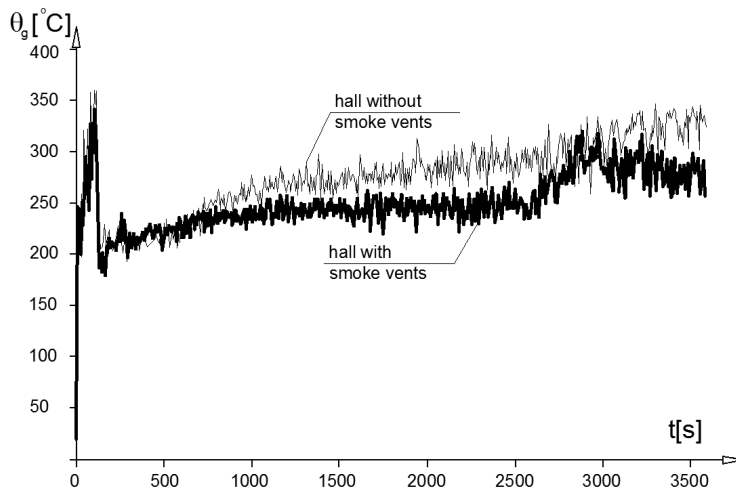


Fig. 11. Changes in the exhaust plume gas temperature inside the considered hall in a location at the distance of 3.00 m from the initial fire axis obtained for the bigger hall, at the height of 6.00 m above floor level – B fire scenario [s]

### 5. Scenario C – fire development simulated in the large-area shopping hall with an increased stacking height

Scenario C differs from scenario B analysed for the large hall in chapter 4 of the current paper only in that the stacking height of the combustible materials has been changed from 3.50 m to 5.50 m. The spatial distribution of the racks has not been changed in any way. The parameters determining the ignition chances of goods placed on these shelves have not been changed in any way as well. This means that, in this case, the volume of empty space above the racks, where the fire plume may freely propagate, is much more restricted. At the same time, due to the added amount of combustible materials, the fire load in the fire compartment has been substantially increased. Because of that, even at the same power of a fire source initiating the fire as in scenario B, in scenario C, a local ignition of the combustible materials stockpiled in the hall is much more probable and, in turn, the cascading propagation of a fire to the neighbouring storage racks.

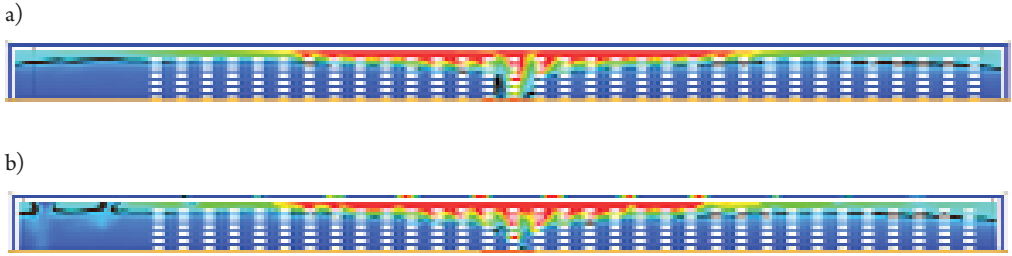


Fig. 12. Exhaust plume gas temperature maps obtained after 60 minutes of fire exposure in the case of a larger hall equipped with smoke vents, considered in C fire scenario, including: a) results obtained for the cross-section located between the smoke vents, b) results obtained for the cross-section located along the smoke vent axis

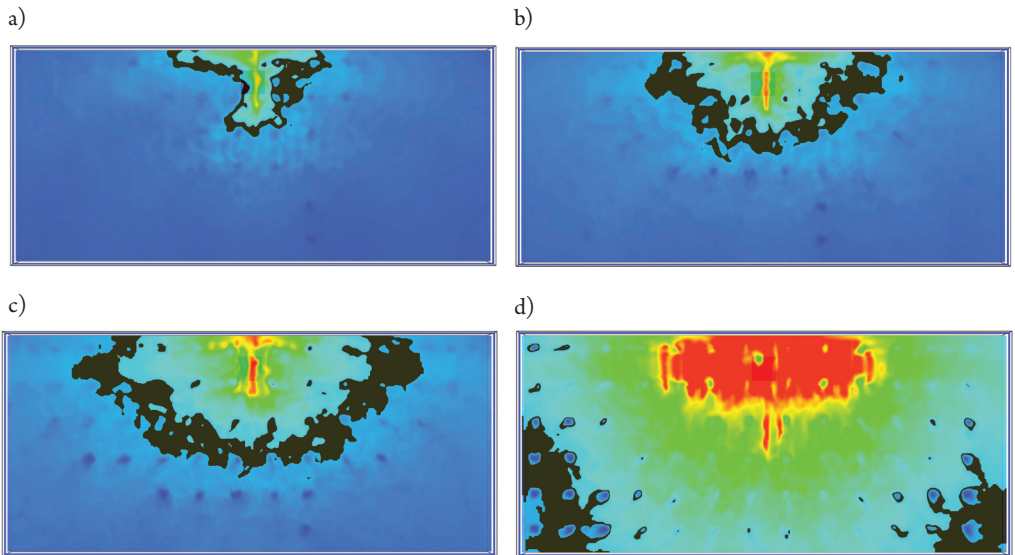


Fig. 13. Fire plume temperature maps obtained for the C fire scenario in the cross-section of the larger hall at the height of 6.00 m above the floor level, under the assumption that the smoke vents are present and operating, after: a) 10 minutes, b) 20 minutes, c) 30 minutes, d) 60 minutes of fire exposure, respectively. The isotherm depicted in black corresponds to the fire plume temperature of 100°C

In Fig. 12, the fire plume temperature maps are depicted for scenario C, after 60 minutes of fire exposure, obtained in the same cross-sections of the considered hall as before. These maps correspond to the analogous maps depicted in Fig. 7. The 100°C isotherm is depicted in black in those pictures as well. The map from Fig. 12a refers to the cross-section located between the smoke vents, while the other one, from Fig. 12b, refers to the cross-section located along the axes of smoke vents. The scenario for a hall devoid of smoke vents has not been considered here.

The maps depicted in Fig. 12 are accompanied by the distributions of fire plume temperatures determined for the C fire scenario, and referred to the horizontal cross-section of the considered hall. These maps are analogous to the maps depicted above in Fig. 9 and referring to the B fire scenario. These maps are gathered together in Fig. 13. One may easily



observe that in the C fire scenario, in spite of the retarding action of smoke vents, just after 20 minutes of fire exposure, the fire engulfed a large area of the hall. Thus, its progress was much faster than in the case identified for the B fire scenario. Furthermore, one may see in Fig. 9 that even without any smoke vents, in the B fire scenario, the fire remained at the stage of a localised fire restricted to a relatively small area even after 30 minutes of fire exposure.

Another substantial difference between the fire plume temperature values obtained during the simulation of a fire conforming to the assumptions of scenario C and scenario B in the same cross-section is clearly visible in Fig. 14. A comparison with Fig. 10 shows that here this temperature is much higher than before. Still, however, the simulated fire retained the characteristics of a localised fire, with a clearly observable extreme temperature at the axis of the fire indicating the location of the initial fire source.

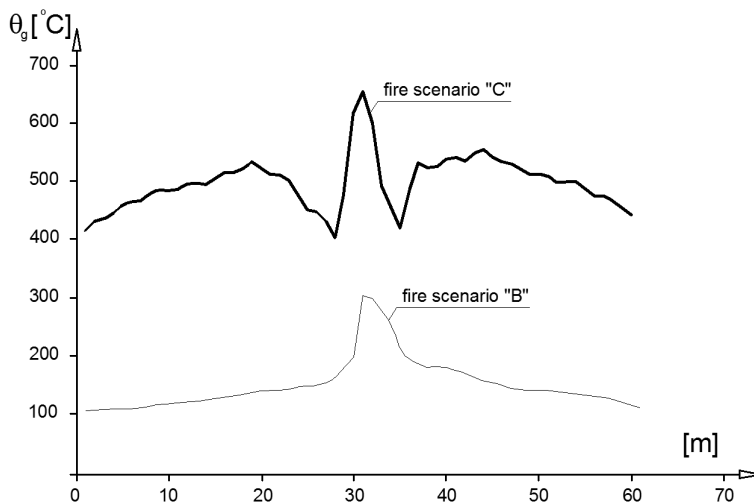


Fig. 14. Fire plume temperature distribution in the cross-section of the larger of considered halls, at the height of 6.00 m above the floor level. The bottom curve has been obtained for scenario B, with operating smoke vents.

The top curve refers to the distribution determined for scenario C, also under the assumption of operating smoke vents

The next important difference in the fire development, clearly distinguishing scenario C from scenario B, lies in the different course of the temperature fluctuations of the fire plume, identified at the distance of 3.00 m from the vertical axis indicating the location of the original source of a fire. The curves specific to the compared scenarios are juxtaposed in Fig. 15. This figure corresponds to the analogous one depicted above in Fig. 11. While in the case of scenario B, the activation of smoke vents did not substantially affect the fire development, as its power proved to be insufficient to ignite the combustible materials stockpiled on the racks adjacent to the initial fire source; this was not true in the case of scenario C. In scenario C, the fire developed rapidly, in general, in a monotonous manner, and the operating smoke vents ensured an unlimited supply of the fire supporting oxygen. Hence, there was no question of the possible fire suppression due to the insufficient availability of oxygen.

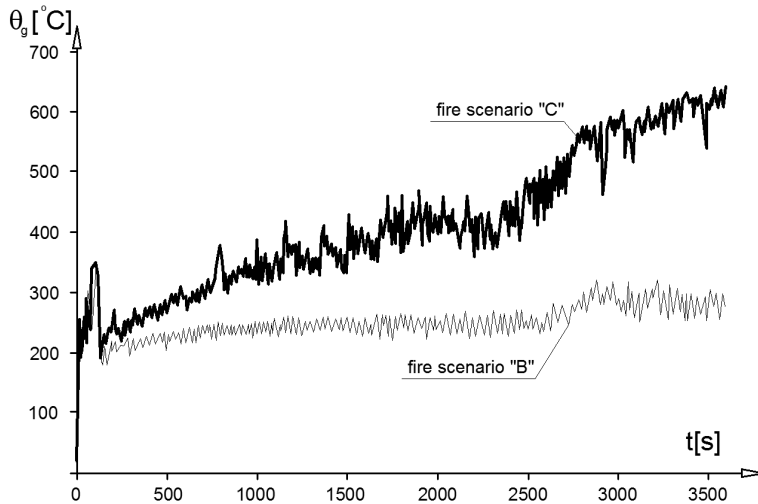


Fig. 15. Changes in the exhaust plume gas temperature inside the considered hall in a location at the distance of 3.00 m from the initial fire axis obtained for the bigger hall at the height of 6.00 m above floor level – comparison of results obtained after simulation of fires developing under assumptions of scenarios B and C

## 6. Concluding remarks

The conducted analyses unequivocally indicate that in the case of large-area shopping halls, the fully developed fire commonly assumed as the authoritative for evaluation and verification of fire safety level warranted to the users may not be so. In many practically important situations, a localised fire with limited intensity and affected zone may be better justified. Parameters of the model are usually determined by the hall's geometry, known a priori, but also the hall's real ventilation capabilities in the case of fire initiation, as well as quality and quantity of the accumulated merchandise representing potential fuel and constituting the fire load. In the authors' opinion, the numerical simulation of fire development, performed within the framework of the FDS computer code, presents an efficient computational tool allowing for a reliable prediction of the most unfavourable, but at the same time probable scenario, which may be realised in the given design situation.

## References

- [1] Fan Shen-Gang, Shu Gan-Ping, She Guang-Jun, Liew Richard J.Y. *Computational method and numerical simulation of temperature field for large-space steel structures in fire*, *Advanced Steel Construction*, Vol. 10, No. 2, 2014, 151–178.
- [2] Maślak M., Pazdanowski M., Woźniczka P. *Impact of the limited oxygen availability on the localized fire development in a large-area building compartment*, *Proceedings of the*

International Scientific Conference „Fire Protection, Safety and Security 2017”, Zvolen, Slovakia, May 3–5, 2017, 99–109.

- [3] Maślak M., Pazdanowski M., Woźniczka P. *Temperature distribution in a large-area shopping hall in the case of a localized fire*, in: Nigro E., Bilotta A. (Eds.) – Proceedings of 2<sup>nd</sup> International Fire Safety Symposium (IFireSS 2017), Naples, Italy, June 7–9, 2017, 853–860.
- [4] Maślak M., Woźniczka P. *Scenariusze rozwoju pożaru w wielkopowierzchniowej hali handlowej – część 1*, Nowoczesne Hale, 1/2017, 27–31.
- [5] Maślak M., Woźniczka P. *Scenariusze rozwoju pożaru w wielkopowierzchniowej hali handlowej – część 2*, Nowoczesne Hale, 3/2017, 64–67.
- [6] Maślak M., Woźniczka P. *Wpływ lokalizacji źródła ognia na rozwój pożaru w wielkopowierzchniowym halowym obiekcie handlowym*, Bezpieczeństwo i Technika Pożarnicza, vol. 45, Issue 1, 2017, 154–169.
- [7] McGrattan K., Hostikka S., McDermott R., Floyd J., Weinschenk C., Overholt K. *Fire Dynamics Simulator user’s guide*, NIST, Gaithersburg, Maryland 2013.
- [8] Wang Y., Burgess I., Wald F., Gillie M. *Performance-based fire engineering of structures*, CRC Press, London 2014.





Edyta Pięciorak  [orcid.org/0000-0001-6664-9927](https://orcid.org/0000-0001-6664-9927)  
epiec@agh.edu.pl

AGH University, Faculty of Mining and Geoengineering, Department of Geomechanics,  
Civil Engineering and Geotechnology

Marek Piekarczyk  [orcid.org/0000-0003-0566-4749](https://orcid.org/0000-0003-0566-4749)

Henryk Ciurej  [orcid.org/0000-0003-4017-6185](https://orcid.org/0000-0003-4017-6185)

Michał Betlej  [orcid.org/0000-0001-7631-0134](https://orcid.org/0000-0001-7631-0134)

Faculty of Civil Engineering, Cracow University of Technology

THE DETERMINATION OF MOMENT RESISTANCE FOR A LINER TRAY  
RESTRAINED BY SHEETING ACCORDING TO EUROPEAN STANDARD  
PN-EN 1993-1-3

---

WYZNACZANIE NOŚNOŚCI PRZY ZGINANIU KASETY ŚCIENNEJ  
USZTYWNIONEJ POSZYCIEM W UJĘCIU NORMY EUROPEJSKIEJ  
PN-EN 1993-1-3

**Abstract**

The paper presents an example of the determination of moment resistance for a liner tray restrained by sheeting according to the rules given in standard PN-EN 1993-1-3 [12].

**Keywords:** liner tray, moment resistance, channel-type section, effective cross section

**Streszczenie**

W artykule przedstawiono przykład obliczeniowy wyznaczania nośności przy zginaniu kasety ściennej usztywnionej poszyciem wg wytycznych normy PN-EN 1993-1-3 [12].

**Słowa kluczowe:** kasetka ścienna, nośność przy zginaniu, przekrój ceowy, przekrój współpracujący

## 1. Introduction

Light gauge steel cassettes, also often named liner trays, are made from cold-formed C-shaped steel sections, typically with the geometry shown in Fig. 1. The idea of a cassette wall construction has its origins in an invention by Baehre in Stockholm in the late 1960s [3]. Extensive research on the behavior of steel cassettes under loading was conducted at that time by Baehre et al. [1, 2, 11, 19, 20] and later by Davies et al. [5–7]. Their results formed the basis of the design clauses given in Eurocode 3, Part 1–3 [4, 12].

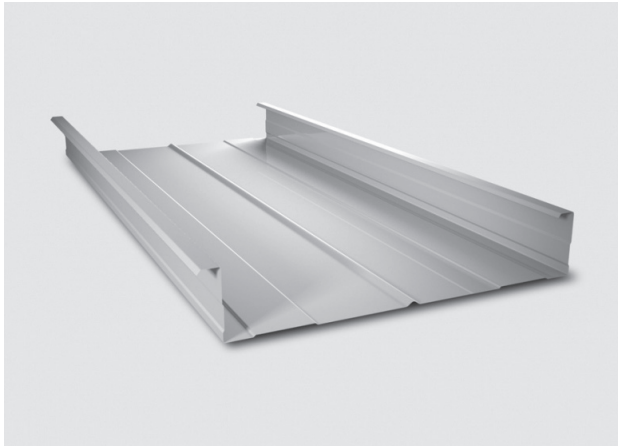


Fig. 1. Example of a liner tray [9]

At present, cassette sections are widely used, mainly for industrial buildings and warehouses as an alternative to traditional wall construction using beams. Figure 2 presents an example of the usage of liner trays as wall members.

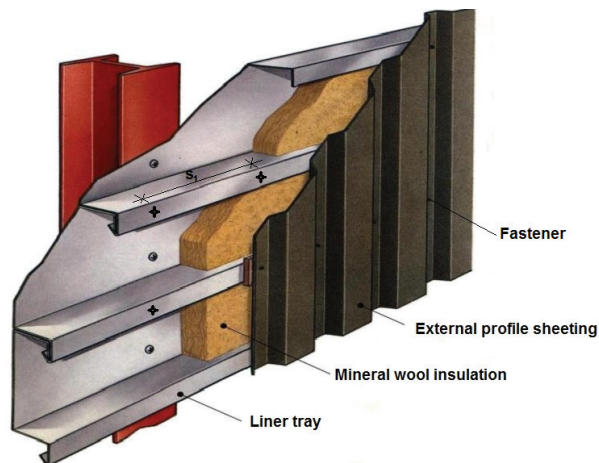


Fig. 2. Example of using liner trays in wall cladding system [10]

Cassette walls are subjected to three primary load combinations: axial load, bending, and shear [8]. This paper presents the design procedures (determination of moment resistance) for trays subjected to bending resulting from wind pressure and suction according to the rules given in the standard PN-EN 1993-1-3 [12].

The behaviour of a cassette section under bending is characterised by the usual relationships that apply to all thin-walled cold-formed sections. However, the design of a cassette with a narrow flange which is under compression (caused by e.g. wind pressure), is a particularly complicated problem because the following four effects should be considered here: local buckling of the web and narrow flanges; distortional buckling of the narrow flange and edge stiffener assemblies; flange curling of the wide flange which is under tension; the effects of shear lag. If the wide flange of a cassette subjected to bending is under compression (caused by e.g. wind suction), the narrow flange and edge stiffener assemblies are under tension and do not buckle. Bending behaviour is dominated by local buckling of the wide flange. PN-EN 1993-1-3 [12] does not propose any special treatment for the interaction of flange curling that occurs in the wide flange under compression and local buckling. This seems to be too difficult; instead, it is suggested in the standard that the conventional effective width procedure should be used but with the material factor  $\gamma_{M0}$  increased to 1.25 [8].

## 2. Typical geometry of liner trays

The elements of a typical cassette section have two narrow flanges ( $b_{f1}$ ,  $b_{f2}$ ), two webs ( $h_1$ ,  $h_2$ ) with intermediate stiffeners ( $h_{u3}$ ), one wide flange ( $b_u$ ) with intermediate stiffeners ( $h_{u1}$  and  $h_{u2}$ ), and two edge stiffeners ( $c$ ), as shown in Fig. 3.

The analytical calculations for the moment resistance of a liner tray were performed with the use of Mathcad 14 [15] for the cross section presented in Fig. 3 [9] and the static scheme as a simply supported beam shown in Fig. 4.

The effective section properties of this element were determined in AutoCAD program [14].

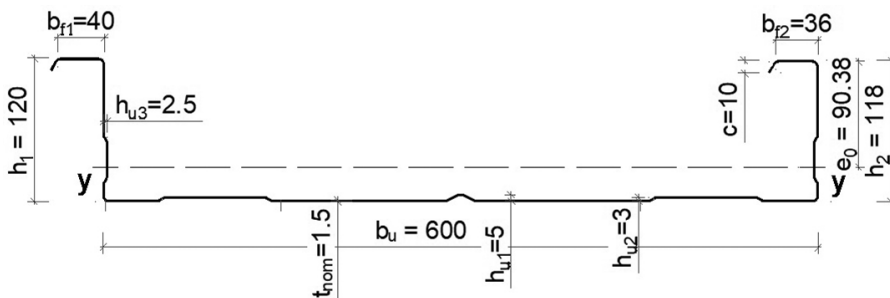


Fig. 3. The geometry of a 600/120 wall cassette

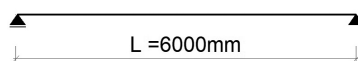


Fig. 4. The static scheme of a 600/120 wall cassette



### 3. Calculation of the thickness of the designed liner tray

After applying formula (3.3c) in [12]:

$$t = t_{cor} = t_{nom} - t_{metallic} = 1.5 - 0.04 = 1.46 \text{ mm}, \quad (1)$$

where:

- $t$  – core thickness of steel material before cold forming,
- $t_{nom}$  – nominal sheet thickness after cold forming (inclusive of zinc or other metallic coating)  $t_{nom} = 1.5 \text{ mm}$
- $t_{cor}$  – the nominal thickness minus zinc or other metallic coating
- $t_{metallic}$  – the thickness of the metallic coating (for the usual Z275 zinc coating,  $t_{zinc} = 0.04 \text{ mm}$ )

### 4. Verification of the standard geometric proportions of the liner tray

The recommendations for the design given in PN-EN 1993-1-3 [12] can be applied to cross sections for which width-to-thickness ratios are within the following ranges as adopted from Table 5.1 in [12] (see Table 1):

Table 1. Maximum width-to-thickness ratios

Element of cross section (see Fig. 3)	Geometric proportions (see Fig. 3)	Maximum value (see Tab. 5.1 in [12])
narrow flange $b_{f1}$	$b_{f1}/t = 40 \text{ mm}/1.46 \text{ mm}$ $b_{f1}/t = 27.40$	60
narrow flange $b_{f2}$	$b_{f2}/t = 36 \text{ mm}/1.46 \text{ mm}$ $b_{f2}/t = 24.66$	60
edge stiffeners $c$	$c/t = 10 \text{ mm}/1.46 \text{ mm}$ $c/t = 6.85$	50
wide flange $b_u$	$b_u/t = 600 \text{ mm}/1.46 \text{ mm}$ $b_u/t = 410.96$	500
web $h_1$	$h_1/t = 120 \text{ mm}/1.46 \text{ mm}$ $h_1/t = 82.19$	$500 \cdot (\sin\phi) = 500 \cdot (\sin 90^\circ) = 500$
web $h_2$	$h_2/t = 118 \text{ mm}/1.46 \text{ mm}$ $h_2/t = 80.82$	$500 \cdot (\sin\phi) = 500 \cdot (\sin 90^\circ) = 500$

where:

- $\phi$  – angle between the wide flange and the web.

In order to provide sufficient stiffness and to avoid primary buckling of the stiffener itself, the size of the stiffener according to (5.2a) in [12] should be within the following range:

$$0.2 < \frac{c}{b} = \frac{10}{40} = 0.25 < 0.6, \quad (2)$$

where, according to Fig. 3:  $c = 10$  mm,  $b = b_{f1} = 40$  mm for the left end

$$0.2 < \frac{c}{b} = \frac{10}{36} = 0.28 < 0.6, \quad (3)$$

and  $c = 10$  mm,  $b = b_{f2} = 36$  mm for the right end.

If  $c/b < 0.2$ , the lip should be ignored ( $c = 0$ ).

It can be concluded that the geometric proportions of this liner tray are appropriate and allow the use of standard PN-EN-1993-1-3 [12].

The moment resistance of a liner tray may be obtained using 10.2 in [12] provided that the geometric properties are within the range given in Table 10.6 [12] and the depths  $h_{u1}$  and  $h_{u2}$  (see Fig. 3) of the corrugations of the wide flange do not exceed  $h/8$ , where  $h$  ( $h_1, h_2$ ) is the overall depth of the liner tray (see Fig. 3). The range of validity of the design procedures according to 10.2 [12] is as follows (see Table 2):

Table 2. The range of validity of the design procedures according to 10.2 [12] in dependence on the geometry of a cross section

Minimum value	Dimensions and geometrical proportions (see Fig. 3)	Maximum value
0.75 mm	$t_{nom} = 1.5$ mm	1.5 mm
30 mm	$b_{f1} = 40$ mm	60 mm
30 mm	$b_{f2} = 36$ mm	60 mm
60 mm	$h_1 = 120$ mm	200 mm
60 mm	$h_2 = 118$ mm	200 mm
300 mm	$b_u = 600$ mm	600 mm
—	$I_a/b_u = 1932$ mm <sup>4</sup> /600 mm $I_a/b_u = 3.22$ mm <sup>4</sup> /mm (see Fig. 5)	10 mm <sup>4</sup> /mm
—	$s_1 = 210$ mm (see Fig. 2)	1000 mm
—	$h_{u1} = 5$ mm	$h_1/8 = 120$ mm/8 = 15 mm $h_2/8 = 118$ mm/8 = 14.75 mm (see Fig. 3)
—	$h_{u2} = 3$ mm	$h_1/8 = 120$ mm/8 = 15 mm $h_2/8 = 118$ mm/8 = 14.75 mm (see Fig. 3)

where:

- $s_1$  – the spacing of fasteners in the narrow flanges (see Fig. 2),
- $I_a$  – the second moment of area of the wide flange  $b_u$ , about its own centroid (a-a), calculated with use of AutoCAD [14]
- $I_a = 1,932 \text{ mm}^4$  (see Fig. 5).

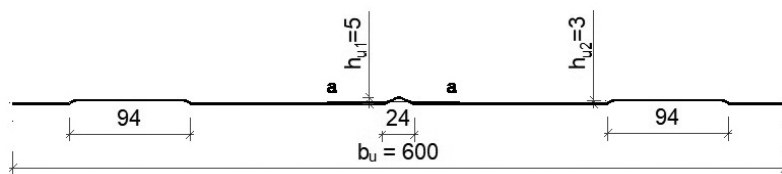


Fig. 5. The geometry of the wide flange of the liner tray

## 5. Design procedures for liner trays restrained by sheeting

### 5.1. Determination of moment resistance of a liner tray section with its wide flange under compression

The moment resistance  $M_{c,Rd}$  of liner trays restrained by sheeting may be obtained as follows, after applying formula (10.19) in [12]:

$$M_{c,Rd} = \frac{0.8 \cdot W_{eff,min} \cdot f_{yb}}{\gamma_{M0}} = \frac{0.8 \cdot 19101 \cdot 320}{1.0} = 4,890 \text{ kNm}, \quad (4)$$

where:

- $f_{yb}$  – the basic yield strength  $320 \text{ N/mm}^2$ ,
- $\gamma_{M0}$  – the partial safety factor equal to 1.0,
- $W_{eff,min}$  – the minimum effective section modulus calculated as follows:

$$W_{eff,min} = \frac{I_{y,eff}}{z_c} = \frac{1177987}{61.67} = 19,101 \text{ mm}^3, \quad (5)$$

and

$$W_{eff,min} = 19,101 \text{ mm}^3 \leq \frac{I_{y,eff}}{z_t} = \frac{1177987}{56.87} = 20,713 \text{ mm}^3, \quad (6)$$

where:

- $I_{y,eff}$  – the effective second moment of area (see Fig. 7 and 5.1.1) about the y-y axis,  $I_{y,eff} = 1,177,987 \text{ mm}^3$ ,
- $z_c$  – the distance from the effective centroidal axis to the system line of the compression wide flange (see Fig. 7),  $z_c = \max(z_{c1}, z_{c2}) = 61.67 \text{ mm}$ ,
- $z_t$  – the distance from the effective centroidal axis to the system line of the narrow flange in tension (see Fig. 7),  $z_t = \max(z_{t1}, z_{t2}) = 56.87 \text{ mm}$ .

### 5.1.1. Determination of the effective width $b_{eff}$ of the wide flange under compression

The relative slenderness  $\bar{\lambda}_p$  according to (4.2) in [13] is:

$$\bar{\lambda}_p = \frac{\bar{b}/t}{28,4\varepsilon\sqrt{k_\sigma}} = \frac{596,6/1,46}{28,4 \cdot 0,857 \cdot \sqrt{4}} = 8,395, \quad (7)$$

where, according to Fig. 6:  $\bar{b} = b_{pu} = 596,6$  mm,  $t = 1,46$  mm, local buckling factor  $k_\sigma = 4,0$

for  $\psi = \frac{\sigma_2}{\sigma_1} = 1$  (uniform compression in the flange  $b_{pu}$ ),  $\varepsilon = \sqrt{\frac{235}{f_{yb}}} = \sqrt{\frac{235}{320}} = 0,857$ .

The reduction factor  $\rho$  of effective width according to (4.2) in [13] is:

$$\rho = \frac{\bar{\lambda}_p - 0,055 \cdot (3 + \psi)}{\bar{\lambda}_p^2} = \frac{8,395 - 0,055 \cdot (3 + 1)}{8,395^2} = 0,116 \leq 1,0, \quad (8)$$

for:

$$\bar{\lambda}_p = 8,395 > 0,5 + \sqrt{0,085 - 0,055\psi} = 0,5 + \sqrt{0,085 - 0,055 \cdot 1,0} = 0,673. \quad (9)$$

The effective width  $b_{u,eff}$  of the wide flange  $b_{pu}$  can be calculated according to Table 4.1 in [13] as follows:

$$b_{u,eff} = \rho \cdot \bar{b} = 0,116 \cdot 596,6 = 69,20 \text{ mm}, \quad (10)$$

where, according to Fig. 6:  $\bar{b} = b_{pu} = 596,6$  mm and formula (8)  $\rho = 0,116$ .

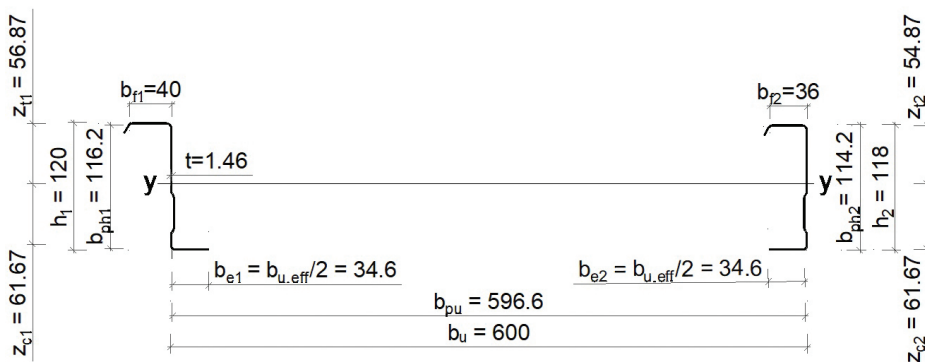


Fig. 6. Effective cross section of the wide flange under compression and the entire cross sections of the webs of a 600/120 wall cassette

The initial values of the effective widths  $b_{e1}$  and  $b_{e2}$  shown in Fig. 6 should be determined according to Table 4.1 in [13] for a doubly supported wide flange  $b_{pu}$  as follows:

$$b_{e1} = b_{e2} = 0.5 \cdot b_{u,eff} = 0.5 \cdot 69.2 = 34.6 \text{ mm.} \quad (11)$$

### 5.1.2. Determination of effective width $h_{eff}$ of the web under bending

The relative slenderness  $\bar{\lambda}_p$  according to (4.2) in [13] is:

**For web  $h_1$ :**

$$\bar{\lambda}_p = \frac{\bar{b}/t}{28,4\epsilon\sqrt{k_\sigma}} = \frac{116.2/1.46}{28,4 \cdot 0.857 \cdot \sqrt{21.93}} = 0.7, \quad (12)$$

where, according to Fig. 6:  $\bar{b} = b_{ph1} = 116.2 \text{ mm}$ ,  $t = 1.46 \text{ mm}$ ,  $\epsilon = \sqrt{\frac{235}{f_{yb}}} = \sqrt{\frac{235}{320}} = 0.857$ , the value of  $k_\sigma$  may be calculated according to Table 4.1 [13] is as follows:

$$k_\sigma = 7.81 - 6.29\psi + 9.78\psi^2 = 7.81 - 6.29 \cdot (-0.92) + 9.78 \cdot (-0.92)^2 = 21.93, \quad (13)$$

for:

$$0 > \psi = -0.92 > -1, \quad (14)$$

with:

$$\psi = \frac{\sigma_2}{\sigma_1} = -\frac{56.87}{61.67} = -0.92, \quad (15)$$

where, according to Fig. 6:  $\sigma_2 = z_{t1} = 56.87 \text{ mm}$  and  $\sigma_1 = z_{c1} = 61.67 \text{ mm}$ .

The reduction factor  $\rho$  of the effective width according to (4.2) in [13] is as follows:

$$\rho = 1.0, \quad (16)$$

for:

$$\bar{\lambda}_p = 0.7 < 0.5 + \sqrt{0.085 - 0.055\psi} = 0.5 + \sqrt{0.085 - 0.055 \cdot (-0.92)} = 0.87. \quad (17)$$

The web is fully effective because the reduction factor of the effective width is  $\rho = 1.0$ . The effective width  $h_{eff}$  of the web can be calculated according to Table 4.1 in [13] is as follows:

$$h_{eff} = \rho \cdot b_c = 1.0 \cdot 61.67 = 61.67 \text{ mm}, \quad (18)$$

where, according to Fig. 6:  $b_c = z_{c1} = 61.67 \text{ mm}$  and formula (16)  $\rho = 1.0$ .

The initial values of the effective widths  $h_{e1}$  and  $h_{e2}$  shown in Fig. 7 should be determined according to Table 4.1 in [13] for a doubly supported web as follows:

$$h_{e1} = 0.4 \cdot h_{eff} = 0.4 \cdot 61.67 = 24.67 \text{ mm}, \quad (19)$$

$$h_{e2} = 0.6 \cdot h_{eff} = 0.6 \cdot 61.67 = 37 \text{ mm}. \quad (20)$$

### For the web $h_2$ :

The analytical calculations for the web  $h_2$  were performed in the same manner as for web  $h_1$ . The initial values of the effective widths  $h_{e1} = 24.67$  mm and  $h_{e2} = 37$  mm are the same as the values calculated before (see Fig. 7).

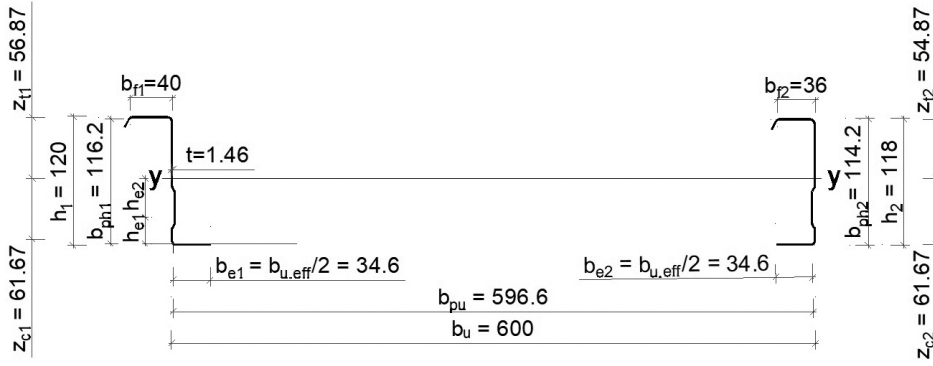


Fig. 7. Effective cross section of the liner tray of a 600/120 wall cassette

The effective moment of inertia for a liner tray (see Fig. 7) with its wide flange under compression about the y-y axis is  $I_{y,eff} = 1,177,987$  mm<sup>3</sup>.

#### 5.1.3. The effects of shear lag

According to (10.2.2.2 (2)) in [12], the effects of shear lag may be neglected here because:

$$\frac{L}{b_{u,eff}} = \frac{6000}{69.20} = 86.71 \geq 25, \quad (21)$$

where, according to Fig. 4:  $L = 6000$  mm and according to formula (10),  $b_{u,eff} = b_{eff} = 69.20$  mm.

### 5.2. Determination of moment resistance of a liner tray section with its narrow flange under compression

The buckling moment resistance  $M_{b,Rd}$  of linear trays restrained by sheeting may be obtained as follows, according to formula 10.21 in [12]:

$$M_{b,Rd} = \frac{0.8 \cdot \beta_b \cdot W_{eff,com} \cdot f_{yb}}{\gamma_{M0}} = \frac{0.8 \cdot 1.0 \cdot 22725.4 \cdot 320}{1.0} = 5.82 \text{ kNm}, \quad (22)$$

and

$$M_{b,Rd} \leq \frac{0.8 \cdot W_{eff,t} \cdot f_{yb}}{\lambda_{M0}} = \frac{0.8 \cdot 47537.1 \cdot 320}{1.0} = 12.17 \text{ kNm}, \quad (23)$$

where:

$f_{yb}$  – the basic yield strength 320 N/mm<sup>2</sup>,

- $\gamma_{M0}$  – the partial safety factor equal to 1.0,
- $\beta_b$  – the correlation factor that depends on the longitudinal spacing of fasteners supplying lateral restraint to the narrow flanges  $s_1$  (see Fig. 2) for  $s_1=210$  mm  $\leq 300$  mm  $\beta_b = 1.0$  and for  $300$  mm  $\leq s_1 \leq 1000$  mm:  $\beta_b = 1.15 \cdot s_1 / 2000$ ,
- $W_{eff,com}$  – the effective section modulus for the maximum compressive stress in a cross section is as follows:

$$W_{eff,com} = \frac{I_{y,eff}}{z_c} = \frac{1822575.8}{80.20} = 22,725.4 \text{ mm}^3, \quad (24)$$

- $W_{eff,t}$  – the effective section modulus for the maximum tensile stress in a cross section is as follows:

$$W_{eff,t} = \frac{I_{y,eff}}{z_t} = \frac{1822575.8}{38.34} = 47,537.1 \text{ mm}^3, \quad (25)$$

where:

- $I_{y,eff}$  – the effective second moment of area (see Fig. 12 and 5.2.1) about the y-y axis,  $I_{y,eff} = 1,822,575.8 \text{ mm}^3$ ,
- $z_c$  – the distance from the effective centroidal axis to the system line of the wide flange under compression (see Fig. 12),  $z_c = \max(z_{c1}, z_{c2}) = 80.20$  mm,
- $z_t$  – the distance from the effective centroidal axis to the system line of the narrow flange in tension (see Fig. 12),  $z_t = \max(z_{t1}, z_{t2}) = 38.34$  mm.

### 5.2.1. Determination of the effective width $b_{u,eff}$ of the wide flange under tension

The effective width  $b_{u,eff}$  of the wide flange under tension (see Fig. 8) allowing for possible flange curling according to (10.20) in [12] is given by:

$$b_{u,eff} = \frac{53.3 \cdot 10^{10} \cdot e_0^2 \cdot t^3 \cdot t_{eq}}{h \cdot L \cdot b_u^3} = \frac{53.3 \cdot 10^{10} \cdot 90.38^2 \cdot 1.46^3 \cdot 3.38}{120 \cdot 6000 \cdot 600^3} = 294.55 \text{ mm}, \quad (26)$$

where, according to Fig. 4:  $L = 6000$  mm and according to Fig. 3:  $e_0 = 90.38$  mm,  $b_u = 600$  mm,  $t = 1.46$  mm (see formula (1)). The value of  $t_{eq}$  may be calculated according to (10.2.2.2 (1)) in [12] as follows:

$$t_{eq} = \left( \frac{12 \cdot I_a}{b_u} \right)^{\frac{1}{3}} = \left( \frac{12 \cdot 1932}{6000} \right)^{\frac{1}{3}} = 3.38, \quad (27)$$

where, according to Fig. 3:  $b_u = 600$  mm, and the second moment of area of the wide flange about its own centroid a-a  $I_a$ , calculated with the use of AutoCAD [14], is equal to  $1,932 \text{ mm}^4$  (see Fig. 5).

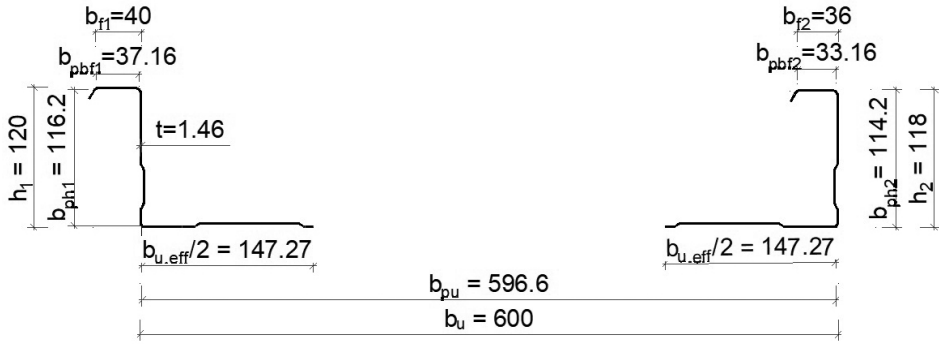


Fig. 8. Effective width  $b_{u,eff}$  of the wide flange of a 600/120 wall cassette under tension

### 5.2.2. Determination of effective width $b_{eff}$ of the narrow flange under compression

The relative slenderness  $\bar{\lambda}_p$  according to (4.2) in [13] is:

**For the narrow flange  $b_{f1}$ :**

$$\bar{\lambda}_p = \frac{\bar{b}/t}{28,4\varepsilon\sqrt{k_\sigma}} = \frac{37.16/1.46}{28,4 \cdot 0.857 \cdot \sqrt{4}} = 0.523, \quad (28)$$

where, according to Fig. 8:  $\bar{b} = b_{pbfl} = 37.16$  mm,  $t = 1.46$  mm, local buckling factor  $k_\sigma = 4.0$

for  $\psi = \frac{\sigma_2}{\sigma_1} = 1$  (uniform compression in the flange  $b_{f1}$ ),  $\varepsilon = \sqrt{\frac{235}{f_{yb}}} = \sqrt{\frac{235}{320}} = 0.857$ .

The reduction factor  $\rho$  of the effective width according to (4.2) in [13] is:

$$\rho = 1.0, \quad (29)$$

for:

$$\bar{\lambda}_p = 0.523 < 0.5 + \sqrt{0.085 - 0.055\psi} = 0.5 + \sqrt{0.085 - 0.055 \cdot 1.0} = 0.673. \quad (30)$$

The narrow flange  $b_{f1}$  is fully effective because the reduction factor of the effective width  $\rho = 1.0$ . The effective width  $b_{eff}$  of the narrow flange  $b_{f1}$  can be calculated according to Table 4.1 in [13] as follows:

$$b_{eff} = \rho \cdot \bar{b} = 1.0 \cdot 37.16 = 37.16 \text{ mm}, \quad (31)$$

where, according to Fig. 8:  $\bar{b} = b_{pbfl} = 37.16$  mm and formula (29)  $\rho = 1.0$ .

The initial values of the effective widths  $b_{e1}$  and  $b_{e2}$  shown in Fig. 9 should be determined with accordance to Table 4.1 in [13] for a doubly supported wide flange  $b_{pbfl}$  as follows:

$$b_{1,e1} = b_{1,e2} = 0.5 \cdot b_{eff} = 0.5 \cdot 37.16 = 18.58 \text{ mm}. \quad (32)$$



**For the narrow flange  $b_{f2}$ :**

$$\bar{\lambda}_p = \frac{\bar{b}/t}{28,4\varepsilon\sqrt{k_\sigma}} = \frac{33,16/1,46}{28,4 \cdot 0,857 \cdot \sqrt{4}} = 0,467, \quad (33)$$

where, according to Fig. 8:  $\bar{b} = b_{pbf2} = 33,16$  mm,  $t = 1,46$  mm, local buckling factor  $k_\sigma = 4,0$

for  $\psi = \frac{\sigma_2}{\sigma_1} = 1$  (uniform compression in the flange  $b_{f2}$ ),  $\varepsilon = \sqrt{\frac{235}{f_{yb}}} = \sqrt{\frac{235}{320}} = 0,857$ .

The reduction factor  $\rho$  of the effective width according to (4.2) in [13] is:

$$\rho = 1,0, \quad (34)$$

for:

$$\bar{\lambda}_p = 0,467 < 0,5 + \sqrt{0,085 - 0,055\psi} = 0,5 + \sqrt{0,085 - 0,055 \cdot 1,0} = 0,673. \quad (35)$$

The narrow flange  $b_{f2}$  is fully effective because the reduction factor of effective width  $\rho = 1,0$ . The effective width  $b_{eff}$  of the narrow flange  $b_{f2}$  can be calculated according to Table 4.1 in [13] as follows:

$$b_{eff} = \rho \cdot \bar{b} = 1,0 \cdot 33,16 = 33,16 \text{ mm}, \quad (36)$$

where, according to Fig. 8:  $\bar{b} = b_{pbf2} = 33,16$  mm and formula (34)  $\rho = 1,0$ .

The initial values of the effective widths  $b_{e1}$  and  $b_{e2}$  shown in Fig. 10 should be determined according to Table 4.1 in [13] for a doubly supported wide flange  $b_{pbf2}$  as follows:

$$b_{2,e1} = b_{2,e2} = 0,5 \cdot b_{eff} = 0,5 \cdot 33,16 = 16,58 \text{ mm}. \quad (37)$$

### 5.2.3. Determination of effective area of the edge stiffener of the narrow flange under compression

Initial values of the effective width  $c_{eff}$  shown in Fig. 9 and Fig. 10 should be obtained for a single edge fold stiffener according to (5.13a) in [12] as follows:

$$c_{eff} = \rho \cdot b_{p,c} = 1,0 \cdot 11 = 11 \text{ mm}, \quad (38)$$

where, according to Fig. 9 for the narrow flange  $b_{f1}$  and Fig. 10 for the narrow flange,  $b_{f2}$ :  $b_{p,c} = 11$  mm and according to formula (42),  $\rho = 1,0$ .

The relative slenderness  $\bar{\lambda}_p$  according to (4.2) in [13] is:

**For the narrow flange  $b_{f1}$  and  $b_{f2}$ :**

$$\bar{\lambda}_p = \frac{\bar{b}/t}{28,4\varepsilon\sqrt{k_\sigma}} = \frac{11/1,46}{28,4 \cdot 0,857 \cdot \sqrt{0,5}} = 0,438, \quad (39)$$

where, according to Fig. 9 and Fig. 10:  $\bar{b} = b_{p,c} = 11 \text{ mm}$ ,  $t = 1.46 \text{ mm}$ ,  $\varepsilon = \sqrt{\frac{235}{f_{yb}}} = \sqrt{\frac{235}{320}} = 0.857$ , local buckling factor (according 5.13b in [12])  $k_{\sigma} = 0.5$  for:

$$\frac{b_{p,c}}{b_p} = \frac{11}{37.16} = 0.3 \leq 0.35, \quad (40)$$

where, according to Fig. 9:  $b_p = b_{pbf1} = 37.16 \text{ mm}$  and for:

$$\frac{b_{p,c}}{b_p} = \frac{11}{33.16} = 0.33 \leq 0.35, \quad (41)$$

where, according to Fig. 10:  $b_p = b_{pbf2} = 33.16 \text{ mm}$ .

The reduction factor  $\rho$  of the effective width for an outstanding compression element according to (4.2) in [13], is:

$$\rho = 1.0, \quad (42)$$

for :

$$\bar{\lambda}_p = 0.438 < 0.748. \quad (43)$$

The geometric properties of the stiffener determined in the AutoCAD program [14]:

**For the narrow flange  $b_{f1}$  (see Fig. 9):**

$$A_{s1} = 42.83 \text{ mm}^2$$

$$I_{s1} = 342.89 \text{ mm}^4$$

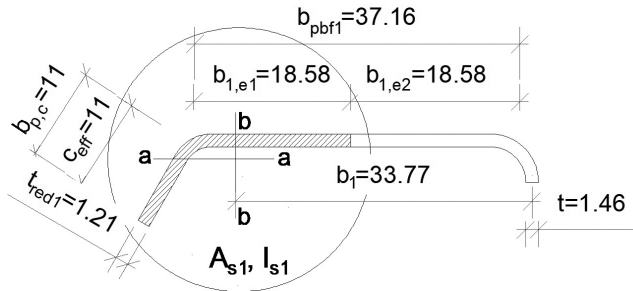


Fig. 9. The edge stiffener in the compressed narrow flange  $b_{f1}$  of a 600/120 wall cassette

The relative slenderness  $\bar{\lambda}_d$  according to (5.12d) in [12] is:

$$\bar{\lambda}_d = \sqrt{\frac{f_{yb}}{\sigma_{cr,s}}} = \sqrt{\frac{320}{406}} = 0.888, \quad (44)$$

where:

- $f_{yb}$  – the basic yield strength 320 N/mm<sup>2</sup>,
- $\sigma_{cr,s}$  – the critical stress in the edge stiffener according to (5.15) in [12] is as follows:

$$\sigma_{cr,s} = \frac{2 \cdot \sqrt{K \cdot E \cdot I_s}}{A_s} = \frac{2 \cdot \sqrt{1.05 \cdot 210000 \cdot 342.89}}{42.83} = 406 \text{ MPa}, \quad (45)$$

where:

- $A_s$  – the effective cross-sectional area of the edge stiffener,  $A_s = A_{s1}$ ,
- $I_s$  – the effective second moment of area of the stiffener, taken as that of its effective area  $A_{s1}$  about the centroidal axis a-a of its effective cross section,  $I_s = I_{s1}$  (see Fig. 9),
- $K$  – the spring stiffness of the edge stiffener per unit length according to (5.10b) in [12] as follows:

$$K = \frac{Et^3}{4 \cdot (1-\nu^2)} \cdot \frac{1}{b_1^2 \cdot h_w + b_1^3} = \frac{210 \cdot 10^3 \cdot 1.46^3}{4 \cdot (1-0.3^2) \cdot 33.77^2 \cdot 116.2 + 33.77^3} = 1.05 \text{ MPa}, \quad (46)$$

where:

- $b_1$  – the distance according to Fig. 9,  $b_1 = 33.77$  mm,
- $h_w$  – the web depth,  $h_w = b_{ph1} = 116.2$  mm (see Fig. 6),
- $\nu$  – the Poisson's ratio,  $\nu = 0.3$ .

For profiles with one flange under tension (when the element is bending about y-y axis)  $k_f = 0$  in (5.10b) in [12].

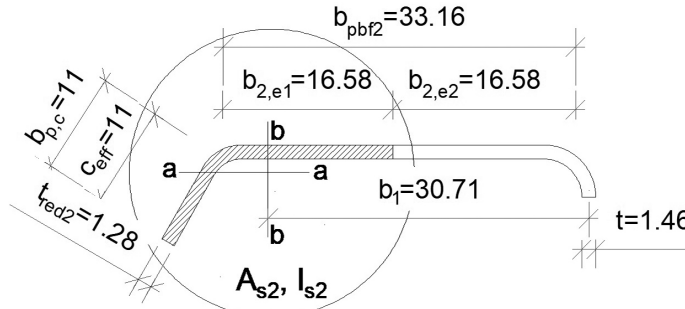


Fig. 10. The edge stiffener in the compressed narrow flange  $b_{f2}$  of a 600/120 wall cassette

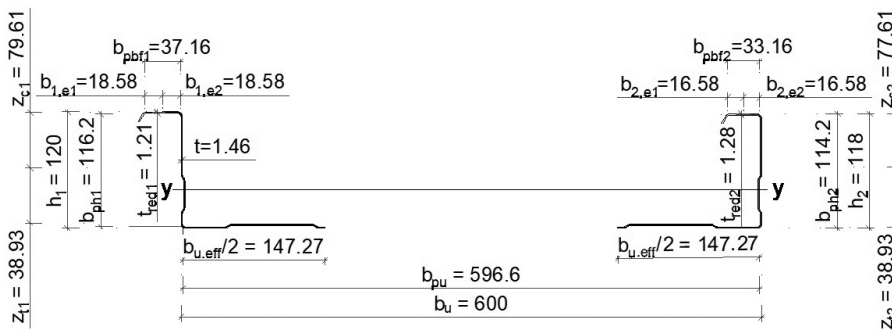


Fig. 11. Effective cross section of the narrow flange under compression and the entire cross sections of the webs of a 600/120 wall cassette

The reduction factor  $\chi_d$  for the distortional buckling resistance (flexural buckling of a stiffener) according to (5.12b) in [12] is:

$$\chi_d = 1.47 - 0.723 \cdot \bar{\lambda}_d = 1.47 - 0.723 \cdot 0.888 = 0.828 < 1.0, \quad (47)$$

for:

$$0.65 < \bar{\lambda}_d = 0.888 < 1.38. \quad (48)$$

The reduced thickness  $t_{red1}$  of the edge stiffener in the compressed flange  $b_{f1}$  is:

$$t_{red1} = \chi_d \cdot t = 0.828 \cdot 1.46 = 1.21 \text{ mm}. \quad (49)$$

The analytical calculations for narrow flange  $b_{f2}$  (see Fig. 10) were performed in the same manner as for narrow flange  $b_{f1}$ . The reduction factor  $\chi_d$  for the distortional buckling resistance of a stiffener according to (5.12b) in [12] is  $\chi_d = 0.88$ .

The reduced thickness  $t_{red2}$  of the edge stiffener in the compressed flange  $b_{f2}$  is:

$$t_{red2} = \chi_d \cdot t = 0.88 \cdot 1.46 = 1.28 \text{ mm}. \quad (50)$$

$$A_{s2} = 39.91 \text{ mm}^2,$$

$$I_{s2} = 332.66 \text{ mm}^4.$$

#### 5.2.4. Determination of effective depth of the webs $h_1$ and $h_2$ under bending

The relative slenderness  $\bar{\lambda}_p$  according to (4.2) in [13] is:

**For web  $h_1$ :**

$$\lambda_p = \frac{\bar{b}/t}{28,4\varepsilon\sqrt{k_\sigma}} = \frac{116.2/1.46}{28,4 \cdot 0.857 \cdot \sqrt{13.23}} = 0.899, \quad (51)$$

where, according to Fig. 6:  $\bar{b} = b_{ph1} = 116.2 \text{ mm}$ ,  $t = 1.46 \text{ mm}$ ,  $\varepsilon = \sqrt{\frac{235}{f_{yb}}} = \sqrt{\frac{235}{320}} = 0.857$ , the

value of  $k_\sigma$  may be calculated according to Table 4.1 [13] as follows:

$$k_\sigma = 7.81 - 6.29\psi + 9.78\psi^2 = 7.81 - 6.29 \cdot (-0.49) + 9.78 \cdot (-0.49)^2 = 13.23, \quad (52)$$

for:

$$0 > \psi = -0.49 > -1, \quad (53)$$

with:

$$\psi = \frac{\sigma_2}{\sigma_1} = -\frac{38.93}{79.61} = -0.49, \quad (54)$$

where, according to Fig. 11:  $\sigma_2 = z_{t1} = 38.93 \text{ mm}$  and  $\sigma_1 = z_{c1} = 79.61 \text{ mm}$ .

The reduction factor  $\rho$  of effective width according to (4.2) in [13] is as follows:



The effective width  $b_{eff}$  for shear lag should be determined according to Section 3 in [13] with use of the relation:

$$b_{eff} = \beta \cdot b_0 = 0.984 \cdot 300 = 295.2 \text{ mm}, \quad (61)$$

where:

$b_0$  – is half the width of an internal element,  $b_0 = 300 \text{ mm}$ ,

$\beta$  – is the effective factor obtained for sagging bending, according to Table 3.1 in [13] as follows:

$$\beta = \frac{1}{1 + 6.4 \cdot \kappa^2} = \frac{1}{1 + 6.4 \cdot (0.05)^2} = 0.984, \quad (62)$$

for:

$$0.02 < \kappa = 0.05 \leq 0.7, \quad (63)$$

with:

$$\kappa = \frac{\alpha_0 \cdot b_0}{L_e} = \frac{1 \cdot 300}{6000} = 0.05, \quad (64)$$

where:

$\alpha_0$  – for the case without longitudinal stiffeners within the width  $b_0$ ,  $\alpha_0 = 1.0$ ,

$L_e$  – is the length between points of the zero bending moment (see 3.2.1(2) in [13],

$L_e = L = 6000 \text{ mm}$  (see Fig. 4).

The effective width  $b_{eff} = 295.20 \text{ mm}$  as a consequence of shear lag according to formula (61) is greater than the effective width  $b_{u,eff} = 294.55 \text{ mm}$  resulting from plate buckling according to formula (26), thus the effects of shear lag can be neglected.

## 6. Conclusion

This paper is a continuation of an analysis of some difficult cases of resistance calculations of sheeting for thin-wall constructions according to the rules given in the standard PN-EN 1993-1-3 (see [17, 18]).

This article presents an example of the determination of the resistance moment  $M_{b,Rd}$  of a 600/120 liner tray with a narrow flange under compression resulting from wind pressure and the resistance moment  $M_{c,Rd}$  of this liner tray with a wide flange under compression resulting from wind suction. The resistance in the case of the wind pressure on the wall of the liner trays  $M_{b,Rd}$  is 5.82 kNm. This is higher than the resistance of the linear tray  $M_{c,Rd}$  equal to 4.89 kNm in the case of wind suction.

The presented example proves that the analytical calculations according to PN-EN 1993-1-3 rules require good knowledge of linear tray performance.

*The contributions of E. Pięciórak, H. Ciurej and M. Betlej in the work were carried out as part of statutory research No. 11.11.100.197 AGH, WGiG, AGH University of Science and Technology in Cracow.*

## References

- [1] Baehre R., Buca J., *Die wirksame Breite des Zuggurtes von biegebeanspruchten Kassetten*, Stahlbau 55(9), 1986, 276–285.
- [2] Baehre R., *Zur Schubfeldwirkung und-Bemessung von Kassettenkonstruktionen*, Stahlbau 56(7), 1987, 197–202.
- [3] Davies J.M., *Cassette wall construction: Current Research and Practice*, Third International Conference on Advances in Steel Structures, Hong Kong, China, 9–11 December 2002, 57–68.
- [4] Davies J. M., *Residential buildings – Chapter 7: Light gauge metal structures Recent advances* (Ronald J. & Dubina D.), CISM International Centre for Mechanical Sciences, Vol. 455, 2005, 143–188.
- [5] Davies J.M., Dewhurst D.W., *The shear behaviour of thin-walled cassette sections infilled by rigid insulation*, Proceedings of International Conference on Experimental Model Research and Testing of Thin-Walled Structures, Prague, September 1997, 209–216.
- [6] Davies J. M., Frogos A. S., *The local shear buckling of thin-walled cassette infilled by rigid insulation – 1. Tests.*, Proceedings of 3<sup>rd</sup> European Conference on Steel Structures – Eurosteel 2002, Coimbra, Portugal, 19-20 September 2002, 669–678.
- [7] Davies J.M., Frogos A.S., *The local shear buckling of thin-walled cassette infilled by rigid insulation*, Journal of Constructional Steel Research, 60 (3–5), Mar-May 2004, 581–599.
- [8] Dubina D., Ungureanu V. and Landolfo R., *Design of Cold-formed Steel Structures*, ECCS 2012, Ernst & Sohn.
- [9] <https://pruszynski.com.pl/kaseta-scienna-600-120,prod,79,1750.php>(access:19.07.2018).
- [10] <http://termolan.pt/en/solutions/industrial-buildings> (access: 19.07.2018).
- [11] König J., *Transversally loaded thin-walled C-shaped panels with intermediate stiffeners*, Swedish Council for Building Research, Stockholm 1978, Sweden.
- [12] PN-EN 1993-1-3:2008. Eurokod 3. Projektowanie konstrukcji stalowych. Część 1-3: Reguły ogólne. Reguły uzupełniające dla konstrukcji z kształtowników i blach profilowanych na zimno.
- [13] PN-EN 1993-1-5:2008. Eurokod 3. Projektowanie konstrukcji stalowych. Część 1-5: Blachownice.
- [14] Program AutoCAD 2017 wersja edukacyjna.
- [15] Program Mathcad 14.
- [16] Program Microsoft Excel 2010.
- [17] Pięciorak E., Piekarczyk M., *Wyznaczanie efektywnego przekroju zginanej blachy trapezowej w ujęciu normy PN-EN 1993-1-3*, Czasopismo Techniczne, R. 109 z. 20. Budownictwo 2012 3-B, s. 113–137.
- [18] Pięciorak E., *The influence of support widths of trapezoidal sheets on local transverse resistance of the web according to PN-EN 1993-1-3*, Czasopismo Techniczne, R. 111 z. 12. Budownictwo 2014 4-B, s. 47–57.
- [19] Thomasson J., *Thin-Walled C-Shaped Panels in Axial Compression*, Swedish Council for Building Research, Stockholm 1978, Sweden.
- [20] Vyberg G., *Diaphragm action of assembled C-Shaped Panels*, Swedish Council for Building Research, Stockholm 1976, Sweden.

If you want to quote this article, its proper bibliographic entry is as follow: Pięciorak E., Piekarczyk M., Ciurej H., Betlej M., *The determination of moment resistance for a liner tray restrained by sheeting according to european standard PN-EN 1993-1-3*, Technical Transactions, Vol. 12/2018, pp. 77–94.

Aleksander Urbański  orcid.org/0000-0002-5544-9134

aurbansk123@gmail.com  orcid.org/0000-0003-3283-5005

Krzysztof Podleś

Institute of Geotechnics, Cracow University of Technology

## A 2D/3D METHOD OF THE GROUNDWATER FLOW AND STABILITY ANALYSIS OF A SLOPE WITH DEWATERING WELLS

---

### METODA ANALIZY 2D/3D PRZEPLYWU WÓD GRUNTOWYCH I STATECZNOŚCI ZBOCZA ODWADNIANEGO PRZY POMOCY STUDNI ODWADNIAJĄCYCH

#### Abstract

This paper presents an approximate method for a groundwater flow analysis in the case of a slope with vertical dewatering wells distributed equidistantly. Firstly, a multi-scale problem of flow to a drainage well is solved and flow model to a perforated tube with a filter screen is shown. Secondly, a method of building quasi-3D flow model of a slope with vertical dewatering wells using a technique of overlapped 2D mesh is shown. A short description of the implementation of this 2D/3D flow model for the ZSoil.PC code is given. The results of the described 2D/3D method are compared with a referential 3D analysis giving an acceptable level of agreement. Finally, the 2D/3D method of flow analysis is used in a two-phase (flow + deformation) formulation of a slope stability problem. The comparison of the results of these analyses with fully 3D (referential) analysis, on an example problem provides a very close accurate stability and deformation estimation; however, the computational time used for the 2D/3D analysis is significantly shorter than required by 3D analysis.

**Keywords:** FEM analysis of groundwater flow, slope stability analysis, dewatering wells

#### Streszczenie

Przedstawiono przybliżoną metodę analizy przepływu wód gruntowych dla przypadku zbocza ze studniami odwadniającymi rozmieszczonymi w równych odstępach. Na wstępie rozwiązano wieloskalowe zagadnienie przepływu do studni odwadniającej i zaprezentowano sposób budowy zhomogenizowanego modelu filtracji do filtra. Następnie zaprezentowano sposób budowy quasi-3D modelu filtracji w zboczu z pionowymi studniami odwadniającymi z wykorzystaniem techniki nakładających się siatek 2D. Podano krótki opis implementacji modelu filtracji 2D/3D w programie ZSoil.PC. Wyniki opisanej metody 2D/3D porównano z referencyjnym modelem 3D dającą akceptowalną zgodność. Na końcu zastosowano metodę analizy przepływu 2D/3D do zagadnień dwufazowych (przepływ + deformacja) dla problemu stateczności zbocza. Porównanie wyników z referencyjną pełną analizą 3D, dla przykładowego problemu daje bardzo dobrą ocenę stateczności i deformacji, ale czas obliczeniowy używany do analizy 2D/3D jest znacznie krótszy.

**Słowa kluczowe:** analiza filtracji MES, stateczność zboczy, studnie odwadniające.



## 1. Introductory remarks and the motivation

Numerical modelling of groundwater flow performed with use of the finite element method may be presented as a separate problem or as a component of a two-phase (flow + deformation) analysis. The first option is often used for the design of water supply (see [6]) or drainage systems. The second option is necessary when attempting to investigate the influence of the presence of water within a soil mass, which is particularly essential in the context of slope stability problems. This concerns both natural and man-made slopes such as an earth dam downstream side slope. It is a widely recognised fact that the introduction of drilled dewatering wells lowers the level of the saturated zone, which is beneficial for the stability of a structure.

An overview of the concerned situation is presented in Fig. 1. where vertical dewatering wells with a filtrating zone (screen filter), located on some depth, are equidistantly distributed in the longitudinal (Z) direction. Even if the filtration properties of the soil are assumed as being constant in the Z-direction (while they may vary in the XY cross section plane), the problem of flow is three-dimensional, but submitted to periodicity constraints. In a recent practice, 3D flow problem set in the domain of one segment (with Z-length  $a$ ) between drainage wells may be solved within an acceptably short timeframe, thus, for flow analysis exclusively there would not be a requirement for an approximate method. However, this is not the case of slope stability analysis basing on two-phase (flow + deformation) formulation and Terzaghi-Bishop principle. Modelling a continuum with a 3D field of water pressure would require full 3D fields of stresses, and what follows, strains and displacements, even in the case when the plane strain (PS) assumptions are commonly accepted, like while performing stability analysis of man-made slopes. Plane strain assumptions are, in considered case, violated. 3D stability analyses performed with use of the  $c-\phi$  reduction method, which might be formulated as well, require considerably more time and computational power than 2D analysis – see the comparison in the example given in section 6. It is worth noting that with these types of problems; dense meshing in zones where strain localisation is expected (which are *a-priori* unknown), is necessary.

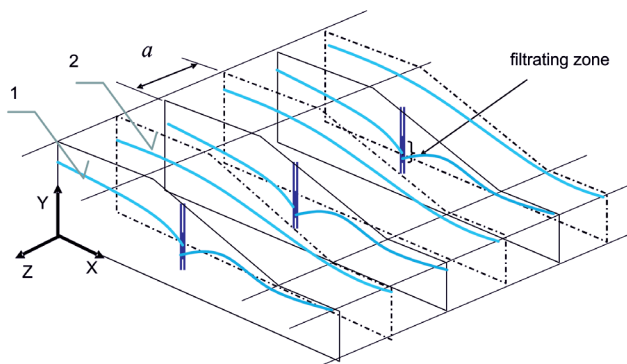


Fig. 1. An overview of a slope with dewatering wells; free surfaces: 1) at the section coming through vertical well, 2) at the section in the mid-distance

The main objective of this article is to perform the analysis of dewatered slopes in the 2D domain of its cross-section, with plane strain assumption and water pressure field being an averaged of these in Z-direction. The developed method is based on an approximate solution of the groundwater flow problem on overlapped meshes describing flow through the slope and flow to the draining wells. An implementation done in custom version of ZSoil.PC code allows to show the robustness and acceptable engineering accuracy of the developed 2D/3D method.

## 2. Flow to a drainage well as a multi-scale problem

The first task to be solved is to develop a proper model of seepage to a filter screen in order to estimate its efficiency. This can be achieved empirically, based on in situ or laboratory testing, which is beyond the scope of this paper, or numerically with the use of the micro-level analysis of flow and the homogenisation technique presented below. The validity of Darcy's law with full saturation condition is assumed. A gravity term in Darcy's law is neglected while performing the described micro-level analysis.

The scale of the geometry of the openings in the filter screen tube is within the range of  $10^{-3}$  m; the scale of macro-level characteristic dimensions may reach  $10^1$  m. In these circumstances, the need for a multi-scale analysis is evident as it is extremely difficult to build a single model dealing with the flow within the vicinity of the drain tube (scale mm) and at a large distance from it. Scale separation leads to multi-scale analysis, which consists of two problems concerning:

- ▶ micro level – set in the 3D domain of periodic cell resulting from the geometry of the filter screen. This analysis is used to establish fluxes  $q$  for the given pressure head  $p$ , see Fig. 2b,
- ▶ macro level – referring to the whole system (2D or 3D), with well modelled as a tube (diameter  $D$ , thickness  $\Delta$ ), and permeability coefficient set by equivalence of flow with these established during micro level analysis .

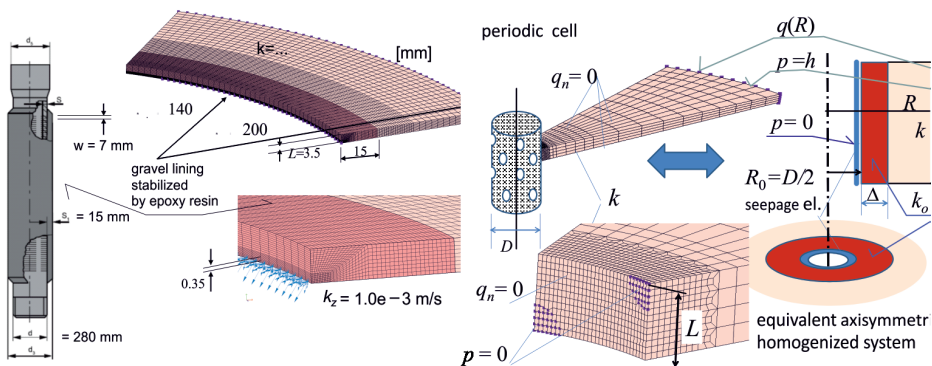


Fig. 2. Multi-scale analysis based on the homogenisation of the flow

Fig. 2a shows an exemplary piece of the filter screen and its surrounding, used in the system which is presented in section 6. In the Fig. 2b, the outlook of following homogenisation procedure is shown. Having given uniform flux  $q(R)$  on the outer boundary of the periodic cell from the solution of 3D micro-level problem, where  $k$  [length/time] is a permeability coefficient of soils surrounding the well, an axi-symmetric problem is solved in order to found such permeability  $k_0$  of fictitious layer of (arbitrarily set) thickness  $\Delta$ , which assure the same flux  $q$  for zero pressure condition on the inner surface of a tube.

In the auxiliary procedure of identification, one has to solve Laplace differential equation  $\nabla^2 p = 0$  for the pressure head distribution in the radial direction with constraints  $\frac{\partial}{\partial \theta} = 0$ ,  $\frac{\partial}{\partial y} = 0$ , coming from assumed axisymmetry of homogenised model of the filter screen, which takes a form of eq. (1):

$$\frac{d^2 p}{dr^2} + \frac{1}{r} \frac{dp}{dr} = 0, \quad (1)$$

with the following boundary and compatibility conditions (eq. 2),

$$p_1(R_0) = 0, \quad p_2(R) = h, \\ k_0 \left. \frac{dp_1}{dr} \right|_{r=R_0+\Delta} = k \left. \frac{dp_2}{dr} \right|_{r=R_0+\Delta}, \quad p_1(R_0 + \Delta) = p_2(R_0 + \Delta), \quad (2)$$

For given  $R_0$ ,  $R$ ,  $k$ ,  $h$ , this leads to a formula for permeability  $k_0$  of fictitious layer with the thickness  $\Delta$ :

$$k_0 = \frac{\beta \ln \frac{R_0 + \Delta}{R_0}}{1 + \beta \ln \frac{R}{R_0 + \Delta}} k, \quad \beta = \frac{qR}{kh} = \frac{Q}{2\pi kh} [-]. \quad (3)$$

Flux  $q$  [length/time] at the radius  $R$ , or total water inflow  $Q$  [length<sup>2</sup>/time] per unit length of a tube can be used in the formula for the dimensionless factor  $\beta$  appearing in eq. (3).

This homogenised model of filter screen will be later used for both 2D/3D as well as 3D macro modelling of dewatering wells.

### 3. Approximate 2D model of the ground flow in a slope with periodically spaced vertical dewatering wells

In ZSoil.PC FE software system stationary or transient ground water flow problem is formulated basing on the modified version of Darcy law, taking into account not fully saturated zone, proposed by Van Genuchten [3]. Moreover, Richards continuity equation is used for modelling internal retention in not fully saturated zone. Another tool enabling modelling

without any user intervention in computation consists of seepage elements, automatically switching boundary condition from fully free flow to no-flow, depending on the pressure at the boundary. For details, see [2, 4, 5]. All mentioned features are active in the present issue.

The idea is to decompose flow field in the dewatered slope at following parts:

- ▶ **flow along the slope**, for which base 2D FE mesh describing geometry of the slope cross-section is built, preserving its permeability properties  $k(X, Y)$  and boundary conditions,
- ▶ **flow towards the well**, performed on a set of overlapped FE meshes, applied in the well influence zone, size of which is related to the distance of wells ( $= 2a$ ) in Z direction (see the Fig. 3). Each of them represents a sector of 3D system. Permeability of materials set in this fictitious media inherits permeability  $k(X, Y)$  from the base mesh but those are finally modified on the principle of geometrical equivalence, assuming radial flow direction with the centre at the well. The equivalence must take into consideration a fact, that plane flow is set for unit thickness  $g = 1.0$  [length] of the model in perpendicular direction. On the length of filter screen, the tube of diameter  $D$  is surrounded by fictitious layer with permeability coming from  $k_o$  of homogenised model and current sectorial geometry. Outside the filter screen, on the tube inner surface, a no-flow condition  $q_n = 0$  is set. Additionally, on the limits of the well influence zone, the condition of equal pressures with base mesh is set by introducing penalty permeability  $k_\infty$  (i.e. equal to a very large value) at the “arms” perpendicular to the base mesh.

It is worth noting, that in a given FE software building a FE model with overlapped meshes must be allowed, like it is in ZSoil.PC.

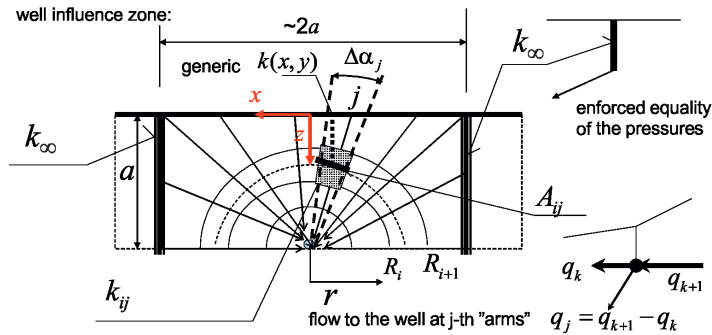


Fig. 3. Details of the equivalent 2D/3D flow model

Number of radii  $m$  is set by the user as well as the number of circles  $n$ . The permeability at the  $ij$  position, considering geometry equals:

$$k_{ij} = k(x, y) \cdot \frac{A_{ij}}{a}, \quad (4)$$

where  $A_{ij}$  is averaged width attached to  $i$ -th zone at  $j$ -th sector of the radial mesh. For regular shape they are given in eq. 5, for the remaining they can be derived analogously

$$F_{ij} = \pi(R_{i+1}^2 - R_i^2) \frac{\Delta \alpha_j}{2\pi}, \quad A_{ij} = \frac{F_{ij}}{R_{i+1} - R_i} = \frac{R_{i+1} + R_i}{2} \Delta \alpha_j, \quad (5)$$

where  $F_{ij}$  is an area.

In a custom version of ZSoil.PC code process of building any model as described above is fully automatized and after creating the base 2D FE mesh the user needs to provide only minimal amount of data describing geometry of wells, additional discretization, permeability  $k_o$  and thickness  $\Delta$  of fictitious layer of homogenised well model, according to p. 2. There may be a few wells modelled at single base mesh, with one objection, i.e. that their influence zones do not overlap.

User interface for wells definition is presented in the Fig. 4.

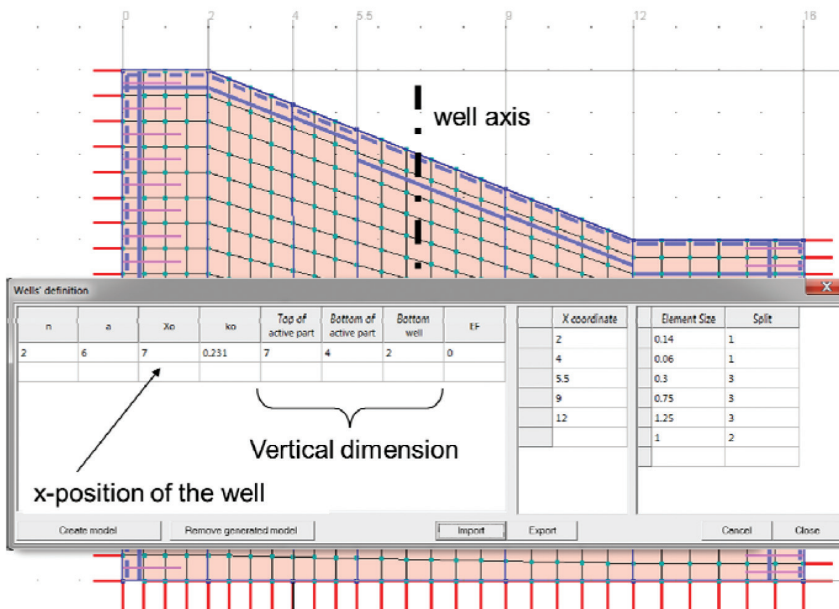


Fig. 4. User interface for wells definition

#### 4. Comparison of results between 2D/3D against 3D flow modelling

The first test example is based on comparison of a result for steady-state flow analysis obtained for full 3D model with results for equivalent 2D/3D model. Draft of the geometry with resulting base FE mesh is presented in Fig. 5. Parameters presented in Fig. 5a were used to generate mesh for 2D/3D model. FE meshes with fluid boundary conditions for 2D/3D method and 3D model are shown in Fig. 6a and 6b respectively. Permeability coefficient is  $k = 1$  m/d for whole domain, despite zone of the filter screen ( $D = 0.28$  m) where homogenised model is applied with  $k_o = 0.231$  m/d at the fictitious layer of thickness  $\Delta = 0.06$  m.

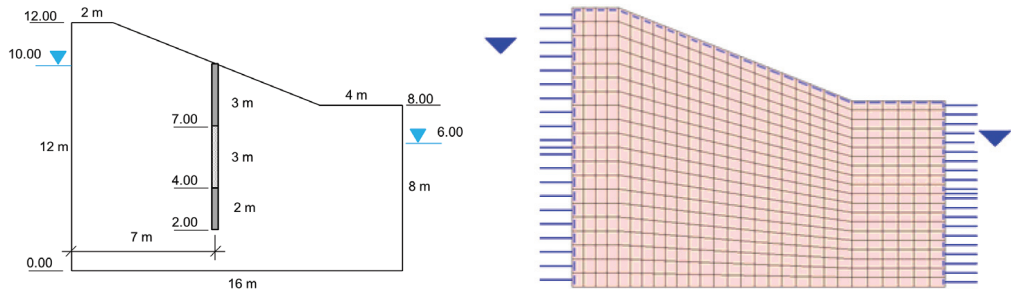


Fig. 5. Geometry of the test model and resulting base FE mesh

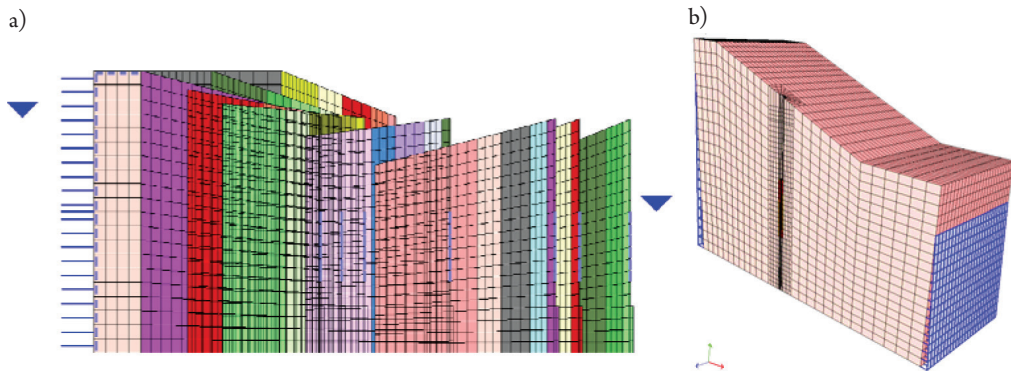


Fig. 6. FE meshes with fluid boundary conditions for: a) 2D/3D model, b) referential 3D model

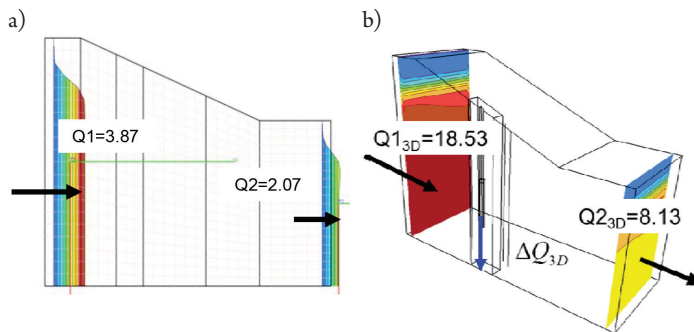


Fig. 7. Fluid velocities distribution in cross sections for: a) 2D/3D model, b) referential 3D model

In order to compare total flow to the dewatering well for both models the integrals of a fluid velocities through cross sections defined on left and right boundary sides are calculated. Fluid velocities distribution in cross sections with resultant integrals for 2D/3D model and 3D model are shown in Fig. 7a and 7b. The assumed distance between wells is  $2a=12\text{m}$ .

Total flow to dewatering well for 2D/3D model equals:

$$\Delta Q_{2,D} = (Q1 - Q2)a = \left( 3.87 \left[ \frac{m^3}{d \cdot m} \right] - 2.07 \left[ \frac{m^3}{d \cdot m} \right] \right) \cdot 6m = 10.79 \left[ \frac{m^3}{d} \right] \quad (6)$$

Total flow to dewatering well for 3D model equals:

$$\Delta Q_{3D} = Q_{1_{3D}} - Q_{2_{3D}} = \left( 18.53 \left[ \frac{m^3}{d} \right] - 8.13 \left[ \frac{m^3}{d} \right] \right) = 10.40 \left[ \frac{m^3}{d} \right] \quad (7)$$

Difference is:

$$e\% = \frac{10.79 - 10.40}{10.40} = 3.75\% \quad (8)$$

The comparison of the pore pressure distribution for 2D/3D model and referential 3D model is shown in Fig. 8. Differences for both models in total flow to dewatering well (less than 4%) and pore pressure distribution are acceptable for engineering applications. Data preparation is much simpler for 2D/3D model with automatic well generation than for 3D model, for which all details of the well and fine mesh around well have to be generated manually. Additionally, mesh generation when a well position is changed is created automatically for 2D/3D model. The 3D model has to be created nearly from the beginning.

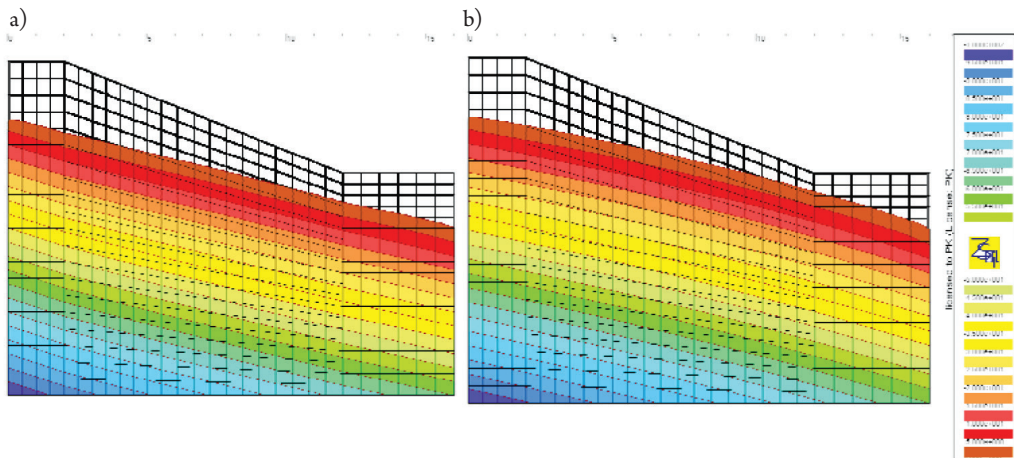


Fig. 8. Pore pressure distribution for: a) 2D/3D model, b) referential 3D model (in the mid-section)

## 5. Application of the 2D/3D method to two-phase (deformation + flow) analysis

The two-phase analysis for 2D/3D model requires special treatment for material properties and boundary conditions. Deformation + flow analysis is performed on 2D base mesh when perpendicular or radial “arms” have influence on flow analysis only. Young modulus is assumed to be close to zero and displacement degrees of freedom are fixed everywhere in the domain of perpendicular “arm” in order to neglect its influence on mechanical analysis. This sub-model has pressure degrees of freedom only. Meshes of the base model and “arms” can be inconsistent. Continuity of pressure fields between both sub-models is preserved by

means of nodal link option available in ZSoil.PC. Such schema of partial separation of flow and deformation+flow sub-models is presented in Fig. 9.

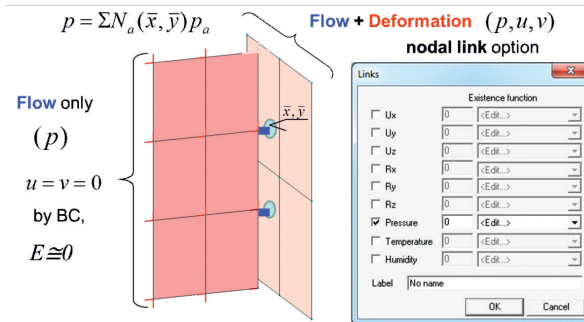


Fig. 9. Partial separation of flow and deformation+flow sub-models for two-phase analysis

## 6. Application of developed method of flow analysis to the slope stability problem

The effectiveness of 2D/3D model compared with full 3D model is presented on an example of slope stability problem. The analysis of pore pressure distribution influences on results of slope stability was performed by Finite Element and  $c-\phi$  reduction method, using ZSoil.PC® code. The applied  $c-\phi$  reduction method was firstly introduced into the early version of ZSoil.PC code (circa 1985); its details may be found in ZSoil documentation [8]. More examples of usage of this method in landslide stability analyses can be found in Truty et al. [2], Zheng et al. [7], Ozbay and Cabalar [1]. The soil continuum was treated as an elastic-plastic one, with Mohr-Coulomb yield condition. The influence of an underground water pressure field in saturated or partially saturated zone was taken into account, with enhancements of the flow theory given in Van Genuchten [3], basing on observed water table.

The geometry of the analysed problem with resulting base FE mesh are presented in Fig. 10 and parameters for mesh generation are shown in Fig. 11. FE meshes with fluid boundary conditions for 2D/3D method and 3D model are shown in Fig. 12 and Fig. 13 respectively.

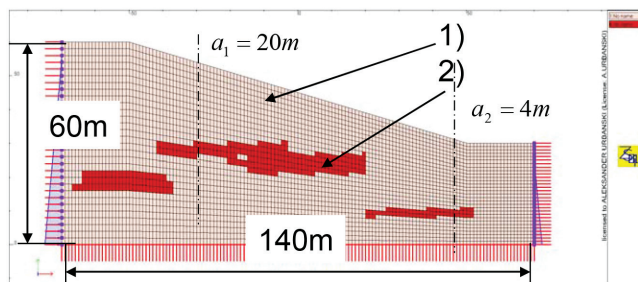


Fig. 10. The geometry of the test model and resulting base FE mesh



n	a	Xo	ko	Top of active part	Bottom of active part	Bottom well	EF
4	20	-30	0.01	35	25	20	0
3	4	45	0.01	25	15	10	0

X coordinate	Element Size	Split
-50	0.14	1
-40	0.06	1
-30	1	2
-20	2	2
-10	3	3
	4	2

n	a	Xo	ko	Top of active part	Bottom of active part	Bottom well	EF
4	20	-30	0.01	35	25	20	0
3	4	45	0.01	25	15	10	0

X coordinate	Element Size	Split
42	0.14	1
44	0.06	1
46	0.3	2
48	0.75	2
50	1	2

Fig. 11. The geometry of the wells and parameters for mesh generation

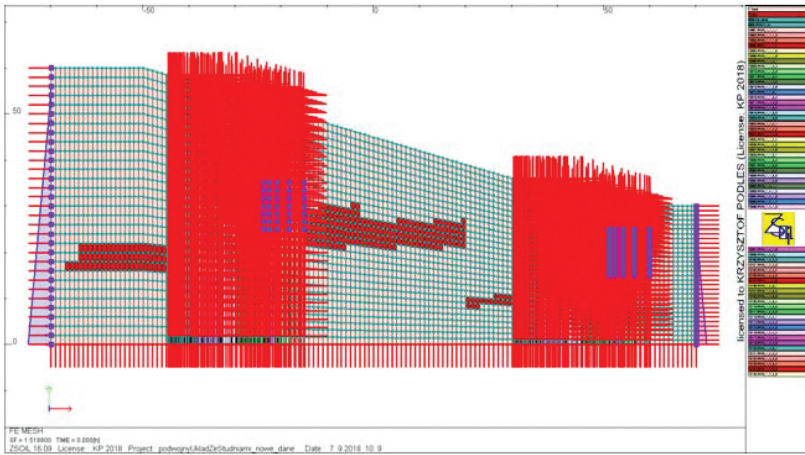


Fig. 12. FE mesh with boundary conditions for 2D/3D model

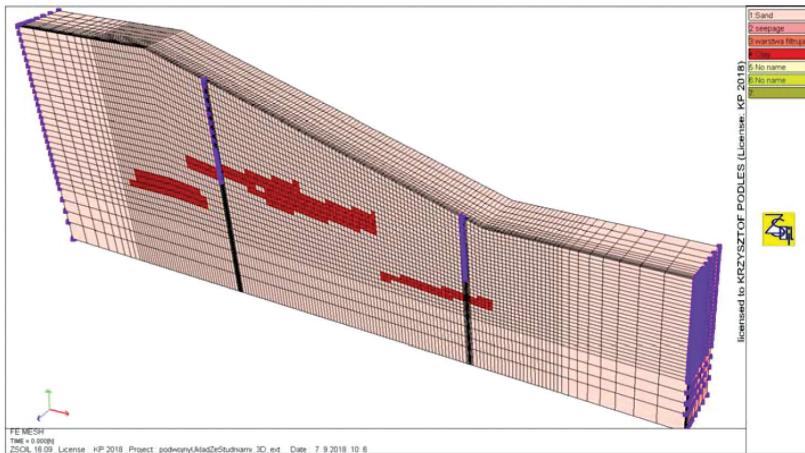


Fig. 13. FE mesh with boundary conditions for referential 3D model

In the analysis following strength and permeability parameters were assumed:

- ▶ material 1:  $c_1 = 3.0$  kPa,  $\varphi_1 = 30^\circ$ ,  $k_1 = 0.0416$  m/d, (sand),
- ▶ material 2:  $c_2 = 20.0$  kPa,  $\varphi_2 = 30^\circ$ ,  $k_2 = 0.0000416$  m/d, (clay);

The results of stability analysis are presented in Fig. 14 and 15. It is worth to mention that almost identical deformation (failure pattern) appears in both approaches. The computed safety factors are very close one to another, as well. For 2D/3D model it equals  $SF_{2D/3D} = 1.519$ , and for referential 3D model  $SF_{3D} = 1.509$ . It is worth mentioning that elapsed time of computations differs substantially, as the analysis for 2D/3D model was performed in 10 minutes, while for 3D model it takes 10 hours, i.e.  $\sim 60$  times more, for the same mesh density in XY plane.

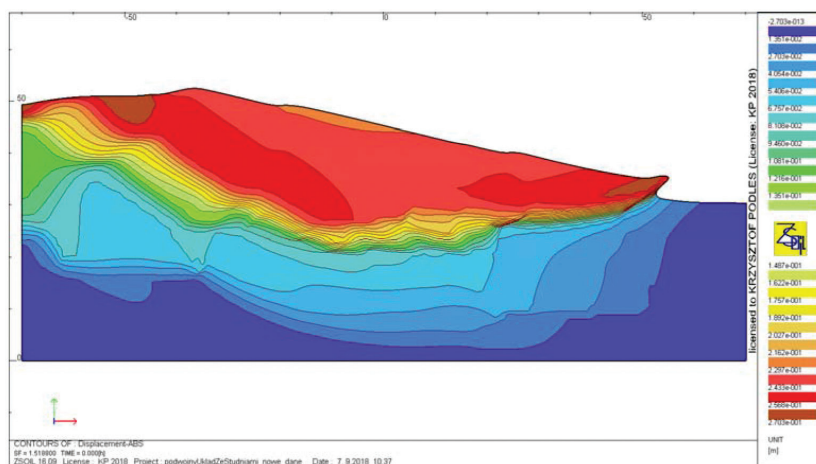


Fig. 14. Distribution of total displacements on deformed mesh for 2D/3D model for safety factor  $SF_{2D/3D} = 1.519$

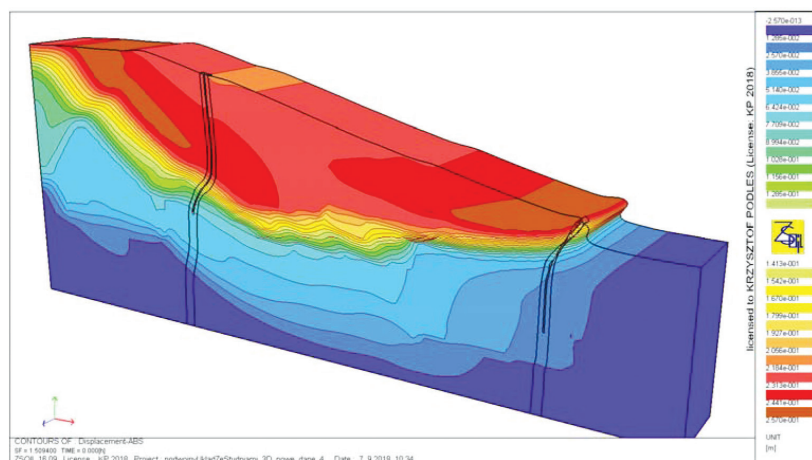


Fig. 15. Distribution of total displacements on deformed mesh for referential 3D model for safety factor  $SF_{3D} = 1.509$

## 7. Conclusions

The presented approximate method of an analysis of the groundwater flow in a slope with vertical dewatering wells; distributed periodically proves to be an efficient tool for engineering problems requiring spatial distribution of the water pressure field.

The main gain is that analysis can be set in 2D domain, instead of 3D modelling, leading to practically very close results remaining within the 5% margin of error. It concerns deformation and stability assessment in case of two-phase analysis, as well as inflow to the wells.

The presented method allows to obtain results in a rapid way. In case of problems with assessment of stability in existing structure, it may be useful tool for prediction of its behaviour in varying condition. In a design process it may serve as a tool to optimize dewatering system in terms of location of the wells or applied drainage capability.

## References

- [1] Ozbay, A., Cabalar, A.F., *FEM and LEM stability analyses of the fatal landslides at Çöllolar open-cast lignite mine in Elbistan, Turkey*. "Landslides", 12/2015, 155–163.
- [2] Truty A., Urbański A., Grodecki M., Podleś K., *Computer aided models of landslides and their protection problems*, "Scientific-Technical Papers of Communication Engineers and Technicians of the Republic of Poland" in Krakow, No. 88, issue 88 (144)/2009, 395–419.
- [3] Van Genuchten M.Th., *A closed form equation for predicting the hydraulic conductivity of unsaturated soils*. "Soil Science Society of America Journal", 44/1980, 892–898.
- [4] Urbański A., Grodecki M., Kot A., *Numerical simulations in analysis of anti-flood ambankments*, "Journal of Civil Engineering, Environment and Architecture", 2016.
- [5] Urbański A., Grodecki M., *FE Approach to coupled transient flow and stability analysis of anti-flood ambankments* "3-rd Int. Conference on Advances of Computer Methods in Geotechnical and Geo-environmental Engineering", Moscow 2000.
- [6] Wilk B.K., Urbański A., *The impact of the shape of screen openings on groundwater flow to a deep drilled well*, "Technical Transactions" 11/2018, to appear.
- [7] Zheng Y., Tang X., Zhao S., Deng C., Lei W.3., *Strength reduction and step-loading finite element approaches in geotechnical engineering*. "Journal of Rock Mechanics and Geotechnical Engineering", 1(1)/2009, 21–30.
- [8] Zimmemann Th., Truty A., Urbański A., Podleś K., *Z\_Soil.PC 2003 manual. Theory*. Elmepress international & Zace Services Ltd., Lausanne, Switzerland 2005.

Andrzej Więckowski  [orcid.org/0000-0001-9633-8097](https://orcid.org/0000-0001-9633-8097)  
awiecko@agh.edu.pl

Karol Ryż  [orcid.org/0000-0001-5567-6436](https://orcid.org/0000-0001-5567-6436)  
Department of Geomechanics, Civil Engineering and Geotechnics, AGH University  
of Science And Technology, Cracow

Wojciech Sikora  
SAWE Production Plant of Girders, Rzeszow

## FAILURES OF SUSPENDED CEILINGS AND EXECUTION ERRORS

### AWARIE SUFITÓW PODWIESZANYCH I BŁĘDY WYKONAWCZE

#### Abstract

When observing the stability of suspended ceilings during operation, sometimes smaller failures are observed, up to disasters, even a few of considerable sizes and serious consequences. The aim of the article is to analyse the causes of damage to a suspended ceiling, with an area of approximately 500 m<sup>2</sup>, as well as testing and checking the applied construction elements. In situ destructive tests as well as tests at the AGH laboratory were carried out. The analyses were carried out in accordance with PN/EN 13964: 2014 (E). It was found that the designed ceiling system solution was correct. Whereas in the performance, an improper spacing of hangers, even by more than 70% of the permissible spacing, and forbidden lengths of brackets from C60 profiles, were applied. Also, about 55% of the connectors had too small diameters of the ends of the mandrels, which allowed for the sliding of broken head and a sudden loss of carrying capacity of the hanger.

**Keywords:** failures, suspended ceilings, metal expansion anchors

#### Streszczenie

Obserwując stateczność sufitów podwieszanych w czasie eksploatacji, zauważa się występowanie mniejszych awarii, aż do katastrof – kilku o znacznych rozmiarach i poważnych konsekwencjach. Celem artykułu jest analiza przyczyn uszkodzeń systemowego sufitu podwieszanego, o powierzchni około 500 m<sup>2</sup> oraz badania sprawdzające zastosowanych elementów konstrukcyjnych. Wykonano badania niszczące in situ oraz w laboratorium AGH. Analizy przeprowadzono zgodnie z PN/EN 13964:2014 (E). Stwierdzono, że zaprojektowane rozwiązanie systemowe sufitu było prawidłowe. Natomiast w wykonawstwie zastosowano, m.in. niewłaściwe rozstawy wieszaków, nawet o ponad 70% większe, niż dopuszczalne oraz niedozwolone długości wsporników z profili C60. Również około 55% łączników posiadało zbyt małe średnice zakończeń trzpieni, które umożliwiały przecięnięcie zerwanej główki i nagłą utratę nośności wieszaka.

**Słowa kluczowe:** awarie, sufity podwieszane, metalowe kotwy rozporowe

## 1. Introduction

Currently, suspended ceilings constitute a standard element of interior finishing in many buildings. In addition to architectural and aesthetic values, they make it possible to separate the space to place various installations, which are very extensive in new buildings. System solutions for suspended ceilings, utilising complete, ready-made elements for assembly during the construction works, in line with the required work method, are typically used. Bespoke solutions, which make it possible to meet atypical criteria, are used more rarely.

When observing the in-service stability of suspended ceilings, one can note the occurrence of minor failures as well as collapses, some of them being of extensive proportions and having serious consequences. It is important to identify the causes and mechanisms of such failures.

Naturally, the system assumptions strictly define the scope of and limitations in the application of the intended solutions, the rules for the preparation of materials and construction, as well as methods of operation. All these conditions must be met unconditionally, since they were assumed at the design stage of the system. The results of testing of a suspended ceiling with an area of 500 m<sup>2</sup>, a central fragment of which, with an area of 30 m<sup>2</sup>, failed. After a lowering of approx. 10 cm was noticed, the ceiling was supported from underneath and repaired.

In situ tests of breaking loads on expansion anchors and laboratory tests of the applied hangers were conducted. The tests of the system elements were conducted in the laboratory of the Department of Geomechanics, Civil Engineering and Geotechnics, AGH, while the admissible loads were tested in line with PN/EN 13964:2014 [5].

Progressive collapse is the most dangerous, as it leads to the complete destruction of the structure in a short time. Such a mechanism was at work in many cases of collapse. The article analyses the mechanical condition of a suspended ceiling as a multi-hanger suspended structure undergoing gradual and progressive degradation. The process of tension redistribution, leading to the successive elimination of hangers in the ceiling's structural system, was investigated. The conducted analyses of the collapses and results of simulations involving model suspended ceilings made it possible to suggest a method of reducing the risk of progressive collapse through the application of additional hangers – safety devices – directing the process of structural failure.

## 2. Failures and collapses of suspended ceilings

Nowadays, suspended ceilings are practically a standard finishing element in public buildings (shopping malls, restaurants, railway/bus stations, auditoriums, halls, etc.). The observation of civil engineering incidents in such buildings has shown that failures or collapses of suspended ceilings are not rare, and may result in fatalities [1]. In mechanical terms, a suspended ceiling is usually a steel multi-hanger scaffold structure fixed to the floor slab. The bottom of the steel scaffold is usually closed by the gypsum board. Such a structure often weighs about 30 kilograms per one square metre, and sometimes much more. Clearly,

in the case of a collapse of a ceiling with an area of several dozen to several hundred square metres, the falling structure can weigh up to a dozen or so tonnes, becoming a threat to the life and health of many people.

Construction failures of suspended ceilings usually involve damages (cracks, fractures, excessive bending) or displacements of whole structures or their fragments. These damages should prompt measures aimed not only at their removal, but also at the identification of their causes, with a view to preventing further damage and a potential collapse. If the symptoms appear early, which is a favourable situation, preventive measures can be taken in advance. Unfortunately, large-scale collapses are rarely preceded by symptoms foreshadowing a real threat.

A construction collapse of a suspended ceiling means an unintended, sudden destruction of the entirety or significant portion of its structure. Unfortunately, one of the characteristic properties of suspended structures is their high sensitivity to progressive collapse over a short period of time (from several to several dozen seconds). An impulse which disengages one or several hangers as a result of the redistribution of forces leads to the breakage of subsequent elements. This triggers an extremely dangerous progressive destruction mechanism, causing the entire structure to collapse. The causes of this impulse, i.e. of the disengagement of first hangers, vary and are associated with design errors, use of faulty elements, construction errors and inappropriate use and maintenance. Often, the collapse has several causes, prompting a search for the primary cause. The scale of destruction can sometimes be extensive, covering areas exceeding 1,000 square metres of ceiling [1]. The weight of the falling structure can reach several dozen tonnes, which is why some collapses result in fatalities.

In 2010, during the construction of a sports hall in the Public School Complex No. 3 in Wadowice, the suspended ceiling over the entire area of the hall collapsed (approx. 1,000 m<sup>2</sup>). The progressive nature of this collapse led to the destruction, in a short period of time, of the entire erected structure – Figure 1. Several people sustained injuries.



Fig. 1. The collapse of the suspended ceiling in the sports hall in Wadowice, 2010

In 2014, approximately 800 m<sup>2</sup> of a suspended ceiling collapsed in a shopping mall in Poznań. Luckily, this collapse took place at night and caused no casualties. Hangers being overburdened with catwalks and the disconnection of some of the hangers for the duration of works were suggested as the primary causes. The secondary cause, leading directly to the triggering of the failure mechanism, was the excessive load on the ceiling by water seeping out of a damaged fire sprinkler system, found by an expert to have been a random cause.

In 2017 in Białystok, a suspended ceiling, with an area of approx. 350 m<sup>2</sup>, collapsed during a fire in a building rented by a wholesale store. The impulse which triggered the collapse was two firemen stepping onto the ceiling structure (local hanger overload). The firemen died as a result of falling from more than 4 metres. The collapse developed in a progressive manner, with an additional possible cause being the rapidly rising temperature in the building on fire.

In January 2018, a suspended ceiling collapsed in the renovated Varketili metro station in Tbilisi, injuring 14 people. The collapse quickly affected a substantial portion of the structure, developing in a way which is characteristic of progressive collapse.

Failures and collapses of suspended ceilings can be observed rather often and commonly. Many construction incidents which, luckily, do not result in any casualties are not reported by the media. The presented examples indicate a similar nature of the origin and development of the collapse mechanism. Usually, it leads to the destruction of the entire structure, which collapses in a short period of time. In this context, a question arises whether suspended ceiling structures must be so commonly exposed to the risk of progressive collapse, for which a local impulse causes degradation to develop on a wide scale. It appears advisable to take measures modifying commonly used structures in such a way that the progressive collapse triggered by an impulse be locally limited.

### **3. The subject and scope of tests**

Suspended ceilings in two identical restaurant rooms in Kraków, with an area of approx. 500 m<sup>2</sup> each, with shapes resembling rectangles, were subjected to testing.

“After noticing a substantial bend in the ceiling edge, which was already approx. 10 cm in the centre, the lowered section was propped and the damage was repaired. Next, testing was commissioned and additional security measures were taken”.

In accordance with as-built documentation, the analysed ceiling was built according to a Knauf system, based on a metal structure [2–4], with gypsum board decking 2 \* 12.5 mm. Between the reinforced concrete slab and suspended ceiling, there are many, densely laid system pipes with various sections, from a dozen or so cm<sup>2</sup> to more than 1 m<sup>2</sup>. Light access panels are fixed in openings in the decking, in irregularly spaced locations, as well as air-conditioning units, ventilation boards, lighting lamps and sprinklers. The densely placed installations and equipment hindered the positioning of hanger axes in straight lines.

The destructive tests for the pull-out resistance of expansion anchors were conducted in situ in the facility and in the laboratory of the Department of Geomechanics, Civil Engineering and Geotechnics, AGH. In addition, breakage tests of the individual elements of the hangers were performed in the laboratory.

#### 4. Erification sizing of the ceiling according to the system applied and the actual spaces between hangers

In the Knauf system, NIDA WGN 20 system, in respect of “Verification sizing of the ceiling”, point 4. Determining the basic geometric parameters, the axial distances of: hangers – a, main runners – c, and support tracks – b, is provided for, in line with Figure 2 and Table 1.

In line with the Knuf system, hangers with a load capacity of 0.30 kN, and – as indicated in Table 1 – axial distances  $c = 110$  cm and  $a = 75$  cm, should have been applied.

On the basis of a survey, it was found that main runner hangers in the failure area were present with the most unfavourable axial spacing of main runners  $c_{\text{Imax}} = 105$  cm and  $a_{\text{Imax}} = 130$  cm. The values permissible according to the Knauf system were exceeded significantly. Furthermore, other errors were observed. Due to the location of an access panel, the main runner was not continuous (one cantilever was 120 cm long and the other was 15 cm long). Some hangers were tensioned and subjected to significant loads, some were less tensioned, and a few were completely loose (this could have been caused by rectification of the floor slab level only in respect of selected hangers, with the adjacent ones remaining unadjusted). A small number of hangers were fixed with an approx. 15% tilt from the vertical due to conflicts with installation routes.

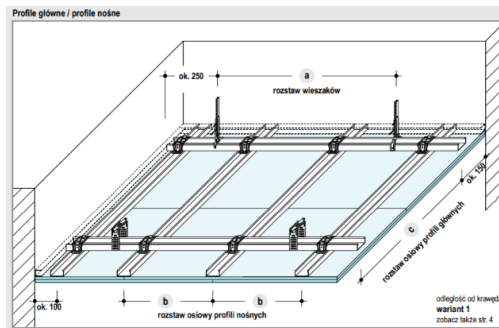


Fig. 2. Geometric parameters according to Knauf NIDA WGN 20

Table 1. According to Knauf, NIDA WGN 20

Maksymalne rozstawy				
• z odpornością ogniową od dołu • bez odporności ogniowej wszystkie wymiary w mm				
Rozstaw osiowy profili głównych c	Rozstaw wiszaków a			Tylko sufit pod sufitem do 0,65 1)
	klasa obciążeni kN/m <sup>2</sup> (zobacz strona 2)			
	do 0,15	do 0,30	do 0,50	
500	1200	950	800	750
600	1150	900	750	700
700	1100	850	700	650
800	1050	800	700	-
900	1000	800	-	-
1000	950	750	-	-
1100	900	750	-	-
1200	900	-	-	-

1) Stosować wiszaki o klasie nośności 0,4kN



## 5. Admissible loads based on destructive tests

The PN/EN 13964:2014 (E) suspended ceilings – Requirements and test methods standard [5] “covers membranes, individual substructure components, substructure kits and suspended ceiling kits intended to be placed on the market”. In accordance with this standard, the admissible hanger load ( $admF$ ) in kN equals:

$$adm F = F_u^{5\%} / \nu, \quad (1)$$

$$F_u^{5\%} = F_u - k_\sigma \cdot s \quad (2)$$

where:

$F_u^{5\%}$  – unfactored load, 5% quantile, kN,

$\nu$  – safety factor,  $\nu = 2.5$ ,

$F_u$  – average breaking load, kN,

$k_\sigma$  – statistical factor,

$s$  – standard deviation.

Depending on the number of  $n$  – tests in a given sample, the values of  $k_\sigma$  factors are determined as per Table 2 in the referenced standard [5].

Table 2. Acceptance factor  $k_\sigma$  [5]

Fractile $\phi$	$\nu = n - 1$												
	Number of test specimens												
	2	3	4	5	6	7	8	9	10	11	12	13	14
$W = 90$ 5%	5.31	3.96	3.40	3.09	2.89	2.75	2.65	2.57	2.50	2.45	2.40	2.36	2.33
NOTE 1 Values for $k_\sigma$ depending on the number of test samples $n$ , the probability ( $W$ ) and the fractile value $\phi$ (assumption – the standard deviation is unknown).													
NOTE 2 For this standard, the probability $W$ and the fractile value $\phi$ have been fixed at 0,90 and 5%, respectively. For $n = 10$ test pieces, the prevailing $k_\sigma$ value is 2,57.													

### 5.1. In situ destructive tests for the pull-out resistance of expansion anchors

The direct cause of the failure of the suspended ceiling in question was the breakage of the heads of KSMM metal expansion anchors, Figures 3a and 3b. Therefore, the in situ tests covered the expansion anchors.

Each NIDA WGN 20 hanger, fixed to the floor slab using one KSMM anchor, was subjected to an increasing force until breaking the connection with the floor. During tests of 11 specimens of the installed KSMM metal expansion anchors, distributed evenly on the entire area of the room, in one case the entire anchor was pulled out of the floor when subjected to a force of 2.29 kN. In six cases, the head of the KSMM expansion anchor broke. In three cases the breakage of the anchor head was observed first, and when greater force was applied, the pins were extracted from the torn anchor wedges together with the head, and

finally, all parts, including the wedges, were extracted from concrete, Figure 3c. Furthermore, tests similar to those described above were conducted in situ, with the application of two anchors fixing each nonius top hanger to the ceiling.

Similar in situ tests for the extraction of anchors were performed on the ceiling from the second restaurant, installed by a different Company 2. In these tests, it was observed in each case that first, the head was torn off; next, the pins were extracted with the head; and finally, all other anchor elements were extracted from concrete, including the torn-off wedges.

The results of tests and calculations, in line with the presented assessment of admissible loads in the individual destructive tests, as per reports (1.1) and (1.2), are listed in Table 2.

KSMM metal expansion anchors with nonius top hangers engaged in a chain design in each case meet the required admissible hanger load requirements for the Knauf system,  $admF \geq 0.3 \text{ kN}$ .

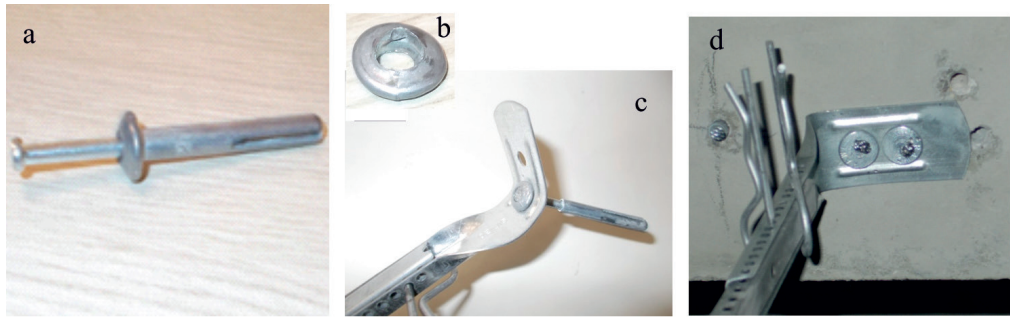


Fig. 3. KSMM metal expansion anchor – a and after the load destructive testing, a – torn off head, b – torn off head with extracted wedge on the pin, d – top hanger fixed with two ZSP expansion anchors, in violation of the approval

It is worth noting that KSMM anchors, installed by Company 1, are characterised by similar breaking loads for head breakage of 1.31 kN and 1.32 kN, respectively, for the breakage of the head only (in approx. 55% of anchors) and for head breakage followed by the extraction of the elements of expansion anchors (in approx. 45% of anchors).

Table 3. The results of breaking load tests and the calculated unfactored values of the applied suspended ceiling kits according to the Knauf system, following the chain design – KSMM metal expansion anchor and nonius top hanger

Company	Description	$F_u$ kN	$s$	$F_u^{5\%}$ kN	$admF$ kN
1	Expansion anchor head breakage	1.31	0.16	0.82	0.33
	Head breakage / expansion anchor extraction	1.32 / 2.89	0.12 / 0.37	0.83	0.33
	2 expansion anchors applied	2.34	0.37	0.87	0.35
2	Head breakage / expansion anchor extraction	1.81 / 2.72	0.23 / 0.79	1.03	0.41

$F_u$  – average breaking load,  $s$  – standard deviation,  $F_u^{5\%}$  – unfactored value, 5%,  $admF$  – admissible hanger load

The breakage of anchor heads only, which was the case in 55% of all hangers fixed by Company 1, suggests a production error. This is indicated by pin end parts, which had smaller diameters than the openings in the torn off heads, which allowed their sliding off the pins. In the remaining cases, the broken head caused the subsequent extraction of the pin, followed by the extraction of the entire external wedge of the anchor – see Figure 3.

When the pin is extracted along with the broken head, the structure is much safer, as after the head is broken by a smaller force, it is followed by the extraction of the pin from the wedge by a force which is, on average, 2.2 times greater, and an evident displacement (lowering) of the hanger, by approx. 2 cm, is observed. Sudden, complete loss of load capacity takes place afterwards, i.e. in the last phase when the broken head, pin and broken wedge are extracted from concrete. Such a sudden loss of load capacity occurs immediately when the heads alone are torn off, on average with a force more than two times lower.

The installed hangers, each on two anchors, Figure 4a, were characterised by an average breaking load of 2.34 kN, which was by 19% and 14% smaller than the breaking loads for single anchors in the case of their extraction with heads, fixed by Company 1 and Company 2, respectively. Therefore, the application of two anchors instead of one correctly installed anchor, does not result in an increase in the average breaking load (at the same time, in accordance with Technical Approval ITB AT-15-7305/2014 Metal expansion anchors, [2], the application of anchors with spacing smaller than 12 cm is forbidden).

When comparing average breaking loads  $F_u$  (breakage of anchor heads), it can be noted that anchors installed by Company 1 were characterised by breaking loads by 27% smaller than those for anchors installed by Company 2. The significant discrepancy between these loads, by more than  $\frac{1}{4}$ , can stem from differences in the load capacity of anchors made by different producers.

## 5.2. Laboratory destructive tests for the applied suspended ceiling elements

Six cycles of breaking load tests for the applied elements of the suspended ceiling were conducted in the laboratory of the Department of Geomechanics, Civil Engineering and Geotechnics, utilising Veb Werkstoffprüfmaschinen Leipzig press No. 28218 13/6062. The results of the tests and calculations as per (1) and (2) are presented in Table 3.

The results of calculations for each test cycle confirm that the condition of admissible hanger load  $admF > 0.3$  kN was met.

The weakest link in the entire chain design – metal expansion anchor and the individual elements of the ceiling structure – was the connection of bottom hanger and CD 60 profile ( $F_u = 0.977$  kN), Figure 4a. In the suspended ceiling which had failed, every connection of bottom hanger and CD 60 profile was additionally reinforced by two 3.5\*25 screws, Figure 4b. This solution was characterised by an average breaking load of  $F_u = 2.00$  kN. Greater average breaking loads, in order from smallest to greatest, characterised bottom hanger rivets ( $F_u = 2.54$  kN), ZSP anchor heads ( $F_u = 3.10$  kN; Figure 4c) and KSMM anchor heads ( $F_u = 3.24$  kN).

Table 4. The results of breaking load tests conducted in the laboratory and the calculated unfactored values of the suspended ceiling elements, following the chain design – metal expansion anchor and nonius top hanger, and the individual elements of the system

Description	$F_u$ kN	s	$F_u^{5\%}$ kN	admF kN
KSMM metal expansion anchor and hanger elements including CD 60 profile (connection breakage: bottom hanger – CD 60 profile, Fig. )	0.977	0.025	0.844	0.338
KSMM metal expansion anchor and hanger elements including CD 60 profile; bottom hanger fixed with two 3.5*25 screws (connection breakage bottom hanger – CD 60 profile, installed as above)	2.00	0.22	0.83	0.33
KSMM metal expansion anchor and hanger elements (bottom hanger rivet breakage)	2.54	0.287	1.02	0.406
KSMM metal expansion anchor and nonius top hanger (KSMM anchor head breakage)	3.24	0.29	1.70	0.68
ZSP metal expansion anchor and nonius top hanger (ZSP anchor head breakage)	3.10	0.34	1.77	0.71
$F_u$ – average breaking load, s – standard deviation, $F_u^{5\%}$ – unfactored value, 5%, admF – admissible hanger load				

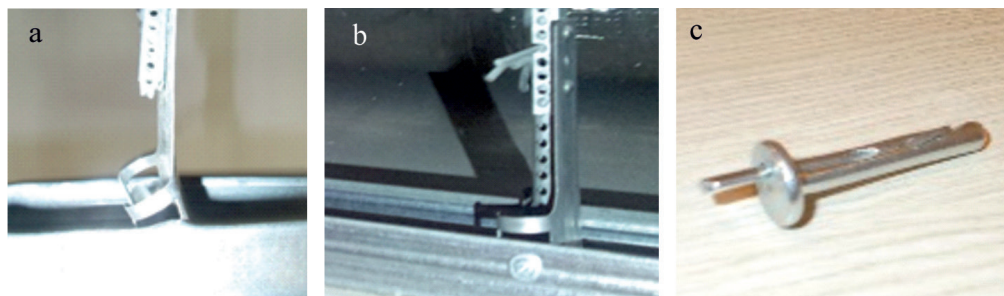


Fig. 4. Deformation of connection of bottom hanger and CD 60 profile – a, additional bonding of elements with two 3.5\*25 screws – b, ZSP metal expansion anchor – c

## 6. Conclusion

The extensive application of suspended ceilings, as well as their failures and collapses involving a sudden drop of entire ceiling planes, which can span as much as several hundred square meters, prompts extended tests which would facilitate more accurate identification of the causes and reduction of the risk of collapse.

The preliminary tests of two identical suspended ceiling systems with 2\*12.5 mm gypsum board decking, with an area of approx. 500 m<sup>2</sup> each, performed by different companies revealed, the following:

- ▶ non-conformances in terms of construction (Company 1)

- ▷ exceeding the maximum distances between hangers, by as much as 73%, and the lack of continuity of the main runner, which resulted in cantilever with a length of 115 cm against 20 cm provided for in the system,
- ▷ non-vertical setting of a dozen or so hangers (where the density of building installations was denser; 15° tilt from the vertical),
- ▶ non-conformances in the manufactured materials
  - ▷ about 55% of the expansion anchors installed in the ceiling, a part of which has failed, indicated a production error, since the end parts of pins had smaller diameters than the openings in the torn-off heads, which made it possible not to extract the pin with greater force after the head was torn off, and thus resulted in decreased load capacity of the entire anchor.

Based on destructive tests, the following was determined:

- ▶ a significant discrepancy between average breaking loads in situ to extract metal expansion anchors, exceeding  $\frac{1}{4}$ , which resulted from a low load capacity of the anchors used by Company 1.
- ▶ faulty assembly of the hangers, each on two anchors, does not lead to average breaking loads being higher than in the case of a single anchor,
- ▶ KSMM anchors ( $F_u = 3.24$  kN) were characterised by greater average breaking loads than ZSP anchors ( $F_u = 3.10$  kN); furthermore, in the case of KSMM anchors, first, the anchor head is broken with a lower force, next the pin is extracted from the anchor wedge on average with even two times greater force with simultaneous displacement of the hanger by approx. 2 cm, and finally we can observe a sudden and complete loss of load capacity.
- ▶ non-systemic application of additional bonding of the bottom hanger and CD 60 profile, using two 3.5\*25 screws, results in the average load capacity of the connection being approx. two times greater.

The results were obtained on a small sample, which is why they may not be generalised.

## References

- [1] Dunaj P., *Katastrofa budowlana w klubie Sportowo Rekreacyjnym w Białymstoku*, XXIV Konferencja Naukowo-Techniczna, Szczecin-Międzyzdroje 2009.
- [2] Aprobata techniczna ITB, AT-15-7305/2014, Metalowe łączniki rozporowe KSMM, KG, ZSP i ZSP-O, Instytut Techniki Budowlanej, ISBN 978-83-249-7634-8, Warszawa.
- [3] Krajowa Deklaracja Zgodności nr. 2/14, Metalowe łączniki rozporowe KSMM, Stalko Sp. z O. O. Sp. K., ul. Torowa 41, 32-050 Skawina.
- [4] Krajowa Deklaracja Właściwości Użytkowych nr 8/2017, Metalowe łączniki rozporowe KSMM Stalko Sp. z o.o. Sp. K., ul. Torowa 41, 32-050 Skawina.
- [5] EN 13964:2014 Suspended ceilings – Requirements and test methods.

Marcin Jaraczewski  [orcid.org/0000-0002-6451-1032](https://orcid.org/0000-0002-6451-1032)  
jaracz@pk.edu.pl

Faculty of Electrical Engineering, Cracow University of Technology

## REACTIVE T-TOPOLOGY FOUR-TERMINAL-NETWORK COMPENSATOR FOR MULTIHARMONIC CURRENT

### REAKTANCYJNY KOMPENSATOR CZWÓRNIKOWY KSZTAŁTU T DLA WIELOHARMONICZNEGO ŹRÓDŁA RZECZYWISTEGO

#### Abstract

This paper presents a new method for passive current compensation of a real multiharmonic power source with the use of a four-terminal network. In contrast to a two-terminal compensator, a four-terminal-network compensator can fully separate the supply circuit from the load. This ensures optimal operating conditions for the source while keeping the voltage and load current unchanged. The source's optimal working conditions mean that the source current reaches its minimal RMS value (becoming the so-called "active current") while it transmits the desired active power to the load.

**Keywords:** active power, optimal current, multiharmonic current

#### Streszczenie

W artykule przedstawiono metodę kompensacji biernego prądu źródła wieloharmonicznego rzeczywistego przy pomocy układu czwórnikowego. Kompensator czwórnikowy, w przeciwieństwie do dwójnikowego, potrafi odseparować obwód zasilania od obwodu odbiornika i zapewnić źródłu optymalne warunki pracy przy jednoczesnym zachowaniu niezmiennych wartości napięcia i prądu odbiornika. Przez optymalne warunki pracy źródła należy tu rozumieć całkowite zminimalizowanie wartości skutecznej prądu źródła zasilania do tzw. prądu aktywnego niosącego zadaną moc czynną ze źródła do odbiornika.

**Słowa kluczowe:** moc czynna, prąd optymalny, źródło wieloharmoniczne

## 1. Introduction

In the case of an AC power-supplying source with an internal impedance, the commonly used reactive current compensation based on one capacitor in parallel does not minimize transmission losses or the RMS value of the source current. When the known equivalent circuit parameters of the energy source are taken into account, minimization of the source current RMS value and transmission losses cannot be achieved with the use of a passive two-terminal-network compensator. This paper presents a synthesis of a four-terminal-network compensator that provides optimal operating conditions for a source and nominal operating conditions for a load using only reactive elements.

## 2. Optimal operating conditions – monoharmonic case

The optimal operating condition of a source is usually formulated as achieving the minimum RMS value of the source's current (minimal transmission losses), under assumption that a given active power is supplied to the load, which can be formulated as the following constrained minimization task [3, 4]:

$$\Pi^* \rightarrow \min$$

$$P = \text{real } I^* E - R_S I^* I \quad (1)$$

where:

$$R_S = 0.5 (Z_S + Z_S^*)$$

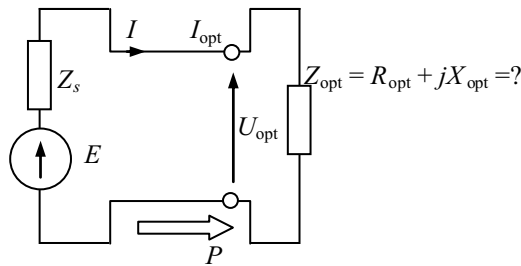


Fig. 1. The minimization task

The solution to this problem is a current which is in phase with the source's EMF [1–3]

$$I = G_e E \quad (2)$$

where  $G_e$  stands for an equivalent conductance seen by the EMF.

Additionally, this current should meet the power equation

$$R_S I^* I - \text{real}(I^* E) + P = 0$$

or

$$R_s G_e^2 - G_e + \frac{P}{|E|^2} = 0$$

which allows us to calculate the optimal conductivity

$$G_e = \frac{1 - \sqrt{1 - \frac{P}{P_{\max}}}}{2R_s} \quad (3)$$

and then the optimal current

$$I_{\text{opt}} = G_e E = \frac{1 - \sqrt{1 - \frac{P}{P_{\max}}}}{2R_s} E \quad (4)$$

where

$$P_{\max} = \frac{|E|^2}{4R_s} \quad (5)$$

### 3. A four-terminal reactive compensator

A passive four-terminal compensator can be created using reactive elements. It must meet the optimum input condition and nominal load condition.

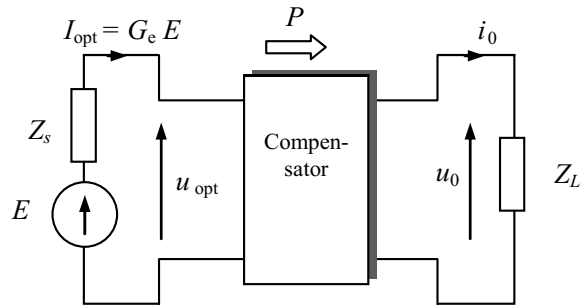


Fig. 2. Four-terminal compensator

Therefore, to determine its parameters it is enough to know the optimum input conditions ( $I_{\text{opt}}$  and  $U_{\text{opt}}$ ) and load impedance  $Z_L$ .

From the minimum current condition under the active-power constraint (formula 1) [3, 4], we obtain the value of the equivalent conductivity  $G_e$  [1, 2, 5]; thus, from the EMF's point of view, the entire system reduces to a resistance equal to  $\frac{1}{G_e}$ , which in turn amounts to impedance  $Z_{\text{opt}}$  in series with inner impedance  $Z_s$  (see Fig 3).



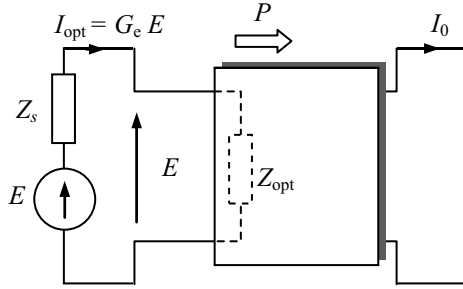


Fig. 3. Equivalent system seen by the EMF after optimization

#### 4. T-topology compensator – monoharmonic case

One possible implementation of a four-terminal reactive compensator is with the use of the T-topology four-terminal network shown in figure 4, which acts as a matching circuit that connects the source and the load.

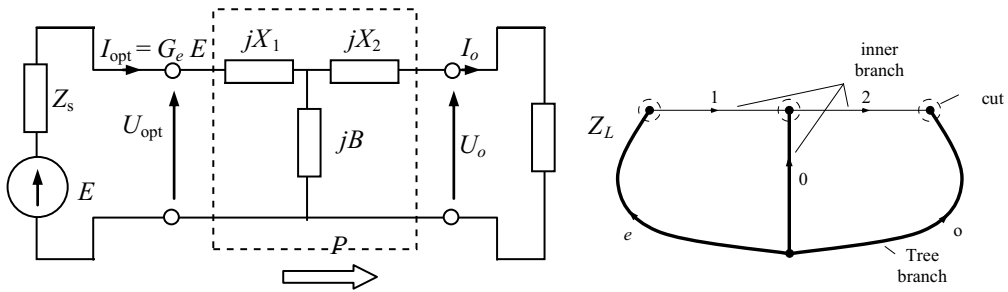


Fig. 4. Left – reactive compensator as a T-topology four-terminal network; right – graph of the circuit

Such a compensator must have at least 3 branches because then we have one independent current or voltage within the circuit's inner branches and this gives us some choice in the selection of reactances [6].

When describing the system with the use of chain equations, we get the following formulas:

$$\begin{aligned} \begin{bmatrix} U_{\text{opt}} \\ I_{\text{opt}} \end{bmatrix} &= \begin{bmatrix} 1 & jX_1 \\ 0 & 1 \end{bmatrix} \begin{bmatrix} 1 & 0 \\ jB & 1 \end{bmatrix} \begin{bmatrix} 1 & jX_2 \\ 0 & 1 \end{bmatrix} \begin{bmatrix} 1 & Z_L \\ 0 & 1 \end{bmatrix} \begin{bmatrix} 0 \\ I_o \end{bmatrix} = \\ &= \begin{bmatrix} 1 - X_1 B & j(X_1 + X_2 - X_1 X_2 B) \\ jB & 1 - X_2 B \end{bmatrix} \begin{bmatrix} 1 & Z_L \\ 0 & 1 \end{bmatrix} \begin{bmatrix} 0 \\ I_o \end{bmatrix} \end{aligned} \quad (6)$$

or

$$\begin{bmatrix} U_{\text{opt}} \\ I_{\text{opt}} \end{bmatrix} = \begin{bmatrix} a & jb \\ jc & d \end{bmatrix} \begin{bmatrix} 1 & R_L + jX_L \\ 0 & 1 \end{bmatrix} \begin{bmatrix} 0 \\ I_o \end{bmatrix} A \begin{bmatrix} 0 \\ I_o \end{bmatrix} \quad (7)$$

where  $Z_L = R_L + jX_L$

Thus, the optimal input impedance is:

$$Z_{\text{opt}} = \frac{A_{12}}{A_{22}} = R_{\text{opt}} + j X_{\text{opt}} \quad (8)$$

Meeting the optimal input condition requires that the impedance seen by the SEM is real and equal to  $1/G_e$ . This condition imposes two equations:

$$R_s + R_{\text{opt}} = R_s + \frac{R_L}{c^2(R_L^2 + X_L^2) + d^2 - 2X_Lcd} = \frac{1}{G_e}$$

$$X_s + X_{\text{opt}} = X_s - \frac{ac(R_L^2 + X_L^2) + X_L(bc - ad) - bd}{c^2(R_L^2 + X_L^2) + d^2 - 2X_Lcd} = 0 \quad (9)$$

Since the compensator has three reactances, the solution of these two equations must depend on the third compensator's parameter, e.g. the B-susceptance, which in a certain range (around zero) gives a real solution for  $X_1$  and  $X_2$ , but only if

$$-\frac{1}{\sqrt{R_L(1/G_e - R_s)}} < B < \frac{1}{\sqrt{R_L(1/G_e - R_s)}}$$

since always  $R_s G_e < 1$ , thus

$$X_1(B) = -X_s + \frac{1}{B} \pm R_{\text{opt}} \sqrt{\frac{1}{R_{\text{opt}} B^2 R_L} - 1}$$

$$X_2(B) = -X_L + \frac{1}{B} \pm R_L \sqrt{\frac{1}{R_{\text{opt}} B^2 R_L} - 1} \quad (10)$$

## 5. A distorted, multi-harmonic source's current

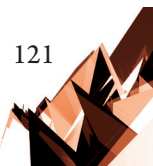
In the case of a multi-harmonic source current, the optimization task (1) takes the form:

$$\sum_h I_h I_h^* \rightarrow \min$$

$$P = \sum_h \text{real } I_h^* E_h - \sum_h R_{S,h} I_h^* I_h \quad (11)$$

where  $h = 1 \dots N$ . Its solution can be obtained in a similar way as in [3, 4, 5] by minimizing the following functional

$$\sum_h I_h I_h^* - \frac{1}{\lambda} \left( \sum_h \text{real } I_h^* E_h - \sum_h R_{S,h} I_h^* I_h \right) \rightarrow \min$$



for  $\lambda > 0$ , we get

$$I_h = \frac{E_h}{2(R_{S,h} + \lambda)} = \frac{E_h}{R_{S,h} + R_{opt,h}} = G_{e,h} E_h$$

and the transmitted  $P$  power condition can be written as

$$\begin{aligned} P(\lambda) &= \sum_h R_{L,h} \frac{|E_h|^2}{|Z_{S,h} + Z_{L,h}|^2} = \\ &= \sum_h \frac{|E_h|^2}{2(R_{S,h} + \lambda)} - \sum_h R_{S,h} \frac{|E_h|^2}{4(R_{S,h} + \lambda)^2} \end{aligned} \quad (12)$$

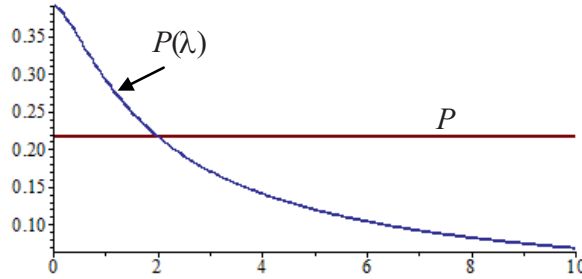


Fig. 5. An example of the variability of  $P(\lambda)$  and imposed  $P$  value

As can be seen from the previous equations (9), the optimal SEM's load for each harmonic fulfills the resonance condition

$$X_{S,h} + X_{opt,h} = 0$$

Equation (9) now takes the form

$$R_{opt,h} = \left[ \frac{R_L}{c^2(R_L^2 + X_L^2) + d^2 - 2X_L cd} \right]_h \quad (13)$$

$$X_{s,h} = \left[ \frac{ac(R_L^2 + X_L^2) + X_L(bc - ad) - bd}{c^2(R_L^2 + X_L^2) + d^2 - 2X_L cd} \right]_h$$

For each harmonic we get

$$X_1(B, h) = -X_{S,h} + \frac{1}{B_h} \pm R_{opt,h} \sqrt{\frac{1}{B_h^2 R_{L,h} R_{opt,h}} - 1} \quad (14)$$

$$X_2(B, h) = -X_{L,h} + \frac{1}{B_h} \pm R_{L,h} \sqrt{\frac{1}{B_h^2 R_{L,h} R_{opt,h}} - 1}$$

Where for every  $h$

$$R_{\text{opr},h} = \frac{1}{G_{e,h}} - R_{E,h} > 0$$

The solution is real only if for each harmonic:

$$\frac{1}{\sqrt{R_{L,h}(1/G_{e,h} - R_{E,h})}} < B_h < \frac{1}{\sqrt{R_{L,h}(1/G_{e,h} - R_{E,h})}}$$

because always  $R_{E,h} G_{e,h} < 1$

After determining the  $\lambda$  value from the non-linear equations (12), the  $R_{\text{opt},h}$  is then

$$R_{\text{opt},h} = R_{S,h} + 2\lambda \quad (15)$$

## 6. T-topology compensator – a multi-harmonic case

The harmonic-dependent susceptance  $B$  and reactance  $X_1, X_2$  of the four-terminal T-topology compensator shown in Figure 4 can be realized as LC filters:

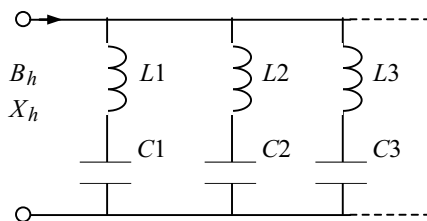


Fig. 6. Implementation of a compensator branch as an LC filter

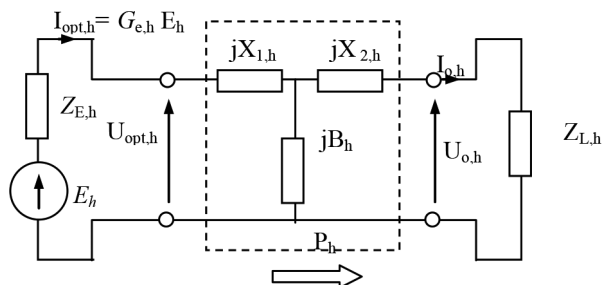


Fig. 7. T-topology four-terminal compensator in the case of multiharmonic current

The susceptance of such a filter has the form

$$B_h = \sum_{n=1..g} \omega_1 C_n \frac{h}{1 - (h/h_n)^2}$$

where:

- $h$  – harmonic number (natural number),
- $g$  – number of the filter's parallel branches,
- $h_n$  – harmonic resonance of  $n$ 's branch,
- $\omega_1 = 2\pi f_1$ ,
- $f_1$  – fundamental frequency.

## 7. Calculation example

Let us consider the optimization task of the two-harmonic source current of the system depicted in Fig. 8 with an RL load

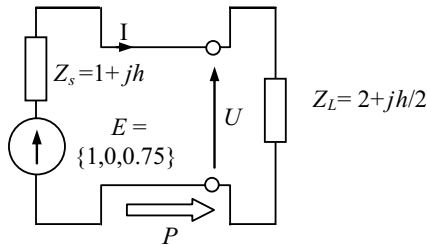


Fig. 8. Two-harmonic power source and its load before optimization

Before optimization:

$$\begin{aligned} |I| &= 0.328 \\ |U| &= 0.70 \\ P &= 0.216 \end{aligned}$$

Solving (12) (Fig. 5) we get  $\lambda = 2$ , thus  $R_{\text{opt}} = 5 \Omega$  (which is constant due to the constant resistance  $R_s$  of the source).

Two solutions of  $X_{1,h}$  and  $X_{2,h}$  that depend on  $B_h$  (14) are thus possible; we choose one of them assuming inductive susceptance  $B_h \sim \frac{1}{h}$

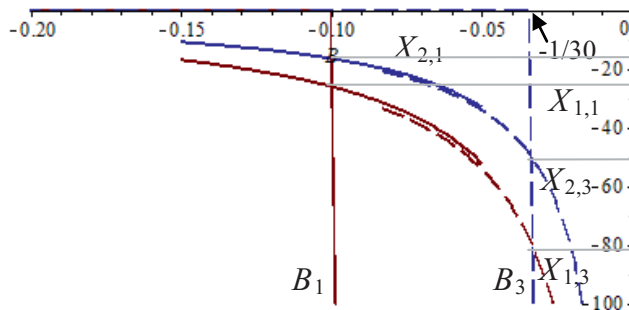


Fig. 9. Example relations of  $X_1, X_2$  with respect to  $B$  ( $L = 31.85$  [mH])

We select  $B_1 = -0.1$  and  $B_3 = -1/30$ , thus capacitive reactances are

$$\begin{aligned} X_{1,1} &= -26.0 & X_{1,3} &= -80.3 \\ X_{2,1} &= -16.5 & X_{2,3} &= -50.3 \end{aligned}$$

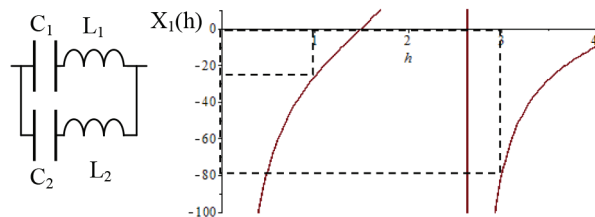


Fig. 10. implementation of  $X_{1,h}$  and its frequency response

Thus, 1<sup>st</sup> branch parameters are i.e.:

$$\begin{aligned} C_1 &= 57.4 & C_2 &= 17.9 \text{ } [\mu\text{F}] \\ L_1 &= 78.5 & L_2 &= 27.8 \text{ } [\text{mH}] \end{aligned}$$

The T-topology four-terminal compensator is depicted in Fig. 11

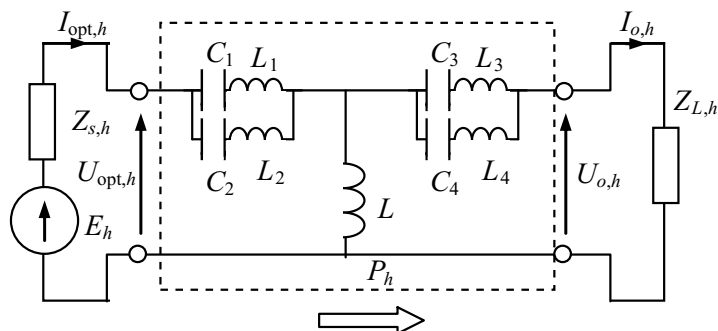


Fig. 11. T-topology four-terminal compensator

After connecting the compensator

$$\begin{aligned} |I_{\text{opt}}| &= 0.207 \\ |U_{\text{opt}}| &= 1.12 \\ |U_o| &= 0.7 \\ P &= 0.216 \end{aligned}$$

Thus, a lossless and reactive four-terminal compensator that completely compensates the source's reactive current is feasible and is shown in Fig. 11.

## 8. Summary

The lossless, four-terminal compensator makes the power-source's voltage and current independent of the load's voltage and current, which makes it possible to ensure optimal operating conditions for the source without any need to modify the load's operating conditions (voltage, current), which is unavoidable in the parallel or serial compensation method. In addition, because of its zero active power branches, such a four-terminal matching compensator can be implemented in the future with the use of so-called 'active filters'.

## References

- [1] Emanuel E.A., *Power components in a system with sinusoidal and nonsinusoidal voltages and/or currents*, IEE Proc. Pt. B, No. 3, 1990.
- [2] Kłosiński R., Siwczyński M., *Algorytm warunkowej minimalizacji prądu rzeczywistego źródła napięcia z okresowo zmiennymi parametrami w dziedzinie czasowej*, XV SPETO, 1992, 481–488.
- [3] Siwczyński M. Jaraczewski M., *Metody optymalizacyjne teorii mocy, przegląd zasad minimum dla obwodu jednooczkowego*, JUEE, 2002, 1/2, 5–15.
- [4] Siwczyński M. Jaraczewski M., *Zasada podobieństwa w równaniach optymalizacyjnych teorii mocy i energii – zadania łączone*, Przegląd Elektrotechniczny (Electrical Review), 87, No. 5/2011.
- [5] Siwczyński M. Kłosiński R., *Current and voltage wave-form optimization with non-linear deformations for real voltage sources*, COMPEL, The International Journal for Computation and Mathematics in Electrical and Electronic Engineering, 1997, Vol. 16, No. 2, 71–83.
- [6] Jaraczewski M., *Reaktancyjne kompensatory czwórnikowe dla przebiegów monoharmonicznych*, Przegląd Elektrotechniczny (Electrical Review), 93, No. 5/2017, 44–47.

Włodzimierz Jefimowski

wlodzimierz.jefimowski@ien.pw.edu.pl

Adam Szelaǳ

Warsaw University of Technology, Power Engineering Institute, Electric Traction  
Division

## ASSESSMENT OF AC TRACTION SUBSTATION INFLUENCE ON ENERGY QUALITY IN A SUPPLYING GRID

### OCENA ODDZIAŁYWANIA PODSTACJI TRAKCYJNEJ PRĄDU PRZEMIENNEGO NA JAKOŚĆ ENERGII ELEKTRYCZNEJ W SIECI ZASILAJĄCEJ

#### Abstract

This article presents investigations performed on a 25 kV AC system with a Scott transformer simulation model. The model includes an energy quality parameter calculation algorithm with consideration to the train timetable. The simulation results enable an analysis of the energy quality parameters at the point of connection of the traction substation to the supplying grid. The presented tool enables the simultaneous calculation of voltage unbalance and harmonic content. The article presents the results of the energy quality analysis at the substation connection point for the specific location. The simulation results of the energy quality parameters are appraised on the basis of standard EN 50160:2010. The tool may prove helpful in the process of designing electrification systems, especially in the choice of traction transformer and power electronics device mitigating an imbalance and harmonic impact.

#### Streszczenie

**Keywords:** AC electrification system, electric energy quality, simulation modelling, Scott transformer

Artykuł przedstawia badania przeprowadzone z wykorzystaniem modelu symulacyjnego systemu zasilania prądu przemiennego 25 kV 50 Hz z transformatorem Scotta, uwzględniającym wszystkie czynniki jakości energii elektrycznej przy uwzględnieniu rozkładu jazdy pociągów. Wyniki badań pozwalają na kompleksową analizę parametrów jakości energii w punkcie przyłączenia podstacji trakcyjnej do systemu elektroenergetycznego przy uwzględnieniu rozkładu jazdy pociągów oraz rodzaju taboru. W porównaniu z innymi opublikowanymi pracami przedstawione narzędzie pozwala na określenie zarówno asymetrii napięciowej jak i harmonicznego napięcia w punkcie przyłączenia podstacji trakcyjnej. Narzędzie może być przydatne w procesie projektowania układu zasilania, w szczególności doboru urządzenia symetryzującego na podstacji trakcyjnej dla danej lokalizacji tak, aby uzyskać spełnienie wymagań normatywnych.

**Słowa kluczowe:** System elektryfikacji prądu przemiennego, jakość energii elektrycznej, modelowanie symulacyjne, transformator Scotta.



## 1. Introduction

Railway electrification systems of 50 Hz AC in Europe are powered by traction substations, which cause a number of disturbances into the power system. They contribute to the deterioration of the energy quality parameters in distribution and transmission networks. In general, three factors can be mentioned that affect the energy quality in power grids supplying traction substations: negative sequence component, harmonic content and load variability. The effects of asymmetry has been thoroughly investigated by a number of researchers [1][2][3][4][5][7][13][20]. A number of solutions to reduce current asymmetry were presented. The second factor affecting the quality of energy is the high harmonic content in traction currents drawn by electric vehicles, in particular the old type of electric vehicles equipped with thyristor rectifiers [8]. The last factor is the variable power consumption and the presence of relatively high peaks of power demand [9]. In most publications, the abovementioned interfering factors and their effects are discussed separately; there are no power supply models that take all factors into account [10]. The impact of these factors depends on the number of loads and their power; therefore, on the traffic situation on railway lines supplied by traction substation. There are no publications which describe the impact of train timetables on the energy quality in the power supply network. This article describes the complete simulation model of a 25 kV AC power system with the Scott transformer, taking into account all the factors of electric energy quality with consideration to parameters of train traffic such as the train timetable. Simulation results can be used in the designing process, especially for sizing of power equipment such as Scott transformers for a given substation location.

## 2. Simulation model

The simulation model consists of two parts: the Scott transformer model and the model of the traction load of the Scott transformer. Corresponding elements are presented later in this paper.

### 2.1. Scott transformer

Figure 1 shows the general scheme of the Scott transformer. The voltages on the secondary side is equal to the module with the shift angle between them  $90^\circ$ , if voltage vectors in the primary side are symmetrical. Figure 2 presents voltage and current vector graphs of the primary and secondary side of the Scott transformer. Figure 2 shows the situation in which the secondary winding currents are not equal to the module and phase; this results in the primary currents being asymmetric. Formulas 1-3 show the relationships between the complex values of the primary currents and the secondary winding Scott transformers [14].

The load on the primary side of the Scott transformer is symmetrical if the values and phase of the secondary currents are equal. The coefficient of the current asymmetry, which is a negative sequence component on the primary side of the Scott transformer, is a function of the modules and phase angles of the secondary side currents.

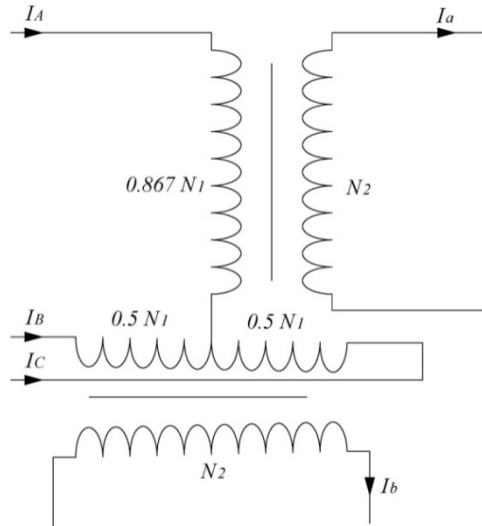


Fig. 1. A general scheme of the Scott transformer

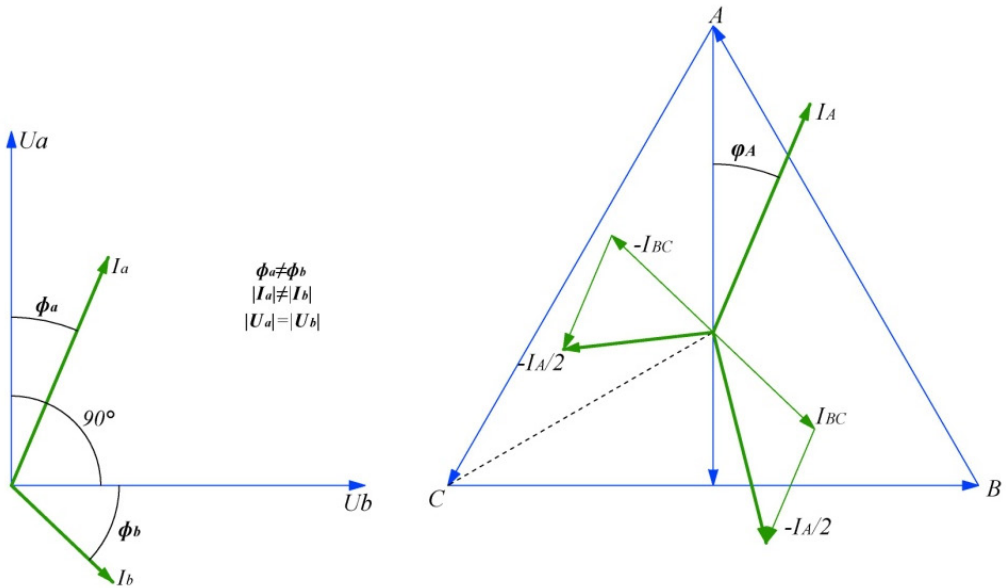


Fig. 2. Vector graphs of the voltage and currents of the Scott transformer in asymmetric load condition

$$I_A = \frac{2}{\sqrt{3}} \frac{N_2}{N_1} I_a \quad (1)$$

$$I_B = \frac{N_2}{N_1} \left( I_b - \frac{1}{\sqrt{3}} I_a \right) \quad (2)$$

$$I_B = -\frac{N_2}{N_1} \left( I_b + \frac{1}{\sqrt{3}} I_a \right) \quad (3)$$

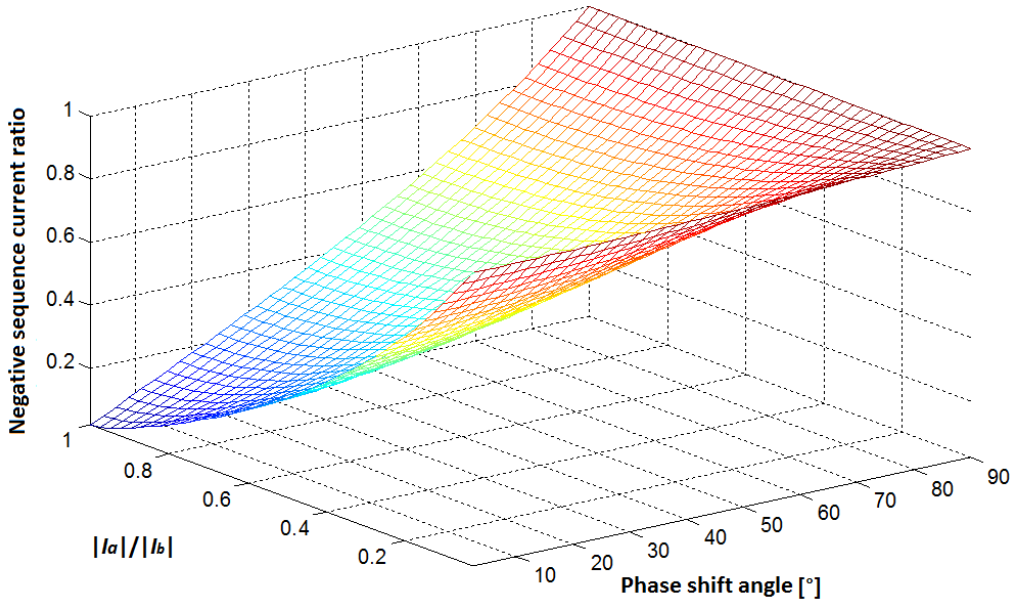


Fig. 3. Graph of the current asymmetry coefficient (negative sequence current ratio) on the primary side of the Scott transformer as a function of the current modules ratio and the difference between the current angle shifts on the secondary side [6][10]

## 2.2. Model of the traction load

The load of the Scott transformer is determined using the simulation program modelling an electrified railway line. It consists of two main elements – the train performance calculation algorithm, which determines the motion parameters of trains driving according to the given timetable, and the power flow algorithm determining the substation load. The flowchart of the whole simulation program is presented in Figure 4. The results of the train performance calculation algorithm, in particular, results relating to electrical power and the position of trains are used in the power flow algorithm at each time step of simulation. Performance of the algorithms is being repeated at every time-step of the simulation.

The acceleration  $a$  of each electric vehicle is calculated in accordance with (4).

$$a(t_i, j) = \frac{dv_j(t)}{dt} = \frac{Ft(v_j, U_j) - W(v_j)}{m(1 + \eta)} \quad (4)$$

In the algorithm, a three-phase drive cycle is modelled. The drive cycle consists of a start-up phase, a constant speed phase, and a braking phase. In a start-up mode, a maximum tractive effort available based on the traction characteristics is generated. The traction

characteristics and rolling resistance versus speed for a five-carriage electric multiple unit are presented in Fig.5. During the constant speed phase, the tractive effort is adjusted by the speed regulator model; the reference speed is given either by the speed limit for a given track or by the maximum value of the train speed.

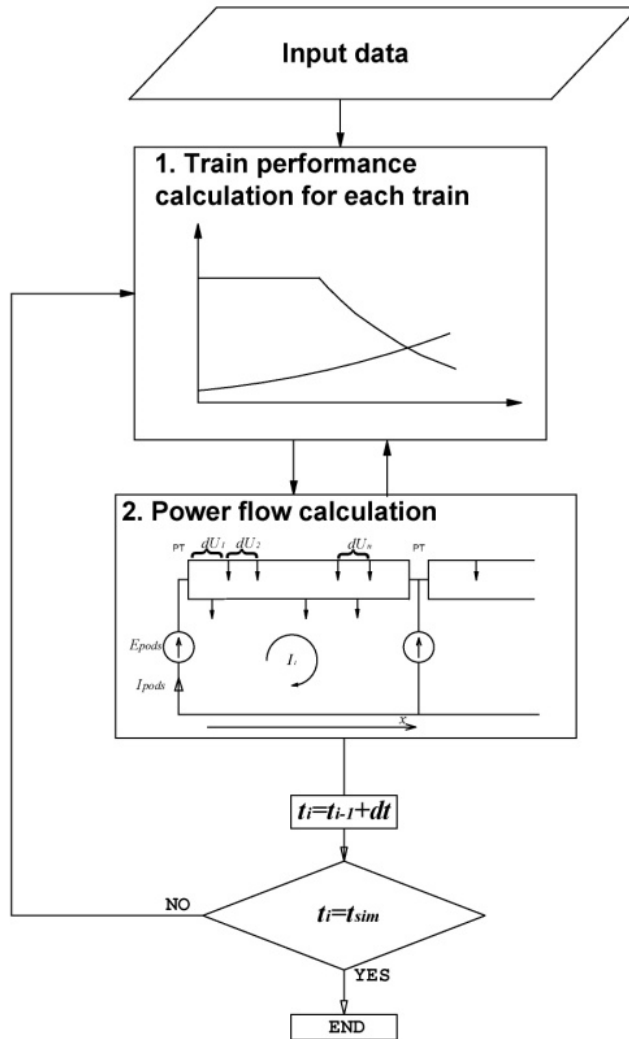


Fig. 4. General flowchart of the model of electrified railway line

A train performance calculation for each time step of simulation is carried out for all trains operating in the modelled electrified line simultaneously. The number of trains modelled is not constant throughout the simulation. Trains operate according to the timetable, where the locations and departure time values are given. In the simulation study, the constant headway time is modelled; the timetable with the headway time is presented in Figure 6.

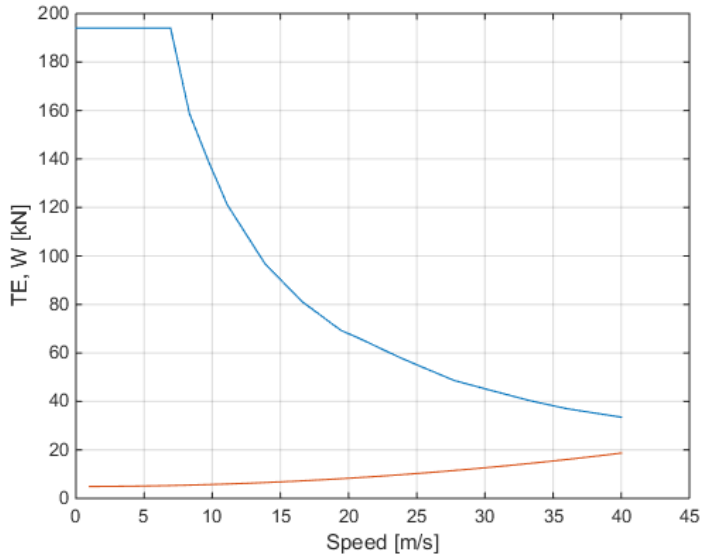


Fig. 5. Traction characteristics and rolling resistance of an electric multiple unit

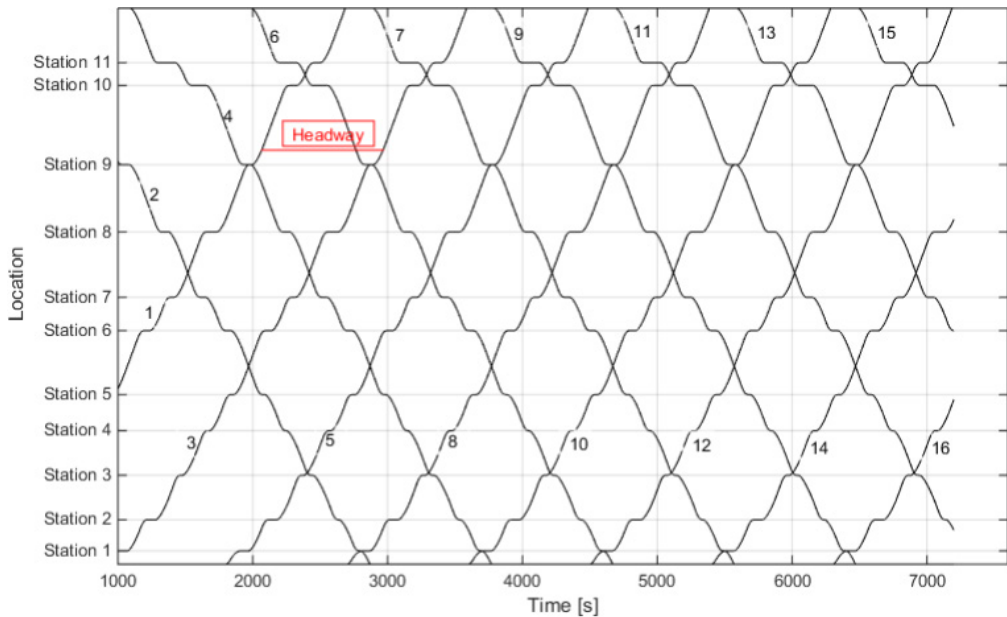


Fig. 6. The timetable modelled in the simulation study.

The power flow algorithm is based on the equivalent circuit presented in Figure 7 [19].

The power flow method is based on the mesh method of circuit analysis. The current in each mesh of the equivalent circuit can be determined based on matrix equation (5).

$$[Z][I]=[U] \quad (5)$$

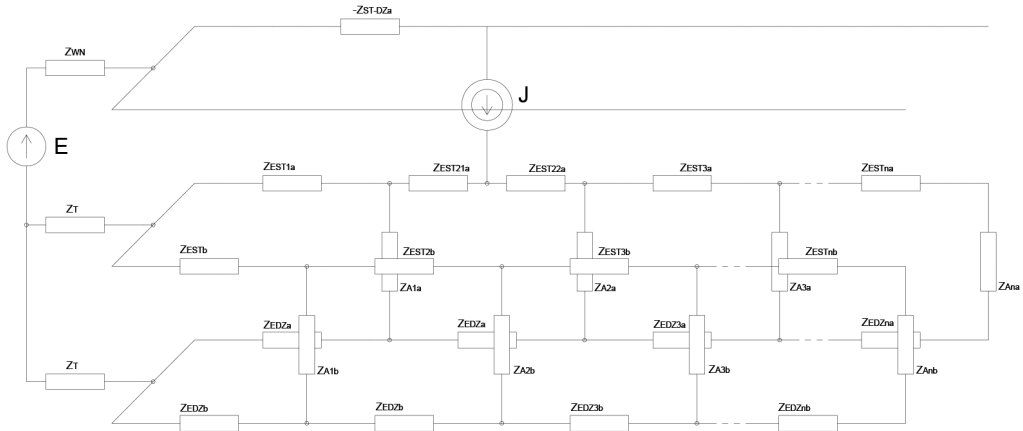


Fig. 7. Circuit model of electrified railway line in 2 x 25 kV system

At the first step, the currents are calculated according to equation (5). The resultant currents are obtained based on the superposition method (6).

$$I_k = \sum_{i=1}^n I_{ki} \quad (6)$$

The current values in each time step of the individual secondary windings of the Scott transformer, as well as the harmonic content in each time step are the final data obtained from the simulation program presented in Figure 4. It is assumed that the supply system is in steady state in each time step of simulation. In the simulation study, the central-side traction substation location is modelled – this is presented in Figure 8.

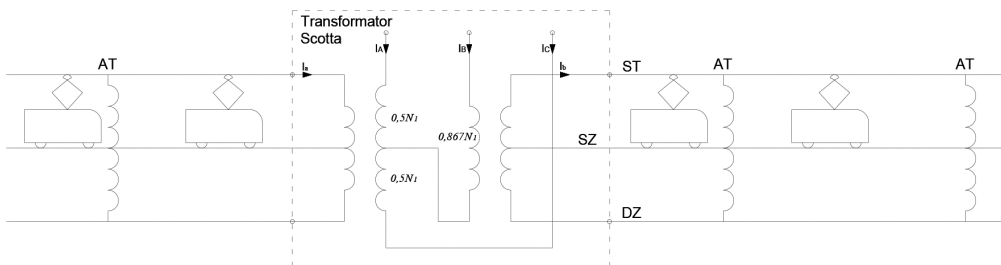


Fig. 8. Scheme of one track power supply system with a central-side traction substation with a Scott transformer

### 3. Simulation model verification

In order to verify the model, the results of computer simulation of the Scott transformer operation were compared with the results of laboratory tests presented in [10]. In [10], the tests on the physical model presented in Fig. 8 were undertaken.

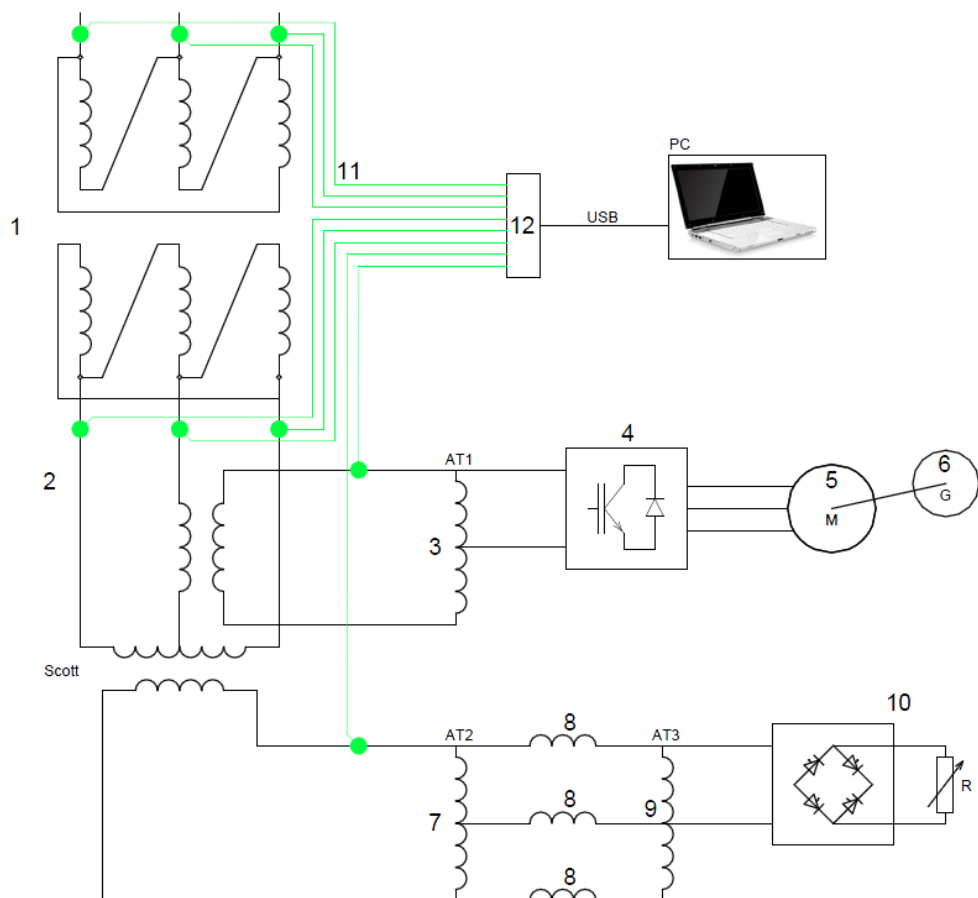


Fig. 9. Diagram of a laboratory model of a Scott transformer feeding nonlinear loads via autotransformers: 1 – step down transformer; 2 - Scott transformer; 3, 7, 9 – autotransformers; 4 – AC/DC/AC converter; 5 – three-phase induction motor; 6 – DC machine; 8 – reactance modelling overhead catenary; running rails and parallel feeder; 10 – diode rectifier and resistor

#### 4. Simulation modelling

The study analyses the influence of the rail power supply system on electric energy quality in the power system for the selected location. A 25 MVA Scott transformer was connected to a 110 kV distribution network with a short-circuit power level of 900 MVA. A number of studies of energy quality in cases of various train timetable was conducted. Different traffic patterns were modelled for different types of trains – suburban electric multiple units and freight trains. The harmonic contents drawn by different train types are different [8][15]. For electric multiple units, the harmonic contents are taken from [15], whereas for the freight trains, they are taken from [8]. The parametric analysis has been performed for different values of short-circuit power.

#### 4.1. Electric multiple units

In the study, a 50 km railway simulation model was constructed with a 25 km central-side traction substation. The assumption is that the first secondary winding of the Scott transformer feeds the section before the substation (km 0–25) and the second winding feeds the section behind the substation (km 25–50). In the positive direction, 7 stations were modelled, while in the negative direction, 11 were modelled. The operation of 10-car multiple units was modelled. The rolling stock data was updated with data provided by the manufacturers for the rolling stock. Figure 9 presents the negative sequence voltage ratio of the primary side of the Scott transformer for the different headway time of train operation. The results of the voltage harmonic content in the voltage supplying traction substation are presented in Figure 10; the time plot of each harmonic is presented.

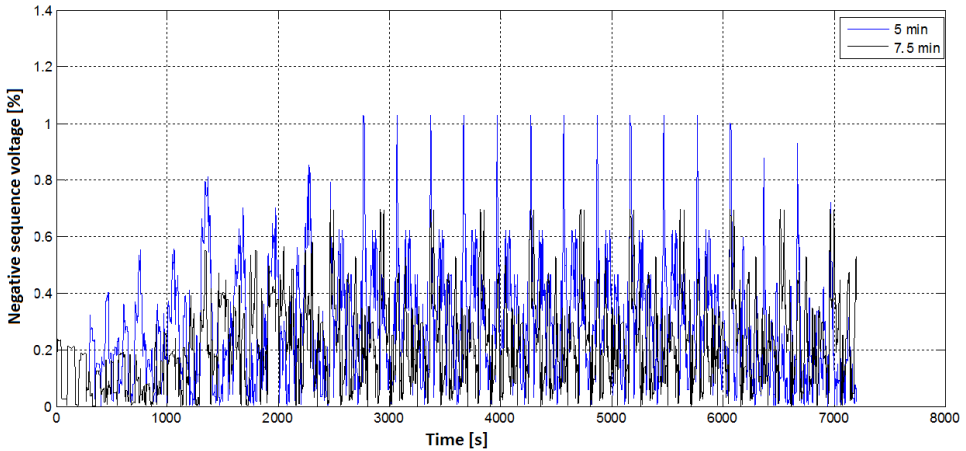


Fig. 10. Negative sequence of the primary side voltage for the different headway time of the electric multiple units operation

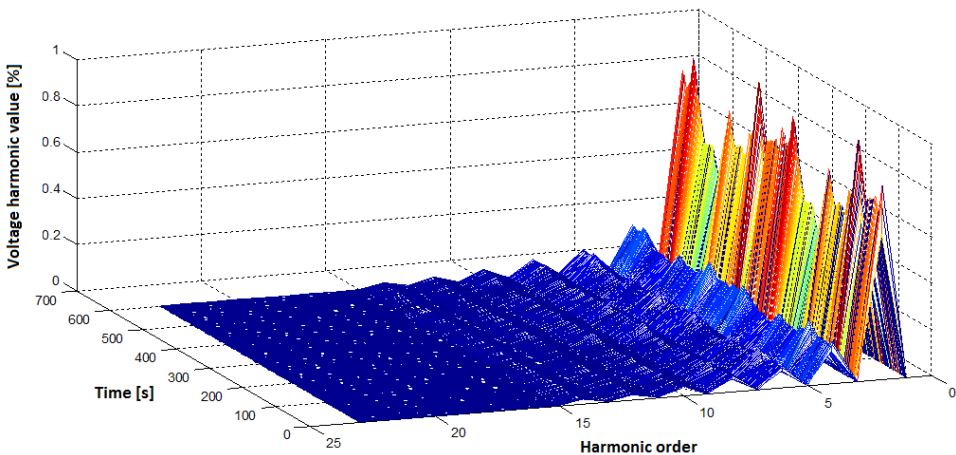


Fig. 11. Voltage harmonic content in the voltage supplying traction substation



## 4.2. Mixed train operation

This section presents the results of simulations of electric multiple units and freight train operation. The situation is modelled in which electric multiple units alternate with freight trains on the railway line. The operation for multiple units was assumed with the headway time of 20 min and the same for the freight trains. Thus, the headway time between *consecutive* trains is 10 min. An assumption of the equal average speed for each type of train was made. Freight trains do not stop on the stations. Figure 11 shows the voltage negative sequence current coefficient for short-circuit power levels of 900 and 1200 MVA. Figure 12 shows the voltage harmonics for the above presented traffic situation for the short-circuit power level of 900 MVA.

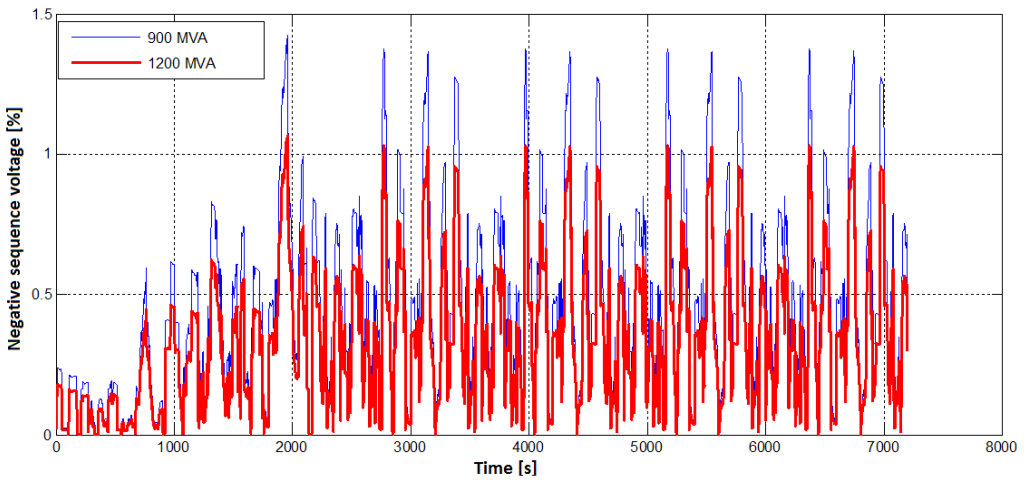


Fig. 12. Time course of the negative sequence voltage for the mixed traffic for the two different short-circuit power levels

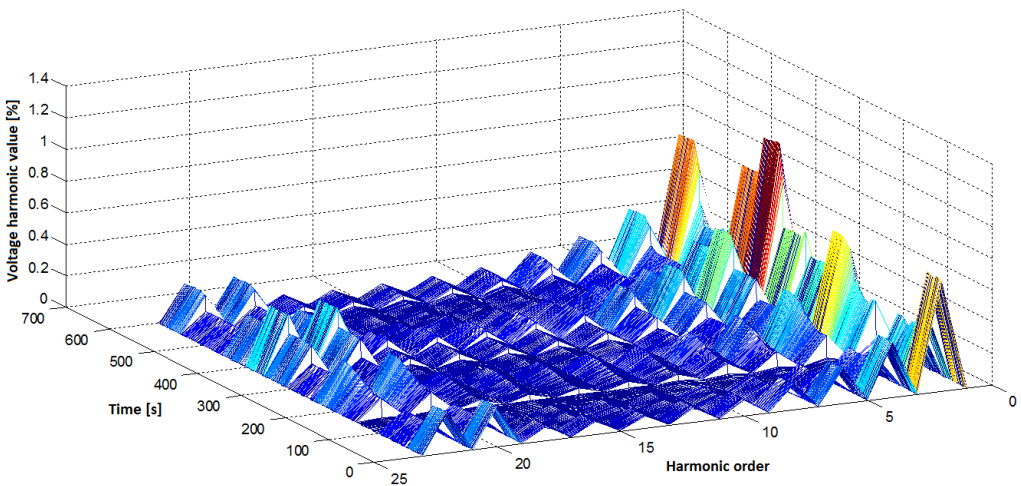


Fig. 13. Voltage harmonic content at the point of connection of the traction transformer to the supply grid

## 5. Conclusions

The results show that at a short-circuit power of the grid of the 900 MVA, the value of the negative sequence voltage in an assumed traffic scenarios does not exceed the 2% limit given in the standard [11]. According to estimates [2,3], when using typical transformers at the AC substation, the required short-circuit power should be (assuming a limit of 2%) at least 50 times the expected power of the asymmetry. Therefore, for the traction power level 25 MVA short circuit power should not be less than 1250 MVA. Thus, in the case in question, the use of the Scott transformer would allow the substation to be connected to a node with considerably lower short-circuit power. Voltage harmonics were not exceeded in any of the simulated scenarios.


The presented simulation tool and the results of the tests allow a comprehensive analysis of the parameters of the energy quality at the point of connection of the traction substation to the power system taking into account the train timetable and the type of rolling stock. Compared to other published works, the presented tool allows determination of both the voltage asymmetry and the harmonic voltage at the point of connection of the traction substation. The tool may be useful in the process of designing power supply systems, in particular, for the sizing of a power device at the traction substation for the given location.

## References

- [1] Altus J., Novak M., Otcenasova A., Pokorny M., Szelağ A., *Quality parameters of electricity supplied to electric railways*, Scientific Letters of the University of Žilina-Communications 2–3/2001.
- [2] Barnes R., Wong K.T., *Unbalance and harmonic studies for the Channel Tunnel railway system*, IEE Proc. B, vol. 138, no. 2, March 1991.
- [3] Matta V., Kumar G. *Unbalance and voltage fluctuation study on AC traction system*. Electric Power Quality and Supply Reliability Conference, 2014, pp. 303–308.
- [4] Kowalski Z., *Jakość energii elektrycznej – Monografie Politechniki Łódzkiej*, 2008.
- [5] Ogunsola A., Mariscotti A., *Electromagnetic Compatibility in Railways. Analysis and Management*, Springer 2013.
- [6] Wang H., Tian Y., Qin-chang G., *Evaluation of negative sequence current injecting into the public grid from different traction substation in electrical railways. Electricity Distribution – Part 1*, 2009. CIRED 2009. 20th International Conference and Exhibition on, vol., no., 8–11 June 2009, pp. 1–4.
- [7] Tien-Trung V., Paleček J. and Kolář V., *Influence of AC Electric Traction on Harmonic Distortion in 110 kV Supply Voltage Network: Measurement and Simulation*. Przegląd Elektrotechniczny 89 (2013).
- [8] ZupanA., TeklicA.T., Filipovic-Grcic B., *Modeling of 25 kV electric railway system for power quality studies*. EUROCON, 2013 IEEE , vol., no., 1–4 July 2013, pp. 844–849.

- [9] Takeuchi H., Goodman C., Sone S., *Peak demand reduction techniques when starting under moving block signaling*. Developments in Mass Transit Systems, 1998. International Conference on (Conf. Publ. No. 453) , vol., no., 20–23 Apr 1998, pp. 280–285.
- [10] Jefimowski W., Burak-Romanowski R., *Disturbing impact of AC railway power supply with a Scott transformer on a supplying grid – laboratory tests*. MET'2015 12th International Conference Modern Electric Transport, Trogir, October 4–7, 2015.
- [11] European standard. *EN 50160:2010 Voltage characteristics of electricity supplied by public electricity networks*. European Committee for Electrotechnical Standardization. 2010.
- [12] Kowalski Z., *Jakość energii elektrycznej*. Monografie Politechniki Łódzkiej, 2008.
- [13] Szeląg A., Patoka M., *Some aspects of impact analysis of a planned new 25kV AC railway lines system on the existing 3 kV DC railway system in a traction supply transition zone*. Power Electronics, Electrical Drives, Automation and Motion (SPEEDAM), 2014 International Symposium on. IEEE, 2014.
- [14] John J., Winders Jr., *Power Transformers Principles and Applications*. Marcel Dekker Inc. New York–Basel 2002.
- [15] Bekele H. M., *Harmonic Analysis in 25 kV AC Railway Electrification system: The case of proposed Ethiopian Railway System*. PhD thesis, Addis Ababa, August 2014.
- [16] Firpo F., Fracchia M. and Savio S., *Locomotive drive harmonic pollution in AC traction systems*. Industrial Electronics, 1993. Conference Proceedings, ISIE'93 – Budapest., IEEE International Symposium on, Budapest, Hungary, 1993, pp. 622–628
- [17] Liu S.M., Chen D.X., Li Q. L., Zhang X.D. and Yu X. P., *The Impact of 350 km/h High-Speed Railway to Grid Power Quality*, 2012 Asia-Pacific Power and Energy Engineering Conference, Shanghai, 2012, pp. 1–4.
- [18] Jefimowski W., *Koncepcja zasilania linii kolejowej dużej prędkości w systemie 2 x 25 kV*. Master of Science Thesis, Electric Traction Division, Warsaw University of Technology, 2011.
- [19] Бородулин Б.М., Векслер М.И., *Система тягового электроснабжения 2 x 25 кВ*, Москва 1989
- [20] Mandić M., Uglešić I., Milardić V., *Design and testing of 25 kV AC electric railway power supply systems*. Tehnički Vjesnik 20, 3(2013), pp. 505–509.

Tomasz Baczyński  [orcid.org/0000-0002-9732-5383](https://orcid.org/0000-0002-9732-5383)  
tomaszb@vistula.wis.pk.edu.pl

Piotr Beńko  [orcid.org/0000-0002-5752-8397](https://orcid.org/0000-0002-5752-8397)  
Chair of Environmental Technologies, Faculty of Environmental Engineering, Cracow  
University of Technology

A COMMENTARY ON THE RESPIROMETRIC EVALUATION  
OF BIODEGRADABLE COD FRACTIONS IN INDUSTRIAL WASTEWATER

---

UWAGI O RESPIROMETRYCZNYM WYZNACZANIU BIODEGRADOWALNYCH  
FRAKCJI CHZT W ŚCIEKACH PRZEMYSŁOWYCH

**Abstract**

This paper presents considerations on selected methodological aspects of respirometric COD fractionation in industrial wastewater which may differ from more common applications of such methodology for municipal wastewater. This concerns: the presence of interfering substances; problems with the elimination of nitrification; the importance of recognising biomass metabolism; differences of growth coefficient; the inclusion of non-canonical COD fractions and toxic effects. The discussion is based on a literature review and the authors' own experience. As a conclusion, a preparatory procedure is proposed to assure the correct performance of respirometric COD fractionation for industrial wastewater, especially for more complex chemical effluents.

**Keywords:** COD fractionation, industrial wastewater, respirometry

**Streszczenie**

Artykuł przedstawia rozważania na temat wybranych aspektów metodycznych respirometrycznego wyznaczenia frakcji ChZT w ściekach przemysłowych, które mogą różnić się od bardziej rozpowszechnionych zastosowań tej metody dla ścieków miejskich. Obejmuje to obecność substancji przeszkadzających, problemy z eliminacją nityfikacji, rozpoznanie metabolizmu biomasy, zróżnicowanie współczynnika wzrostu, uwzględnianie niekanonicznych frakcji ChZT i efektów toksycznych. Dyskusję oparto na przeglądzie literatury oraz własnych doświadczeniach autorów. W podsumowaniu zaproponowano przygotowaną procedurę mającą zapewnić prawidłowe wykonanie respirometrycznego wyznaczenia frakcji ChZT dla ścieków przemysłowych, zwłaszcza tych o bardziej skomplikowanym, „chemicznym” charakterze.

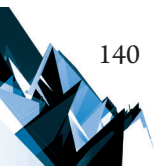
**Słowa kluczowe:** frakcjonowanie ChZT, respirometria, ścieki przemysłowe

## 1. Introduction

Traditional methods for assessing the organic contamination of wastewater such as total chemical oxygen demand (COD) or biochemical oxygen demand (BOD) measurements are not sufficient for the proper control of modern biological wastewater treatment plants (WWTPs). The advanced biological nutrients removal and the mathematical modelling of biological treatment processes require a more detailed characterisation of organic substrates. This issue is pursued as a so-called COD fractionation; this is the division of all wastewater organic contamination (expressed as COD) into fractions on the basis of their treatability and other parameters. In case of biodegradable industrial effluent, such COD fractionation is even more important than for municipal wastewater as it could help to evaluate the potential effectiveness of the removal of organic contaminants and provide other important information.

COD fractionation of municipal wastewater can be accomplished by several methods, fully described in previous literature [3, 14]. In Poland, guidelines of German ATV-131P are fairly frequently applied; these rely upon filtered and unfiltered COD measurements of influent and effluent wastewater as the basis for COD division into fractions. Such a simplified approach, and possibly other methods employing physical-chemical separation (e.g. filtration/coagulation), may work reasonably effectively for municipal effluents, which are of more or less similar characteristics. However, industrial wastewater, especially from the chemical industry, is more complex. Therefore, use of respirometric methods of COD fractionation seems more appropriate. In these methods, electron acceptor (oxygen or nitrate, depending on conditions) consumption by biomass is measured and then recalculated into the COD of the degraded substrate. Their advantage is that much more information can be gained from a test regarding the characteristics of wastewater organic contamination, specifically: biodegradability and toxicity (both of particular importance for industrial effluents), and degradation kinetics.

There are several approaches for performing respirometric tests; these have been fully discussed in literature [22]. The most reliable seem to be those which are based on the 'liquid phase, static gas' principle, with the liquid phase either static or flowing, as this enables eliminating the need for the inclusion of oxygen mass transfer (from gas to liquid phase) in calculations. Automatic instruments which can operate under such conditions are available commercially, but it is also possible to perform such a test using the following simple equipment: a closed measuring chamber (e.g. a bottle) with a dissolved oxygen (DO) sensor and mixing of the content, periodically re-filled with mixed liquor from a large continuously aerated tank in which the wastewater of interest is dosed at the start of measurements. All vessels should be placed in a water bath, maintaining a constant mixed liquor temperature, typically 20 or 25°C. The decrease of DO concentration in the measuring chamber is recalculated into the oxygen uptake rate (OUR,  $\text{mgO}_2/\text{min}\cdot\text{dm}^3$ ), and the OUR changes over time create a respirogram (sometimes termed 'a short-term BOD'). Evaluation of such an OUR profile enables the identification of degradable COD fractions and their quantification. In a simpler approach, this evaluation could be achieved by delineating areas under the



OUR curve which correspond to oxygen utilisation for the degradation of individual COD fractions, using characteristic points [3, 15]. The advanced method involves the application of simulation models such as International Water Association activated sludge models (ASMs). Non-biodegradable fractions can be estimated by assessing a biodegradable COD in a respirometric test and subtracting it from the total COD; this is done using filtered and unfiltered wastewater for evaluation of soluble and particulate inert fraction respectively [20].

Respirometric COD fractionation has long been applied for the analysis of municipal wastewater. However, such analyses with industrial discharges are sometimes very specific, and the methodology commonly used for municipal wastewater cannot be transferred directly and without thorough consideration, as that may lead to serious mistakes. In this paper, the most important methodological aspects (according to authors' experience) are addressed. These are discussed in the context of the literature review and also illustrated by examples from the authors' own research.

## 2. General remarks

The use of biomass well-adapted to tested wastewater is of even more importance than in the case of municipal effluents. Several chemicals are not degraded by non-adapted activated sludge; furthermore, the presence of toxic substances requires the prior acclimatisation of biomass. Industrial wastewater is often nutrient-deficient; thus, the supplementation of nitrogen, phosphorus and micronutrients may be necessary. Suggestions of trace element solutions and their dosage can be found in literature [26]. Another important issue to ensure appropriate conditions for respirometric testing is pH regulation to within the optimal range for used biomass.

## 3. Interfering substances

Hydrogen peroxide ( $\text{H}_2\text{O}_2$ ), present in high concentration in effluents from wood pulp and textile bleaching, and in wastewater pre-treated with this oxidant (e.g. pre-oxidation by the Fenton process), may cause problems in respirometric COD fractionation. This may concern: 1) overestimation of the total COD in analytical determination when using the dichromate method; 2) dissolved oxygen supersaturation, which could make the OUR measurements unreliable; 3) possible disturbance of biomass activity. One of the methods proposed for avoiding  $\text{H}_2\text{O}_2$  interference on analytical COD measurement is  $\text{H}_2\text{O}_2$  reduction with sodium sulfite ( $\text{Na}_2\text{SO}_3$ ; [28]). Removal of the remaining peroxide with  $\text{Na}_2\text{SO}_3$  was tested by the authors for chemo-thermo-mechanical pulping effluent from the paper industry. In such a way, a correct respirogram was obtained (Fig. 1). However, attention must be given to eliminate residual excess of  $\text{Na}_2\text{SO}_3$ ; otherwise it would cause additional oxygen demand during measurements.

Similar problems can be expected with the presence of chlorine in wastewater, disturbing DO measurements. Inorganic compounds readily oxidised by dissolved oxygen, such as sulfite and

sulfide, should also be removed before the determination of organic COD fractions. The presence of nitrite requires the use of a nitrataion (the second step of nitrification) inhibitor (see below).

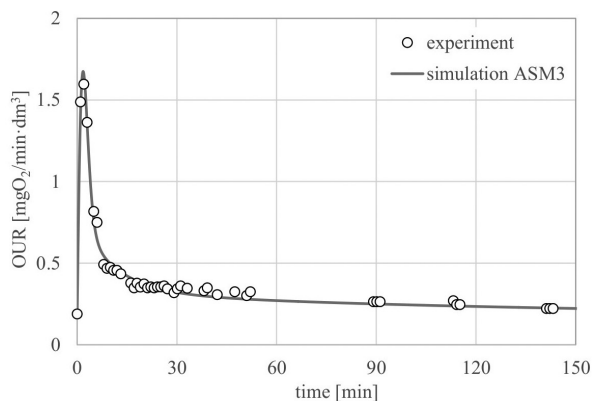


Fig. 1. Batch respirometric test with chemo-thermo-mechanical pulping wastewater after hydrogen peroxide removal: experimental results and simulation using ASM3-type model

#### 4. Inhibition of nitrification

In aerobic conditions, oxygen can be consumed not only by heterotrophic bacteria but also by nitrifying organisms present in biomass used for respiration testing. Therefore, the respirometric determination of COD fractions is possible only by fitting an elaborate simulation model covering both the oxidation of organic matter and the oxidation of nitrogen compounds to the experimental results. Such an approach is problematic as a large number of variables and coefficients may result in great estimation inaccuracy. Thus, the most common practice while performing respiration tests is to suppress nitrification using nitrification inhibitor allylthiourea (ATU) at a dose of 10–20 mg/dm<sup>3</sup>. In this way, only oxygen uptake for organic compounds degradation is to be considered.

ATU is a strong selective inhibitor of the ammonia monooxygenase enzyme, stopping the first stage of nitrification – the oxidation of ammonia to nitrite (nitrification [9]). However, it has recently been reported that the adaption of biomass to this chemical may occur, resulting in incomplete inhibition of nitrification or even ATU degradation [17, 22]. It seems likely that such adaptation can be found especially in the case of biomass from WWTPs treating industrial effluents [18]. ATU may not be effective against ammonia-oxidising archaea [16], which could also occur in activated sludge.

An alternative nitrification inhibitor occasionally used in respiration tests is nitrapyrin (2-chloro-6-(trichloromethyl)pyridine) [22, 24]. It is also recommended for use in 5-day BOD tests (e.g. Hach nitrification inhibitor formula 2533, containing 2% nitrapyrin coated on sodium sulfate). However, nitrapyrin has low water solubility (40 mg/dm<sup>3</sup>) which makes its use questionable when high or rapid dosing is required. Other alternatives to ATU can be selected from several other compounds exhibiting selective inhibiting properties towards

nitrification and used as additives to fertilizers. Examples of such substances can be found in literature [19, 30]. The efficiency of selected nitrification inhibitors should be verified by comparing biomass respiration rates before and after subsequent pulse additions of ammonia and an inhibitor (an example can be found in [9]).

In the case of nitrite presence in wastewater, the use of a selective inhibitor of first step nitrification, such as ATU, will not eliminate oxygen uptake by the oxidation of nitrogen compounds. The use of a nitrification (oxidation of nitrite to nitrate) inhibitor is then necessary. Chlorate is commonly used for this purpose at a concentration of 10–20 mM [18, 23]. However, it should be noted that this compound is not always effective [18]. Another selective inhibitor of nitrite oxidation is azide, effective in doses of 0.24  $\mu\text{M}$  [9].

## 5. Type of metabolism

Older biodegradation models (ASM1 and similar) assumed that the substrate present in wastewater was directly utilised for biomass growth. In newer models (e.g. ASM3), a different approach for substrate usage is adopted, assuming that substrate is first taken up and stored, then growth occurs at the expense of stored products. This type of metabolism is supposed to develop in biomass subjected to alternate ‘feast and famine’ phases (availability and absence of external substrate). Such conditions may occur, for example, in plants with anoxic and aerobic zones/periods with variable loading, while stable loading and aeration only may prefer ASM1 – type behaviour of biomass. More recent investigations (e.g. [10]) indicate that in reality, the utilisation of wastewater substrate by biomass is even more complex – a part is directly utilised for growth, while the other part is stored. A simulation model of such simultaneous metabolism can be found, for example, in a paper by Fan et al. 2012 [8].

Although modelling of full-scale WWTPs can be successfully achieved using ASM1 only [25], conditions of batch scale respirometric tests require the selection of the correct metabolic model to avoid considerable estimation errors. For example, the application of traditional respirometric methods of readily degradable COD fraction determination, either at a low food to microorganism ratio (F/M) [7] or at a high F/M [29] with biomass exhibiting substantial substrate storage behaviour will produce a serious underestimation of the actual concentration of this fraction. The identification of an appropriate substrate utilisation mechanism could be accomplished by running a batch respiration test with the biomass of interest and an easily biodegradable soluble reference substrate, such as sodium acetate. The existence of substrate storage can be recognised by a characteristic ‘tailing’ of the initial peak – the OUR does not drop to the endogenous value but remains above it, gradually declining (Fig. 3). By contrast, direct utilisation of substrate manifests in one-phase respirogram, where the OUR reaches an initial peak and then quickly returns to the endogenous respiration value with no apparent ‘tail’.



## 6. Growth coefficient

An issue of critical importance for proper respirometric determination of COD fractions is the correct adjustment of the heterotrophic biomass yield (growth) coefficient  $Y_H$  (mg COD biomass/mg COD degraded). This factor relates the measured amount of oxygen  $\Delta O_2$  utilised in respirometric tests to the amount of degraded COD ( $COD_{degr}$ ), according to the equation [22]:

$$COD_{degr} = \frac{\Delta O_2}{(1 - Y_H)} \quad (1)$$

Thus, even a small inaccuracy of the assumed  $Y_H$  value may result in a serious error of COD estimation. For example, replacement of the actual value of 0.60 by 0.67 (which is the default value in the ASM1 model for domestic wastewater) will cause a 21% overestimation of biodegradable COD fractions.

Considering domestic wastewater from different settlements,  $Y_H$  remains fairly constant. Orhon et al. [20] quoted experimentally determined values in the range of 0.62–0.67, which is close to the default values of ASM1 (0.67) and ASM2 (0.63). However, in the case of industrial effluents,  $Y_H$  is much more variable. The range of experimental values reported by Orhon et al. [20] is 0.55–0.69. The authors' own experiments with specific chemical industry wastewater indicated a value of ~0.58.

All the abovementioned evidence points to the necessity for the experimental determination of  $Y_H$ , especially in the case of more complex wastewater. A typical procedure of such estimation involves running a respiration test with the addition of the wastewater of interest, and with periodical measurements of soluble COD. A removal of soluble COD is compared to corresponding total oxygen consumption reduced by oxygen utilized for endogenous respiration by biomass at the same time (example of such determination could be found e.g. at [24]).  $Y_H$  can then be calculated through transformation of Equation (1). However, attention must be paid to two issues. Firstly, the added wastewater of interest has to be filtered/coagulated etc. so that it contains only soluble substrates; otherwise, oxygen consumption would also include the degradation of particulate substrate, which would be not accounted for in soluble COD measurements and would result in the underestimation of  $Y_H$ . Secondly, in the case of substrate storage metabolism (such as in ASM3), instead of the direct assimilation of readily biodegradable substrate (such as in ASM1), the removal of soluble COD precedes its utilisation for growth. The automatic application of the abovementioned procedure of  $Y_H$  determination would then lead to overestimation of its value.

If biomass exhibit considerable substrate storage behaviour, a method proposed by Karahan-Gül et al. [15] for the determination of the storage yield of  $Y_{STO}$  [mg COD substrate stored/mg COD substrate removed] should be applied. With this method, oxygen utilisation corresponding to the area of initial respirogram peak limited by a line linking the starting endogenous respiration point with the turning point between peak's descending slope and its 'tail' is compared to a soluble COD decrease, using transformed Equation (1). Next, the yield coefficient for growth on the stored substrate  $Y_H$  can be derived from simulation of

a whole test. Alternatively, this coefficient could be roughly estimated with results from a long respirometric test with low F/M conditions, continued until the OUR is close to endogenous respiration, using the Equation (2):

$$Y_H = \frac{1 - \frac{\Delta O_{2,tot}}{COD_{degr,tot}}}{Y_{STO}} \quad (2)$$

where  $\Delta O_{2,tot}$  is the total oxygen consumption reduced by oxygen utilization for endogenous respiration and  $COD_{degr,tot}$  is the total soluble COD removal. This relationship is simplified as it does not include oxygen utilisation for the oxidation of the stored substrate ('respiration' of storage products in ASM3). It should be noted, however, that this respiration in a batch test with a low F/M ratio is low compared to the oxygen uptake for storage and growth; thus, the estimation error of  $Y_H$  is small.

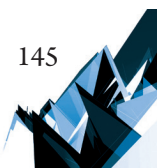
## 7. Non-canonical COD fractionation

With regard to municipal wastewater, four COD fractions are usually distinguished: soluble easily biodegradable  $S_s$ ; soluble inert (non-degraded)  $S_i$ ; particulate slowly biodegradable (hydrolysable)  $X_s$ ; and particulate inert  $X_i$ . Together, these comprise the total COD of wastewater, which should be equal to COD estimated by a chemical method. In the case of industrial effluents, such division may not be sufficient to describe the degradation kinetics of organic substrates; this requires the accommodation of additional fractions. Their biodegradation may proceed simultaneously (as in ASM models) or sequentially, i.e. degradation of the second fraction takes place after the first fraction is exhausted. The modelling of the latter case can be achieved through the inclusion of a 'switch' function in the degradation/growth rate equation for the second fraction (e.g. in [6]):

$$\frac{K_{S1}}{K_{S1} + S_{S1}} \quad (3)$$

where  $K_{S1}$  is a saturation constant for the first fraction and  $S_{S1}$  is the first fraction concentration. Such a situation may take place when the generation and accumulation of an intermediate product occur with its subsequent utilisation for growth [13]. Babu and Varghese [2] reported that in the mixture of cyclohexanone and cyclohexanol, degradation of the second compounds only started when about 90% of cyclohexanone had been exhausted, while both chemicals were degraded without delay when added separately.

Cokgor et al. [6] described a case of chemical wastewater (mainly from personal care and pharmaceutical production) with three separate sequentially used readily biodegradable fractions and an additional slowly biodegradable (hydrolysable) fraction. Helle and Duff [11] identified two to five readily biodegradable fractions of different biodegradation rates in bleached Kraft mill (wood pulping) effluent, all of which were degraded simultaneously. Similar conclusions were drawn by the author for another stream of paper industry



wastewater [4]. Industrial wastewater composed of three readily biodegradable fractions, all of them simultaneously degraded, was also described by Coen et al. [5]. Orhon et al. [20] also recommended adopting a dual hydrolysis model for industrial wastewater with high concentration of slowly biodegradable substrate, assuming the existence of a rapidly hydrolysable fraction (soluble) and slowly hydrolysable fraction (particulate).

The initial recognition of COD fractionation in wastewater can be achieved by analysing a batch respirogram curve. Peaks or plateaus followed by rapid drops of the OUR indicate the presence of readily degradable fractions; gradual declines denote hydrolysable substrates. A more precise choice of COD fractions division could be accomplished by the fitting of a customised model to experimental data using specialised simulation programs, e.g. AQUASIM [1]; this is free software allowing users to develop their own models and calibrate them on the basis of experimental data. Typically, such models are simplified to cover only activity of heterotrophic organisms: their growth, endogenous respiration, storage (if needed) and hydrolysis of substrate. Figure 2 presents an example of a respirogram obtained for paper industry wastewater. Its shape suggests the existence of at least two readily biodegradable fractions, used simultaneously, and at least one rapidly hydrolysable fraction. This was simulated using ASM3-type model, assuming substrate storage.

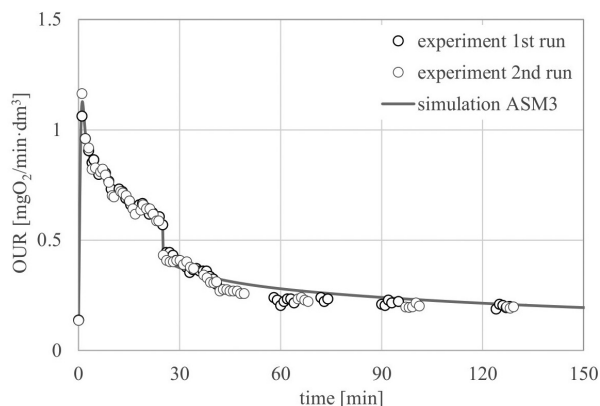


Fig. 2. Batch respirometric test with paper industry wastewater stream: experimental results (two runs) and simulation using an ASM3-type model with two readily degradable fractions

## 8. Toxic effects

An additional quality of respirometric measurements is the possibility for the assessment of inhibitory or toxic effects of substances that could be present in industrial wastewater. Traditionally, for non-biodegradable toxicants, such test is done by comparison of maximal exogenous (after deduction of endogenous respiration) OUR obtained with an easily degradable reference substrate (e.g. acetate) dosed together with different concentrations of tested chemical. However, the factor affecting toxic response can be not only the size of the toxicant dose but also the time of contact between the biomass and the tested compound.

Spanjers and Vanrolleghem [22] reported three types of contact time-dependent behaviour: a constant effect; an increasing (stronger) effect; a decreasing effect (adaptation of biomass). According to these authors, sometimes even a stimulation could be noted, that is, OUR can be higher with toxicant than without it. Running such a toxicity test with a mixed model substrate containing both COD and ammonia nitrogen may allow the simultaneous determination of toxic effects against heterotrophic and nitrifying microorganisms.

More information about toxic effects on different processes of biomass metabolisms can be obtained through the evaluation of a whole OUR profile of a respiration test and fitting an appropriate simulation model [12]. This also refers to biodegradable toxicants, where a self-inhibition of biodegradation (substrate inhibition) may occur. This manifests in a slow exponential increase of OUR in an initial phase of a test. A typical example of such a substance is phenol. Commonly, such a phenomenon is simulated using Haldane-type biodegradation kinetics; examples of such applications can be found in [6] and [21].

An initial gradual increase of OUR can also be observed in tests without toxic substances. In such cases, it should be ascribed to transient phenomena associated with sudden changes of substrate concentration, such as the activation of enzymes, substrate diffusion into biomass flocs, dynamics of dissolved oxygen measurements, etc. [27]. These authors [27] proposed the following formula to include this response in simulation models:

$$\mu_{obs} = \left(1 - e^{-\frac{t}{\tau}}\right) \cdot \mu \quad (4)$$

where  $\mu$  is the maximum growth rate of microorganisms in given conditions,  $\mu_{obs}$  is the actual (observed) growth rate,  $t$  is time and  $\tau$  is the time constant. Figure 3 presents a respirogram obtained for a caprolactam (cyclic amide of 6-aminohexanoic acid) degradation test with an attempt to fit a ASM3-like degradation model, including both Haldane degradation inhibition kinetics and the transient response formula, which gave the closest fit compared to the individual application of these equations.

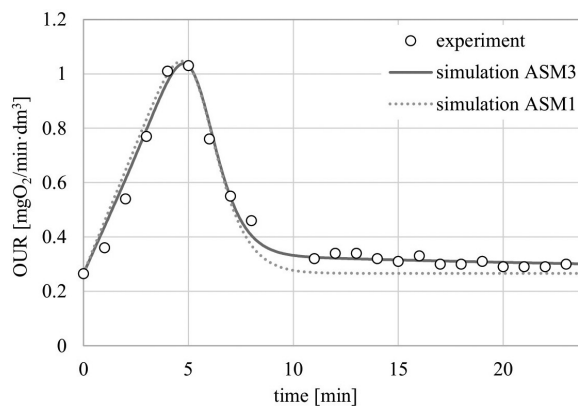


Fig. 3. Batch respirometric test with caprolactam: experimental results and ASM3- and ASM1-type simulations including Haldane inhibition kinetics and transient response formula

## 9. Conclusions

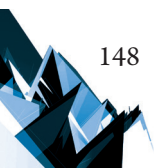
On the basis of the above considerations, a preliminary procedure can be proposed as a prerequisite for the correct evaluation of COD fractions in industrial wastewater. This procedure is as follows:

- ▶ used biomass must be well-adapted for investigated chemicals/wastewater streams;
- ▶ wastewater should be checked with regard to potentially interfering substances such as oxidising and reducing agents (e.g. peroxide, chloride, sulfite, sulfide) and nitrite;
- ▶ the effectiveness of nitrification inhibitors should be verified for used biomass; if nitrite is present in the tested wastewater inhibitors of nitrification should be checked as well;
- ▶ the type of metabolism should be identified for used biomass, using a reference substrate (e.g. acetate): if substrate is utilised directly (as in ASM1 model) or if it is stored (as assumed in ASM3);
- ▶ the growth coefficient(s) should be estimated for the chemicals/wastewater of interest.

After applying the above procedure, proper tests can be run, maintaining optimum pH and providing adequate nutrients and micronutrients. COD fractions identification and quantification should preferably be performed by fitting simulation models. This, however, should be done in a flexible manner – it might be necessary to customise the model by changing the canonical form of ASMs in terms of COD fractions division and/or biodegradation kinetics.

## References

- [1] AQUASIM, <http://www.eawag.ch/en/department/siam/software/> (access: 07.06.2018).
- [2] Babu G., Varghese W., *Biodegradation of cyclohexanone and cyclohexanol by the activated sludge process*, Journal of Scientific & Industrial Research, Vol. 58/1999, 864–868.
- [3] Baczyński T., *Przegląd metod służących wyznaczaniu frakcji ChZT w ściekach*, “Gaz, Woda i Technika Sanitarna”, Vol. 84 (10)/2010, 29–35.
- [4] Baczynski T., Kulakowski P., *Biodegradable fractions in paper industry wastewater*, [In:] *IWA Specialized Conference on Nutrient Management in Wastewater Treatment Processes and Recycle Streams*, LEMTECH Consulting, Krakow 2005, 1345–1349.
- [5] Coen F., Petersen B., Vanrolleghem P., Vanderhaegen B., Henze M., *Model-based characterisation of hydraulic, kinetic and influent properties of an industrial WWTP*, “Water Science and Technology”, Vol. 37 (12)/1998, 317–326.
- [6] Cokgor E.U., Insel G., Aydin E., Orhon D., *Respirometric evaluation of a mixture of organic chemicals with different biodegradation kinetics*, “Journal of hazardous materials”, Vol. 161 (1)/2009, 35–41.
- [7] Ekama G.A., Dold P.L., Marais G.V., *Procedures for determining influent COD fractions and the maximum specific growth rate of heterotrophs in activated sludge systems*, “Water Science and Technology”, Vol. 18 (6)/1986, 91–114.



- [8] Fan J., Vanrolleghem P.A., Lu S., Qiu Z., *Modification of the kinetics for modeling substrate storage and biomass growth mechanism in activated sludge system under aerobic condition*, "Chemical engineering science", Vol. 78/2012, 75–81.
- [9] Ginestet P., Audic J.M., Urbain V., Block J.C., *Estimation of nitrifying bacterial activities by measuring oxygen uptake in the presence of the metabolic inhibitors allylthiourea and azide*, "Applied and Environmental Microbiology", Vol. 64 (6)/1998, 2266–2268.
- [10] Guisasaola A., Sin G., Baeza J.A., Carrera J., Vanrolleghem P.A., *Limitations of ASM1 and ASM3: a comparison based on batch oxygen uptake rate profiles from different full-scale wastewater treatment plants*, "Water Science and Technology", Vol. 51 (10–11)/2005, 69–77.
- [11] Helle S.S., Duff S.J., *Multi-component kinetics of activated sludge treatment of bleached kraft mill effluent*, "Water Science and Technology", Vol. 50 (3)/2004, 11–20.
- [12] Insel G., Karahan O., Özdemir S., Pala L., Katipoğlu T., Cokgör E.U., Orhon D., *Unified basis for the respirometric evaluation of inhibition for activated sludge*, "Journal of Environmental Science and Health Part A", Vol. 41 (9)/2006, 1763–1780.
- [13] Insel G., Celikyilmaz G., Ucisik-Akkaya E., Yesiladali K., Cakar Z.P., Tamerler C., Orhon D., *Respirometric evaluation and modeling of glucose utilization by Escherichia coli under aerobic and mesophilic cultivation conditions*, "Biotechnology and bioengineering", Vol. 96 (1)/2007, 94–105.
- [14] Jaromin K. M., Szaja A., Łagód G. *Charakterystyka ścieków komunalnych określana na podstawie udziału frakcji ChZT*, [In:] *Polska Inżynieria Środowiska. Prace. Tom I*, eds. M. R. Dudzińska, A. Pawłowski, Komitet Inżynierii Środowiska PAN, Lublin 2012, 115–130.
- [15] Karahan-Gül Ö., Artan N., Orhon D., Henze M., Van Loosdrecht M.C., *Respirometric assessment of storage yield for different substrates*, "Water Science and Technology", Vol. 46 (1–2)/2002, 345–352.
- [16] Lehtovirta-Morley L.E., Verhamme D.T., Nicol G.W., Prosser J.I., *Effect of nitrification inhibitors on the growth and activity of Nitrosotalea devanattera in culture and soil*, "Soil Biology and Biochemistry", Vol 62/2013, 129–133.
- [17] Marx C., Ahnert M., Krebs P., Kühn V., *The adaptation of nitrifying microorganisms to inhibiting substances at meso- and psychrophilic temperature conditions*, "Water Science and Technology", Vol. 68 (1)/2013, 83–90.
- [18] Nowak O., Schweighofer P., Svardal K., *Nitrification inhibition—a method for the estimation of actual maximum autotrophic growth rates in activated sludge systems*, "Water Science and Technology", Vol. 30 (1)/1994, 9–19.
- [19] Nelson D.W., Huber D., *Nitrification inhibitors for corn production*, [corn.agronomy.wisc.edu/Management/pdfs/NCH55.pdf](http://corn.agronomy.wisc.edu/Management/pdfs/NCH55.pdf) (access: 07.06.2018).
- [20] Orhon D., Babuna F.G., Karahan O., *Industrial wastewater treatment by activated sludge*, IWA Publishing, London 2009.
- [21] Rezouga F., Hamdi M., Sperandio M., *Variability of kinetic parameters due to biomass acclimation: case of para-nitrophenol biodegradation*, "Bioresource Technology", Vol. 100 (21)/2009, 5021–5029.



- [22] Spanjers H., Vanrolleghem P.A., *Respirometry*, [In:] *Experimental methods in wastewater treatment*, eds. van Loosdrecht M.C., Nielsen P.H., Lopez-Vazquez C.M., Brdjanovic D., IWA publishing, London 2016.
- [23] Surmacz-Gorska J., Gernaey K., Demuyne C., Vanrolleghem P., Verstraete W., *Nitrification monitoring in activated sludge by oxygen uptake rate (OUR) measurements*, "Water Research", Vol. 30 (5)/1996, 1228–1236.
- [24] Tünay O., Zengin G.E., Kabdaşlı I., Karahan Ö., *Performance of magnesium ammonium phosphate precipitation and its effect on biological treatability of leather tanning industry wastewaters*, "Journal of Environmental Science and Health, Part A", Vol. 39 (7)/2004, 1891–1902.
- [25] Van Loosdrecht M.C., Lopez-Vazquez C.M., Meijer S.C., Hooijmans C.M., Brdjanovic D., *Twenty-five years of ASM1: past, present and future of wastewater treatment modelling*, "Journal of Hydroinformatics", Vol. 17 (5)/2015, 697–718.
- [26] Van Loosdrecht M.C., Nielsen P.H., Lopez-Vazquez C.M., Brdjanovic D., *Experimental methods in wastewater treatment*, IWA publishing, London 2016.
- [27] Vanrolleghem P.A., Sin G., Gernaey K.V., *Transient response of aerobic and anoxic activated sludge activities to sudden substrate concentration changes*, "Biotechnology and Bioengineering", Vol. 86 (3)/2004, 277–290.
- [28] Wang Y., Li W., Irini A., *A novel and quick method to avoid H<sub>2</sub>O<sub>2</sub> interference on COD measurement in Fenton system by Na<sub>2</sub>SO<sub>3</sub> reduction and O<sub>2</sub> oxidation*, "Water Science and Technology", Vol. 68 (7)/2013, 1529–1535.
- [29] Wentzel M.C., Mbewe A., Ekama G.A., *Batch test for measurement of readily biodegradable COD and active organism concentrations in municipal waste waters*, "WATER SA-PRETORIA", Vol. 21/1995, 117–124.
- [30] Wissemeier A.H., Linzmeier W., Gutser R., Weigelt W., Schmidhalter U., *The new nitrification inhibitor DMPP (ENTECC®) – Comparisons with DCD in model studies and field applications*, [In:] *Plant Nutrition*, eds. Horst H.J. et al., Springer, Dordrecht 2001, 702–703.

Andrzej Bąkowski  
Leszek Radziszewski  
Paweł Świetlik  
pswietlik@tu.kielce.pl

Kielce University of Technology, Faculty of Mechatronics and Mechanical Engineering

Milan Žmindak  
University of Žilina

ANALYSIS OF INFORMATION CONTENT OF IN-CYLINDER PRESSURE  
SIGNAL DEVIATIONS FROM THE MEAN VALUES

---

ANALIZA ZAWARTOŚCI INFORMACYJNEJ SYGNAŁU ODCHYLEK CIŚNIENIA  
OD ICH WARTOŚCI ŚREDNICH W CYLINDRZE SILNIKA

**Abstract**

This paper analyses the option of using pressure signal new descriptors for controlling a selected object. Pressure signal deviations from the pressure mean values were selected to be the example descriptors. Diesel fuelled with mineral- and bio-fuels was chosen to be the reference object. The in-cylinder pressure signal ( $p_c$ ) was recorded during the combustion process.

**Keywords:** signal descriptors, diesel, control, combustion, biofuel

**Streszczenie**

W pracy przeanalizowano możliwość wykorzystania nowych deskryptorów sygnału ciśnienia do sterowania wybranym obiektem. Odchylenia wartości sygnału ciśnienia od ich wartości średnich zostały wybrane jako przykładowy deskryptor. Jako obiekt referencyjny wybrano silnik Diesla zasilany olejem napędowym lub biopaliwami. Sygnał ciśnienia w cylindrze ( $p_c$ ) rejestrowano podczas procesu spalania.

**Słowa kluczowe:** deskryptory sygnałów, silnik Diesla, sterowanie, spalanie, biopaliwa



## 1. Introduction

An in-cylinder pressure signal can be used to control the fuelling process of combustion engine cylinders [3]. The purpose of this system is to optimise combustion in each cylinder in terms of performance, fuel consumption and emissions [5]. The pressure signal values are used to determine the descriptors directly involved in the control process, such as the mean indicated pressure, maximum pressure, or the crank angle for which half dose of fuel has been burnt. To calculate the values of these parameters with appropriate uncertainty, complicated algorithms and thermodynamic models have to be developed, along with the use of high processing power microcontrollers. Hence, the need to look for easy and fast methods of computing combustion process descriptors: the start of combustion angle or the angle corresponding to the maximum heat release rate. Some of the combustion parameters can be evaluated based on the mean value and the standard deviation of the measured in-cylinder pressure [6]. These estimates are easy to calculate, but are useful only when the values of the parameters are Gaussian distributed. The review of the literature [1] shows that the signal of pressure deviations from the mean is also easy to determine and that it can have a significant informational load. This is what the authors of this paper decided to investigate. The researchers in [2] proposed a new method of determining characteristic points of the diesel operation, based on signal deviations from their mean values and presented the results of preliminary investigations. This paper analyses the potential for the application of this method to various operating conditions of an engine powered with mineral fuel and biofuel. Calculations of the measurement results were performed using the R statistical package.

## 2. Experimental facilities and same test results

The experimental study was carried out on a three-cylinder diesel Perkins AD3.152 UR [4]. The measuring system consists of four measurement chains: in-cylinder-, in-injection pipe-pressure, injector needle lift and the crankshaft angle. Pressure was measured by quartz piezoelectric transducers and injector needle lift was measured by an inductive displacement sensor. The in-cylinder pressure was measured using a piezoelectric sensor AVL QC34D mounted directly in the cylinder head and cooled with a water. Piezoelectric properties of materials decline along with the rising temperature. A rapid decrease in piezoelectric properties of quartz is observed at a temperature of 523 K while at 846 K the piezoelectric properties disappear. Cooling with a liquid prevents the transducer from overheating, reduces thermal drift, and enables installation of the transducer directly in the combustion chamber. It is important that the cooling system of the engine provide a constant temperature, and the pulse-free flow of the coolant. Very high temperatures of the combustion process impose high thermal loads on pressure sensors. When the cooling system operates properly, the temperatures in the front zone reach 373 K and the temperatures of the measuring element are about 20 K higher than that of the liquid [7]. Large variations in pressure and temperature values cause the sensor sensitivity to change up to 1%. The pressure in the injection pipe

near the injector was measured using a piezoelectric sensor CL31 ZEPWN Marki, which prevented the need to cool it with water to minimize the effects of thermal shock. Table 1 summarizes the parameters of the piezoelectric transducers used for pressure measurements.

Table 1. Specification of the piezoelectric transducers used in the study

Parameter	Transducer AVL QC34D	Transducer CL31 ZEPWN Marki
Measurement range	0÷25 MPa	0÷100 MPa
Sensitivity	190 pC/Mpa	126 pC/MPa
Non-linearity	≤ 0.2%	≤ 0.5%
Overload capacity	20%	10%
Resonant frequency	69 kHz	50 kHz
Eigencapacity	10 pF	8 pF
Working temperature	293÷353 K	253÷323 K

Analysis of the data from Table 1 indicates that both transducers vary primarily in sensitivity, non-linearity and resonant frequency. In pressure measurements, the CL111 ZEPWN Marki charge amplifier was also used. Analog voltage signals from the amplifiers were converted into digital values using a 12-bit analog-to-digital converter KPCI-3110 manufactured by Keithley Instruments Inc. In each experiment, the values of the parameters measured were recorded as a function of the crank angle, with a resolution of 1.4°, which gave 512 measurement points for one working cycle of the engine. This was possible owing to the PFI60 shaft rotation-to-impulse converter produced by INTROL included in the measurement system, and the unit for sensing and synchronizing the crankshaft position, manufactured by ZEPWN Marki. The values obtained from fifty full working cycles were recorded for all the working conditions [4].

The scope of the tests covered the work of the engine under full- and part- load condition for loads from 4 to 20 kW, at speeds from  $n = 1000$  to 2000 rpm. In both cases the engine was fuelled with diesel or biofuel FAME (methyl esters of fatty acids). Examples of pressure trace recorded during the measurements were presented in [2]. From the results of the  $p_c$  signal analysis conducted using the fast Fourier transform (FFT) is evident that the 13.3 Hz component is dominant, which results from the cyclic manner of the engine operation at the crankshaft speed of 1600 rpm. The analysis shows the component of a frequency of about 50 Hz and low amplitude which is not related to the processes taking place in the combustion chamber. The value of frequency of this component suggests interference coming from the electromagnetic field. A similar component was noticed for all the loads in the engine operating at 1600 rpm.

To see whether the analysed signal includes the components of other frequencies and low amplitudes, the authors deprived the signal of constant components related to particular crank angles. The resultant signal is represented by the deviations of  $p_c$  from the mean values, determined according to equation (1). Considering the location of maximum values of  $p_c$

relative to the crank angle, and the fact that the registered signal is related to the process cycles, this signal can be regarded as close to the periodic signal with period  $T = 120/n$ . Based on the investigations [1], this signal can also be regarded as stationary due to the mean value and standard deviation. Verification of the agreement between the maximum  $p_c$  values distribution and the normal distribution indicated that for all cases, no grounds were found to reject the null hypothesis (the investigated variable is normally distributed) at the 5% level of significance. Since signal  $p_c$  can be regarded as close to the periodic signal, it can be represented in the form of a matrix with dimensions  $[i j] = [512 50]$ , where the columns show pressure values for consecutive working cycles, and the rows show the values related to the crank angles for which  $p_c$  was recorded. Deviations of  $p_c$  from their mean values can be calculated from [2]

$$\Delta p_c(i, j) = p_c(i, j) - \bar{p}_c(i) \tag{1}$$

where index  $i$  can take values from  $i = 1$  to  $I = 512$ . The mean pressure values related to this  $i$ -th crank angle can be calculated using the following algorithm

$$\bar{p}_c(i, j) = p_c(i, j) - \bar{p}_c(i) \tag{2}$$

The deviations determined using equation (1) can be represented in the form of vector  $\Delta p_c(k)$ , in which they are arranged chronologically, where index  $k = 512 \cdot (j - 1) + i$ . Figure 1 shows the plot of consecutive deviation values computed in this way for the engine working under load conditions.

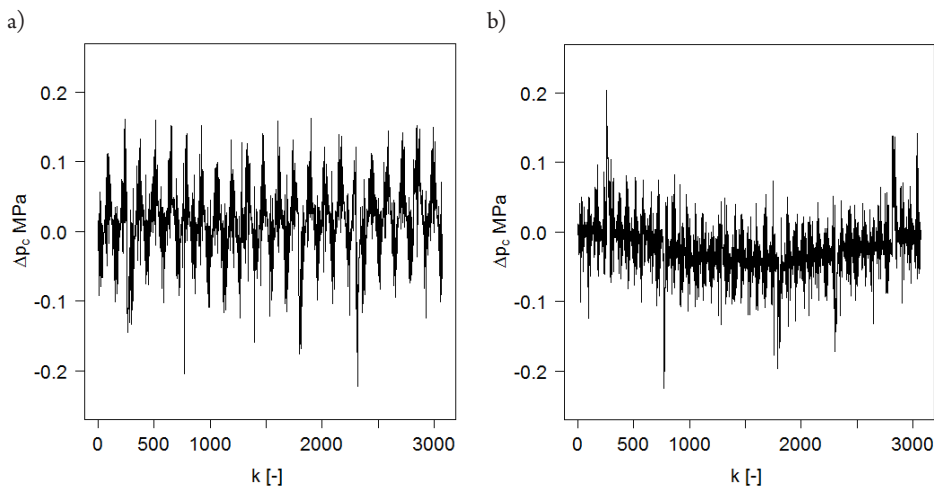


Fig. 1. In-cylinder pressure deviations from the mean values for the engine working under part- load conditions at a speed of 1600 rpm and load  $N_e = 20$  kW: a) diesel-powered engine, b) FAME – powered engine – for the first six measurement cycles

The results from the FFT analysis of pressure deviations from their mean values. confirms the presence of the disturbing component with the frequency of about 50 Hz [2]. For further calculations, the original signal was filtrated and the component with the frequency of about 50 Hz was removed. The filtered signals were used in all further calculations.

### 3. The descriptors of the in-cylinder pressure signal

Determining the location of the points that characterize the  $p_c$  changes in real time can be useful for the engine working cycle control. The authors decided to calculate the start of combustion angles  $\alpha_{ps}$  and the angles for which heat release rate reaches the maximum  $\alpha_{\dot{Q}_{\max}}$  using the  $\Delta p_c(i, j)$  signal. For this purpose, the squared deviations ( $\Delta p_c^2$ ) were determined for individual crank angles. Analysis of the results in the spatial distribution leads to the conclusion that the highest values of the module occur in the angular interval for which the combustion takes place. To calculate the sought values of  $\alpha_p$  and  $\alpha_{\dot{Q}_{\max}}$  the authors determined the sum of the squared deviations  $\sum \Delta p_c^2$  for the particular crank angles. Figure 2 shows the plot of this signal. The analysis of this plot leads to the assumption that it can be used for determining the start of combustion angles ( $\alpha_p$ ) and the angles for which the heat release rate reaches the maximum ( $\alpha_{\dot{Q}_{\max}}$ ). The authors of this paper claim that the position of the maximum value of signal  $\sum \Delta p_c^2$  (Fig. 2) corresponds to angle  $\alpha_{\dot{Q}_{\max}}$ , while the angle from which a rapid increase of  $\sum \Delta p_c^2$  starts shows the start of combustion point.

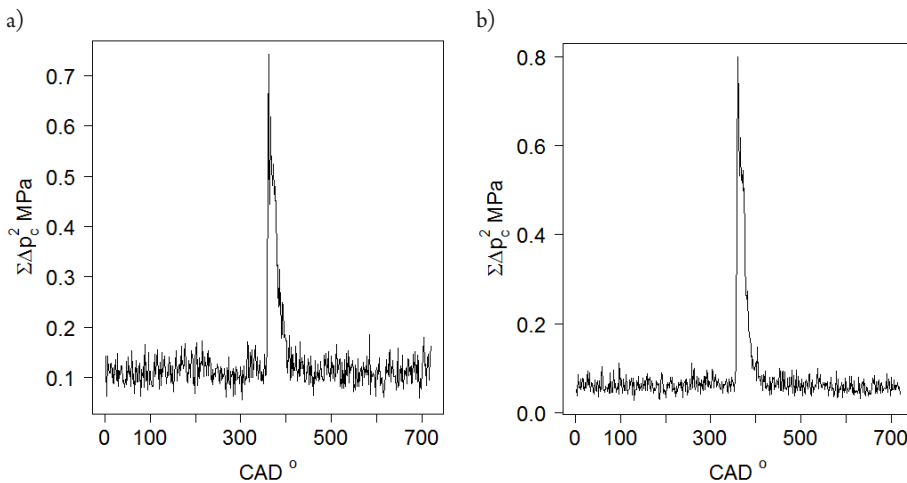


Fig. 2. The sum of the squared for the engine operating under part-load ( $N_e = 20$  kW) conditions at a speed of 1600 rpm a) diesel-powered b) FAME-powered

Script 1 written in the R application language helps determine and graphically represent the values of  $\sum \Delta p_c^2$ .

**Script 1.** Determining the sums of the pressure squared deviations from the mean values.

```
%script1.R
rm(list = ls())
pc <- read.table("c:/on/1600/20/pc", header=FALSE, sep=";", na.strings="NA",
dec=".", strip.white=TRUE)
pc<-data.matrix(pc)
owk <- read.table("c:/on/1600/20/owk", header=FALSE, sep=";",
na.strings="NA", dec=".", strip.white=TRUE)
owk<-data.matrix(owk)
sredpc<-0
for (i in 1:512)
{
sredpc[i] <- mean(pc[i,])
}
od<-pc-sredpc
sum2od<-0
for (i in 1:512)
{
sum2od[i] <- sum((od[i,])^2)
}
par(family="Arial", font=2, ps=18, mar=c(4.2, 5.5, 1, 1))
plot(owk, sum2od, xlab=expression(paste(CAD, '
'^o)), ylab=expression(paste(Sigma, Delta, p[c]^2, "
MPa")), main="", pch=19, type="l", las=1)
```

The crank angles  $\alpha_{ps}$  and  $\alpha_{Q_{max}}$  values calculated based on the analysis of for engine operating under part-load conditions agreed satisfactorily with the values of angles reported in the literature [4]. The differences between obtained values were within the range  $\pm 1.4^\circ$  [2].

Table 2. Comparison of angles determined based on the analysis of  $\alpha_{Q_{max}}$  and on the values reported in the literature [4]; DIESEL/FAME powered engine operating under full-load conditions in the rotational speed range of  $n = 1000 - 2000$  rpm

n [rpm]	$\alpha_{ps}$	$\alpha_{ps}$ Lit.	$\alpha_{Q_{max}}$	$\alpha_{Q_{max}}$ Lit.
DIESEL				
1000	351,6	349,6	355,8	355,8
1200	351,6	349,2	355,8	357,2
1400	353,0	351,2	357,2	357,2
1600	350,2	352,4	357,2	358,4
1800	355,8	353,8	358,6	360,0

2000	357,2	354,4	361,4	360,0
FAME				
1000	348,8	350,1	353,0	353,0
1200	350,2	351,6	354,4	354,4
1400	350,2	353,0	355,8	355,8
1600	353,0	354,4	357,2	355,8
1800	354,4	354,4	358,6	357,2
2000	355,8	355,8	360,0	358,6

In order to verify the method proposed for determining the position of  $\alpha_{ps}$  and  $\alpha_{\dot{Q}_{max}}$ , the calculations were made according to the same procedure but for the case of a diesel or FAME powered engine working under full-load conditions at speeds ranging from 1000 to 2000 rpm/min. Table 2 summarizes the results of these calculations.

The values of angles  $\alpha_{ps}$  and  $\alpha_{\dot{Q}_{max}}$  calculated based on the analysis of  $\sum \Delta p_c^2$  and shown in table 2 agreed satisfactory with the values of angles reported in the literature.

#### 4. Concluding remarks

The Pearson, Lilliefors and Shapiro-Wilk tests conducted for all the crank angles, for which deviations  $\Delta p_c(i, j)$  were determined, in 90% of cases did not provide sufficient evidence to reject H0 about deviations from the mean values being normally distributed. It follows from the above that the sum of the squared pressure deviations  $\sum \Delta p_c^2$ , computed for each crank angle can be used for real-time determination of combustion process characteristic angles  $\alpha_{ps}$  and  $\alpha_{\dot{Q}_{max}}$ , which can be used to control the engine working cycle.

To find and represent the  $\sum \Delta p_c^2$  values graphically, Script 1 was written in the Rapplication language. This script can be implemented on a simple type ATmega microcontroller. The maximum of signal  $\sum \Delta p_c^2$  corresponds to  $\alpha_{\dot{Q}_{max}}$  angle, whereas the angle of the rapid  $\sum \Delta p_c^2$  increase defines the start of combustion point. Good agreement was demonstrated between the results obtained for various engine operating conditions and those reported in the literature. To validate this method, the values of the sought angles were additionally determined by analysing the FFT module for signal  $p_c$  related to individual crank angles. The results obtained from each case analysed here were identical. The FFT procedure, however, extended the time necessary to make the calculations by about 50%.

## References

- [1] Bąkowski A., Radziszewski L., *Determining selected diesel engine combustion descriptors based on the analysis of the coefficient of variation of in-chamber pressure*, "Bulletin of the Polish Academy of Sciences, Technical Sciences", Vol. 63, No. 2, 2015, 457–464.
- [2] Bąkowski A., Radziszewski L., Žmindák M., *Analysis of selected pressure signal descriptors used to control combustion engine*, "Solid State Phenomena", Vol. 248, 2016, 211–216.
- [3] Delvecchio S., Bonfiglio P., Pompoli F., *Vibro-acoustic condition monitoring of Internal Combustion Engines: A critical review of existing techniques*, "Mechanical Systems and Signal Processing", Vol. 99, Issue 1, 2018, 661–683.
- [4] Łagowski P., *Methodology of determining and evaluation of diagnostics parameters of indicated plot for an internal combustion engine*, PhD thesis, Kielce University of Technology, Kielce 2010.
- [5] Maurya R.K., Pal D. D., Agarwal A. K., *Digital signal processing of cylinder pressure data for combustion diagnostics of HCCI engine*, "Mechanical Systems and Signal Processing" Vol. 36, Issue 1, 2013, 95–109.
- [6] Pha P. X., Bodisco T. A., Ristovski Z. D., Brown R. J., Masri A. R., *The influence of fatty acid methyl ester profiles on inter-cycle variability in a heavy duty compression ignition engine*, "Fuel", Vol. 116, 2014, 140–150.
- [7] Payri F., Lujan J.M., Martin J., Abbad A., *Digital signal processing of in-cylinder pressure for combustion diagnosis of internal combustion engines*, "Mechanical Systems and Signal Processing", Vol. 24, Issue 6, 2010, 1767–1784.

Łukasz Dragun

Jerzy Jaroszewicz

Department of Production Faculty of Engineering Management, Management, Białystok  
University of Technology

Leszek Radziszewski

Faculty of Mechatronics and Machine Design, Kielce University of Technology

Vladimir Antoniuk

viadi@tut.by

Zjednoczony Instytut Budowy Maszyn Narodowej Akademii Białorusi

## SELECTED OPERATING PROBLEMS OF CENTRAL PUMPS

---

### WYBRANE PROBLEMY EKSPLOATACYJNE POMP WIROWYCH

#### Abstract

The article presents problems of maintaining the Z-type supply pumps and network operated in ENEA Wytwarzanie Sp. z o.o. Heat Segment, Białystok Branch with the use of thermovision and vibrodiagnostic studies. The practical aim is to select parameters of the supply pumps (multistage) which ensure energy efficient operation despite a serious operational wear - a 20-year working period. Commissioning of a Z-type feed pump and thermovision tests of selected machine construction elements constituted the subject of the research.

**Keywords:** centrifugal pumps, feed pumps

#### Streszczenie

W artykule przedstawiono problematykę utrzymania ruchu pomp zasilających typu Z i sieciowych eksploatowanych w ENEA Wytwarzanie Sp. z o.o. Segment Ciepło, Oddział Białystok z wykorzystaniem badań termowizyjnych oraz wibrodiagnostycznych. Celem praktycznym jest dobór parametrów pomp zasilających (wielostopniowych), zapewniających energooszczędną eksploatację mimo poważnego zużycia eksploatacyjnego – 20 letni okres pracy. Przedmiotem badań był rozruch pompy zasilającej typu Z oraz badania termowizyjne wybranych elementów konstrukcyjnych maszyny.

**Słowa kluczowe:** pompy wirowe, pompy zasilające



## 1. Introduction

Z-type supply pumps are multi-stage pump constructions. These pumps consist of pressed and suction bodies and stepped rings joined together with tie bolts.

Housings have horizontal paws in the axial plane to support the pump on the foundation slab. Each member consisting of a step ring, a rotor and a steering wheel is one pump stage. The tightness between individual step rings is ensured by the pressure of lapped sealing surfaces. The pump shaft is guided in radial slide bearings and in a two-way sliding Michella bearing type. Bearings are circulated by oil under pressure. In the place of passage through the gland, the shaft is protected by exchangeable sleeves and sealed with an intense cooling water sealant. Glands together with stuffing box covers are attached to the suction and discharge body of the pump. The axial thrust of the rotating assembly is balanced by the unloading disc and the sliding axial bearing. In addition to inlet and outlet chutes, the pumps have two others: the first one allows for the injection of steam and the second for connecting the pump with the minimum controlled flow valve.



Fig. 1. Steam water pump for the Z-type steam boiler

The valve ensures a minimum flow of water through the pump to protect it from fogging and consequent obliteration. This does not exclude the need to ensure that the suction of

the pump is properly inflated, which is always determined. The pump is covered with an insulating mattress and a sheet steel cover. In Fig. 1, photographs illustrate a feed water pump operated at ENEA Wytwarzanie Sp. z o.o. Heat Segment, Białystok Branch.

## 2. Experimental tests for starting a Z-type power pump

The research was carried out at ENEA Wytwarzanie Sp. z o.o. – Segment Ciepło Białystok Branch. The test object was a Z-type pump supplying a steam boiler.

The scope of the tests included the measurement of vibration of slide bearings mounted on the shaft and checking the correctness of the occurrence of the so-called “Lubricating wedge”.

For testing of bearing shells, DIAMOND 401 high quality measuring equipment (Fig. 4) was used together with sensors. The tests were supplemented with measurements from a KSD 400 computerized vibration analyzer. The results of the measurements were presented in graphical form in Figs. 6 and 7.

Fig. 2 presents the rotor model made in the Autodesk Inventor Professional environment. Fig. 5 presents selected results of thermovision tests carried out on bearing housings.

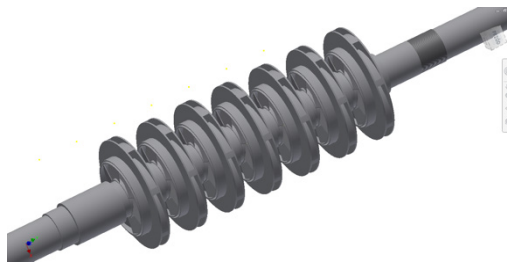


Fig. 2. Rotor model of the Z-type feed pump

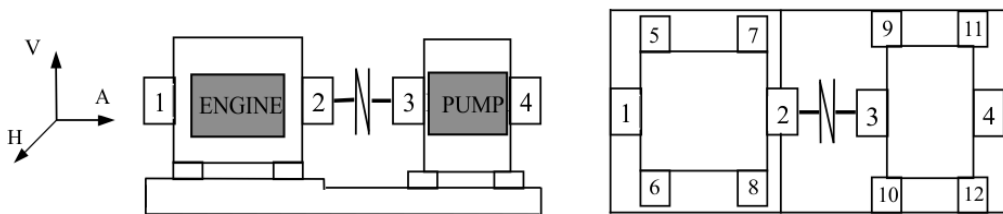


Fig. 3. Scheme of measurement points on the pump set

The measurements were carried out using a KSD 400 vibration analyzer with an eddy current sensor. The effective value of vibration velocity (in mm/s) was measured with automatic selection of bandwidth and filtration.

The performed tests allowed for determination whether the shaft of the rotor machine, in this case the Z-pump “rubs” against the slide bearing, which caused resonance vibrations, and ultimately led to the least expected cause of machine failure.

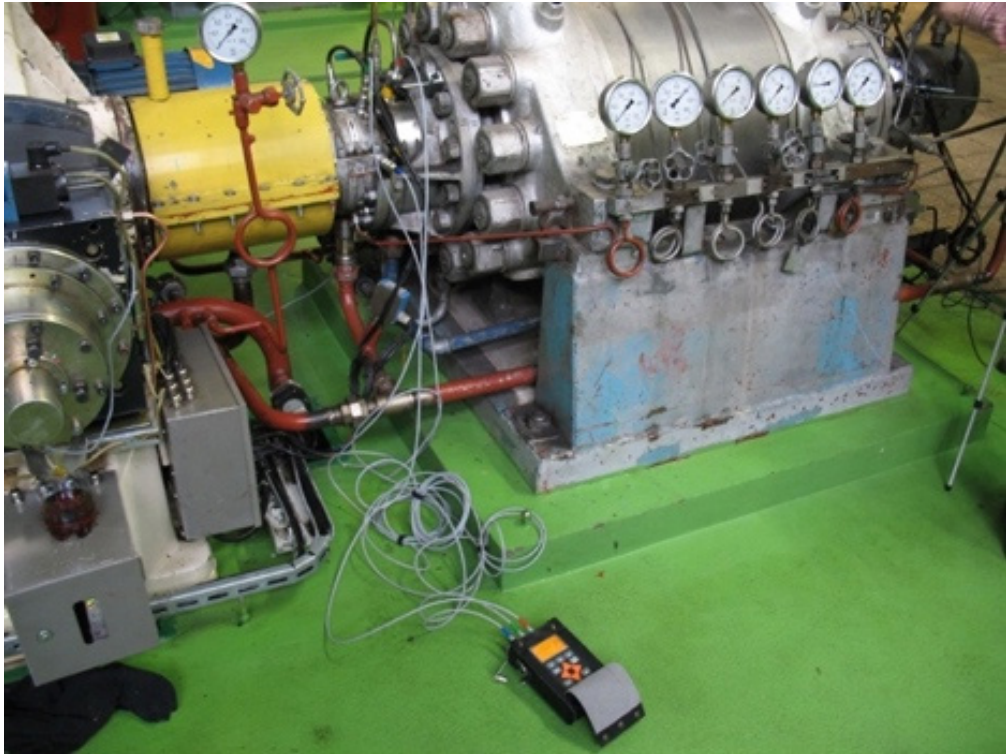


Fig. 4. Diagnostic apparatus used during experimental research

Mainly used acetules, spigots and other retaining elements are the most frequently observed damages of the Z-pump in question. Lack of axially and the occurrence of a high level of machine vibrations may indicate disturbances and breaks in lubrication, which causes the disappearance of the oil film. The disappearance of the oil film in the final effect leads to the destruction of the surface layer of the sliding bearing shells, to the so-called machine smearing.

Self-excited vibrations generated in bearings while meeting strictly defined conditions constitute another major problem closely related to the lubrication of rotor machine. The most often evoked causes of self-excited vibrations include too low loads (which occurs in our case) and large radial clearances. The vibrations rise irregularly at a rapid rate [1,5].

In order to prevent the occurrence of a given phenomenon, which is a potential cause of the defect and can cause a real failure of the rotor machine, it is necessary to reduce (as much as possible) the risk of instability by correcting misalignment, eliminating excessive slack and possibly changing the slide bearing geometry. Each intervention in the geometry of the machine's structural elements must be made by the manufacturer of the machine, otherwise the failure of the machine may result in an operational catastrophe, as was the case with the carbon ball mill, which was presented in the earlier part of the dissertation.

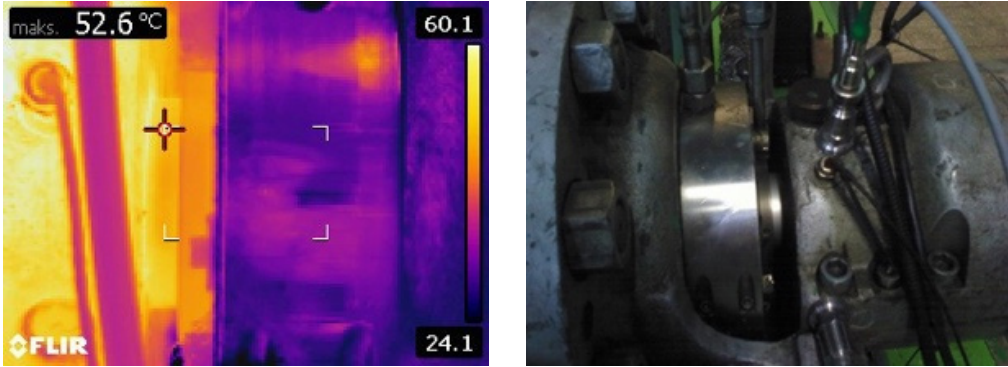


Fig. 5. Testing with the FLIR thermovision camera Z-pumps

On the basis of the vibration spectrum of the rotor shaft, it is possible to recognize the type of work performed by a given shaft [5,8].

Incomplete load of the tested Z-pump (Fig. 1) results from water supply to only one boiler. This type of pump load occurs in summer periods due to a lower demand for thermal energy. The pump shows resonant vibrations, which indicates the need to perform the above-mentioned diagnostic tests to prevent unforeseen emergency stoppages.

The results of the diagnostic tests are presented below in a simple graphical form (Figs. 6 and 7).

It can be stated that at the beginning (below 1500 revolutions per minute) there appears non stability synchronized by the rotation of the shaft, bearing the name of an oil whirl. This phenomenon is manifested in a graphical form as a loop filled with red.

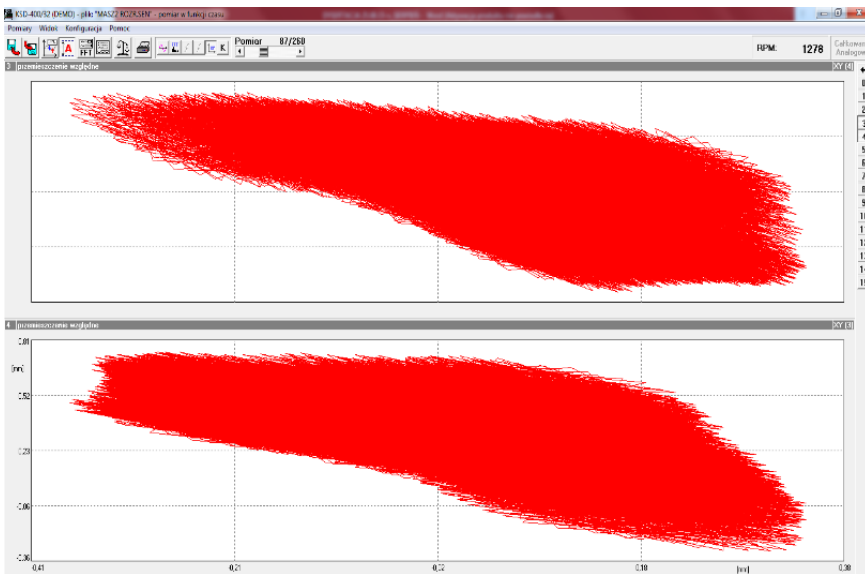


Fig. 6. Screenshot of the KSD 400/32 program - measurement 87 - RPM 1278

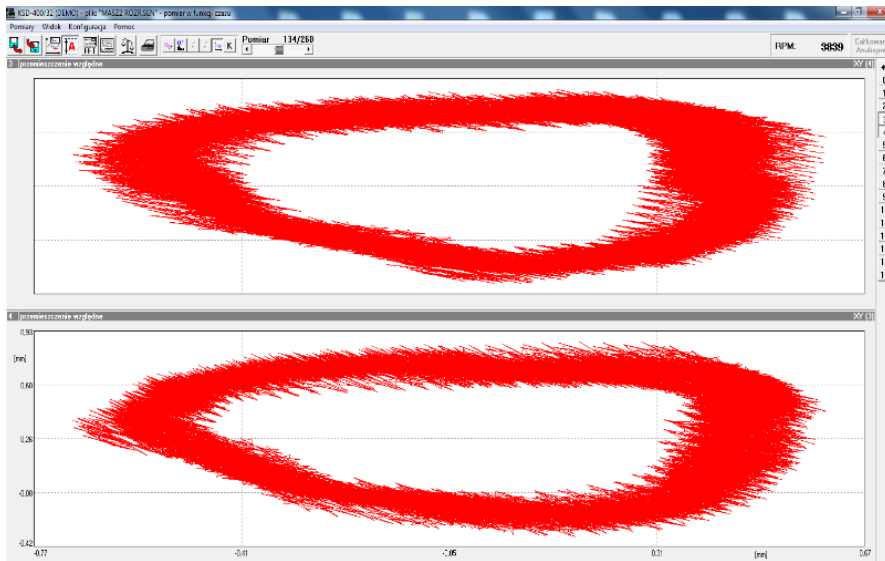


Fig. 7. Screenshot of the KSD 400/32 program - measurement 134 - RPM 3839

The loop begins to take the form of an ellipse with an open center after exceeding 3000 rpm, because the forces caused by rotation are then sufficient to stabilize the oil film. The rotor speed of the rotor stabilizes within the range of 3600–4000 rpm. A further increase in rotor speed would lead to instability, oil vortex, up to the speed corresponding to two times the vibratory frequency of the rotor. Above this speed, the rotor frequency (flexural vibrations) becomes the synchronizing factor.

### 3. Summary

In many branches of the economy, in particular in power and heat engineering, pumping costs can be a dominant component of production costs. Therefore, it is becoming more and more important to use reliable, high efficiency pump units, correctly selected for the systems and, properly, most economically controlled.

Pumps should be maintained at a high technical level through well-made (periodic) repairs. Stopping the pump for renovation should not be after a certain time but after exceeding the economic threshold (efficiency) or mechanical (vibration) [9].

Every now and then pumps (especially large ones) should be subjected to modernization repairs, which would allow (to industrial practice) progress in the construction of flow elements and thus reduce the energy consumption of the pumping process.

The benefits of repairs carried out according to the technical condition assessment result in the increased reliability and prolongation of life of individual components, and thus the reduction of maintenance costs. Before starting the renovation carried out with this method,

critical elements of the device, evaluation criteria and methods of testing should be clearly identified.

The above activities should lead to obtaining qualifying results for its collection after the refurbishment during receiving measurements of the pump set.

*The research was carried out as part of the work no. S/WZ/1/2015 and financed from funds for education of the Ministry of Science and Higher Education.*

## References

- [1] Jaroszewicz J., Jermołaj M., Ostapkowicz P., Łapiński R., *Wpływ masy czujnika na pomiar drgań własnych płyty kołowej utwierdzonej na obwodzie*, Zeszyty Naukowe Politechniki Białostockiej, Nauki Techniczne, No. 140, Budowa i Eksploatacja Maszyn, z. 8, 2001.
- [2] Jaroszewicz J., Kopciewski S., *Modernizacja promieniowych uszczelnień gazowych, zwłaszcza wodorowych w generatorach*, Zeszyty Naukowe Politechniki Białostockiej, Nauki Techniczne, No. 132, Budowa i Eksploatacja Maszyn, No. 7, 2000, 139–148.
- [3] Jaroszewicz J., Kopciewski S., *Energooszczędna eksploatacja pomp wirowych, zwłaszcza w energetyce i ciepłownictwie*, Przegląd Mechaniczny, 2001.
- [4] Jaroszewicz J., Kopciewski S., *Niewyważenie hydrauliczne jako źródło niesprawności w diagnostyce drganiowej pomp wirowych*, Przegląd Mechaniczny, 2003.
- [5] Jaroszewicz J., Zoryji L., *Metody analizy drgań i stateczności kontynuualno-dyskretnych układów mechanicznych*, Rozprawy Naukowe Politechniki Białostockiej No 54, Białystok, 1997.
- [6] Jędrał W., *Pompy wirowe odśrodkowe. Teoria, Podstawy projektowania, Energo-oszczędna eksploatacja*, Oficyna Wydawnicza Politechniki Warszawskiej, Warszawa 1996.
- [7] Jędrał W., *Rekonstrukcja uszczelnień wewnętrznych sposobem na energooszczędną eksploatację pomp wirowych*, Gospodarka Paliwami i Energią, No. 6, 1995.
- [8] Łączkowski R., *Drgania elementów turbin ciepłych*, Wydawnictwo Naukowo-Techniczne, Warszawa 1974.
- [9] PN-IEC 34-14 Maszyny elektryczne wirujące. Drgania mechaniczne określonych maszyn o wzniosach osi wału 56 mm i większych. Pomiar, ocena i wartości graniczne drgań.



**Monika Krzywicka**

monika.gruszecka@up.lublin.pl

Fundamentals of Technology Chair, Faculty of Production Engineering, University of Life Sciences in Lublin

**Szymon Tofil**

Centre for Laser Technology of Metals, Faculty of Mechatronics and Machine Design, Kielce University of Technology

**Krzysztof Pałka**

Department of Materials Engineering, Faculty of Mechanical Engineering, Lublin University of Technology

SELECTION OF PARAMETERS FOR LASER SURFACE TEXTURING OF  
TITANIUM ALLOYS

---

DOBÓR PARAMETRÓW LASEROWEGO TEKSTUROWANIA POWIERZCHNI  
STOPU TYTANU

**Abstract**

This paper shows a parameters selection method providing an ablative laser treatment removal of materials. A laser for generating laser beams of ultraviolet light in picosecond pulses at a frequency to 400 kHz was used in the experiment. The quality of the marks was examined by scanning electron microscopy. On the basis of the analysis, it is recommended to conduct micromachining at a frequency of 100 kHz and exposure times within the range of 62.5 ms to 125 ms.

**Keywords:** laser surface texturing, titanium alloys

**Streszczenie**

W pracy przedstawiono metodę doboru parametrów mikroobróbki laserowej zapewniającą ablacyjne usuwanie materiału. W eksperymencie zastosowany został laser generujący wiązkę promieniowania ultrafioletowego w impulsach pikosekundowych z częstotliwością do 400 kHz. Jakość wytworzonych śladów została oceniona metodą elektronicznej mikroskopii skaningowej. Na podstawie przeprowadzonej analizy rekomenduje się prowadzenie mikroobróbki przy częstotliwości 100 kHz i czasie oddziaływania impulsów lasera od 62,5 ms do 125 ms.

**Słowa kluczowe:** laserowe teksturowanie powierzchni, stopy tytanu



## 1. Introduction

Due to biocompatibility, high resistance to corrosion in the tissue environment, the most similar mechanical properties to natural bones and density among the previously used materials, titanium alloys are the most promising group of materials used for joint endoprosthesis [1]. Poor tribological properties are the limitations in the use of titanium alloys. The wear products may cause for e.g.: allergic and inflammation reactions, osteolysis and finally the loosening of the implant [2].

Laser surface texturing has enormous potential for structuring biomaterials [3]. Laser micromachining is one of the methods of limiting wear and friction of biobearing [4, 5]. It also has a beneficial effect on cell adhesion, distribution of biological fluids, osseointegration and endurance on the bone-to-implant direct contact [3, 6, 7].

The selection of parameters for laser surface texturing involves the use of appropriate radiation wavelength, which affects the ability of the material to absorb radiant energy and the possibility of focusing of a laser beam. The efficiency and depth of penetration of radiation into the surface are smaller for a smaller radiation wavelength. It is also important to choose the fluence, which has an impact on the shape of surface texture elements and the homogeneity of the radiation interaction. At higher fluence, the heterogeneous nucleation of bubbles with steam leads to normal boiling. The length of a laser pulse is another aspect of laser micromachining. In general, since the duration of the pulse is shortened, the energy is rapidly accumulated in the material, which leads to its faster excretion. The ablation processes with femto- and picosecond pulses is called cold laser ablation, because the heat-affected zone is not observed in the material [8, 9, 10].

Laser surface texturing is considered by performance and accuracy of the process. The accuracy of micromachining can be considered in terms of the precise geometry of texture elements and a removal of the material [8, 9]. One of the main advantages of a laser as a tool for surface treatment of materials is the possibility of precise control over energy deposition place and level. The desired modification of the material is achieved due to the appropriate selection of laser processing parameters [10].

The analysis of laser processing parameters influencing morphology on the surface of the element made of Ti6Al7Nb is the aim of the study.

### 2. Materials and methods

The analyses were conducted on samples made of Ti6Al7Nb. The chemical composition of the alloy was in accordance with ISO 5832-11: Fe max. 0.25%, O max. 0.2%, N max. 0.05%, C max. 0.08%, H max. 0.009%, Al 5.5–6.5%, Nb 6.5-7.5%, Ta max. 0.5%, remainder Ti.

The experiment was carried out by using a stand for microprocessing equipped with a TruMicro 5000 model 5325c picosecond laser with max 5 W average power, pulse energy up to 12.6  $\mu\text{J}$  and quality of the radius of  $M^2 < 1.3$ . The maximum pulse frequency is 400 kHz and can be modified by the introduction of a pulse divider taking the values of 200 kHz, 133, 33 kHz, 100 kHz, 80 kHz, 66, 66 kHz, etc. The radiation wavelength of a TruMicro 5325 c laser is 343 nm. It consisted in evaluating the impact of laser pulses on the processed material by changing the frequency of pulses and their duration. The energy value of a single pulse was

12.6  $\mu\text{J}$  at 100% of power. The exposure times were within the range of 12.5 ms to 250 ms. As a result, changes in the number of individual pulses acting on the sample in the range of  $N = 78$  to  $N = 100\,000$  were obtained (table 1). During the processing of a sample, beams were placed in the focus, and the processing zone was shielded with argon.

Table 1. List of selected laser microprocessing parameters of samples tested

f [kHz]	t [ms]				
	12, 5	25	62, 5	125	250
400	5000	10 000	25 000	50 000	100 000
200	2500	5000	12 500	25 000	50 000
100	1250	2500	6250	12 500	25 000
50	625	1250	3125	6250	12 500
25	312	625	1562	3125	6250
12, 5	156	312	781	1562	3125
6, 25	78	156	390	781	1562

*f* – frequency of laser pulses [kHz]; *t* – the exposure time [ms]

The assessment consisted in observing the shape and form of the obtained trace of the impact of the laser beam on the material and in identifying processes such as melting of the material, loss with no signs of melting and the outbreak of the material. The surface morphologic observations were carried out by scanning electron microscopy (NovaNanoSEM 450, FEI).

## 2. Results

Exemplary SEM views of the picosecond laser beam traces of the impact on Ti6Al7Nb were showed in Figure 1.

Small particles, which created a concentric zone of material deposition, are visible on the edges of the microcavities. During the point impact of the picosecond laser carried out at the frequency of 50 kHz or lower for the range of pulses from 1562 to 12500, a bigger number of particles is visible as the range of pulses increase. With a small range of pulses, the energy of laser interaction is sufficient only for the coarse defragmentation of the material and much larger particles are formed as a result of the phase explosion. Moreover, the force of the explosion is not able to discharge defragmented particles to the periphery of the trace and therefore they remain in the centre of the track. For the range of pulses below 2500, the defragmented particles remain in the centre. Regular cavities were obtained using the frequency of 400, 200 and 100 kHz for the full range of pulses. For the range of pulses from 5000 to 100000 and the frequency of 400 kHz and 200 kHz, cavities were irregular in nature and had the shape of a tapering crater. As the number of impulses increases, the depth of the produced cavity increases. For the range of pulses from 6250 to 100 000, corrugations on



the sheet of cavities are visible. For frequencies from 6.25 to 50 kHz cavities appear at min. 1562 pulses. Therefore, the use of processing with the frequency of 100 kHz and the range of pulses from 6250 to 12 500 is the most favourable for Ti6Al7Nb.

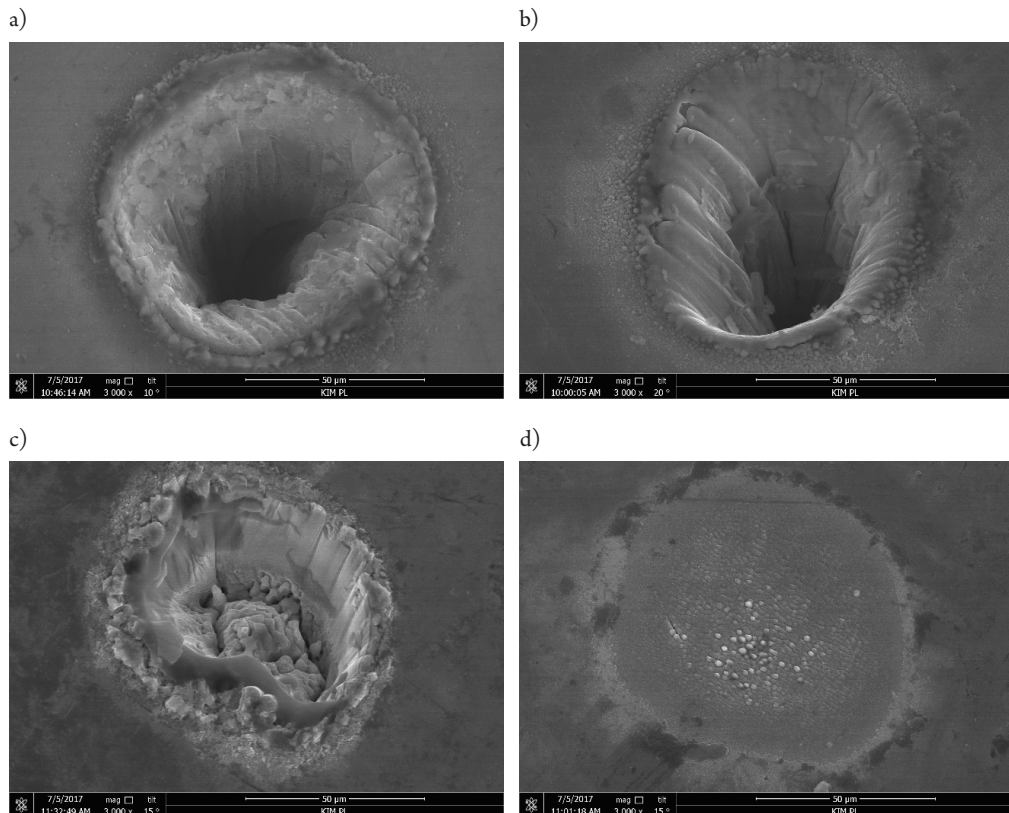


Fig. 1. Selected SEM views of the picosecond laser beam traces of the impact on Ti6Al7Nb: a) 400 kHz, 250 ms, N = 100000, b) 200 kHz, 125 ms, N = 25000, c) 50 kHz, 62.5 ms, N = 3125, d) 6.25 kHz, 12.5 ms, N = 78

### 3. Conclusions

The results show that using the frequency of 100 kHz and the range of pulses from 6250 to 12 500 is the most favourable for Ti6Al7Nb. A selection of incorrect parameters of microprocessing can cause the insufficient treatment capacity of materials as well as ablation with remelting.

### References

- [1] Crisan N., Trunfio A.M., Stoica G., Bajenescu T., Gheorghiu H., *Tribological behavior of new titanium alloys – a comparative study*, Applied Mechanics and Materials, Vol. 528, 2014, 19–24.
- [2] Majkowska B., Jajdżewska M., Miotke D., Wołowiec E., Zieliński A., *Evaluation of wear resistance of Ti alloys used for elements friction of knee endoprosthesis*, Solid State Phenomena, Vol. 225, 2014, 123–130.
- [3] Cunha A., Serro A.P., Oliveira V., Almeida A., Vilar R., Durrieu M.Ch., *Wetting behaviour of femtosecond laser textured Ti-6Al-4V surfaces*, Applied Surface Science, Vol. 265, 2013, 688–696.
- [4] Qin L., Lin P., Zhang Y., Dong G., Zeng Q., *Influence of surface wettability on the tribological properties of laser textured Co-Cr-Mo alloy in aqueous bovine serum albumin solution*, Applied Surface Science, Vol. 268, 2013, 79–86.
- [5] Tianchang H., Litian H., Qi D., *Effective solution for the tribological problems of Ti-6Al-4V: Combination of laser surface texturing and solid lubricant film*, Surface-co&Coatings Technology, Vol. 206, 2012, 5060–5066.
- [6] RamosSaenz C.R., Sundaram P.A., DiffootCarlo N., *Tribological properties of Ti-based alloys in a simulated bone-implant interface with Ringer's solution at fretting contacts*, Journal of the Mechanical Behavior of Biomedical Materials, Vol. 3, 2010, 549–558.
- [7] Mirhosseini N., Crouse P.L., Schmidh M.J.J., Lia L., Garrod D., *Laser surface micro-texturing of Ti-6Al-4V substrates for improved cell integration*, Applied Surface Science, Vol. 19, 2007, 7738–7743.
- [8] Antoszewski B., Radek N., Tofil Sz., Bronček J., *Dobór parametrów laserowej mikroobróbki powierzchniowej elementów panewek brązowych*, Przegląd Elektrotechniczny, Vol. 1, 2017, 41–44.
- [9] Antoszewski B., *Warstwy powierzchniowe z teksturą – kształtowanie wybranymi technologiami wiązkowymi oraz właściwości tribologiczne*, Kielce, Wydawnictwo Politechniki Świętokrzyskiej, 2010.
- [10] Antoszewski B., Sęk P., *Influence of laser beam intensity on geometry parameters of a single surface texture element*, Archives of Metallurgy and Materials, Vol. 3B, 2015, 2215–2219.





Dariusz Kurczyński

kdarek@tu.kielce.pl

Piotr Łagowski

Department of Automotive Vehicles and Transportation, Faculty of Mechatronics  
and Machine Engineering, Kielce University of Technology

Vasyl Tomyuk

Department of Automobiles and Tractors, Lviv National Agrarian University

## SELECTED ASPECTS OF DUAL-FUELLING OF THE PERKINS 1104D-E44TA ENGINE WITH NATURAL GAS AND DIESEL FUEL

---

### WYBRANE ASPEKTY DWUPALIOWEGO ZASILANIA SILNIKA PERKINS 1104D-E44TA GAZEM ZIEMNYM I OLEJEM NAPĘDOWYM

#### Abstract

The paper presents selected test results of the PERKINS 1104D-E44TA engine, adjusted to being dual-fuelled with compressed natural gas and Diesel fuel. The tests were carried out with maximum possible dosing of natural gas and then with lowering its dosing by approximately half. The obtained test results were compared with the results of tests carried out when the engine was powered with Diesel fuel only.

**Keywords:** internal combustion engines, engine fuels, natural gas, dual-fuel power supply

#### Streszczenie

W artykule przedstawiono wybrane wyniki badań silnika PERKINS 1104D-E44TA przystosowanego do zasilania dwupaliwowego sprężonym gazem ziemnym i olejem napędowym. Badania przeprowadzono przy maksymalnym możliwym dawkowaniu paliwa gazowego i po jego zmniejszeniu o około połowę. Otrzymane wyniki badań porównano z wynikami uzyskanymi przy zasilaniu silnika olejem napędowym.

**Słowa kluczowe:** silniki spalinowe, paliwa silnikowe, gaz ziemny, zasilanie dwupaliwowe

## 1. Introduction

Liquid fuels, gasoline and Diesel fuels obtained from oil are conventional fuels for powering piston combustion engines. Their characteristics determine constructional properties of engines. Using alternative fuels for combustion engines is possible, but it usually requires adopting engines for such fuels. An engine powered with alternative fuel should have similar operation properties but less harmful impact upon natural environment. With regard to Diesel engines, alternative fuels may also include vegetable oil esters [1, 2, 3]. Using esters requires no constructional modifications in the engine or other feeding system. It is possible because of similar physical and chemical properties of both vegetable oil esters and Diesel fuels, obtained from oil. Also, gas fuels are an interesting alternative for powering combustion engines. However, using such fuels demands the employment of completely different feeding systems than those for liquid fuels. Currently, a bi-fuelling system is being employed, that is, powering engine with either liquid or gas fuel. It is a universal and commonly applied solution. Diesel engines may be adopted for dual-fuelling, which means powering the engine with both gas and liquid fuel at the same time. The issue of powering combustion engines with alternative fuels is currently the scope of extensive research and numerous tests.

## 2. Natural gas as fuel in transportation

Natural gas is a source of energy which may allow for diminishing harmful impact upon natural environment, when compared to oil and coal, due to the fact that natural gas is mainly composed of methane – one of the simplest coal-hydrogen compounds (up to 85÷99% content) [4]. Apart from methane, natural gas contains other volatile hydrocarbons, such as propane, butane, pentane, hexane, and others [5], as well as slight amounts of inert gases and noble gases, such as nitrogen, argon or helium. Natural gas may also contain heavier hydrocarbons, compounds of sulphur, water and slight amounts of carbon dioxide. The properties of natural gas are determined by the properties of methane.

Natural gas is an organic fossil fuel, formed as a result of anaerobic decomposition of organic substances in deep layers of soil [6]. Deposits of natural gas may occur independently or with deposits of oil and coal. It may be used in a compressed (Compressed Natural Gas – CNG) or liquefied form (Liquefied Natural Gas – LNG). The technology of using the compressed form (CNG) for powering combustion engines is explored better, but efforts are being currently made to develop the technology of utilising the liquefied form (LNG). The possibilities of using natural gas for powering combustion engines are widely discussed in literature [7, 8, 9]. Using such fuels, however, requires designing and installing feedings systems which are adequate for the properties of gas fuels.

The European Union prioritises the increase of alternative fuels compared with petrol and Diesel fuels [10, 11, 12]. This means that the interest in natural fuel as an energy source for powering piston combustion engines will be growing.

### 3. Test stand and tested item

A Perkins 1104D-E44TA Diesel engine with direct fuel injection system was the tested item. It is equipped with a Common Rail injection system that employs electromagnetic injectors. The feeding system and the entire engine are controlled by the electronic controlling unit. The Perkins 1104D-E44TA engine installed on the engine testing station was adopted for being dual-fuelled with Diesel fuel and compressed natural gas (Diesel+CNG). The engine may be powered with both fuels at the same time or with Diesel fuel only. A flowchart of the testing station with the Perkins 1104D-E44TA engine is presented in Figure 1.

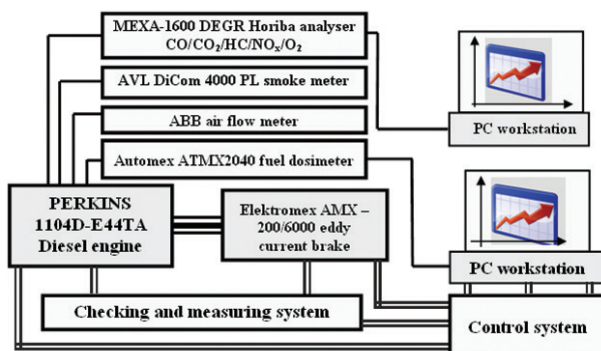


Fig. 1. Testing station flowchart

### 4. Selected test results

During the tests, the PERKINS 1104D-E44TA Diesel engine was operating under load characteristic for the rotational speed of the crankshaft of 1800 rpm and it was dual-fuelled with natural gas and Diesel fuel. The tests were carried out with maximum natural gas dosage (Diesel+CNG), specified during the calibration of natural gas feeding system, and with natural gas dosage reduced by approximately half (Diesel+1/2CNG). In addition, one test included an engine powered with Diesel fuel only. Figure 2 presents energy shares of natural gas in the entire amount of energy supplied into the engine cylinders with maximum natural gas dosing (Diesel+CNG) and with natural gas dosing reduced by half (Diesel+1/2CNG). Figures 3 and 4 present a comparison of the hourly fuel consumption (FC) and brake specific fuel consumption (BSFC) of the Perkins 1104D-E44TA engine, powered with Diesel fuel only and dual-fuelled with Diesel fuel and natural gas with maximum (Diesel+CNG) and reduced (Diesel+1/2CNG).

Figures 5, 6, 7, 8 and 9 present a comparison of the concentration levels of the carbon monoxide (CO), carbon dioxide (CO<sub>2</sub>), total hydrocarbons content (THC) in and smokiness of exhaust fumes of the Perkins 1104D-E44TA engine, powered with Diesel fuel and dual-fuelled with Diesel fuel and compressed natural gas, with maximum (Diesel+CNG) and reduced (Diesel+1/2CNG) natural gas dosing.



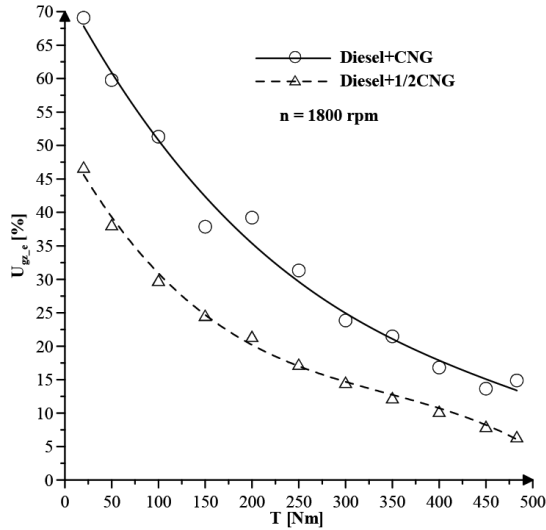


Fig. 2. The energy share of natural gas ( $U_{eCNG}$ ) in total energy amount supplied into the cylinders of the Perkins 1104D-E44TA engine, dual-fuelled with natural gas and Diesel fuel with maximum (Diesel+CNG) and reduced (Diesel+1/2CNG) dosing

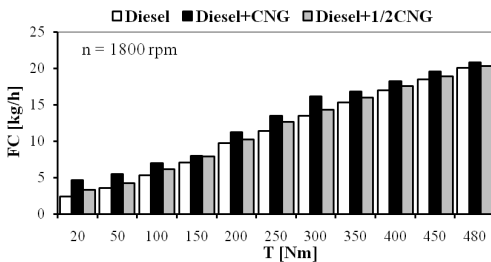


Fig. 3. Comparing the hourly fuel consumption (FC) of the Perkins 1104D-E44TA engine, powered with Diesel fuel only and dual-fuelled

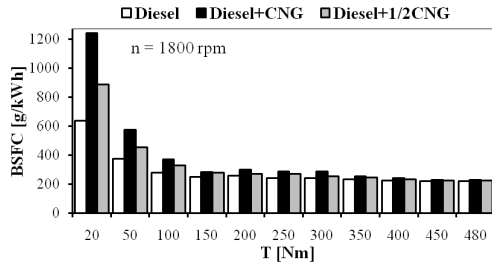


Fig. 4. Comparing brake specific fuel consumption (BSFC) of the Perkins 1104D-E44TA engine, powered with Diesel fuel and dual-fuelled

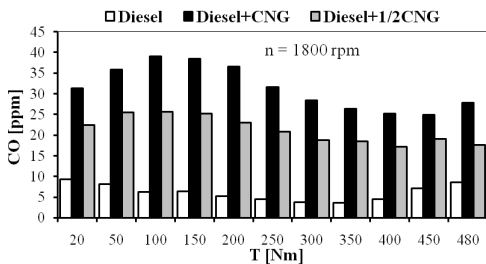


Fig. 5. Comparison of the concentration levels of carbon monoxide (CO) in the exhaust fumes of the Perkins 1104D-E44TA engine, powered with Diesel fuel only and dual-fuelled

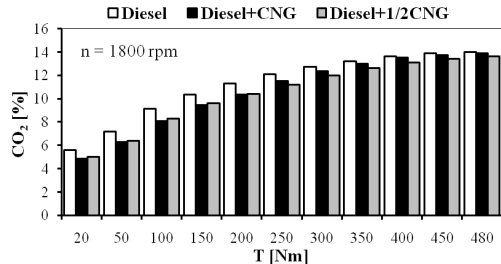


Fig. 6. Comparison of the concentration levels of Carbon dioxide (CO<sub>2</sub>) in the exhaust fumes of the Perkins 1104D-E44TA engine, powered with Diesel fuel only and dual-fuelled

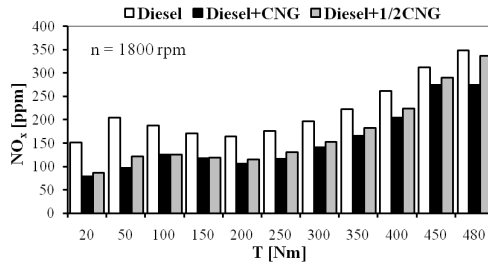


Fig. 7. Comparison of the concentration levels of nitric oxides ( $\text{NO}_x$ ) in the exhaust fumes of the Perkins 1104D-E44TA engine, powered with Diesel fuel only and dual-fuelled

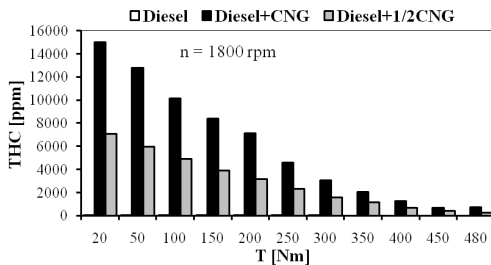


Fig. 8. Comparison of the concentration levels of total hydrocarbons (THC) in the exhaust fumes of the Perkins 1104D-E44TA engine, powered with Diesel fuel only and dual-fuelled

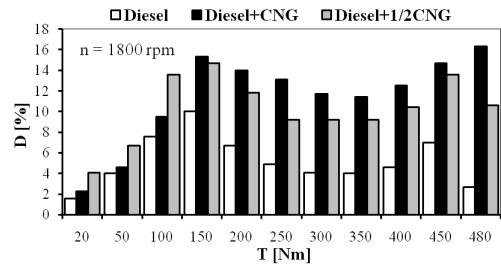


Fig. 9. Comparison smokiness of the exhaust gases (D) of the Perkins 1104D-E44TA engine, powered with Diesel fuel only and dual-fuelled

### 3. Summary

With the Perkins 1104D-E44TA Diesel engine dual-fuelled with natural gas and Diesel fuel, and with its operation under the load characteristic, the hourly and specific fuel consumption was higher than with the engine powered with Diesel fuel only. With reduced natural gas dosing, the hourly and specific fuel consumption were lower than with maximum natural gas dosing.

The reduction of the content of nitric oxides and carbon dioxide in the engine's exhaust fumes was a positive outcome of using natural gas for powering the engine. The concentration levels in each measurement point were lower when compared to the engine being powered with Diesel fuel only. With maximum natural gas dosing, the concentration levels of nitric oxides in exhaust gases were lower than with reduced natural gas dosing.

When the Perkins 1104D-E44TA engine was dual-fuelled with natural gas and Diesel fuel, it resulted in higher concentration level of carbon monoxide as well as a multiple increase of total hydrocarbons in the exhaust fumes. It is most likely caused by incomplete combustion of methane as well as deteriorated conditions of the combusting process of Diesel fuel in the dual-fuelled engine. Also, a higher concentration of methane in exhaust gases may be caused by its outflow with the air through the exhaust valves during the load exchange process in a cylinder.

When the engine was dual-fuelled with natural gas and Diesel fuel, a significant reduction of natural gas dosing resulted in lower concentration levels of carbon monoxide,

hydrocarbons as well as smokiness of exhaust fumes compared with the maximum natural gas dosing. However, these concentrations and smokiness are still considerably higher than in the exhaust fumes of the engine powered with Diesel fuel only, as adopted by the manufacturer.

In order to reduce concentration levels of carbon monoxide and hydrocarbons in the exhaust fumes of a dual-fuelled engine, as well as their smokiness, it is necessary to modify the air-fuel mixture content as well as the course of the combustion process, mainly by means of changing parameters of the process of injecting Diesel fuel into cylinders.

## References

- [1] Ambrozik A., Ambrozik T., Kurczyński D., Łagowski P., *The Influence of Injection Advance Angle on Fuel Spray Parameters and Nitrogen Oxide Emissions for a Self-Ignition Engine Fed with Diesel Oil and FAME*, "Polish Journal of Environmental Studies" Vol. 23, No 6/2014, 1917–1923.
- [2] Demirbas A., *Characterization of Biodiesel Fuels*, Energy Sources, Part A, 31/2009, 889–896.
- [3] Millo F., Debnath B.K., Vlachos T., Ciaravino C., Postrioti L., Buitoni G., *Effects of different biofuels blends on performance and emissions of an automotive diesel engine*, Fuel 159/2015, 614–627.
- [4] Gruden D., *Umweltschutz in der Automobilindustrie*, Vieweg+Teubner-GWV Fachverlage GmbH, Wiesbaden 2008.
- [5] Safety data sheet. Natural gas (p<200kPa). PGNiG – Polish Oil and Gas Company, <http://pgnig> (access: 14.12.2017).
- [6] What should know about natural gas, Orlen Upstream, [www.ornlenupstream.pl/PL/GazZiemny/Strony/Publikacje.aspx](http://www.ornlenupstream.pl/PL/GazZiemny/Strony/Publikacje.aspx) (access: 14.12.2017).
- [7] Khan M. I., Yasmin T., Shakoor A., *Technical overview of compressed natural gas (CNG) as a transportation fuel*, Renewable and Sustainable Energy Reviews 51, 2015, 785–797.
- [8] Korakianitis T., Namasivayam A.M., Crookes R.J., *Natural-gas fueled spark-ignition (SI) and compression-ignition (CI) engine performance and emissions*, Progress in Energy and Combustion Science 37, 2011, 89–112.
- [9] Engerer H., Horn M., *Natural gas vehicles: An option for Europe*, Energy Policy 38, 2010, 1017–1029.
- [10] Communication from the Commission to the European Parliament, the Council, the European Economic and Social Committee and the Committee of the Regions. Clean Power for Transport: A European alternative fuels strategy, Bruksela, 24.01.2013, <http://eur-lex.europa.eu> (access: 19.12.2017).
- [11] Directive 2014/94/EU of the European Parliament and of the Council of 22 October 2014 on the deployment of alternative fuels infrastructure. Official Journal of the European Union, <http://eur-lex.europa> (access: 19.12.2017).
- [12] The national policy framework for the development of alternative fuels infrastructure, Ver 2.6, 2017, <http://bip.me.gov.pl> (access: 19.12.2017).

**Medard Makrenek**

fizmm@tu.kielce.pl

Katedra Matematyki i Fizyki, Wydział Zarządzania i Modelowania Komputerowego,  
Politechnika Świętokrzyska

**Wojciech Żórawski**

Centrum Laserowych Technologii Metali, Wydział Mechatroniki i Budowy Maszyn,  
Politechnika Świętokrzyska

**Anna Góral**

Instytut Metalurgii i Inżynierii Materiałowej PAN, Kraków

USING THE TAGUCHI METHOD TO OPTIMIZE CONTROLLED VARIABLES  
IN THE EXPERIMENT TO PRODUCE A Ti COATING BY COLD SPRAYING

---

OPTIMALIZACJA ZMIENNYCH KONTROLOWANYCH W WYTWARZENIU  
POWŁOKI Ti METODA ZIMNEGO NATRYSKU

**Abstract**

The article presents a method for optimizing technological parameters utilizing the G. Taguchi procedure. Optimization algorithm of controlled variables was presented in order to obtain the greatest value of nanohardness, microhardness and elastic modulus.

**Keywords:** optimization, orthogonal array, nanohardness, microhardness, elastic modulus.

**Streszczenie**

W artykule przedstawiono metodę optymalizacji parametrów technologicznych wykorzystującą procedurę G. Taguchi. Zaprezentowano algorytm optymalizacji zmiennych kontrolowanych, tak by uzyskać jak największą wartość nanotwardości, modułu elastyczności i mikrotwardości.

**Słowa kluczowe:** optymalizacja, tablice ortogonalne, nanotwardość, mikrotwardość, moduł elastyczności.

## 1. Introduction

Production of coatings with required properties is the major research challenge. In the manufacturing process it is necessary to indicate controllable parameters and properties expected from the resulting coating. A multitude of controlled parameters and their values make a large number of combinations effects high costs. It is necessary to minimize the number of test experiments. The objective is to select the best combination of control parameters so that the product is most robust. Statistical methods allow for minimizing the number of experiments [1]. One such method is the method of G. Taguchi, which was used in this study. The purpose of the research was to determine the value of technological parameters (controlled variables): the hardness H, the elastic modulus E and the microhardness  $HV_{0.3}$  assume the highest value. The Cold Spray technique was used to produce a Ti coating. The G. Taguchi method with P4, L3 orthogonal table for optimization was used.

## 2. Experimental

The quality of the experiment requires specifying necessary steps to ensure proper quality of work, They include a determination of input parameters, the range of values of controlled variables, the range of permissible changes in the parameter value and the establishment of a research plan – experimental planning. The next step is to conduct an experiment. This is a very time consuming and laborious stage. The results obtained should be analyzed statistically. This is the most important stage in terms of interpretation of results and elimination of possible errors. Determining controlled parameters has the greatest impact on the outcome of the process. The final stage is to identify the variables controlled to ensure realization of this objective. Orthogonal arrays are not unique to Taguchi. They were discovered earlier. However, Taguchi has simplified their use by providing tabulated sets of standard orthogonal arrays and corresponding linear graphs to fit specific projects [2]. A typical tabulation is present in Table 1 (P = 4, L = 3).

Table 1. Orthogonal array P = 4, L = 3

Taguchi, P = 4, L = 3				
Run	P1	P2	P3	P4
1	1	1	1	1
2	1	2	2	2
3	1	3	3	3
4	2	1	2	3
5	2	2	3	1
6	2	3	1	2
7	3	1	3	2
8	3	2	1	3
9	3	3	2	1

In this array, the columns are mutually orthogonal. That is, for any pair of columns, all combinations of factor levels occur; and they occur an equal number of times. Here there are four parameters P1-P4, each at three levels L. This is called an “L 9” design, with 9 indicating the nine rows. Specific test characteristic for each experimental evaluation are identified in the associated row of the table (Run). Thus, L 9 means that nine experiments are to be carried out to study four variables at three levels. That is that design reduces 81 (3<sup>4</sup>) configurations to 9 experimental evaluations.

Ti powder was used to coat the coatings. The establishment of well-defined technological parameters is the major aspect of quality control. Hardness (H), elastic modulus (E), HV were taken into account. The present objective of experiments focuses on the selection of control parameters to obtain the highest H, E, HV. The G. Taguchi method contains system design, parameter design, and tolerance design procedures to achieve a robust process and result for the best product quality [3, 4]. The base of Taguchi’s techniques is the use of parameter design which is an engineering method for product design that focuses on determining parameter settings producing the best levels of quality characteristic with minimum variation. G. Taguchi designs provide a powerful and efficient method for designing processes that operate consistently and optimally over a variety of conditions [3, 4]. The concept of loss function, quality of the signal to noise ratio (S/N) and orthogonal tables [5, 6] is essential in the Taguchi method..

In the experiment, the larger the better method was used: (nanohardness, elastic modulus, HV)

$$Tta = -10 \log_{10} \frac{1}{n} \sum_{i=1}^n \frac{1}{y_i^2} \quad (1)$$

where:

- $n$  – number of measurements,
- $y$  – analyzed feature.

In this experiment, 4 controlled factors (T, p, d, V) can take 3 values as indicated in Table 2. The number of experiments is equal to the number of combinations L<sup>P</sup>.

Orthogonal tables of parameters P = 4 and number of levels L = 3 were prepared for the experiments. The best suitable orthogonal array is L<sub>9</sub> [4, 5, 7]. The use of 9 experiments have allowed for effective optimization by the G. Taguchi method. The following table shows the values of the controlled variables.

Table 2. The values of the controlled factors used in the preparation of a coating on the substrate of Ti Al 7075

T (°C)	p (bar)	d (mm)	V (mm/s)
700	30	30	300
750	37	40	400
800	45	50	500

After the experiment, the distribution of the results obtained was checked by applying a normal curve to the diagram. Before optimization, basic ANOVA was carried out.



### 3. Results and discussion

As mentioned above, the control parameters were, among others, hardness H and modulus of elasticity E obtained for the load of 20 mN and loading rate of 80 mN/min. For each of the 9 configurations, 49 measurements were made to form a  $180 \times 180 \mu\text{m}$  map containing measurement points every  $30 \mu\text{m}$  (Fig. 1).

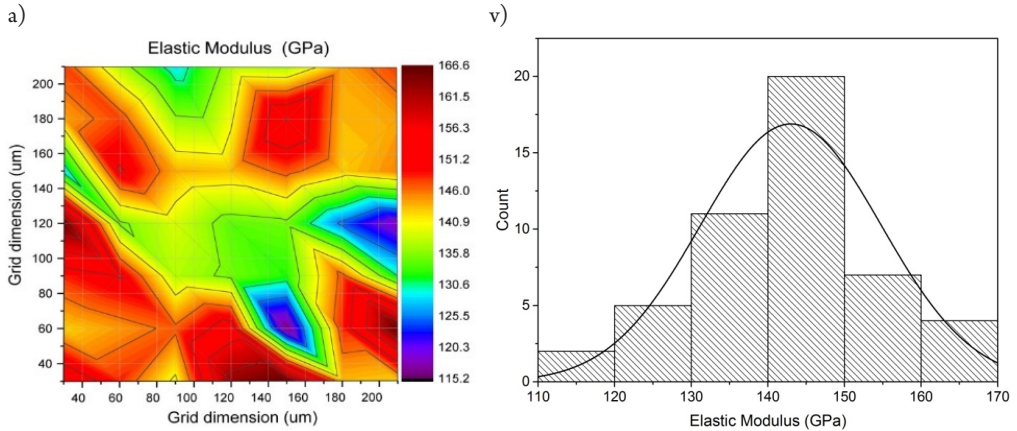


Fig. 1. Map of 49 measurement points obtained for load 20 mN and loading rate 80 mN/min: a) map of elastic modulus, b) distributions of the elastic modulus and normal curve

A normal distribution occurs for most of the values. Deviation of the curve is resulted by the heterogeneity of the coating structure Fig. 1b). Before Taguchi optimization, the normal distribution of the tested values was checked. After performing all 9 experiments, optimal parameters were determined using the method indicated by G. Taguchi [7]. The following tables show the basic statistical parameters characterizing the results.

Table 3. Average value of Eta and expected S/N ratio under optimum conditions  $T = 800^\circ\text{C}$ ,  $p = 45$  bar, coatings distance  $d = 50$  mm,  $V = 500$  mm/s

Effect	Average Eta by Factor Levels (Ti na Al) Mean = 12.8679 Sigma = 1.02618				
	Level	Means	Paramet. Estimate	St.Dev.	St.Error
TEM	T-70C	12.43975	-0.428146	1.708753	0.573454
	T-75C	12.75096	-0.116940	0.520015	0.316349
	T-80C	13.41298	0.545085	0.529871	0.319333
PRESS	p-30	12.56622	-0.301677	1.816080	0.591189
	p-37	12.87566	0.007760	0.224669	0.207937
	p-45	13.16182	0.293917	0.772893	0.385673
DYST	dyst-30	11.87318	-0.994719	1.225356	0.485613
	dyst-40	13.30697	0.439070	0.192684	0.192567
	dyst-50	13.42355	0.555649	0.661100	0.356692
V	V-300	12.22128	-0.646615	1.550298	0.546219
	V-400	13.09531	0.227407	0.808561	0.394471
	V-500	13.28711	0.419209	0.432011	0.288341

Factor	Expected S/N Ratio under Optimum Conditions (Ti na Al) Mean = 12.8679 Sigma = 1.02618 * - effect excluded from model		
	Level	Effect Size	Standard Error
{1}TEM	T-80C	0.54509	0.297873
*PRESS	p-45	0.29392	
{3}DYST	dyst-50	0.55565	0.297873
{4}V	V-500	0.41921	0.297873
Expected S/N		14.38784	

Table 3 shows the best configuration of control parameters, while the following Figure 2 presents the influence of control factors on Eta-value. The pressure has a smaller influence on

Eta, and coating distance has a bigger one. The average Eta for this group of parameter is 12.87. The graphical presentation of control factors indicates their individual impact on Eta (Fig. 2).

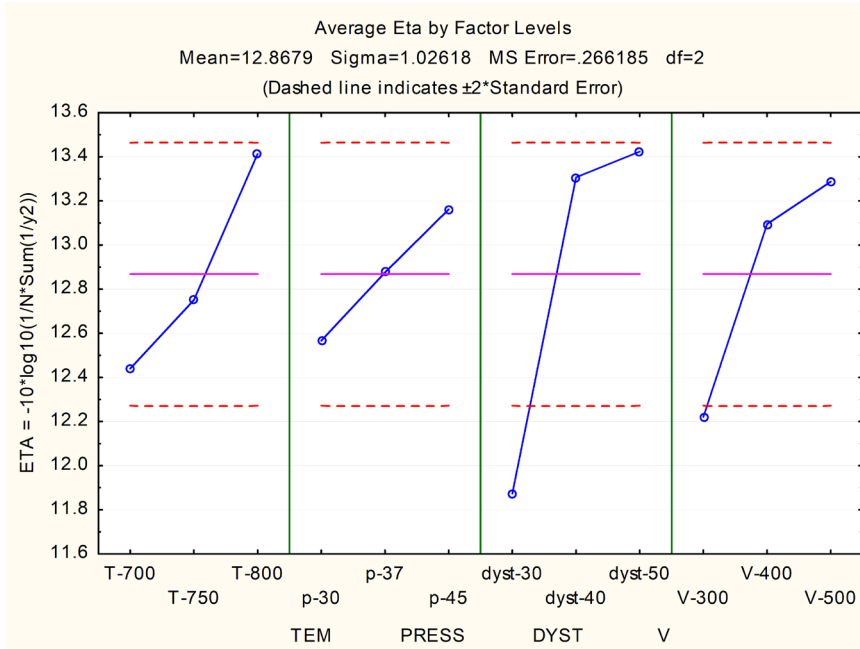


Fig. 2. The influence of individual control factors on the Eta value calculated as the bigger the better

Table 4 shows the values of the control parameters under which H, E and HV take the highest values.

Table 4. Indication of control parameters in S/N group the larger the better

sample	parameters	T (°C)	p (bar)	Coating distance (mm)	V (mm/s)	S/N
Ti 7075	HV, H, E,	800	45	50	500	14.38

From the group of 9 experiments, one was selected using the Taguchi method.

#### 4. Conclusion

An overview of the Taguchi method has been presented and the steps involved in the method were briefly described. Overall, the Taguchi method is a powerful tool which can offer simultaneous improvements in quality and cost. Furthermore, the method can aid integrating costs and engineering functions through the concurrent engineering approach required to evaluate cost over the experimental design. The article presents the Taguchi method applied for the process of optimization and its application in the area of surface engineering. An



example is presented of the method application for the optimization of the parameters value of technological parameters necessary to obtain the required coating of Ti. Application of Taguchi method for scatter value optimization enables one to decrease the number of needed experiments even if there is a deviation from the normal distribution. The optimization process succeeded. The Ti coatings significantly improved their properties as expected.

The Taguchi method emphasizes pushing quality back to the design stage, seeking to design a product which is insensitive or robust to causes of quality problems. It is a systematic and efficient approach to determining the optimum experimental configuration of design parameters for performance, quality, and cost. Principal benefits include considerable time and resource savings; determination of important factors affecting operation, performance and cost; and quantitative recommendations for design parameters which achieve the lowest cost, high quality solutions.

*The work reported herein has been undertaken as part of the Additive Manufacturing Processes and Hybrid Operations Research for Innovative Aircraft Technology Development. Project founded by the National Center for Research and Development under the INNOLOT Programme.*

## References

- [1] Phadke S.M., *Quality Engineering Using Robust Design*, Prentice Hall, Englewood Cliffs, NJ, 1989
- [2] Taguchi G., Konishi S. *Orthogonal Arrays and Linear Graphs*; American Supplier Institute Inc.: Dearborn, MI, USA, 1987.
- [3] Karna S.K., Sahai R., *An Overview on Taguchi Method*, International Journal of Engineering and Mathematical Sciences Jan.–June 2012, Vol. 1, 2319–4537.
- [4] Ross R.J. *Taguchi Techniques for Quality Engineering*, McGraw-Hill, New York 1989.
- [5] Byrne D.M. , Taguchi S., *The Taguchi approach to parameter design*, Quality Progress, vol. 20 (12), 1987, 19–26.
- [6] Taguchi G., Konishi S., *Orthogonal Arrays and Linear Graphs*; American Supplier Institute Inc.: Dearborn, MI, USA, 1987.
- [7] Pietraszek J., *Metoda Taguchi optymalizacji jakości*, [www.statsoft.pl](http://www.statsoft.pl) (access: July 2014).

Tomasz Miłek

tmatm@tu.kielce.pl

Department of Metal Science and Materials Technologies, Faculty of Mechatronics and Mechanical Engineering, Kielce University of Technology

THE EFFECT OF DEGREE OF DEFORMATION ON FORWARD SLIP IN  
EXPERIMENTAL RESEARCH ON COLD LONGITUDINAL ROLLING OF FLAT  
BARS MADE FROM EN AW-6063 ALUMINIUM ALLOY

---

WPLYW STOPNIA ODKSZTAŁCENIA NA WYPRZEDZENIE W BADANIACH  
DOŚWIADCZALNYCH WALCOWANIA WZDŁUŻNEGO NA ZIMNO  
PŁASKOWNIKÓW ZE STOPU ALUMINIUM EN AW-6063

**Abstract**

The paper presents experimental results that concern cold longitudinal rolling of flat bars made from EN AW-6063 aluminium alloy. The investigations aimed at determining the impact of the degree of deformation of material on the forward slip. The forward slips were calculated from Fink's, Drezden's and Vinogradov's formulae. On the basis of investigations of the cold longitudinal rolling of flat bars made from aluminium EN AW-6063, it was found that the forward slip increases with an increase in degree of deformation of material.

**Keywords:** longitudinal rolling, forward slip, EN AW-6063

**Streszczenie**

W artykule przedstawiono wyniki badań doświadczalnych walcowania wzdłużnego płaskowników na zimno ze stopu aluminium EN AW-6063. Ich celem było określenie wpływu stopnia odkształcenia na wyprzedzenie materiału. Wielkość wyprzedzenia była obliczana ze wzorów Finka, Drezdena i Vinogradova. Na podstawie przeprowadzonych badań stwierdzono m.in., że wyprzedzenie wzrasta wraz ze wzrostem stopnia odkształcenia materiału.

**Słowa kluczowe:** walcowanie wzdłużne, wyprzedzenie, EN AW-6063

## 1. Introduction

The rolling process belongs to compressive deformation processes and has been classified on the basis of kinematics, tool and workpiece geometry. Based on kinematics, the rolling process can be classified as longitudinal, cross and skewed [1–3]. In longitudinal rolling (Fig. 1), the workpiece moves through the rolling gap perpendicular to the axis of the rolls, without rotation about the workpiece axis [1–3]. In the exit zone of deformation, the horizontal component of the roll circumferential velocity is less than the workpiece velocity. This phenomenon is called the forward slip [1].

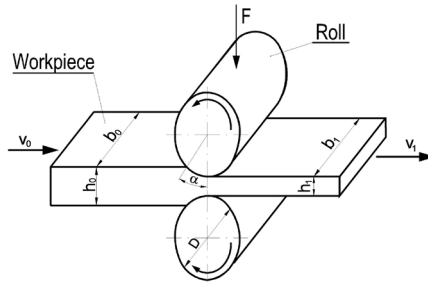


Fig. 1. Nomenclature in flat longitudinal rolling

Values of the forward slip were calculated from Fink's, Drezden's and Vinogradov's formulae [1, 4]. The forward slip is given by the equation of Fink below (1) [1,4]:

$$S_w = \frac{[h_1 + D(1 - \cos \gamma)] \cos \gamma}{h_1} - 1 \quad (1)$$

where:

$h_1$  – height of the material after deformation (mm),

$D$  – the diameter of a mill roll (mm),

$\gamma$  – parting plane angle is given by Ekelund formula (2) [4]:

$$\gamma = \sqrt{\frac{\Delta h}{2D} - \frac{\Delta h}{2D\rho}} \quad (2)$$

where:

$\rho$  – the friction angle can be determined by the following formula (3) [4]:

$$\cos \rho = \frac{1}{\sqrt{1 + \mu^2}} \quad (3)$$

where:

$\mu$  – the friction coefficient is (4) [4]:

$$\mu = \sqrt{\frac{1}{\left(1 - \frac{\Delta h_{\max}}{D}\right)} - 1} \quad (4)$$

where:

$\Delta h_{\max}$  – the high reduction for maximum deformation.

The following formula can be used to obtain the forward slip of Drezden theory (5) [1, 4] :

$$S_w = \frac{R}{h_1} \gamma^2 \quad (5)$$

The forward slip may be estimated from Vinogradov's formula given below (6) [1, 4]:

$$S_w = \frac{\left[ b_0 + \Delta b \left( 1 - \frac{\gamma}{\alpha_{ch}} \right) \right] \left[ h_1 + D(1 - \cos \gamma) \right] \cos \gamma}{(b_0 + \Delta b) h_1} \quad (6)$$

where:

$b_0$  – width of the material before deformation (mm),

$\Delta b$  – spreading of the material (mm),

$\alpha_{ch}$  – roll bit angle can be determined by (7) [4]:

$$\alpha_{ch} = \arccos \left( 1 - \frac{\Delta h}{D} \right) \quad (7)$$

The degree of deformation of materials for rolling are defined in literature [1–4]. They are given in Table 1.

Table 1. Degrees of deformation of material after rolling [4]

Relationship is valid for:	height reduction	spreading	elongation
	of flat bar		
Geometrical relationship, mm	$\Delta h = h_0 - h_1$	$\Delta b = b_1 - b_0$	$\Delta l = l_1 - l_0$
Relative strain	$\varepsilon_{wh} = \frac{\Delta h}{h_0}$	$\varepsilon_{wb} = \frac{\Delta b}{b_0}$	$\varepsilon_{wl} = \frac{\Delta l}{l_0}$
Percent deformation, %	$G_h = 100 \varepsilon_{wh}$	$G_b = 100 \varepsilon_{wb}$	$G_l = 100 \varepsilon_{wl}$
Ratio of strain	$\gamma = \frac{h_1}{h_0}$	$\beta = \frac{b_1}{b_0}$	$\lambda = \frac{l_1}{l_0}$
Logarithmic strain	$\varepsilon_h = \ln \gamma$	$\varepsilon_b = \ln \beta$	$\varepsilon_l = \ln \lambda$

Cold longitudinal rolling process of flat bars and the design of the tooling have been reported in some studies [5–8].

The paper presents experimental results that concern cold longitudinal rolling of flat bars made from aluminium EN AW-6063. The investigations aimed at determining the impact of the degree of deformation of material on the forward slip. The friction factor was determined by formula (4) and forward slips were calculated by means of Fink's, Drezden's and Vinogradov's

formulae (1), (5), (6). The degrees of deformation of material in investigations were defined as relative strain  $\varepsilon_w$  and logarithmic strain  $\varepsilon$  (formulae are given in Table 1). EN AW-6063 alloy aluminium was selected as the testing material in these investigations due to its good formability and wide applications in industry [9, 10].

## 2. Methodology

Samples made from aluminium EN AW-6063 constituted the material for experimental investigations into cold longitudinal rolling process. Chemical composition of material [11] is shown in Table 2.

Table 2. Chemical composition of EN AW-6063 alloy aluminium [%] [11]

Mg	Si	Fe	Ti	Zn	Cr	Mn	Cu	Unspecified other elements		Al minimum
								Each	Total	
0.45–0.9	0.20–0.6	max. 0.35	max. 0.10	max. 0.10	max. 0.10	max. 0.10	max. 0.10	max. 0.05	max. 0.15	rem

Mechanical properties of the material were determined by static tensile testing ( $R_m = 260$  MPa,  $A_{11.3} = 13,8\%$ ,  $Z = 11.2\%$ ). The tensile test was conducted on *LabTest5.20SPI* testing machine (*LABORTECH* firm) with 20 kN force. The machine was calibrated by PN-EN ISO 7500-1:2005 and meets the metrological requirements for class 0.5.

The samples used in experimental investigations into cold longitudinal rolling were made of segments of flat bars with the height of  $h_0 = 5$  mm, width of  $b_0 = 20$  mm and length of  $l_0 = 40$  mm. The longitudinal rolling process is conducted at a special stand – rolling mill DUO-100. The rolling mill has two mill rolls at diameter  $D$  which equals 102 mm [12].

The samples were rolled by using extraction naphtha as lubricant. Extraction naphtha is a complex mixture of hydrocarbons obtained by treatment of petroleum fraction with hydrogen in the presence of a catalyst. It consists of hydrocarbons with a number of carbon atoms ranging from  $C_4$  to  $C_{11}$ , where the range of boiling point is from  $-20^\circ\text{C}$  to  $190^\circ\text{C}$ . It is used as a solvent in the paint and varnish industry as well as in metal and rubber industry. Extraction naphtha is applied to the production of adhesives. It is used to cleaning and degreasing in dry cleaners and tanneries as well as in service workshops. Extraction naphtha is a colorless liquid with a flash point below  $0^\circ\text{C}$ . Its density at  $15^\circ\text{C}$  ranges from 0,62 to 0,88 g/cm<sup>3</sup>. It can be dissolved in most organic solvents, hydrocarbons, alcohols, ethers, carbon disulphide, carbon tetrachloride and chloroform [13].

### 3. Results and analysis

The friction factor was determined by the method of the roll bite angle. This method involves rolling samples at maximum degree of deformation. On the basis of geometric parameters of samples after deformation measurements, the value of the roll bite angle ( $\alpha_{ch} = 15.58^\circ$ ) friction factor ( $\mu = 0.28$ ) and forward slips were calculated from formulae (1)÷(7). The deformation ratios of material in paper were defined as relative strain  $\varepsilon$  and logarithmic strain  $\varepsilon$ : on the high  $\varepsilon_{wh}$ ,  $\varepsilon_h$ ; on the width  $\varepsilon_{wb}$ ,  $\varepsilon_b$  and on the length  $\varepsilon_{wl}$ ,  $\varepsilon_l$  respectively. The nomenclature in table formulae is shown in Fig. 1. For the calculation of the forward slip formulae, the following have been considered: Fink (1), Drezden (5) and Vinogradov (6). Of these formulae, those of Fink and Drezden do not take into account spreading of material  $\Delta b$  and its influence on the forward slip. However, in all these formulae the parting plane angle  $\gamma$  is calculated neglecting the influence of spreading.

The influence of relative strain and logarithmic strain on the forward slip in cold longitudinal flat rolling for specimens made from aluminium EN AW-6063 is shown in diagrams (in Fig. 2 and Fig. 3, respectively).

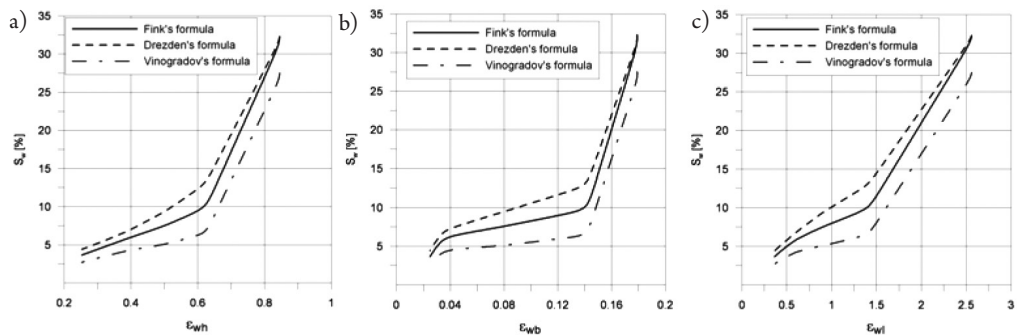


Fig. 2. Influence of relative strain on the forward slip in cold longitudinal flat rolling for specimens made from EN AW-6063 alloy aluminium (extraction naphtha as a lubricant of rolls): a) strain calculated on height  $\varepsilon_{wh}$ , b) strain calculated on width  $\varepsilon_{wb}$ , c) strain calculated on length  $\varepsilon_{wl}$

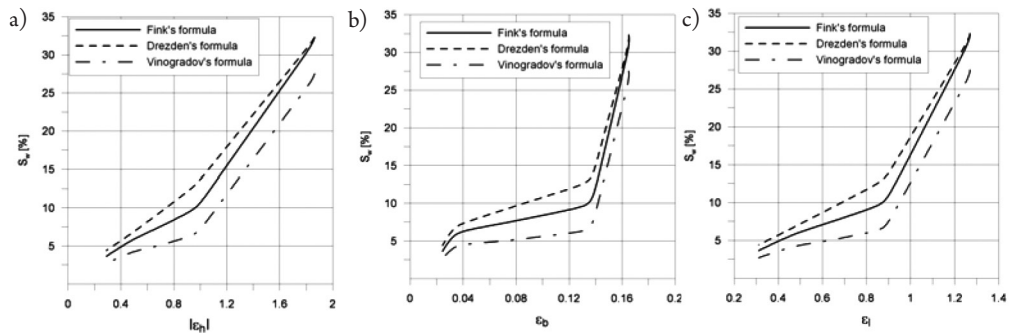


Fig. 3. Effect of logarithmic strain on the forward slip in cold longitudinal flat rolling for specimens made from EN AW-6063 alloy aluminium (extraction naphtha as a lubricant of rolls): a) strain calculated on height  $\varepsilon_h$ , b) strain calculated on width  $\varepsilon_b$ , c) strain calculated on length  $\varepsilon_l$

The values of logarithmic strain on the high  $\varepsilon_h$  were less than zero and therefore they were assumed as algebraic modules in the graph (Fig. 3a). Calculated forward slips increase with an increase in relative and logarithmic strain (extraction naphtha as lubricant).

#### 4. Summary

On the basis of investigations carried out into cold longitudinal rolling of flat bars made from aluminium EN AW-6063 (extraction naphtha as a lubricant of rolls), it can be stated as follows:

1. Calculated forward slips  $S_w$  in all cases (Fink's, Drezden's and Vinogradov's formulae) increase with an increase in relative and logarithmic strain.
2. Values of forward slips calculated by means of Fink's, Drezden's and Vinogradov's formulae (1), (5), (6) did not differ much at the same friction factor  $\mu = 0.28$  and in all cases considered they were the greatest for Drezden's formula (5), whereas the lowest values were obtained for Vinogradov's formula (6).
3. Fink's (1), Drezden's (5) and Vinogradov's (6) formulae, used for calculating the forward slip in longitudinal rolling can be applied in engineering practice. Its knowledge is necessary to determine the workpiece velocity in the exit zone of deformation.

#### References

- [1] Wusatowski Z., *Fundamentals of rolling*, Śląsk, Katowice 1969.
- [2] Lange K., *Handbook of metal forming*, McGraw-Hill Book Company, 1985.
- [3] Morawiecki M., Sadok L., Wosiek E., *Przeróbka plastyczna. Podstawy teoretyczne*. Wydawnictwo Śląskie, Katowice 1977.
- [4] Sińczak J. et al., *Procesy przeróbki plastycznej – ćwiczenia laboratoryjne. Podstawy teoretyczne i wykonawstwo ćwiczeń*. AKAPIT, Kraków 2001.
- [5] Engler O., Schäfer C., et al., *Flexible rolling of aluminium alloy sheet—Process optimization and control of materials properties*, Journal of Materials Processing Technology, Vol. 229, 2016, 139–148.
- [6] Gjønnnes, L., Andersson B., *Mechanisms of surface deformation during cold rolling of aluminium*, Journal of Materials Science, Vol. 33, 1998, 2469–2476.
- [7] Ścieżor W., Mamala A., Kwaśniewski P., *Analysis of properties of selected aluminium alloys, obtained by twin roll casting method and subjected to cold rolling process*, Key Engineering Materials, Vol. 641, 2015, 202–209.
- [8] Grydin O., Bondarenko S., Stolbchenko M., et al., *Rolling of flat Aluminum strips with tailored mechanical properties*, Materials Science Forum, Vol. 854, 2016, 87–92.
- [9] Hirsch J., *Aluminium in innovative light-weight car design*, Materials Transactions, Vol. 52, 2011, 818–824.

- [10] Davis J.R., *Aluminum and Aluminum Alloys*, ASM Specialty Handbook, ASM International, Ohio 1993.
- [11] EN 573-3:2013 Skład chemiczny i rodzaje wyrobów przerobionych plastycznie. Cz. 3 Skład chemiczny i rodzaje wyrobów.
- [12] Dokumentacja techniczna walcarki DUO-100. WMiBM. Politechnika Świętokrzyska. Poland
- [13] Karta charakterystyki substancji chemicznej zgodnej z Rozporz. (UE) nr 453/2010. Benzyna ekstrakcyjna niskoaromatyczna. PPHU „Chem-Rozlew”, 2013, s. 10. Poland







Łukasz J. Orman

orman@tu.kielce.pl

Faculty of Environmental, Geomatic and Energy Engineering, Kielce University  
of Technology

Norbert Radek

Faculty of Mechatronics and Machine Design, Kielce University of Technology

Andrej Kapjor

Faculty of Mechanical Engineering, University of Zilina, Slovakia,

Dariusz Karpisz

Institute of Applied Informatics, Cracow University of Technology

## PASSIVE METHODS OF BOILING HEAT TRANSFER ENHANCEMENT

---

### PASYWNE METODY INTENSYFIKACJI WYMIANY CIEPŁA PRZY WRZENIU

#### **Abstract**

The paper presents the issue of boiling heat transfer enhancement with the use of different passive techniques, namely the application of wire mesh coatings, capillary porous layers, pin – fins and laser treatment. Enhanced boiling heat transfer has been described as well as the research data of the authors that deals with microstructural coatings. The conducted experimental tests confirm the possibility of increasing heat fluxes transferred at the same superheat value due to the use of heat transfer enhancing techniques.

**Keywords:** boiling heat transfer, microstructures

#### **Streszczenie**

W artykule przedstawiono zagadnienie intensyfikacji wymiany ciepła przy wrzeniu poprzez zastosowanie różnych pokryć tj. struktur siatkowych, kapilarno – porowatych, mikrożeber czy obróbki laserowej. Przybliżono zagadnienie intensyfikacji wymiany ciepła przy wrzeniu i opisano wyniki badań autorów, dotyczące intensyfikacji wrzenia na mikropowierzchniach strukturalnych. Przeprowadzone badania potwierdzają możliwości zwiększenia gęstości odbieranych strumieni ciepła przy tym samym przegrzaniu.

**Słowa kluczowe:** wymiana ciepła przy wrzeniu, mikrostruktury

## 1. Introduction

Nucleate boiling enables the transfer of significant heat fluxes as small temperature differences. Such phase – change heat exchangers are widely used in many engineering applications such as refrigeration, cooling of electronic devices, etc. The enhancement of heat transfer can occur through passive or active techniques (which require the supply of additional energy and, thus, are much less common). The use of specially designed microstructural coatings is a passive method and is the focus of this paper.

The article deals with metal wire meshes, capillary porous structures produced with fine metal fibers, pin – fins made with mechanical treatment as well as laser treated surfaces. Generally, any surface modification can influence heat flux dissipated from the heaters, however, some methods of heat transfer enhancement are very efficient, while others produce the opposite effect and actually reduce heat flux transferred from the surface.

## 2. Boiling heat transfer on microstructure coated surfaces

There are many kinds of microstructures used for boiling heat transfer enhancement. They range from surface treatment with emery paper (to produce proper roughness) to specially designed and produced coatings.

Capillary porous structures made of stainless steel were investigated by Kalawa et al. [3] and made of copper by Wójcik [8]. The microstructures were produced by sintering in the reduction atmosphere. The results prove a favourable impact of the covering on heat flux enhancement in comparison to the smooth surface.

Finned surfaces are also widely known to enhance heat transfer. Pin – fins used for boiling augmentation can be effective in both pool and flow boiling. Pastuszko [6] performed tests of FC-72 and water pool boiling on the fin arrays covered with a porous structure and without any covering. Microfins of two heights were used: 0.5 mm and 1.0 mm. It was reported that in comparison with plain microfins, heat transfer coefficient of structures covered with the porous layer could be two times as high. Orman [4] presented experimental results of water and ethyl alcohol boiling on horizontal surfaces covered with microfins of various heights and distance between them. The application of such pin – fins considerably enhanced boiling in relation to the surface without the fins. Heat flux was even ca. eight times higher for the microstructure covered heater.

Hasegawa et al. [2] investigated a different type of coating, namely meshes. The tests were performed on a horizontal heater of 15 mm in diameter and covered with one or two meshes made of stainless steel and bronze. The considered meshes had the wire diameter of 0.065 – 0.295 mm. It was stated in the conclusions that the application of mesh layers improves heat transfer. Asakavičjus et al. [1] considered boiling of R-113, ethyl alcohol as well as water in the heat pipe. The meshes were made of copper and stainless steel, while their number was 2, 8 and 12 layers applied on the surface. The authors also noticed a favourable impact of the meshes on boiling heat transfer. However, this effect diminishes with rising heat flux

values. Heat transfer coefficient was 1.8 to 3.5 times higher in the case of water boiling than of ethanol and R-113. The material from which the coating was made also played a significant role. The use of the copper mesh led to heat transfer coefficient being 1.3 times higher than in the case of stainless steel coating.

The experiments performed by the authors of the present paper generally confirm the possibility of heat transfer intensification with the application of mesh microstructures. Fig. 1 presents the ratio of heat flux dissipated from the heater (on which copper meshes were sintered) to the heat flux dissipated from the smooth heater – without any coating. The number of meshes forming each coating ranged from one to three. Two values of superheat (the difference between the heater temperature and the saturation temperature of the liquid) have been selected for analysis, namely 7 K and 10 K.

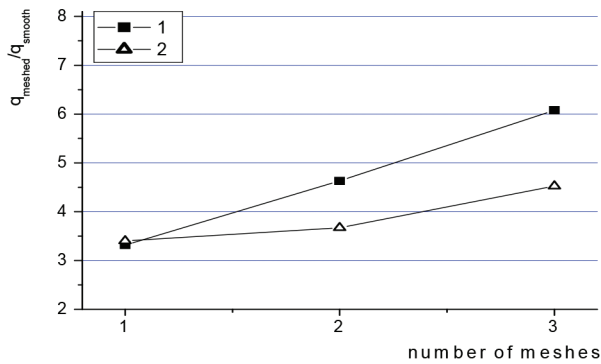


Fig. 1. The enhancement ratio for different number of mesh layers and two superheat values (1–7 K, 2–10 K) – data according to [5] for distilled water as the boiling liquid

The analysis of the above figure indicates that the highest enhancement possibilities within the considered superheat values are offered by the coating that consists of three mesh layers. In this case the heat flux transferred from the heating surface with the microstructural covering was over six times higher in comparison with the smooth surface. The lowest value of the ratio amounted to ca. 3.4 and was almost identical for both temperature differences. However, it needs to be noted that the most significant enhancement occurred for the lower value of superheat. This observation typically confirms literature data on this issue.

### 3. Laser treated heat exchangers

The authors' tests were performed on a resistance ribbon (Fig. 2) whose dimensions are ca. 40 mm x 4 mm x 0.5 mm. The ribbon itself served as a heater surface as electricity was supplied to it. The subsequent laser treatment was performed with a Nd:YAG type laser working in the pulse mode. The laser spot diameter was 0.7 mm, the beam shift rate: 1200 mm/min, the nozzle-sample distance: 6 mm, while the pulse duration was 0.45 ms.

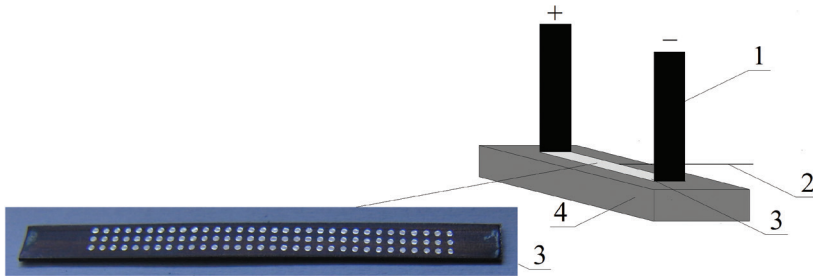


Fig. 2. Heater unit: 1 – electrical connections, 2 – thermocouple, 3 – sample (heater surface), 4 – bakelite insulation plate

As a result of the laser treatment, the morphology of the heater surface was changed. Cavities of different geometry are produced. Figures 3–5 present the morphological details of three laser treated samples.

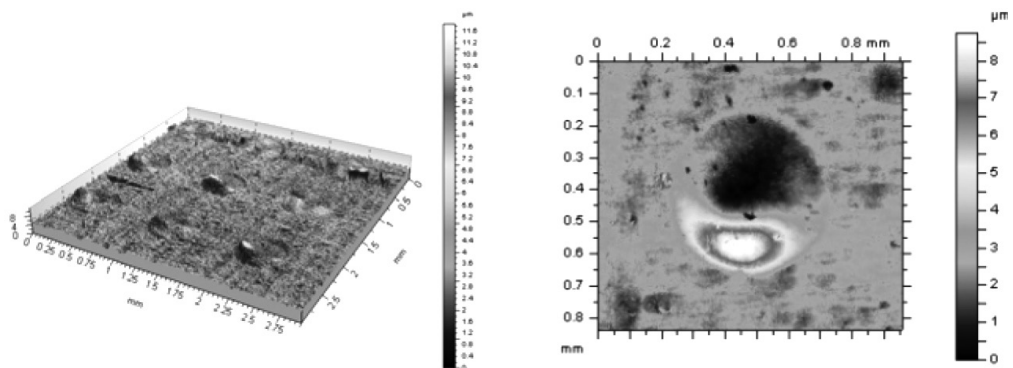


Fig. 3. Sample no 1; cavity depth: 1.9  $\mu\text{m}$ , cavity diameter: 0.22 mm

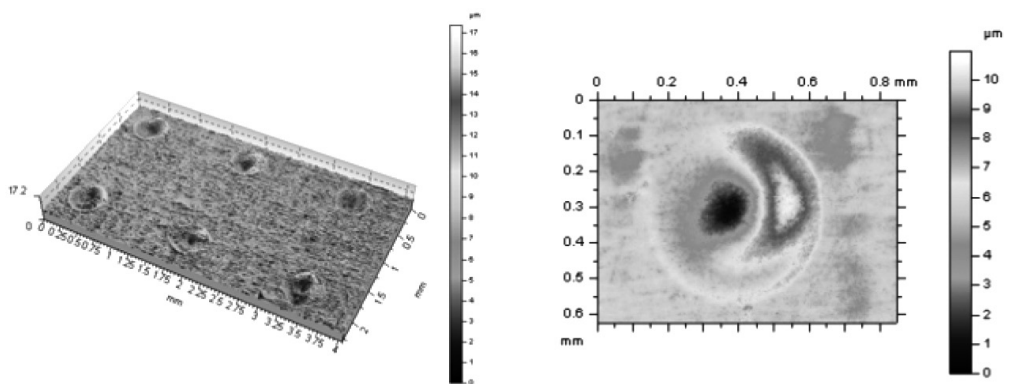


Fig. 4. Sample no 2: cavity depth: 4.0  $\mu\text{m}$ , cavity diameter: 0.21 mm

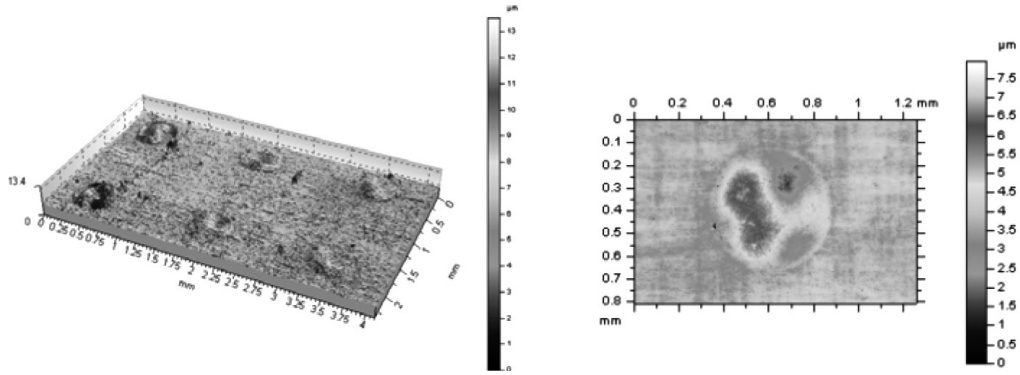


Fig. 5. Sample no 3: cavity depth: 2.0  $\mu\text{m}$ , cavity diameter: 0.20 mm

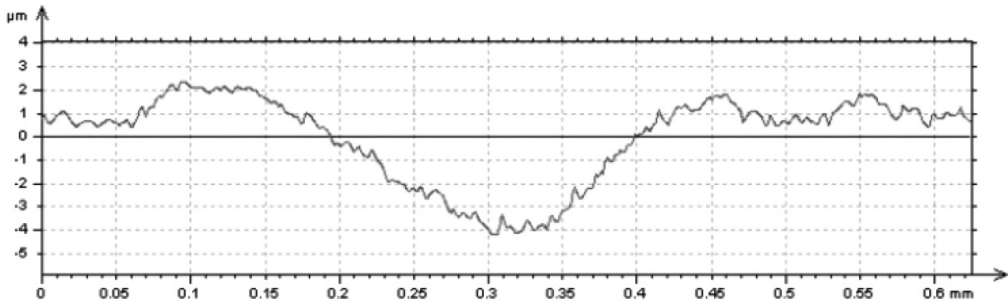


Fig. 6. Surface profile of sample no 2.

The tests were carried out in such a way that the experimental stand presented in Fig. 2 was located in the pool of liquid (distilled water and ethyl alcohol). Electric current supplied to the resistance ribbon of known electrical resistance value increased its temperature as well as the temperature of the liquid in the vessel. This supply was controlled and changed with the autotransformer. The temperature of the heater was determined with a K-type thermocouple. During the measurements, temperature was recorded as a function of rising heat flux value. As a consequence, the thermal performance of the surface modified with the laser beam could be determined as a function of increasing heat flux dissipated to the pool of liquid vs. superheat values.

The testes were primarily focused on the enhancement ratio, which considered heat flux transferred from the laser treated surfaces to the heat flux dissipated from the smooth reference surface of the ribbon. The best performance was provided with sample no 1. In the case of this surface the heat flux was almost two times higher than for the smooth surface of the resistance ribbon without any additional modification. Consequently, the produced heat exchangers can be smaller (and, thus lighter, which is vital for practical applications) or transfer twice as much heat at the same temperature difference as in the case of using smooth heat exchanging surfaces. Differences between the two boiling liquids used in the experiments (water and ethanol) have been observed for different samples. Boiling of ethanol

produces smaller bubbles (due to the lower value of surface tension for this alcohol) and, thus, the thermal performance of surfaces with smaller cavities produced with the laser beam should be better.

#### 4. Conclusions

Boiling heat transfer is a phase – chance phenomenon and provides a possibility of dissipating considerable heat fluxes. These values can be even higher if special surface modification techniques are used, for example metal mesh microstructures, capillary porous coatings, microfins or laser treatment of the heaters. As a consequence of the application of these methods, heat flux values dissipated from the heating surfaces at the same temperature differences can be much higher than in the case of smooth surfaces. Also, heat exchangers produced with such surfaces can be smaller due to reduced surface areas. Although the test results presented in the paper deal with pool boiling mode, microstructures can also affect the enhancement of flow boiling heat transfer as indicated by Piasecka [7].

#### References

- [1] Asakavičius I.P., Žukauskas A.A., Gajgalis V.A., Eva V.K., *Teplootdača freona-113, etilovogo spirta i vody v setčatych fitiljach*, Lietuvos TSR Moksly akademijos darbai, B serija, I (104), 1978, 87–93.
- [2] Hasegawa S., Echigo R., Irie S., *Boiling characteristics and burnout phenomena on heating surface covered with woven screens*, Journal of Nuclear Science and Technology, vol. 12 (11), 1975, 722–724.
- [3] Kalawa W., Wójcik T.M., Piasecka M., *Heat transfer research on enhanced heating surfaces in pool boiling*, EPJ Web of Conferences, 143, 2017, 02048-1-6.
- [4] Orman Ł.J., *Enhancement of pool boiling heat transfer with pin-fin microstructures*, Journal of Enhanced Heat Transfer, vol. 23(2), 2016, 137–153.
- [5] Orman Ł.J., Orzechowski T., *Analysis of boiling heat transfer on the non-isothermal surface covered with selected wire mesh structures*, 7th World Conference on Experimental Heat Transfer ExHFT-7, 28 June - 03 July, Kraków 2009, 2159–2166.
- [6] Pastuszko R., *Pool boiling on micro – fin array with mesh structures*, International Journal of Thermal Sciences, vol. 49(12), 2010, 2289–2298.
- [7] Piasecka M., *Heat transfer research on enhanced heating surfaces in flow boiling in a minichannel and pool boiling*, Annals of Nuclear Energy, 73, 2014, 282–293.
- [8] Wójcik T., *Heat transfer enhancement and surface thermostabilization for pool boiling on porous structures*, EPJ Web of Conferences, 25, 2012, 01100-1-6.

## **LIST OF REVIEWERS OF TECHNICAL TRANSACTIONS 2018:**

Vadym Abyzov, Kyiv's National University of Culture and Arts, Ukraine  
Mohamad Achour, Mirpur University of Science and Technology, Pakistan  
Victor Aguilar, Auburn University, USA  
Taliat Azizov, Pavlo Tychyna Uman State Pedagogical University, Ukraine  
Dmytro Babyuk, Chernivtsi National University, Ukraine  
Tomasz Baczyński, Cracow university of Technology, Poland  
K. Balachandran, Bharathiar University, India  
Dalibor Barta, University of Žilina, Slovakia  
Nagaraj Basavegowda, Yeungnam University, South Korea  
Krzysztof Bieda, Warsaw University of Technology, Poland  
Agata Bonenberg, Politecnico di Milano, Italy  
Joanna Bzówka, Silesian University, Poland  
Lukas Capek, Technical University of Liberec, Czech Republic  
Catalin Capraru, Technische Universität Wien, Austria  
Jaroslav Chabaniuk, Lublin University of Technology, Poland  
Pavel Chebotarev, University at Albany, USA  
Malgorzata Chorowska, Wroclaw University of Science and Technology, Poland  
Jacek Chróścielewski, Gdańsk University of Technology, Poland  
Ewa Cichy-Pazder, Kielce University of Technology, Poland  
Stephane Commend, GeoMod Ingénieurs Conseils SA, Switzerland  
Marek Czernicki, École nationale supérieure de chimie de Lille, France  
Jiri David, Technical University of Ostrava, Czech Republic  
Wojciech Dąbrowski, Cracow University of Technology, Poland  
Jaroslav Dorogy, National Technical University of Ukraine, Ukraine  
Anatoliy Doroshenko, National Academy of Sciences of Ukraine, Ukraine  
Mykhaylo Dorozhovets, Rzeszow University of Technology, Poland  
Timothy Douglas, Lancaster University, UK  
Ewa Dresler, The Institute of Heavy Organic Synthesis „Blachownia” (ICSO) in Kędzierzyn-Koźle, Poland  
Łukasz Drobiec, Silesian University of Technology, Poland  
Jewgeni Dshalalow, Berlin Technical University, Germany  
Krzysztof Duda, AGH University of Science and Technology, Poland  
Leszek Dulak, Silesian University of Technology, Poland  
Ludmila Dulebová, Technical University of Kosice, Slovakia  
Ulyana Dzelendzyak, Lviv Polytechnic National University, Ukraine  
Piotr Dziurdzia, AGH University of Science and Technology, Poland  
Mark Everett, Texas A&M University, USA  
Tomasz Falborski, Gdańsk University of Technology, Poland



Albert Fekete of Szent István University, Hungary  
Ado Franchini, Politecnico di Milano, Italy  
Gabriel Furtos, Babes-Bolyai University, Romania  
Matija Gams, Slovenian National Building And Civil Engineering Institute, Slovenia  
Richard Gawel, AGH University of Science and Technology, Poland  
Wiesław Gazda, Silesian University of Technology, Poland  
Justin Geistefeldt, Ruhr University Bochum, Germany  
Alfred Geroldinger, University of Graz, Austria  
Amir SJ Gilani, University of California, USA  
Aneta Gluszek, Cracow University of Technology, Poland  
Sergey Golitsynskiy, University of Northern Iowa, USA  
Beata Grabowska, AGH University of Science and Technology, Poland  
Tomisław Gołębiowski, Cracow University of Technology, Poland  
Andrzej Gruchot, University of Agriculture in Krakow, Poland  
Jacek Gyurkovich, Cracow University of Technology, Poland  
Mateusz Gyurkovich, Cracow University of Technology, Poland  
Andrew Hale, University of Exeter, England  
Carter Hamilton, Miami University, USA  
Tomáš Hanák, Brno University of Technology, Czech Republic  
Hadi Hasanzadehshooili, University of Guilan, Iran  
Ryszard Hejmanowski, AGH University of Science and Technology, Poland  
Leonel Francisco Castaneda Heredia, University of Technology and Life Sciences, Colombia  
Vladimir Hlavna, University of Žilina, Slovakia  
Karin Hofert, Polytechnic University of Catalonia, Spain  
Šárka Hošková-Mayerová, University of Defence, Czech Republic  
Eugeniusz Hotała, Wrocław University of Technology, Poland  
Martin Hudec, Slovak University of Technology, Slovakia  
Jacek Hulimka, Silesian University of Technology, Poland  
Ivan Hyben, Technical University of Košice, Slovakia  
Yuliya Idak, Lviv Polytechnic National University, Ukraine  
Orest Ivakhiv, Lviv Polytechnic National University, Ukraine  
Ilona Jacyna-Gołda, Warsaw University of Technology, Poland  
Ernest Jamro, AGH University of Science and Technology, Poland  
Artur Jasiński, Andrzej Frycz Modrzewski Krakow University, Poland  
Natalia Junakova, Technical University of Kosice, Slovakia  
Matevž Juvancic, University of Ljubljana, Slovenia  
Elżbieta Kaczmarska, Andrzej Frycz Modrzewski Krakow University, Poland  
Mikołaj Karpiński, University of Bielsko-Biala, Poland  
Krzysztof Kawrowski, Gdańsk University of Technology, Poland  
Dominika Tetiana Kazantseva, Lviv Polytechnic National University, Ukraine  
Ivan Kelnar, Institute of Macromolecular Chemistry, Czech Republic  
Tomasz Kisilewicz, Cracow University of Technology, Poland

Katarzyna Klemm, Lodz University of Technology, Poland  
Krzysztof Kluza, AGH University of Science and Technology, Poland  
Radoslaw Klosinski, University of Zielona Góra, Poland  
Michał Knauff, Warsaw University of Technology, Poland  
Andrzej Kosecki, AGH University of Science and Technology, Poland  
Wojciech Kosiński, Andrzej Frycz Modrzewski Krakow University, Poland  
Peter Kravets, National Technical University of Ukraine, Ukraine  
Christian Kreisler, The Helmut Schmidt University, Germany  
Katarina Kristanova, Slovak University of Technology in Bratislava, Slovakia  
Jadwiga Królikowska, Cracow University of Technology, Poland  
Dominika Kuśnierz-Krupa, Cracow University of Technology, Poland  
Jan Król, Warsaw University of Technology, Poland  
Jurij Kryworuczko, Lviv Polytechnic National University, Ukraine  
Józef Kuczmaszewski, Lublin University of Technology, Poland  
Mieczysław Kula, Silesian University, Poland  
Karolina Kurek, University of Agriculture in Krakow, Poland  
Vincent Kvočák, Technical University of Košice, Slovakia  
Tone Lerher, University of Maribor, Slovenia  
J. Krzysztof Lenartowicz, Lublin University of Technology, Poland  
Paweł Lewiński, The Building Research Institute, Poland  
Yasser Loksha, Sinai University, Egypt  
Zbigniew Lozia, Warsaw University of Technology, Poland  
Krzysztof Ludwinek, Kielce University of Technology, Poland  
Katarzyna Łakomy, Cracow University of Technology, Poland  
Aneta Łukaszek-Chmielewska, Main School of Fire Service, Poland  
Mateusz Malinowski, University of Agriculture in Krakow, Poland  
Carlos Marmolejo Duarte, Polytechnic University of Catalonia, Spain  
Massimo Martelli, IMAMOTER – CNR, Italy  
Justyna Martyniuk-Pęczek, Gdańsk University of Technology, Poland  
Kaisa Matomäki, University of Turku, Finland  
Jerzy Merkiś, Poznan University of Technology, Poland  
Czesław Miedziałowski, Białystok University of Technology, Poland  
Ryszard Miller, AGH University of Science and Technology, Poland  
Phu Minh Vuong Nguyen of University of Chile, Santiago, Chile  
Waldemar Minkina, Czestochowa University of Technology, Poland  
Moghtada Mobedi, Shizuoka University, Japan  
Susana Mora Alonso-Muñoyerro, Technical University of Madrid, Spain  
Ryszard Moszumański, Cracow University of Technology, Poland  
Konstantin Naumenko, Otto-von-Guericke-Universität Magdeburg, Germany  
Pavel Neuberger, Czech University of Life Sciences in Prague, Czech Republic  
P.L. Ng, The University of Hong Kong, Hong Kong  
Paweł Nowak, Jagiellonian University, Poland

Janusz Nowicki, Institute of Heavy Organic Synthesis „Blachownia”, Poland  
Rafał Obrzud, Karakas & Français SA, Switzerland  
Paweł Ocoń, Cracow University of Technology, Poland  
Farouk Okasha, Mansoura University, Egypt  
Jan Ondrus, ESSEC Business School, France  
Marek Pabich, Lodz University of Technology, Poland  
Krzysztof Pacholski, Lodz University of Technology, Poland  
Marian Paluch, Silesian University of Technology, Poland  
Vladimir N. Paramonov, National Research University Higher School of Economics, Russia  
Doncho Partov, University of Structural Engineering and Architecture (VSU) “Lyuben Karavelov”, Sofia, Bulgaria  
Iwona Pasiecznik, Wrocław University of Science and Technology, Poland  
Hartmut Pasternak, Brandenburg University of Technology Cottbus – Senftenberg, Germany  
Zbigniew Pawelski, Lodz University of Technology, Poland  
Bonawentura Maciej Pawlicki, The Podhale State Higher Vocational School in Nowy Targ, Poland  
Michael Peterek, Frankfurt University of Applied Sciences, Germany  
Szczepan Piszczatowski, Bialystok University of Technology, Poland  
Daniel Piteruszcak, Kazimierz Pulaski University of Technology and Humanities Radom  
Matthias Pietsch, Anhalt University of Applied Sciences, Germany  
Zbigniew Pilch, Silesian University of Technology, Poland  
Julian Plewa, Münster University of Applied Sciences, Germany  
Elżbieta Płaza, KTH Royal Institute of Technology, Sweden  
Paweł Popielski, Warsaw University of Technology, Poland  
Elżbieta Radziszewska-Zielina, Cracow University of Technology, Poland  
Janusz Rak, Rzeszow University of Technology, Poland  
Mar Ríos-Gutiérrez, University of Valencia, Spain  
Oleksandr Rolik, National Technical University of Ukraine, Ukraine  
Piotr Rosik, Institute of Geography and Spatial Organization, Polish Academy of Science, Poland  
Agnieszka Roznowska-Sadraei, Tower of London, England  
Ludmiła Ruban, Kiev National University of Construction and Architecture, Ukraine  
Adam Ruszaj, Cracow University of Technology, Poland  
Dorota Rutkowska-Zbik, Jagiellonian University, Poland  
Boris Ryabko, Siberian State University, Russia  
Tomasz Rydzkowski, University of Warmia and Mazury in Olsztyn, Poland  
Tomasz Rydzkowski, Technical University of Koszalin, Poland  
Katarzyna Rzeszut, Poznan University of Technology, Poland  
Sarah Sadykova, Eurasian National University Astana, Kazakhstan  
Michael Scheffler, Otto-von-Guericke-Universität Magdeburg, Germany  
Jan-Christoph Schlage-Puchta, University of Rostock, Germany  
Grażyna Schneider-Skalska, Cracow University of Technology, Poland

Subarna Shakya Tribhuvan University, Katmandu  
Dmitry Sidorov, Dnepropetrovsk National University, Ukraine  
Krzysztof Skabek, Silesian University of Technology, Poland  
Massoud Sofi, University of Melbourne, Australia Alicja Sołowczuk, West Pomeranian University of Technology Szczecin, Poland  
Adolf Sotoca, Polytechnic University of Catalonia, Spain  
Marzena Smol, Mineral and Energy Economy Research Institute, Polish Academy of Science, Poland  
Jacek Snamina, AGH University of Science and Technology, Poland  
Sławomir Spadło, Kielce University of Technology, Poland  
Michael Sprysch, University of Applied Sciences and Arts HAWK, Germany  
Arunachalam Srinivasan, Jaypee University of Engineering and Technology, Guna, India  
Klaudia Stala, Cracow University of Technology, Poland  
Ekaterina Stepanova, Perm State University, Russia  
R. Sundaravadivelu, Indian Institute of Technology Madras, India  
Andrzej Strużyński, University of Agriculture in Krakow, Poland  
Dariusz Sykutera, University of Technology and Life Sciences in Bydgoszcz, Poland  
Piotr Szatkowski, AGH University of Science and Technology, Poland  
Marek Szostak, Poznan University of Technology, Poland  
Maciej Szumigała, Poznan University of Technology, Poland  
Adam Szymkiewicz, Gdańsk University of Technology, Poland  
Rafał Ślęfarski, Poznan University of Technology, Poland  
Martin Štroner, Czech Technical University of Technology, Czech Republic  
Ewa Szalińska von Overdijk, AGH University Science and Technology, Poland  
Dawid Taler, Cracow University of Technology, Poland  
Tadeusz Tatara, Cracow University of Technology, Poland  
Barabra Tchórzewska-Cieślak, Rzeszow University of Technology, Poland  
Vasyl Tesyluk, Lviv Polytechnic National University, Ukraine  
Renata Tomczak-Wandzel, Aquateam COWI, Norway  
Sylwia Tomecka-Suchoń AGH University of Science and Technology, Poland  
Cezary Toś, Cracow University of Technology, Poland  
Zbigniew Trzeciakiewicz, Silesian University of Technology, Poland  
Paweł Twardowski, Poznan University of Technology, Poland  
M. Uthayakumar, Kalasalingam University, India  
Yasushi Uematsu, Tohoku University, Japan  
Elżbieta Urbańska-Galewska, Gdansk University of Technology, Poland  
Aleksander Urbański, Cracow University of Technology, Poland  
Andrea Vallati, Università di Roma, Italy  
Krzysztof Wach, Cracow University of Economics, Poland  
Petr Waclavik, Institute of Geonics of the CAS, Czech Republic  
Stanisława Wehle-Strzelecka, Kielce University of Technology, Poland  
Tomasz Węclawowicz, Andrzej Frycz Modrzewski Krakow University, Poland

Tomasz Węgiel, Cracow University of Technology, Poland  
Marek Węglowski, Instytut Spawalnictwa, Poland  
Dariusz Więckowski, Automotive Industry Institute, Poland  
Joanna Wilk, Rzeszow University of Technology, Poland  
Ersel Yilmaz, Adnan Menderes University, Turkey  
Agata Zachariasz, Cracow University of Technology, Poland  
Fedro Zazueta, University of Florida, USA  
Shouliang Zhao, Huazhong University of Science and Technology, Wuhan, China  
Wiesław Zwierzycki, Poznan University of Technology, Poland  
Monika Żubrowska-Sudoł, Warsaw University of Technology, Poland